The STAR Beam Use Request for Run-21, Run-22 and data taking in 2023-25

The STAR Collaboration

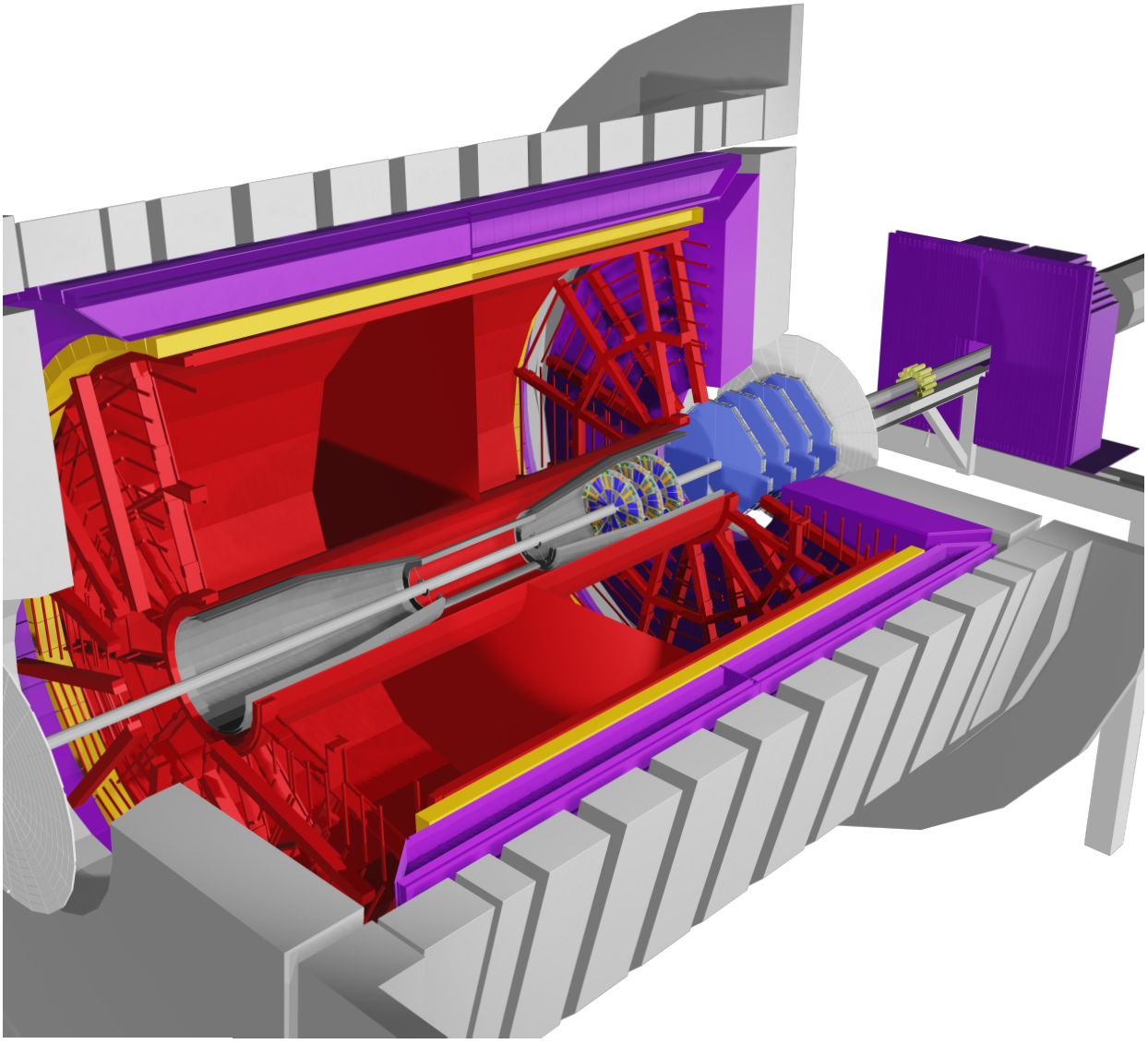

Executive Summary

This Beam Use Request outlines the physics programs that compels the STAR collaboration to request data taking during the years 2021-2025.

STAR's **highest scientific priorities** for Run-21 and Run-22 are to complete the NSAC-endorsed second phase of the Beam Energy Scan (BES-II) program, and initiate the "must-do" Cold QCD forward physics program enabled by the newly completed suite of forward detectors via the collection of transversely polarized p+p data at 510 GeV. From 2023-25 we will use a combination of soft and hard probes to explore the microstructure of the QGP and continue the forward physics program via the collection of high statistics Au+Au, p+Au and p+p data at $\sqrt{s_{\rm NN}}$ = 200 GeV.

The BES-II program has so far been very successful. As shown in Table 1, we have recorded collisions at $\sqrt{s_{\rm NN}}$ = 9.2-27 GeV in collider mode, and $\sqrt{s_{\rm NN}}$ = 3-7.7 GeV in fixed target (FXT) mode. We expect to complete data collection at $\sqrt{s_{\rm NN}}$ = 9.2 GeV by the end of Run-20b. In Run-21, as shown in Table 2, our number one priority is to complete the BES-II by recording 100 M good events at $\sqrt{s_{\rm NN}}$ = 7.7 GeV.

Table 1: Summary of all BES-II and FXT Au+Au beam energies, equivalent chemical potential, event statistics, run times, and date collected.

Beam Energy (GeV/nucleon)	$\sqrt{s_{\rm NN}}$ (GeV)	$\mu_{\rm B}$ (MeV)	Run Time	Number Events Requested (Recorded)	Date Collected
13.5	27	156	24 days	(560 M)	Run-18
9.8	19.6	206	36 days	400 M (582 M)	Run-19
7.3	14.6	262	60 days	300 M (324 M)	Run-19
5.75	11.5	316	54 days	230 M (235 M)	Run-20
4.59	9.2	373	in progress	160 M[1]	Run20+20b
31.2	7.7 (FXT)	420	0.5+1.1 days	100 M (50 M+112 M)	Run-19+20
9.8	4.5 (FXT)	589	0.9 days	100 M (108 M)	Run-20
7.3	3.9 (FXT)	633	1.1 days	100 M (117 M)	Run-20
19.5	6.2 (FXT)	487	1.4 days	100 M (118 M)	Run-20
13.5	5.2 (FXT)	541	1.0 day	100 M (103 M)	Run-20
5.75	3.5 (FXT)	666	0.9 days	100 M (116 M)	Run-20
4.59	3.2 (FXT)	699	2.0 days	100 M (200 M)	Run-19
3.85	3.0 (FXT)	721	4.6 days	100 M (259 M)	Run-18
3.85	7.7	420	11-20 weeks	100 M	Run-21[2]

[1] Run-20b is still in progress at the time of submission of this BUR, we expect to reach our goals
[2] Data not yet collected, Run-21 forms part of this year's BUR.

Based on guidance from the Collider-Accelerator Department (C-AD) and past experience we expect that the bulk of Run-21 will be devoted to Au+Au collisions at $\sqrt{s_{\rm NN}}$ =7.7 GeV,

Table 2: Proposed Run-21 assuming 24 -28 cryo-weeks, including an initial one week of cool-down, one week for CeC ,and a one week set-up time for each collider energy and 0.5 days for each FXT energy.

Single-Beam Energy (GeV/nucleon)	$\sqrt{s_{\rm NN}}$ (GeV)	Run Time	Species	Events (MinBias)	Priority
3.85	7.7	11-20 weeks	Au+Au	100 M	1
3.85	3 (FXT)	3 days	Au+Au	300 M	2
44.5	9.2 (FXT)	0.5 days	Au+Au	50 M	2
70	11.5 (FXT)	0.5 days	Au+Au	50 M	2
100	13.7 (FXT)	0.5 days	Au+Au	50 M	2
3.85	3 (FXT)	3 weeks	Au+Au	2 B	3
8.35	17.1	2.5 weeks	Au+Au	250 M	3
100	200	1 week	O+O	400 M 200 M (central)	3

the lowest collider energy of the program. Collection of these events is our highest priority. However, if we assume optimistic, but not overly so, rates and up-times, and 28 cryo-weeks, we project that the opportunity to collect of other exciting datasets will arise.

The *second highest priority* for Run-21 identified by the STAR collaboration is four short FXT runs; the collection of 300 M good events at $\sqrt{s_{\rm NN}}$ = 3 GeV and 50 M good events at each of three higher beam energies ($\sqrt{s_{\rm NN}}$ = 9.2, 11.5, and 13.7 GeV). 300 M events at 3 GeV with the enhanced iTPC and eTOF coverage gives access to the proton higher moments, precision ϕ, hypernuclei and dilepton measurements. The higher $\sqrt{s_{\rm NN}}$ FXT data combined with the collider data at the same energy will provide full proton rapidity coverage allowing us to probe in detail the mechanisms of stopping at play in heavy-ion collisions. We estimate the total run time required to collect all these datasets is 6 days.

The STAR collaboration also finds important scientific opportunities are presented by the collection of our *third highest priority* datasets:

- 2 B good events at $\sqrt{s_{\rm NN}}$ = 3 GeV in FXT mode. These enhanced statistics make possible the measurements of mid-rapidity proton 5-th/6-th order moments/cumulants, the system size dependence of ϕ meson production and a potential discovery of the double-Λ hypernuclei.

- A sixth collider beam energy at $\sqrt{s_{\rm NN}}$ =17.1 GeV. These data will provide for a finer scan in a range where the energy dependence of the net-proton kurtosis and neutron density fluctuations appear to undergo a sudden change.

- O+O data at $\sqrt{s_{\rm NN}}$ = 200 GeV, in the context of understanding the early-time conditions of small systems. These data would allow for a direct comparison with a similarly proposed higher-energy O+O run at the LHC, and further motivate the case for a small

system scan complementary to ongoing efforts by the NA61/SHINE collaboration at SPS energies, and other proposed light-ion species at the LHC.

The sequence with which we collect these datasets is currently somewhat fluid; we do not want to take partial datasets. We expect to refine the ordering of our goals as Run-21 progresses. Collection of these data during future RHIC running periods is also of interest to the collaboration.

For Run-22, as shown in Table 3, we propose **a dedicated 20 cryo-week transversely polarized p+p run at $\sqrt{s} = 510$ GeV**. This run will take full advantage of STAR's new forward detection capabilities, consisting of a Forward Calorimeter System (FCS) and a Forward Tracking System (FTS) located between $2.5 < \eta < 4$, and further capitalizes on the recent BES-II detector upgrades.

These data will enable STAR to explore, with unprecedented precision, forward jet physics that probe both the high-x (largely valence quark) and low-x (primarily gluon) partonic regimes.

Table 3: Proposed Run-22 assuming 20 cryo-weeks, including an initial one week of cool-down and a two weeks set-up time.

$\sqrt{s}$ (GeV)	Species	Polarization	Run Time	Sampled Luminosity	Priority
510	p+p	Transverse	16 weeks	400 pb^{-1}	1

Looking further out, the STAR collaboration has determined that there is a compelling scientific program enabled by the first opportunity to capitalize on the combination of the BES-II and Forward Upgrades in the data collected from Au+Au, p+Au, and p+p collisions at $\sqrt{s_{\rm NN}} = 200$ GeV as outlined in Table 4.

Significantly increased luminosities, the extended acceptance at mid-rapidity due to the iTPC, improved event plane and triggering capabilities of the EPD, and the ability to probe the previously inaccessible forward region are all exploited in our Hot QCD program, that informs on the microstructure of the QGP, and our Cold QCD program that will utilize transverse polarization that sets the stage for related future measurements at the EIC.

Table 4: Proposed Run-23 - Run-25 assuming 24 (28) cryo-weeks of running every year, and 6 weeks set-up time to switch species in 2024. Sampled luminosities assume a "take all" triggers.

$\sqrt{s_{\rm NN}}$ (GeV)	Species	Number Events/ Sampled Luminosity	Date
200	Au+Au	10B / 38 nb^{-1}	2023
200	p+p	235 pb^{-1}	2024
200	p+Au	1.3 pb^{-1}	2024
200	Au+Au	10B / 52 nb^{-1}	2025

Contents

1 Highlights from the STAR Program

1.1 Highlights from the Heavy Ion Program

1.1.1 Heavy-Ion Jet Measurements

Jet quenching, the modification of parton showers due to interactions in the QGP, is manifest in several distinct ways: energy transport to large angles, observable via jet energy loss and large-angle energy recovery; multiple-soft and single-hard coherent scatterings off of plasma constituents, observable via jet deflection or acoplanarity; and the modification of jet substructure. This broad spectrum of phenomena provides unique and incisive probes of the microscopic structure of the QGP. It also provides a robust experimental program, in which different observables with different systematic sensitivity probe the same underlying physics, providing stronger constraints on theoretical models of jet quenching than single measurements. STAR has a comprehensive jet quenching program which covers the full spectrum of these phenomena, using hadrons, direct photons, and reconstructed jets as probes.

STAR has led the development of essential analysis techniques for the challenging task of measuring reconstructed jet observables in heavy-ion collisions at RHIC. These include a data-driven Mixed-Event technique to measure uncorrelated jet background for semi-inclusive observables [1], enabling unbiased jet measurements over a broad phase space in heavy-ion collisions, notably low jet p_{T} ($\sim$ 10 GeV/c) and large jet resolution parameter ($R \sim 0.5$); and sub-jet observables that are robust to the underlying event and yet sensitive to the jet splitting kinematics, applying them as a tool to access the resolution scale in jet-medium interactions [2].

Jet quenching measurements have traditionally utilized p+p collisions to provide an unmodified reference, and p+A collisions to measure initial state effects that may mask signals of quenching in the final state. More recently it has become evident that small systems themselves exhibit QGP-like flow signatures for event selection corresponding to high Event Activity (EA), and an urgent question in the field is whether evidence can likewise be found for jet quenching in such systems. The STAR jet quenching program therefore includes measurements in (unpolarized) p+p and p+Au collisions, as well as Au+Au collisions.

In this section we present recent highlights of the STAR jet quenching program. The STAR papers published in this area in the past year can be found in Refs. [3–7].

Inclusive and semi-inclusive jet yield suppression: Inclusive jet yield suppression is a hallmark of jet quenching in heavy-ion collisions. STAR has recently reported the first measurement at RHIC of inclusive charged-particle jet distributions in central and peripheral Au+Au collisions at $\sqrt{s_{\mathrm{NN}}} = 200$ GeV [7], together with measurements of their yield suppression, R_{AA} (normalized by the yield in p+p collisions calculated by PYTHIA tuned to other STAR data [8]) and R_{CP}. Figure 1 shows the extracted R_{CP} compared to a similar measurement by ALICE, and to charged-hadron R_{CP} measured at both colliders. A striking similarity is seen between the two inclusive jet measurements, and between the two

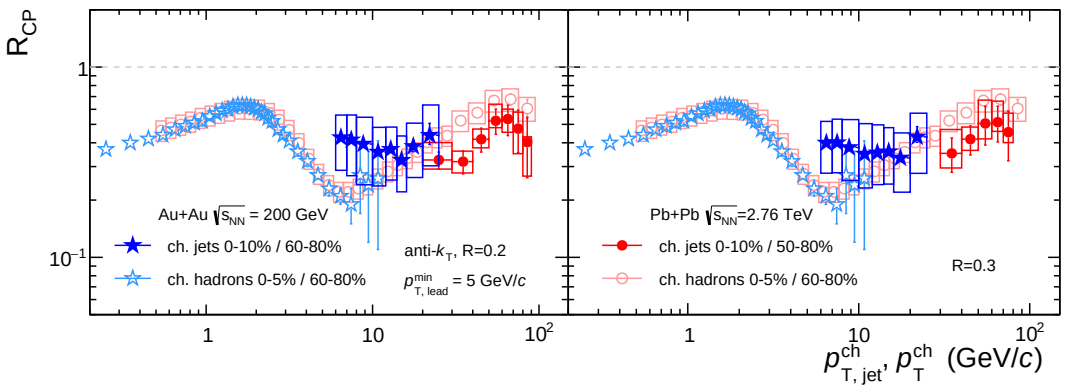

Figure 1: Measurement of $R_{\rm CP}$ as a function of $p_{\rm T,jet}^{\rm ch}$ for charged-particle jets (anti-$k_{\rm T}$, $R = 0.2$ and 0.3) measured by STAR (blue points) [7], compared to charged-jet $R_{\rm CP}$ at the LHC and to inclusive hadron $R_{\rm CP}$ at RHIC and the LHC. Note the different centrality selections.

inclusive hadron measurements. The $p_{\rm T}$-dependence of $R_{\rm CP}$ is stronger for hadrons in the region of overlap. While there remain differences in centrality selection between the datasets, this is the most direct comparison to date of reconstructed jet measurements at RHIC and the LHC.

This paper also reported the ratio of jet yields in central and peripheral Au+Au collisions for R =0.2 and 0.4, which is a probe of jet shape and its in-medium modification. Consistency to theoretical calculations is found within uncertainties. However, the calculations exhibit significant spread in the jet shape ratio, presenting an opportunity for more precise measurements to discriminate between them. A measurement of the inclusive jet yield in Au+Au collisions including both charged and neutral particle constituents using the much larger data set recorded in 2014, corresponding to 9.9 nb^{-1} [9] is underway. STAR also has full jet measurements in p+p collisions for use for the $R_{\rm AA}$normalization.

A recent STAR measurement, likewise using the 9.9 nb^{-1} 2014 dataset, extends the semi-inclusive measurement of charged jets (anti-$k_{\rm T}$, $R = 0.2$ and 0.5) recoiling from a high-$E_{\rm T}$ photon trigger to photon triggers in the range $15 < E_{\rm T}^{\rm trig} < 20$ GeV [10]. Currently, the recoil jet yield suppression for 0–15% Au+Au collisions ($I_{\rm AA}$) is determined by comparison to the yield in p+p collisions calculated using PYTHIA-6 (STAR tune [8]) and PYTHIA-8. Significant yield suppression in central Au+Au collisions is observed for $R = 0.2$, with less suppression for $R = 0.5$. Theoretical calculations predict a stronger dependence of $I_{\rm AA}$ on $p_{\rm T,jet}^{\rm ch}$ for $R = 0.5$ than observed. A measurement of this observable in p+p collisions is in progress, to provide a data reference rather than PYTHIA calculations for $I_{\rm AA}$.

Jet yield suppression is an indirect measurement of energy loss, because it convolutes out-of-cone energy loss with the shape of the jet spectrum – a fixed energy loss generates greater suppression for a steeper spectrum. Since the jet spectrum shape depends strongly on the choice of observable (inclusive, semi-inclusive) and collision energy, direct comparison of different jet quenching measurements requires this effect to be taken into account. Figure 2

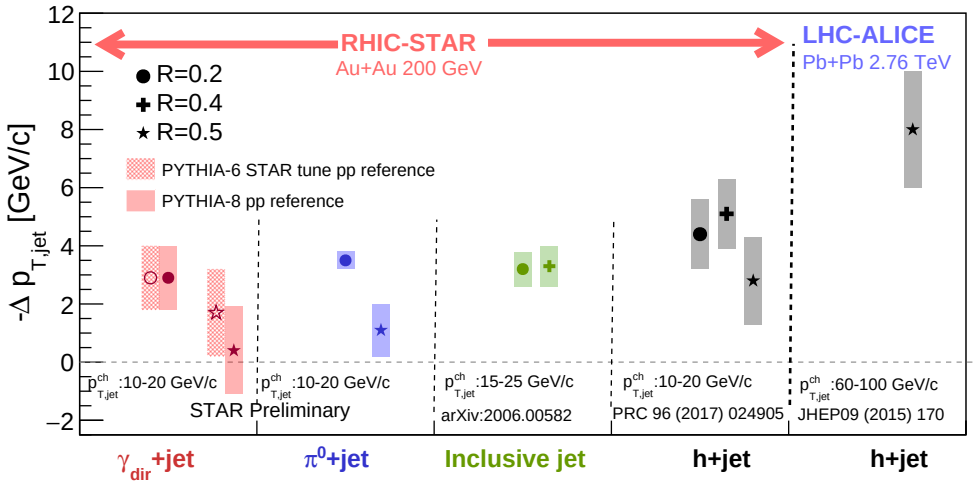

Figure 2: Out-of-cone jet energy loss derived from jet yield suppression measurements in A+A collisions (see text) for $\gamma_{\rm dir}$+jet, π^0+jet, inclusive jet, and h+jet measurements at RHIC, and h+jet measurements at the LHC [9, 10]. Note the different $p_{\rm T,jet}$ ranges.

shows the $p_{\rm T,jet}$ shift needed between jet spectra measured in a reference system (p+p or peripheral A+A collisions) and in central A+A collisions, for several jet yield suppression measurements at RHIC and the LHC [9, 10]. The absolute magnitude of medium-induced jet energy loss is similar for several different observables at RHIC, and is smaller than the LHC measurement. Note that the $p^{\rm ch}_{\rm T,jet}$ range is significantly higher for the LHC h+jet measurement, so that the *relative* energy loss is smaller than at RHIC.

This is a first look at comparing medium-induced out-of-cone radiation at RHIC and the LHC. Clearly, as the measured $p_{\rm T,jet}$ range at RHIC moves up and that at the LHC moves down in upcoming measurements, more precise comparisons can be made. Nevertheless, Fig. 2 already provides significant constraints on jet quenching calculations that seek to model RHIC and LHC measurements in a unified way.

Jet-structure modifications: The Fragmentation Function (FF), normalized per jet, provides information of the longitudinal momentum fraction ($z = p_{\rm T,trk}\cos(\Delta r)/p_{\rm T,jet}$) of charged particles projected along the jet axis. While FF have been measured previously at the LHC [11,12], STAR has utilized the semi-inclusive approach to measure the FF of charged jets for the first time at RHIC [13]. The Mixed-Event approach developed in [1] is extended for the FF measurement, and utilized for the correction of uncorrelated jet contributions. The fully corrected FF are shown in Fig. 3 for jets of varying $p^{\rm ch}_{\rm T,jet}$ for mid-peripheral 40-60% collisions compared to PYTHIA-8 [14] predictions shown by the dashed curved. The FF shape in data is reproduced by PYTHIA-8 in these peripheral collisions. Measurements are ongoing to extend to central collisions where one expects a larger path length for the recoil jet and enhanced medium effects.

Another observable of the jet transverse profile is the differential jet shape, measured in

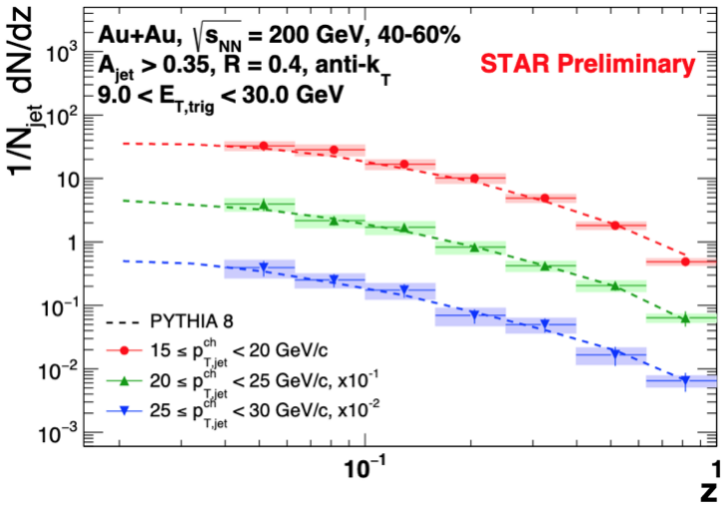

Figure 3: Fragmentation functions for recoil charged-particle jets of varying $p_{\mathrm{jet,T}}^{\mathrm{ch}}$ with trigger $9.0 < E_{\mathrm{T}} < 30.0$ GeV in 40–60% peripheral events compared to PYTHIA-8 simulations in the dashed curves.

radial annuli around the jet axis ($\rho(\Delta r)$). Utilizing the hard-core jet selection [15] which provides a pure sample of hard-scattered jets with a high constituent threshold, the fully corrected ρ as a function of Δr (distance between the constituent tracks and the jet axis) of leading jet with $20 < p_{\mathrm{T,jet}} < 40$ GeV/c for central (0–10%) and mid-central (20–50%) events are calculated. To probe possible in-medium modification of the jet structure and its dependence on the path length in medium, this observable is also differentially measured based on the jet's orientation with respect to the event plane for 20–50% mid-central collisions, as shown in Fig 4. High-$p_{\mathrm{T,trk}}$ particles are found closer to the jet core, whilst softer constituents are more evenly distributed around the jet. In comparing the soft particle production for in-plane vs. out-of-plane jets one finds subtle hints of path-length dependence.

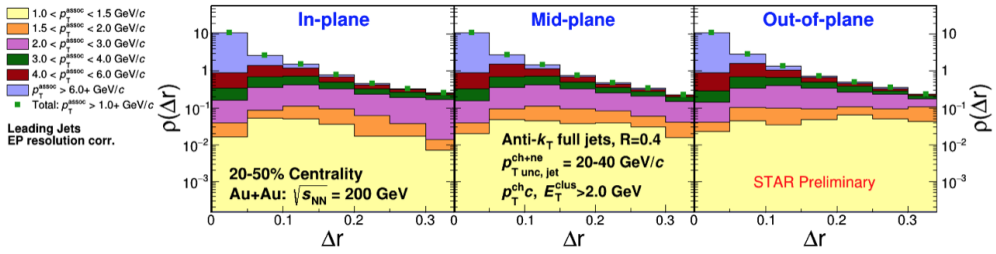

Figure 4: Differential measurement of the leading jet ($20 < p_{\mathrm{T,jet}} < 40$ GeV/c) shapes in 20–50% central Au+Au collisions shown for different jet azimuthal angles with respect to the event-plane angle. The $p_{\mathrm{T,trk}}$-dependence of the associated tracks are shown in the different stacked histograms. Results are corrected for event-plane resolution effects.

Jets in p+Au collisions: STAR has searched for jet-medium interactions in p+Au collisions by looking at potential modifications of semi-inclusive charged-particle jet yields and jet substructure observables such as the jet mass and SoftDrop groomed jet mass. p+Au collisions are classified as low or high event-activity (EA) according to the particle multiplicity in the Au-going direction as measured by the BBC-East detectors.

The charged-particle jet spectra, normalized per HT trigger (uncorrected for detector effects) are shown on the left of Fig. 5 where the open (full) makers correspond to low (high) EA. The different colored markers represent the azimuthal separation between the trigger and

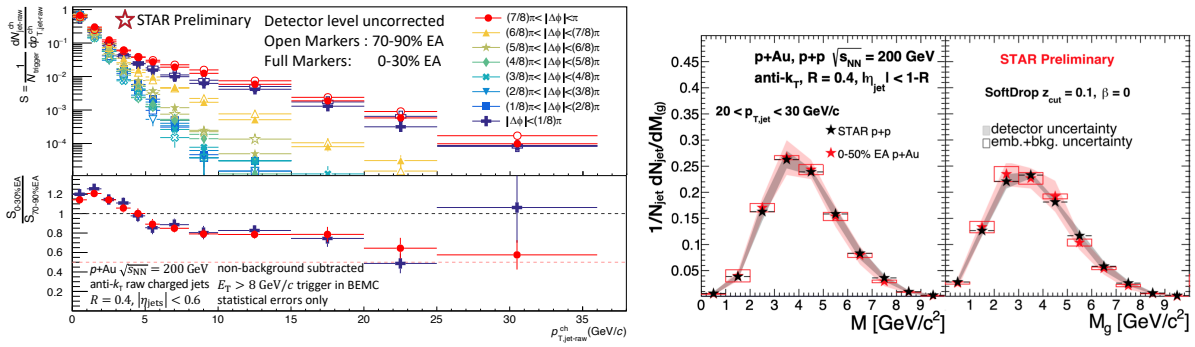

Figure 5: Left: Semi-inclusive charged jet spectra in p+Au collisions for high and low event-activity (EA) events, the ratio is shown in the bottom panel. Right: Fully corrected (groomed) jet-mass distributions in p+Au with high EA and p+p collisions.

the recoil jet. We see for jet with $p_{\mathrm{T,jet-raw}} > 10$ GeV/c, a significant suppression in high to low EA events for both the trigger-side and recoil-side spectra. These suppression ratios are qualitatively different from jet suppression in Au+Au collisions, where the recoil jets traverse more QGP on average and are suppressed compared to the trigger-side. In investigating if this suppression is a result of modification of jet structure, STAR also measured the fully corrected jet-mass and groomed jet-mass distributions, normalized per jet, on the right of Fig. 5. The distribution in high EA p+Au collisions is comparable to that in p+p collisions within the systematic uncertainties, and this leads to the conclusion that CNM effects do not significantly affect the jet substructure.The jet mass measurements in p+Au will be followed in a more differential fashion by studying finer EA classes and rapidity selections which can isolate jets originating from the Au vs p side. Both of these measurements from STAR point to lack of jet modification from nuclear effects and also to a more fundamental selection bias when identifying classes of high vs low activity events in asymmetric collisions.

1.1.2 Bulk Correlations

Over the past years, the STAR collaboration has performed a series of correlation measurements directed towards a comprehensive understanding of the QCD phase diagram and the bulk properties of the QGP phase. Here we highlight the most recent STAR results on bulk correlations, which are expected to shed light on the QCD phase diagram as well as on the transport properties of the QGP.

Net-proton number fluctuations and the QCD critical point: One of the main goals of the STAR Beam Energy Scan (BES) program is to search for possible signatures of the QCD critical point (CP) by scanning the temperature (T) and the baryonic chemical potential (μ_B) plane by varying the collision energy. When the system produced in the heavy ion collisions approaches the CP, the correlation length diverges. Higher order cumulants of conserved net-particle multiplicity distributions are sensitive to such correlation lengths as the divergence of correlation length leads to enhanced fluctuations in the net-particle multiplicity distributions.

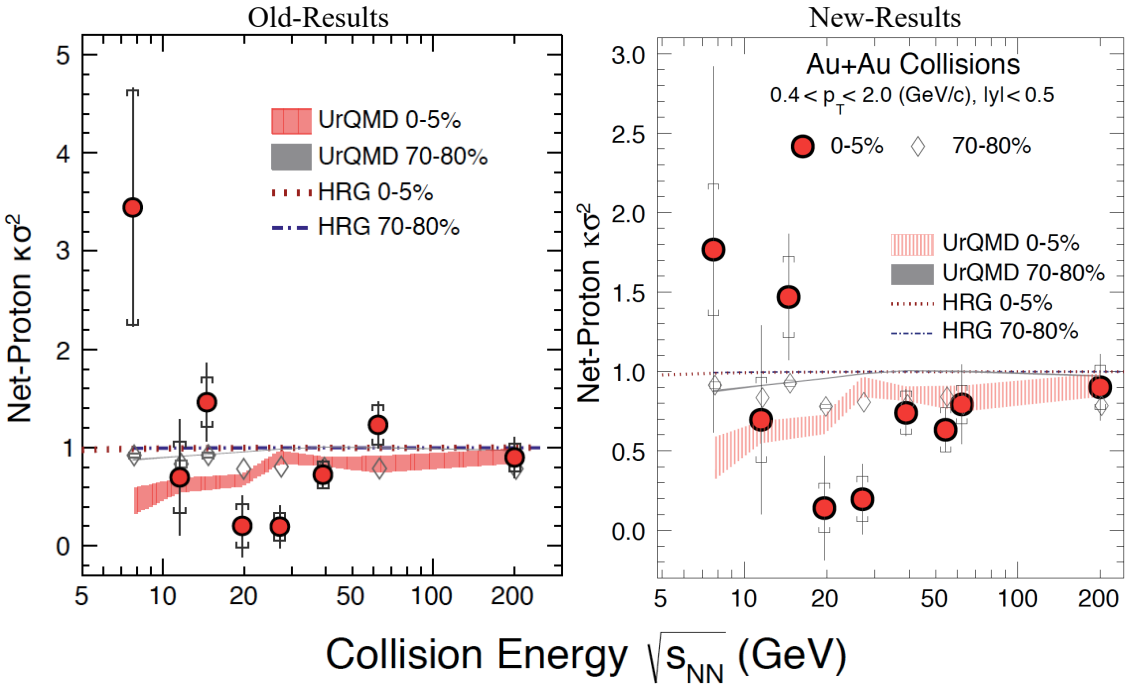

Figure 6: $\kappa\sigma^2$ as a function of collision energy for net-proton distributions measured in central (0-5%) and peripheral (70-80%) Au+Au collisions within $0.4 < p_T$ (GeV/c) < 2.0 and $|y| < 0.5$. The error bars and caps show statistical and systematic uncertainties, respectively. The dashed and dash-dotted lines correspond to results from a hadron resonance gas (HRG) model. The shaded bands are the results of a transport model calculation (UrQMD). The model calculations utilize the experimental acceptance and incorporate conservation laws for strong interactions, but do not include the dynamics of phase transition or critical point. The new results are obtained after removing the spoiled events, the largest changes are seen in central Au+Au collisions at 7.7 and 62.4 GeV.

The ratios of the cumulants of identified net-particle multiplicity distributions, such as net-protons, have been predicted to be ideal observables sensitive to the onset of the QCD

phase transition and the location of the CP. A non-monotonic variation of these ratio of cumulants, such as C_4/C_2 ($=\kappa\sigma^2$), as a function of collision energy has been proposed to be an experimental signature of the CP. Taking the ratios of cumulants has advantages as it cancels the volume fluctuations to first order. Further, these ratios of cumulants are related to the ratio of baryon-number susceptibilities at a given T and μ_B. Near the critical point, QCD-based calculations predict the net-baryon number distributions to be non-Gaussian and susceptibilities to diverge, causing these ratios to have non-monotonic variation as a function of collision energy. However, the finite-size and finite-time effects in heavy-ion collisions limit the growth of correlation length, and hence it could restrict the values of $\kappa\sigma^2$ from its divergence as a function of collision energy.

Figure 6 shows the collision energy variation of net-proton $\kappa\sigma^2$ for central and peripheral Au+Au collisions within the acceptance of $0.4 < p_T < 2.0$ GeV and $|y|<0.5$. In central collisions, a non-monotonic variation with beam energy is observed for $\kappa\sigma^2$ with a significance of 3.0 σ. In contrast, monotonic behavior with beam energy is observed for the statistical hadron gas (HRG) model, and for a nuclear transport UrQMD model without a critical point, and experimentally in peripheral collisions.

High statistics data from the ongoing BES-II program can provide precision measurements at higher μ_B region in the QCD phase diagram. In addition, due to the iTPC [16] and eTOF [17] upgrades, a differential measurement in $|y|<1.5$ and $p_T > 0.15$ GeV/c will be explored. The study of acceptance dependence of net-proton $\kappa\sigma^2$ and other cumulants ratios are important to understand critical fluctuation. Furthermore, the forward Event-Plan Detector (EPDs) [18] can also be used to determine the centrality selection in heavy-ion collisions for this measurement.

Global polarization measurements at 27 GeV: In heavy-ion collisions, many theoretical models propose that the large angular momentum in the collisions of two nuclei [19–21] can be transferred to the microscopic constituent of the created matter. Consequently, the spin of the produced quarks and gluons might be polarized along the direction of the global angular momentum due to spin-orbit coupling. The direction of the global angular momentum is perpendicular to the reaction plane, as defined by the incoming beam and the impact parameter vector. This direction can be determined from directed flow measurements of the spectators. STAR observed significant non-zero polarization of hyperons [20] with increasing strength with decreasing collision energy (from 200 to 7.7 GeV).

We recently report more differential measurements using our newly installed EPDs in Au+Au collisions at 27 GeV as functions of the hyperon's transverse momentum, and pseudo-rapidity. In Fig. 7 left panel we observe that the polarization does not show a strong dependence on p_T, albeit large uncertainties. There are several expectations on the p_T dependence on the polarization. If global polarization is generated by the vorticity of the initial state that does not have a strong p_T dependence then the result is compatible with expectations. Alternatively, at lower p_T, due to the smearing effect caused by scattering at later stages of the collisions, we might expect a decrease of the polarization. In addition, one might expect a decrease in the polarization at higher p_T due to the expected larger

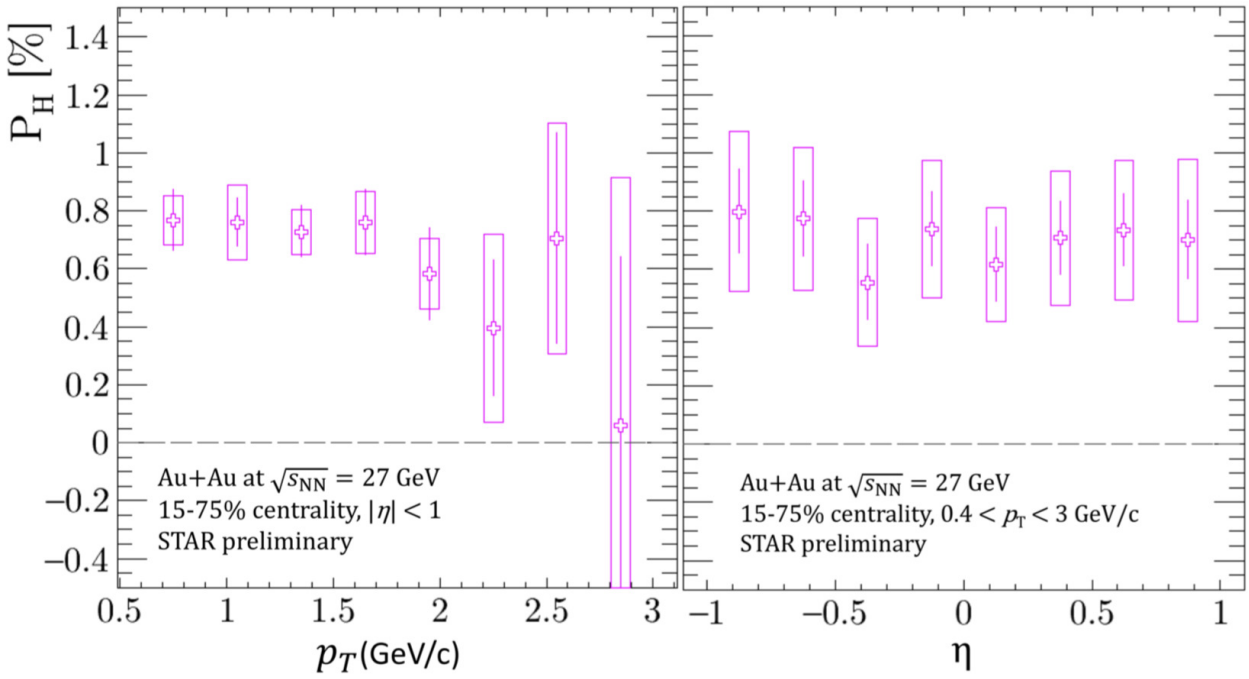

Figure 7: The global polarization measurements as a function of p_T and η in 15-75% central Au+Au collisions at $\sqrt{s_{\rm NN}}$ = 27 GeV. The figure is taken from Ref [22].

contribution from jet fragmentation. Fig 7 right panel shows the pseudo-rapidity dependence of the polarization measurement, no η-dependence of the polarization is observed within uncertainties. The vorticity is expected to decrease at larger rapidity, but might also have a local minimum at η=0 due to complex shear flow structure [21, 23, 24] however, this might be difficult to observe within STAR's acceptance. This preliminary observation of no p_T or η dependence of the polarization is consistent with our previous measurements at 200 GeV [19]. STAR plans to perform the same measurement with an extended pseudo-rapidity coverage using the iTPC detector upgrade and with higher statistics BES-II data set enabling higher a precision result.

Global spin alignment of K^{*0} and ϕ: Unlike the self-analyzing (anti)Λ, the polarization of vector mesons such as $\phi(1020)$ and $K^{*0}(892)$ cannot be directly measured since vector mesons mainly decay through the strong interaction in which parity is conserved. The spin alignment of vector mesons can be given by a 3×3 spin density matrix with unit trace [25]. The spin density matrix diagonal elements ρ_{nn}, n=0,1 and -1, represent the probabilities for the spin component along the quantization axes. When there is no spin alignment this means that all three spin states (ρ_{nn}) have equal probability to be occupied meaning $\rho_{nn} = 1/3$. Out of the three diagonal elements, only the n=0 case is independent of the other two. Consequently, it is intriguing to experimentally investigate the ρ_{00} of vector mesons.

Figure 8 shows the centrality dependence of ρ_{00} for both vector meson species for Au + Au collisions at 200 GeV. The ϕ-meson results are presented for transverse momentum

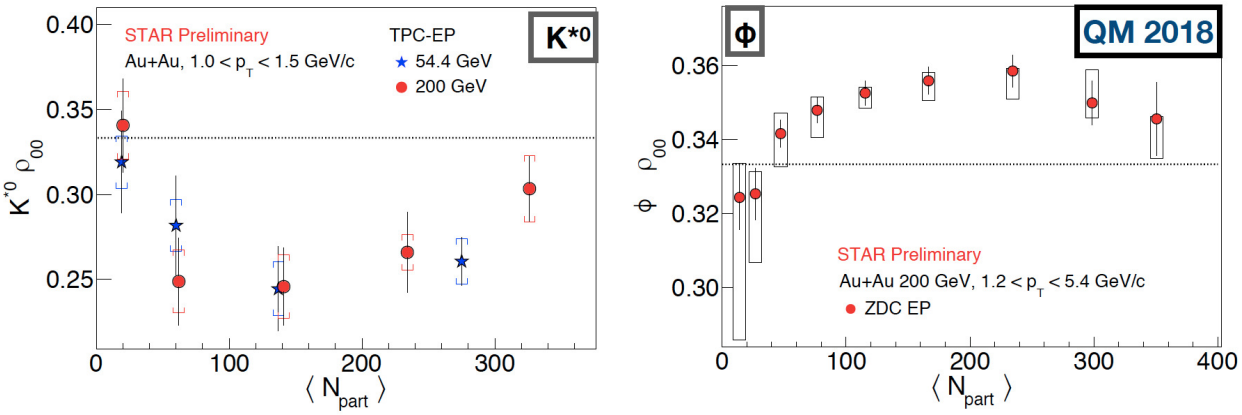

Figure 8: The spin alignment ρ_{00} measurements of vector mesons K^{*0} and ϕ as a function of N_{part} for the indicated p_T range of the Au+Au collisions at 200 and 54.4 GeV. The figure is taken from Ref [26].

$1.2 < p_T < 5.4$ GeV/c, and ρ_{00} for this species is significantly above 1/3 for mid-central collisions, indicating finite global spin alignment. The K^{*0}-meson results are presented for transverse momentum $1.0 < p_T < 1.5$ GeV/c, and the magnitude of ρ_{00} for this particle species is observed to be significantly less than 1/3 for mid-central collisions.

The distinction between the global spin alignment for K^{*0} and ϕ may be assigned to different in-medium interactions due to the difference in the lifetime (ϕ-meson is 10 times larger than K^{*0}-mesons), and/or a different response to the vector meson field. These global spin alignment results are expected to shed light on the possible vector meson fields [27, 28]. Such investigations are extremely important since vector meson fields are a crucial part of the nuclear force that binds nucleons to atomic nuclei and are also central in describing properties of nuclear structure and nuclear matter.

Nuclear deformation measurements: Deformation is a fundamental property of atomic nuclei that reflects the correlated nature of the dynamics of nucleons within the quantum many-body system. The majority of atomic nuclei possess an intrinsic deformation, most of which is an axial quadrupole, or ellipsoidal, deformation.

Prior relativistic heavy-ion collision measurements from STAR reported strong signatures of nuclear deformation using detailed comparisons between Au+Au collisions and U+U collisions [29]. These measurements suggest that U+U collisions being much more deformed in their ground state. Consequently, we can say that these detailed comparisons between Au+Au and U+U collisions enabled us to examine the geometry of the colliding nuclei.

The study of mean transverse momentum dependence of the elliptic and triangular flow harmonics in Au+Au and U+U collisions are recently proposed by theory calculations [31] that are more sensitive to the deformation of the colliding nuclei.

Figure 9 shows the scaled mean p_T dependence of v_2 and v_3 for the central Au+Au and U+U collisions. STAR preliminary data show a clear positive correlation for v_2 and v_3 in Au+Au collisions that is in agreement with the v_3 from U+U collisions. In contrast, a nontrivial negative correlation is observed in v_2 as a function of scaled mean p_T in U+U

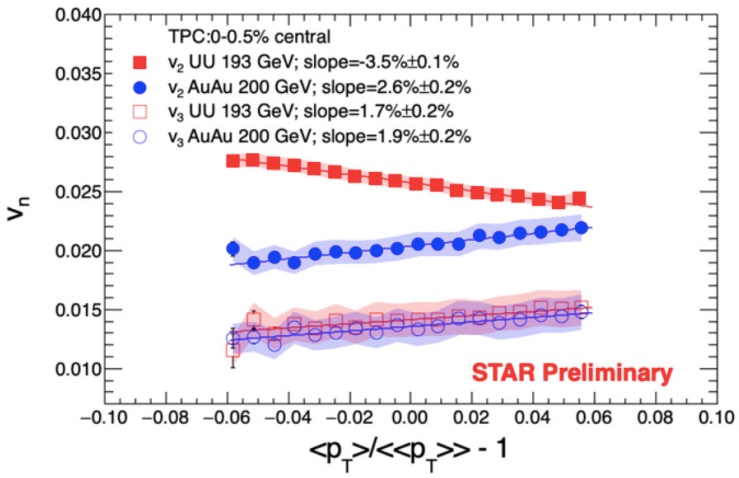

Figure 9: The scaled mean p_T dependence of the elliptic and triangular flow harmonics for 0-0.5% central Au+Au and U+U collisions. The figure is taken from Ref [30].

collisions. Also these preliminary results are consistent with the theoretical expectation for a deformed U nuclei [31].

Flow correlations and fluctuations measurements: Flow harmonics (v_n) calculated from the Fourier expansion of the particle azimuthal distributions are commonly employed to quantify the azimuthal anisotropy of particle emission relative to the collision symmetry planes. While the lower-order Fourier coefficients (v_2 and v_3) are more directly related to the corresponding eccentricities of the initial state, the higher-order flow harmonics ($v_{n>3}$) can be induced by a non-linear (mode-coupled) response to its lower-order harmonics and also with a linear response to the same-order anisotropy. These higher-order flow harmonics and their linear and mode-coupled contributions can be used to constrain the initial conditions and the transport properties of the medium in the theoretical calculations.

The v_2 and v_3 harmonics are sensitive to the respective influence of the initial-state eccentricity and the final-state viscous attenuation, which have proven difficult to disentangle. The mode-coupled coefficients show characteristically different dependencies on the viscous attenuation and the initial-state eccentricity [32]. Therefore, they can be used in conjunction with measurements for the v_2 and v_3 harmonics to leverage additional unique constraints for initial-state models, as well as reliable extraction of transport coefficient.

Figure 10 shows the mode-coupled response coefficients, $\chi_{4,22}$ and $\chi_{5,23}$, with a weak centrality dependence, akin to the patterns observed for similar measurements at the LHC for Pb+Pb collisions at 2.76 TeV [34]. These patterns suggest that the mode-coupled response coefficients are dominated by initial-state eccentricity couplings which is known from models to have a weak dependence on beam energy. The correlations of the event plane angles, $\rho_{4,22}$ and $\rho_{5,23}$ show a strong centrality dependence that agrees well with the LHC measurements for Pb+Pb collisions at 2.76 TeV. The predictions from viscous hydrodynamic models [35, 36] give a good qualitative description of the mode-coupled response coefficients and the

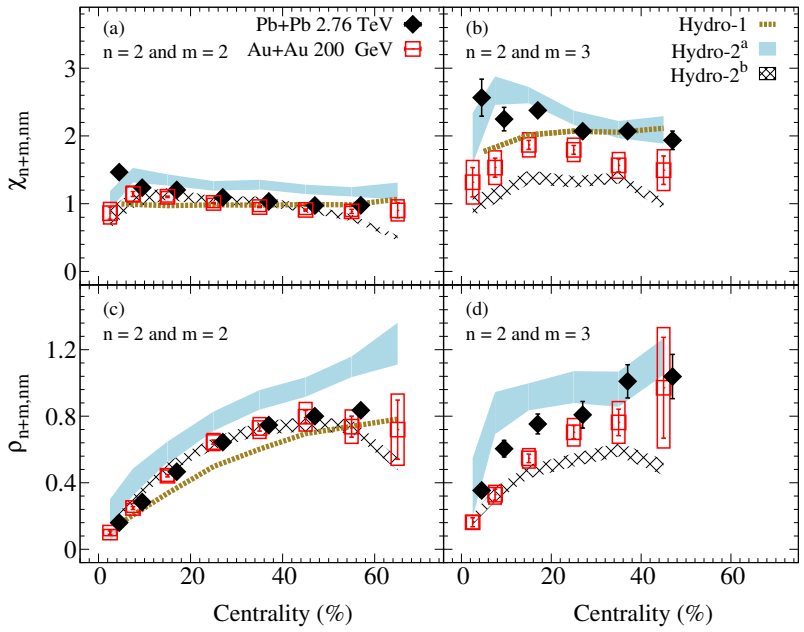

Figure 10: Results as a function of centrality for Au+Au collisions at 200 GeV [33]. Panels (a) and (b) shows the mode-coupled response coefficients, and panels (c) and (d) show the correlations of event plane angles. The closed-symbols represents similar LHC measurements [34]. The shaded bands indicate hydrodynamic model predictions Hydro-1 [35], Hydro-2^a and Hydro-2^b [36].

correlation of event plane angles.

Small system measurements: The comparisons of theoretical models to the flow harmonics, v_n, continue to be an essential avenue to evaluate the transport properties of partonic matter produced in large to moderate-sized collision systems [37–39]. For the small collision-systems formed in p/d/^{3}He+Au and p+Pb collisions, collective flow might not develop due to the presence of large gradients in the energy-momentum tensor that could trigger non-hydrodynamic modes [40, 41]. Certainly, the most important question that divided our field is whether an alternative initial-state-driven mechanism [42] dominates over hydrodynamic expansion for these collision systems.

Current measurements for p/d/^{3}He+Au collisions, which supplement earlier measurements at both RHIC [43] and the LHC [44] aim to address the respective influence of collision-system size and its subnucleonic fluctuations, and viscous attenuation on the measured v_n.

Figure 11 shows the $v_2(p_T)$ and $v_3(p_T)$ values for p/d/^{3}He+Au collisions at 200 GeV before and after non-flow subtraction, compared for all three subtraction techniques. The presented results show non-flow contributions which are system-dependent, but the non-flow subtracted v_2 (top panels) and v_3 (bottom panels) are method-independent within the uncertainties.

These STAR measurements with non-flow subtracted show that for the comparable charged-hadron multiplicity (N_{ch}) events v_2 and v_3, values are independent of collision sys-

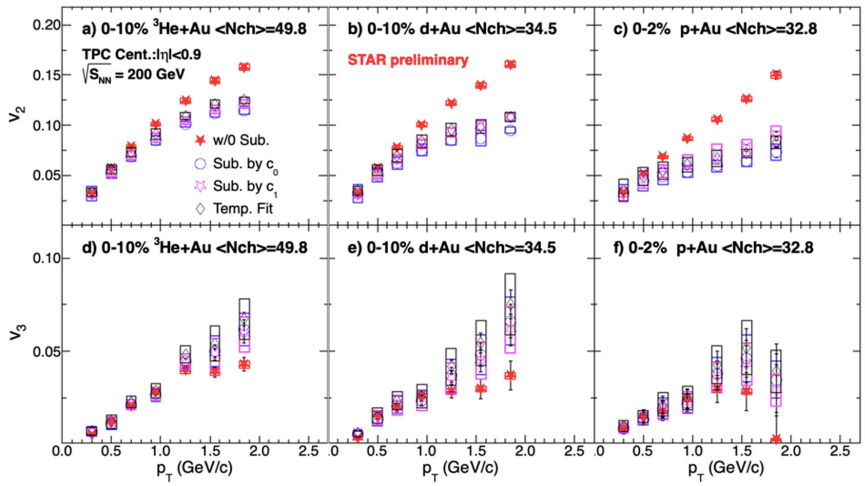

Figure 11: Comparison of the $v_{2,3}(p_T)$ values for p/d/^{3}He+Au collisions at 200 GeV, before and after non-flow subtraction. The figure is taken from Ref [45].

tem. These observations are compatible with the significant influence of the subnucleonic fluctuations-driven eccentricities, $\epsilon_{2,3}$, in a system whose size is primarily determined by N_{ch}. However, they are incompatible with the notion of shape engineering in p/d/^{3}He+Au collisions.

1.1.3 Light Flavor Spectra and Ultra-peripheral Collisions

The Light Flavor Spectra and Ultra-peripheral Collisions (LFSUPC) physics working group is responsible for the measurements of calibrated production yields and spectra in inclusive ion-ion collisions, ultra-peripheral collisions, and exclusive p+p collisions.

In ion-ion collisions, analysis efforts can be grouped based on the methodology and physics issues. The general categories include light charge hadrons (π, K, p), strange hadrons (ϕ, Λ, Ξ, Ω), light nuclei (d, t, ^3He, ^4He), and hyper-nuclei ($^3_\Lambda H$ and $^4_\Lambda H$). Examples of recent results from light nuclei and hyper-nuclei are shown in other sections (see sections 2.2.1 and 2.2.2). Here some recent results will presented from the light charged hadron and strange hadron analyses.

Light hadron production: Light charged hadron spectra and yields are measured using particle identification through dE/dx in the TPC, $1/\beta$ in the time-of-flight detectors and careful study of the acceptance and efficiency of the detectors. These studies are particularly useful in defining the basic thermal properties (T and μ_B) of the system. Previous studies of the light charged hadrons from BES-I measured the spectra and yields at midrapidity. The newest results now include rapidity dependence which allows for a better understanding of baryon stopping, which is key to the dependence of μ_B with $\sqrt{s_{NN}}$. New preliminary π, K, and p transverse mass spectra are shown as a function a rapidity in Fig. 12 for Au+Au collisions at $\sqrt{s_{\rm NN}}$ = 27 GeV. Additional pre-preliminary results have been produced from fast offline pre-calibration quality assurance productions from the other BES-II collider and

fixed-target energies.

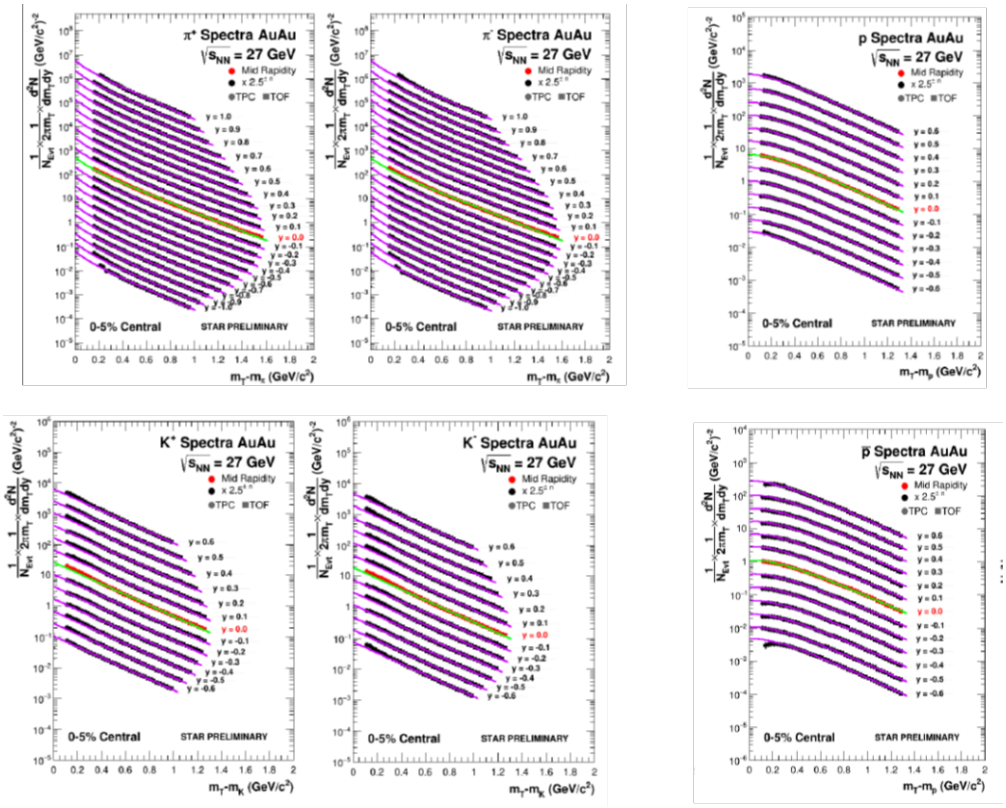

Figure 12: Transverse mass spectra for pions, Kaons, and protons from Au+Au collisions at $\sqrt{s_{\rm NN}}$ = 27 GeV as a function of rapidity.

Strange hadron production: Strange hadron spectra and yields are measured by determining the invariant mass from the charged daughters from weak decays of neutral strange hadrons. These studies define the role of the strange quark in the thermodynamic evolution of the system. STAR has recently implemented a new V^0 finding routine called *KFparticle* which increases the sensitivity of our strange hadron studies. The highlights of recent measurements have come from the newest fixed-target data. The fixed-target energy range covers the production threshold energies for Ξ^- (3.247 GeV), Ω^- (4.09 GeV), Ξ^+, Ξ^- (4.52 GeV), and Ω^+, Ω^- (5.22 GeV). Figure 13 shows the invariant mass plots for measurements of Λ's, Ξ's, and Ω's for fixed-target Au+Au at $\sqrt{s_{NN}}$ of 3.0 and 7.2 GeV. Additional pre-preliminary measurements have been made at other collider and fixed-target energies. In addition, studies of the production of the ϕ meson have been made at 3.0 and 7.2 GeV.

exclusive production: Central exclusive production is measured in p+p collisions using the very forward roman pot detectors to identify the the two colliding protons and the TPC to measure the products. Figure 14 shows the invariant mass of pion pairs in exclusive p+p events at 200 GeV. These are the first measurements at this energy and show significant

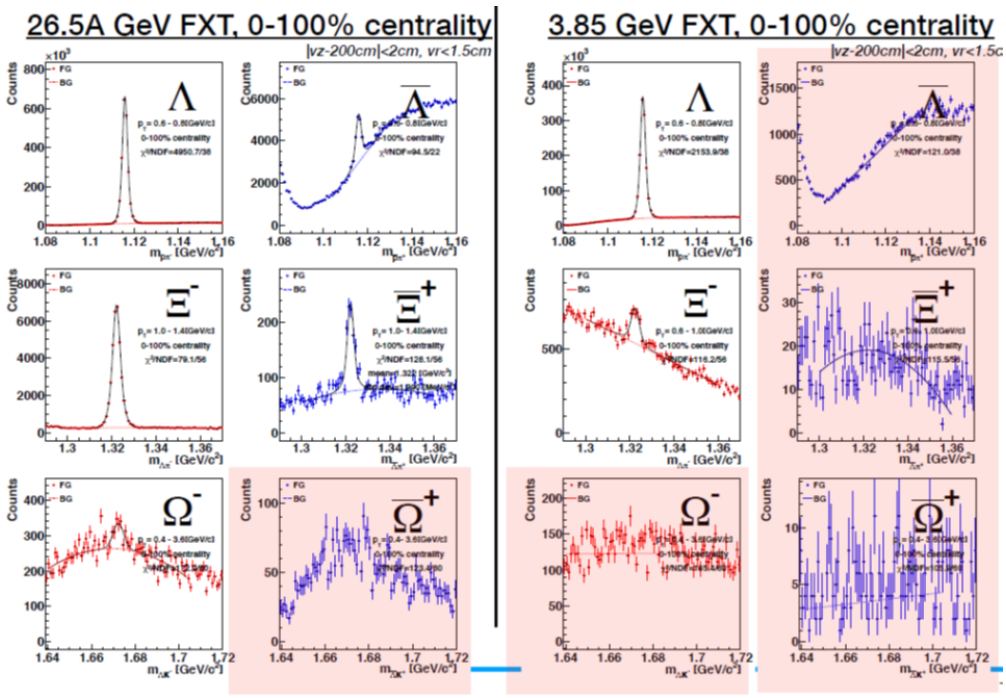

Figure 13: Invariant mass plots for measurements of Λ's, Ξ's, and Ω's for fixed-target Au+Au collisions at $\sqrt{s_{NN}}$ of 3.0 and 7.2 GeV (single beam energies of 3.85 and 26.5 GeV respectively).

peaks in the invariant mass spectra that were not predicted by the models. Similar results are available for kaon and proton pairs.

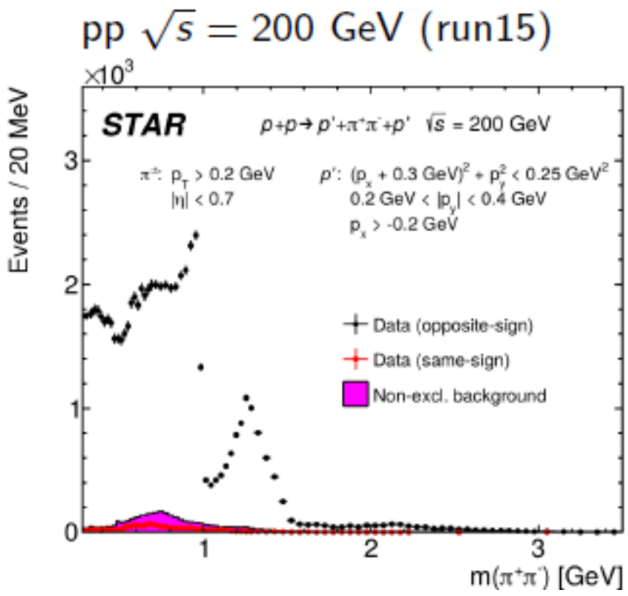

Figure 14: Invariant mass spectra for pion pairs from exclusive p+p events at 200 GeV.

Electromagnetic probes: Electromagnetic radiation from high-energy heavy-ion collisions provides rich information about the properties of the produced medium. Dileptons directly probe the in-medium electromagnetic correlator of hadronic currents [46, 47]. Dynamical information on in-medium spectral functions encodes not only changes in degrees of freedom, chiral symmetry restoration [48–50], transport properties of medium like the electrical conductivity [51, 52], but also the life time and average temperature of the interacting fireball [53], and the emission history and origin of the radiation [54–57].

STAR reported measurement of thermal dilepton radiation ranging from $\sqrt{s_{\rm NN}}$ = 200 GeV down to 19.6 GeV [58–61]. A significant excess in the low-mass region when compared to the known hadronic sources has been observed. It was shown that the predictions of hadronic manybody theory for a melting ρ meson, coupled with QGP emission utilizing a modern lattice QCD-based equation of state [51, 62], yield a quantitative description of dilepton spectra in heavy-ion collisions [58, 61]. This is demonstrated in Fig. 15 (left panel). Moreover, it has been shown that the integrated low-mass excess radiation provided a direct measure of the total fireball lifetime [60]. Secondary vertex rejection employing information provided by the Heavy Flavor Tracker installed for Run 2014 and 2016 will enable unique temperature measurements of the QGP.

The low-mass line shape will provide a critical test of the ρ-melting scenario (which is consistent with expectations of chiral symmetry restoration) at vanishing baryon chemical potential. A precision measurement at top RHIC energy will provide additional constraints that can be directly tested against the lattice QCD predictions and will be put in focus in runs 2023 - 2025 (see section 2.4.3).

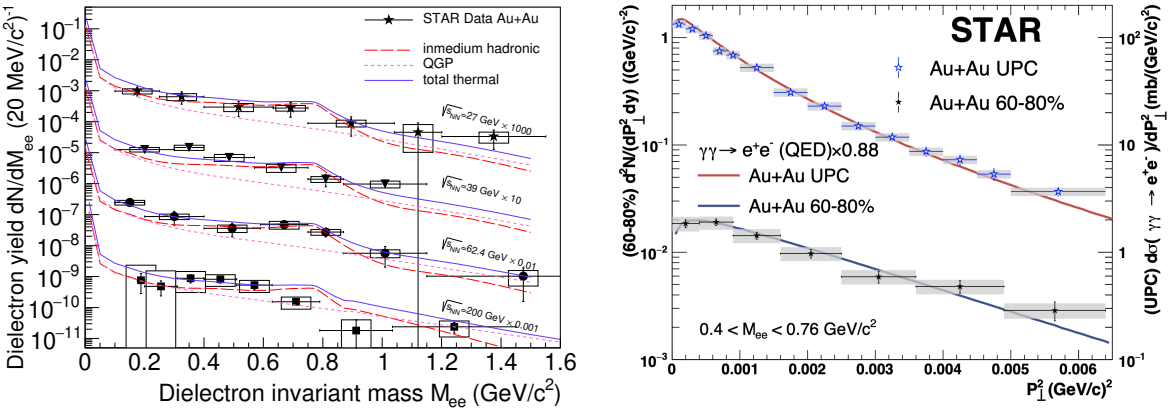

Figure 15: Left: Acceptance-corrected dielectron excess mass spectra, normalized by dN_{ch}/dy, for Au+Au collisions at $\sqrt{s_{NN}} = 27, 39, 62.4, 200$ GeV. Right: Comparison of the P_T^2 distribution in 60 − 80% central Au+Au collisions with that in UPCs [63].

Dileptons generated by the intense electromagnetic fields accompanying the relativistic heavy nuclei at large impact parameters [**?**], in ultra-peripheral collisions (UPC) where there is no nuclear overlap has recently become experimentally accessible, offering several opportunities. According to the equivalent photon approximation (EPA), the electromagnetic field generated by an ultra-relativistic nucleus can be viewed as a spectrum of quasi-real pho-

tons coherently emitted by the entire nucleus and the dilepton production process can be represented as $\gamma + \gamma \rightarrow l^+ + l^-$. Recently, the STAR and ATLAS collaborations made measurements of dileptons at small impact parameters with nuclear overlap, and found that the electromagnetic production of dileptons can also occur in hadronic collisions. Furthermore, a significant $P_\perp$ broadening as shown in Fig. 15 (right panel) effect for lepton pairs produced by the two photon scattering process has been observed in hadronic collisions compared to measurements in UPC and to EPA calculations. Precision measurements will provide an important constraints for quantitative theoretical analyses of magnitude and duration of initial magnetic fields. It was perceived that photons participating in such collisions are quasi-real with transverse-momentum $k_t \simeq 1/R$ (30 MeV/c) reflecting the virtuality and uncertainty principle of their origin. This led to the implementation in many EPA models that the initial transverse momentum of the dilepton pairs does not depend on impact parameter and the transverse space coordinates where the pair are created are randomly distributed due to the same principles. Our new measurements of centrality dependence and azimuthal distributions have shown that the photons behave like real photons in all observables and the renewed models and theories have demonstrated that correction to the real photon approximation is suppressed at the order of $1/\gamma)^2$ even to the pair's transverse momentum distribution. The discovery of the Breit-Wheeler process and the utilization of linearly polarized photons in UPC are conceptually and experimentally highly nontrivial. With future high statistics data with larger TPC acceptance in UPC, we can explore the phase space of photon collisions in transverse momentum, rapidity and momentum-space-spin correlations in extreme QED field [64, 65] (see section 2.4.3).

1.1.4 Heavy-Flavor

The production of heavy-flavor (HF) quarks proceeds predominately via the hard scatterings of partons in p(A)+p(A) collisions. This fact gives rise of the utility of heavy-flavor hadron measurements in heavy-ion experiments since they are produced independently of the QCD medium and probe it's properties by scattering with the medium constituents. Topics of medium-induced parton energy loss, QGP transport properties, hadronization mechanisms, and quarkonia melting are some of the pivotal studies that have emerged within the HF category. Besides the highlights discussed in detail below, the following measurements have been recently published: First Measurement of Λ_c Baryon Production in Au+Au Collisions at $\sqrt{s_{\rm NN}}$=200 GeV [66]; Measurement of inclusive J/ψ suppression in Au+Au collisions at $\sqrt{s_{\rm NN}}$=200 GeV through the dimuon channel at STAR [67]; First Observation of the Directed Flow of D^0 and $\bar{D}^0$ in Au+Au Collisions at $\sqrt{s_{\rm NN}}$=200 GeV [68].

Recent measurements of D^0 [69] and D^+ (shown at the Hard Probes 2020 conference) meson yields as a function of transverse momentum (p_T) in heavy-ion collisions show a significantly suppressed spectrum with respect to $p+p$ collisions. The two mechanisms that predominately produce suppressed meson distributions are parton energy loss in the QGP and different hadronization schemes. The latter is nicely illustrated via the measurement of the Λ_c^+/D^0 yield ratio [66], which is significantly enhanced with respect to the expectation in $p+p$ collisions and is attributed to baryon production via coalescence hadronization.

Recently, STAR has measured the ratio of D_s^+/D^0 yields in heavy-ion collisions, which is important as it probes charm hadronization and strangeness enhancement mechanisms. Utilizing the excellent pointing resolution resolution of the Heavy Flavor Tracker (HFT), the D_s is measured in 2014 and 2016 data and is topologically reconstructed using a multi-variate analysis (MVA) optimized for signal selection. The final results of D_s^+ yield with respect to D^0 were reported in the 2019 Quark Matter conference, and are shown in Figure 16. The ratios are split into 0-10% (blue points) and 10-40% (red points) centrality regions and are consistent within experimental uncertainties. Shown in the left panel are the ratios averaged over $p+p/e+p/e+e$ collisions, PYTHIA, and a model calculation (TAMU) including coalescence hadronization for 10-40% centrality. Shown in the right panel are model calculations including sequential (solid lines) and simultaneous (dashed lines) coalescence for both Au+Au collisions at RHIC and Pb+Pb collisions at LHC energies. Data from ALICE are also shown in the right panel, and are consistent within uncertainties with STAR data. The data show the D_s yield is significantly enhanced in Au+Au collisions with respect to that of elementary $p+p/e+p/e+e$ collisions. Comparing the STAR data to model calculations, the model of sequential coalescence is able to better capture the trends in data.

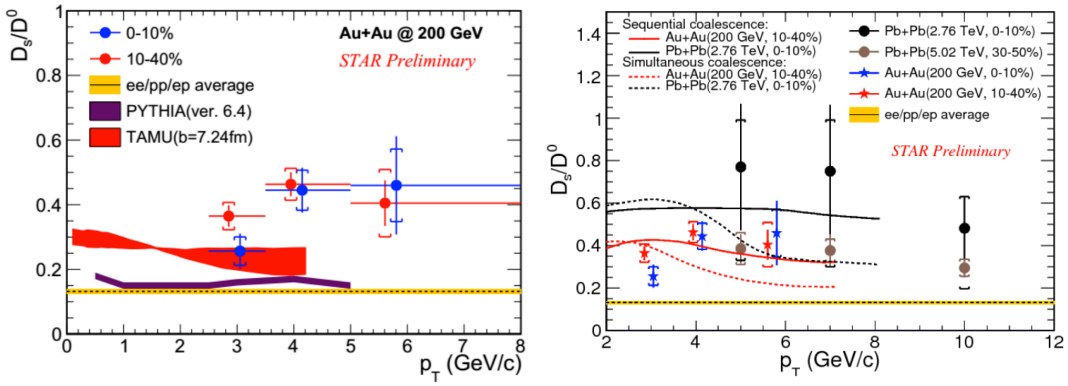

Figure 16: Left: STAR measurement of the D_s/D^0 ratio in 0-10% (blue circles) and 10-40% (red circles) centrality Au+Au collisions as a function of D_s p_T. The yellow shaded band shows the average from $p+p/e+p/e+e$ collisions. The purple and red shaded bands show the expectations from PYTHIA and TAMU model calculations, respectively. Right: STAR D_s/D^0 ratio measurements compared to model calculations including sequential (solid lines) and simultaneous coalescence (dotted lines) hadronization, and data from the ALICE measurements (blue and brown circles) and the respective model calculations at LHC energies.

The mass dependence of parton energy loss has been probed in heavy-ion collisions with the measurements of light- and heavy-flavor hadron nuclear modifications factors (R_{AA}). At high p_T, where mass effects are predicted to significantly modify the quark energy loss from gluon radiation in the QGP, the values of light-flavor and charm hadron R_{AA} are measured to be degenerate, and can be explained by mechanisms that are not related to parton energy loss (e.g, see [70]). In that respect systematic comparisons of both bottom and charm hadron nuclear modification factors are predicted to be a clean probe of the

mass dependence of parton energy loss by several model calculations [71–74]. However, from an experimental point of view measuring bottom hadrons have been difficult at RHIC due to the low bottom quark production cross-section, and have only been accessible via the measurement of displaced electrons or charmed hadrons. STAR has now reported at the 2019 Quark Matter conference an updated measurement of single electrons from bottom semileptonic decays utilizing both 2014 and 2016 data sets. The contribution of bottom- and charm-decayed electrons, and backgrounds, are topologically separated using the three-dimensional distance-of-closest approach (DCA) utilizing the HFT detector. In contrast to previous measurements utilizing the transverse dimension DCA (DCA_{xy}), the 3D DCA is able to separate charm- and bottom-decay electrons with greater significance since the longitudinal and transverse DCA have similar resolution. The updated STAR measurement also includes an improved electron identification selection, which is based off a projective likelihood MVA. The improvement in the mis-identified hadron fraction is a factor of two when compared to traditional cut-based particle identification. The results of bottom- and charm-decayed electron R_{AA} are shown in Figure 17 in the top panel, and their ratio in the bottom panel. A constant fit to the double ratio is used to quantify the enhanced $b \rightarrow e$ R_{AA} and is measured to be 1.92±0.25(stat.)±0.21(syst.). Shown in the bottom panel as the hashed blue curve is a null hypothesis where we assume equal values of R_{AA} for charm and bottom hadrons and then fold the distributions to the decay-electron, and subsequently take a double ratio. Performing this exercise shows the effects from different production spectra, fragmentation, and decay phase-space of charm and bottom hadrons, and it is clearly seen these effects have a small impact on the double ratio. The double ratios of $b \rightarrow e$ to $c \rightarrow e$ R_{CP} are also measured and a similar constant fit as in the R_{AA} case is performed and found to be 1.68±0.15(stat.)±0.12(syst.) and 1.38±0.08(stat.)±0.03(syst.) for the ratios of R_{CP}(0-20%/40-80%) and R_{CP}(0-20%/20-40%), respectively. We additionally compare the data to a modified Langevian transport model (DUKE) [72] which includes the mass dependence of parton energy loss, and within uncertainties the data and model are consistent in both the absolute R_{AA} data and the double ratios of R_{AA} and R_{CP}. Combining the agreement between model and experiment, and the quality of the data, these observations represent, for the first time, evidence of mass-ordering of parton energy loss in heavy-ion collisions.

Measurements of heavy-flavor flow are also essential to understanding the QGP properties as particle flow and yield provide a test-bed for model calculations to simultaneously describe the data. It has already been established by STAR [75] in 200 GeV Au+Au collisions that D^0 hadrons have a significant elliptic flow that is comparable to light-flavor hadrons after taking into account particle mass and number of constituent quarks. Measurements of heavy-flavor hadron flow at lower collision energies have been explored via the measurements of single electron elliptic flow in the 2017 and 2018 data sets, and was reported at the 2020 Hard Probes conference. Previous STAR measurements of heavy-flavor electron v_2 in 62.4 and 39 GeV Au+Au collisions [76] were statistically limited and within experimental uncertainties consistent with zero. The data collected during Run-17 and Run-18 at $\sqrt{s_{\rm NN}}$ 54.4 and 27 GeV Au+Au collisions, respectively, are more than an order of magnitude larger in statistics and allow for a more precise measurement. The heavy-flavor decay electron v_2 is extracted

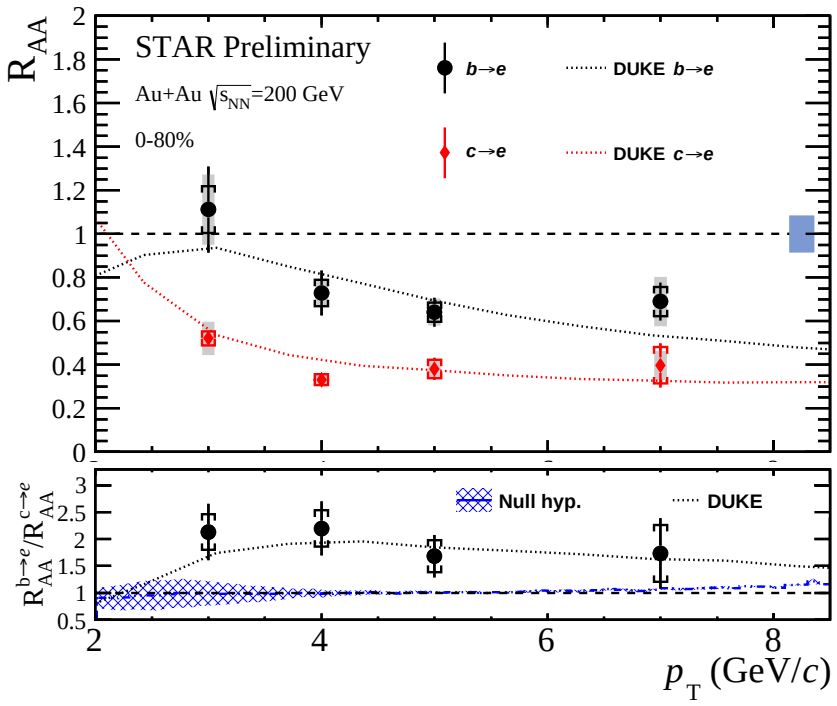

Figure 17: Top: Data for bottom- (blue stars) and charm-decay (red diamonds) electron R_{AA} as a function of electron p_T. The DUKE model calculation are shown as the respectively colored dotted lines. Bottom: The double ratio of bottom to charm R_{AA}, and the null hypothesis (explained in the text) shown as the blue shaded band and DUKE calculation as the dotted line.

from the inclusive electron v_2 by correcting for electron v_2 from hadron and photon decays. The data are shown in Figure 18 for both 54.4 and 27 GeV Au+Au collisions, and compared to previously published STAR data in 200 GeV Au+Au collisions [76]. The 54.4 GeV data show a significant v_2 that is comparable to 200 GeV Au+Au collisions, indicating heavy-flavor hadrons gain significant collective flow in the produced medium in 54.4 GeV Au+Au collisions. The data at 27 GeV indicate a hint of non-zero v_2, but still have considerable uncertainties due to a lower signal-to-background ratio.

STAR has also recently reported at the 2019 Quark Matter conference charm-decayed electron v_1 and v_2, and bottom-decay electron v_2 in 200 GeV Au+Au collisions utilizing the HFT to isolate charm- or bottom-decayed electrons, respectively. The measurement of charm-decayed electron v_1 and v_2 was compared to previous STAR data of D^0 mesons, and show consistency between the two measurements. In the former case the measured slope of the charm-decayed electron v_1 versus rapidity corroborated the recently measured large negative v_1 slope by STAR [68], and with an improved significance of 5σ. The bottom-decay electron v_2 was measured to have a non-zero v_2 with a significance of about 3.4σ, and is consistent in magnitude with expectations from the DUKE model [72]. This is the first significant measurement of bottom hadron v_2 at RHIC.

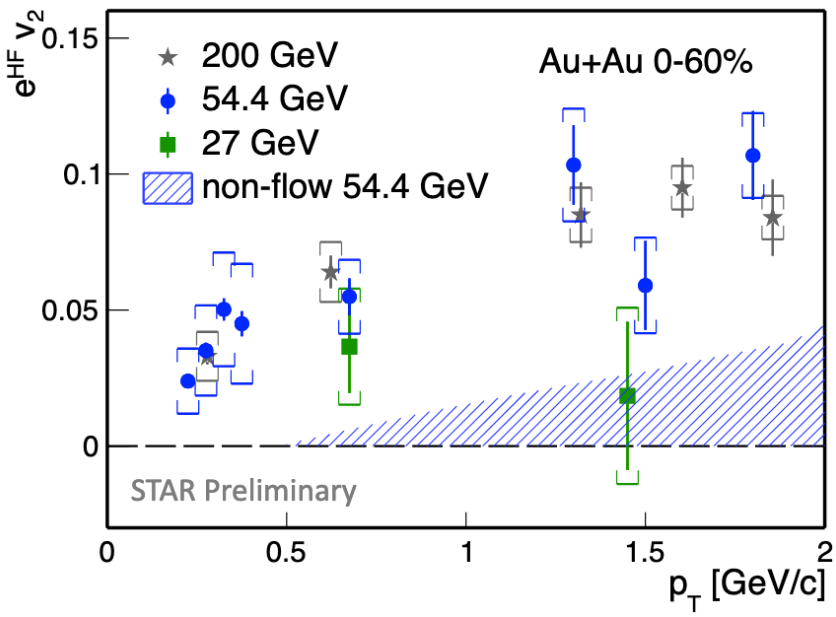

Figure 18: Heavy-flavor electron v_2 as a function of electron p_T in 54.4 (blue circles) and 27 (green squares) GeV Au+Au collisions. The STAR published data at 200 GeV are also shown as the gray stars. The shaded blue histogram shows the estimated non-flow contribution in the 54.4 GeV data.

Recent measurements of quarkonia have opened up new ways to probe production mechanisms by measuring their distributions with jets. It has been observed that there is no simultaneous description of models to the J/ψ spectra and polarization data. It has also been shown that measurements of quarkonia fragmentation functions in jets can have good discriminating power between different models. Recently reported at the 2020 Hard Probes conference, was the measurement of J/ψ mesons within jets as a function of the J/ψ p_T fraction ($z = p_T(J/\psi)/p_T(jet)$). The results are shown in Figure 19 for a given set of jet reconstruction requirements, and unfolded to account for detector smearing. The dependence on cone size was also investigated and the data showed as the cone sized is increased the z distribution became more populated at lower values. Compared with the data in the same plot is the expectation of PYTHIA simulations (shown as the gray shaded histogram). The data show a clear discrepancy with PYTHIA, suggesting J/ψ mesons are not produced mostly in isolation. This new measurement is expected to provide valuable input to the theory community.

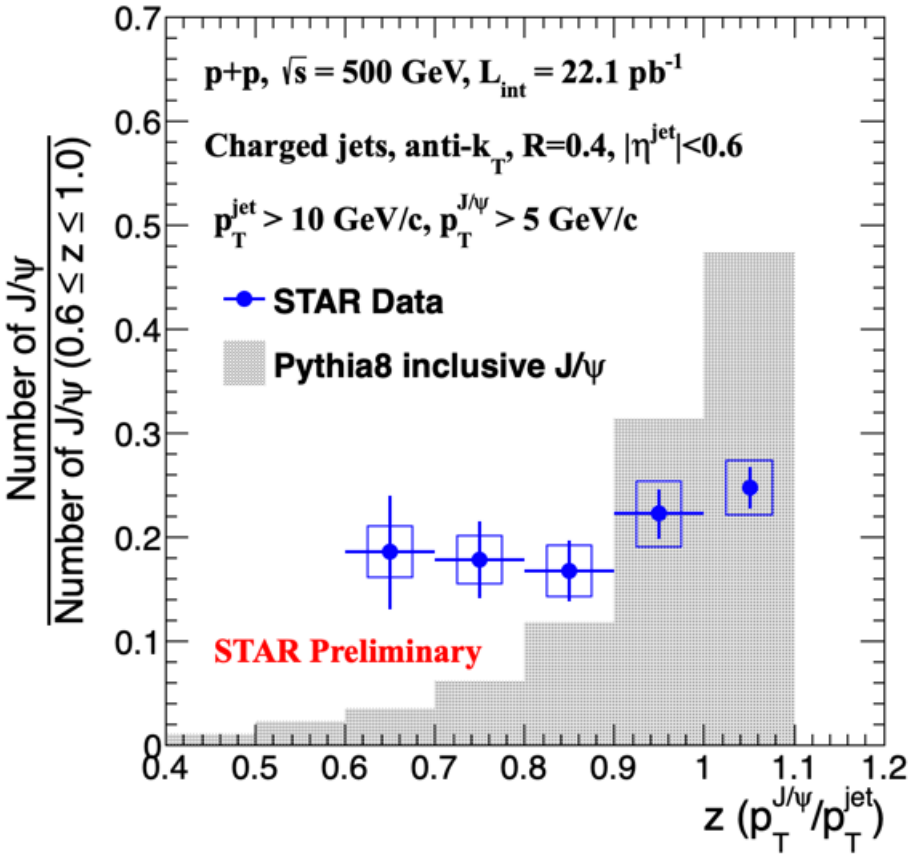

Figure 19: J/ψ momentum fraction in jets in 500 GeV p+p data for a given set of jet reconstruction parameters listed. Also shown is the expectation from PYTHIA simulation as the gray histogram.

1.2 CME Search and Isobar Run

1.2.1 Introduction

Finding a conclusive experimental signature of the Chiral Magnetic Effect (CME) has become one of the major scientific goals of the heavy-ion physics program at the Relativistic Heavy Ion Collider (RHIC). The existence of CME will be a leap towards an understanding of the QCD vacuum, establishing a picture of the formation of deconfined medium where chiral symmetry is restored and will also provide unique evidence of the strongest known electromagnetic fields created in relativistic heavy-ion collisions [77, 78]. The impact of such a discovery goes beyond the community of heavy-ion collisions and will possibly be a milestone in physics. Also, as it turns out, the remaining few years of RHIC run and analysis of already collected data probably provides the last chance for dedicated CME searches in heavy-ion collisions in the foreseeable future. Over the past years significant efforts from STAR as well as other collaborations have been dedicated towards developing new methods and observables to isolate the possible CME-driven signal and non-CME background contributions in the measurements of charge separation across the reaction plane. Many clever ideas have been proposed and applied to existing data. The general consensus is that measurement from the isobar collisions, Ruthenium+Ruthenium (Ru+Ru) that has $10-18\%$ higher B-field than Zirconium+Zirconium (Zr+Zr), provides the best solution to this problem. During the time when this beam user request document is being written, the analysts from the STAR collaboration are about to start the final step of the (four-step) blind analysis of the isobar data that we discuss at length in the following section.

1.2.2 Modality of Isobar Running at RHIC

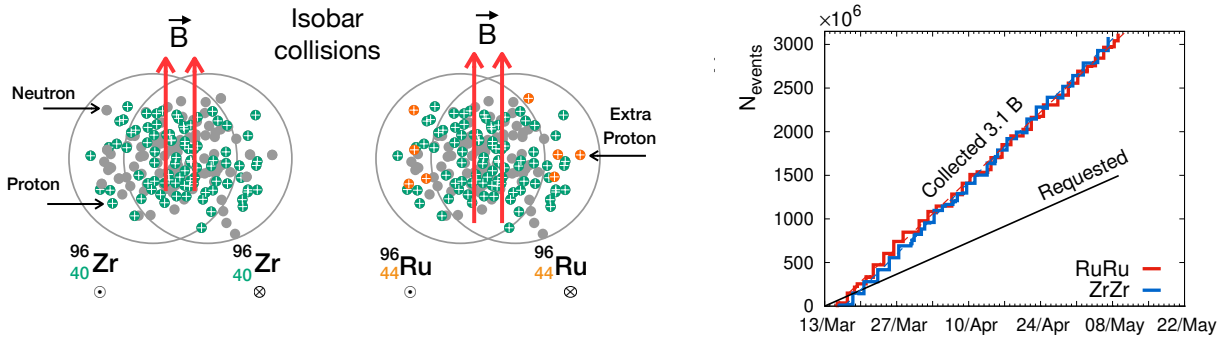

Figure 20: Left: Cartoon of the isobar collisions, about $10-18\%$ stronger B-field is expected in Ru+Ru collisions as compared to Zr+Zr collisions due to four extra protons in each Ru nucleus. Right: Summary of the data collected for isobar collisions during Run 18 – almost a factor of two more events were collected than the request 1.5 Billion events over the course of 3.5 weeks.

The idea of colliding isobar, particularly Ru+Ru and Zr+Zr to make a decisive test of

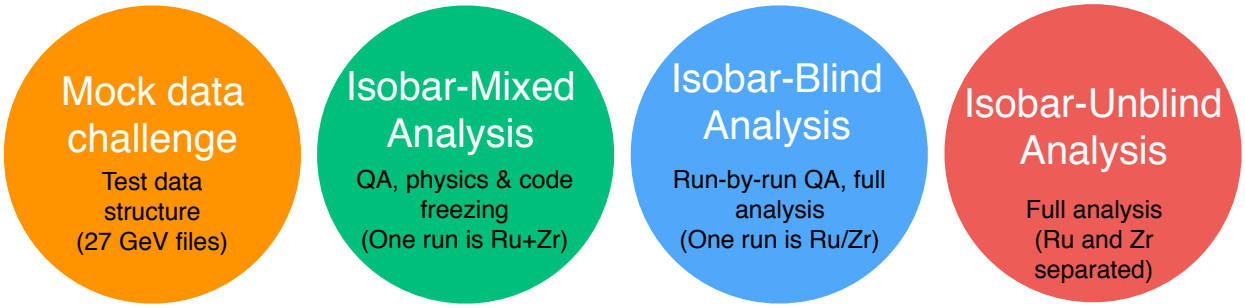

Figure 21: The steps of isobar blind analysis. This cartoon is based on the procedure for the blind analysis of isobar data that have been outlined in Ref [84]. During the time when this document is being written STAR collaboration has finished first three steps and about to begin the final step of isobar-unblind analysis (shown in red).

CME was proposed by Voloshin in Ref [79], the same paper which also proposed to use Uranium collisions to disentangle signal and background of CME. The possible difference in the signals relies on the $10-18\%$ higher B-field in Ru+Ru compared to Zr+Zr [80] in contrast to about 4% difference in flow driven background [36]. Such estimates are sensitive to details of shapes, charge distribution and neutron skin thickness of the two isobar nuclei [80–82]. In the 2017-18 RHIC beam user request [83] STAR collaboration therefore proposed to collect data for two 3.5 week runs in the year 2018. The projection was based on the prospect of achieving five-sigma significance in a scenario where the measurement of $\Delta\gamma$ has 80% non-CME background. This however corresponds to the fact that the systematic uncertainty in the measurements has to be within a few percent and below the statistical uncertainty of the measurements. This started a large scale collaboration wide effort in synergy with the RHIC collider accelerator department to plan for the isobar running in the year 2018. Based on the studies of previous years of data from $Au+Au$ and $U+U$ collisions several major sources of systematics in the measurement of $\Delta\gamma$ were identified. The major sources include: run-to-run variation of detector response due to loss of acceptance, change in efficiency and variation in luminosity that affects the number of reconstructed tracks in the Time Projection Chamber. This eventually leads to uncorrectable systematic uncertainties in $\Delta\gamma$, the main observable to measure charge separation across event plane. In order to minimize such systematics the proposal were to: 1) switch species in RHIC between stores and, 2) keep long stores to level the luminosity aiming for specific rates in the coincidence measurements of beam fragments by the STAR zero-degree calorimeters. The aim was to maintain exact balance of run and detector conditions for the two species so that observations in the two systems are equally affected and can later on be largely eliminated in the ratios of observables.

1.2.3 Blinding of Data Sets and Preparation for Analyses

With the successful conclusion of the isobar run in the year 2018 STAR experiment collected more than 3 billion events for each isobar species. The next step was to develop the plans for a blind analysis, the main idea behind which is to eliminate possible unconscious biases.

A total of five institutional groups are expected to perform the analysis of the data. The analysts from each group will focus on a specific aspect of the analysis described in the previous section although in many cases there are substantial overlap in some analyses that will help cross check the results. An important part of the blind analysis is the blinding of the data. The details of the blinding of the data structure is decided by members of a blinding-committee who are not part of the team of analysts and will work in close collaboration with STAR experts who are part of the production team. The idea is to provide the analysts the access to data in files where species-specific information are disguised or removed before the final step of unblinding. A careful consideration is taken by the blinding-committee to make sure only the essential information to do the analysis-specific quality assurance of the data is available to the analysts. Some of the quality assurance, calibration and centrality determination work that require species information are done only by STAR experts who are not a part of the team of analysts. Above all, the main goal of the committee is to make sure that under no circumstances physics analysts can access un-blinded data that can jeopardize the blind analysis. For example, all the data sets are produced with pseudo-run-number that cannot be used by the analysts to retrieve the exact species information.

1.2.4 Methods for the Isobar Blind Analyses

The detailed procedure for the blind analyses of isobar data have been outlined in Ref [84]. Figure.21 is a cartoon that summarizes the four steps and the main idea.

In the zeroth step shown in the extreme left of Fig.21 (by orange circle) is the mock data challenge which is not exactly a step of the isobar data analysis but a crucial step to familiarize the analysts with the technicalities of the data structures that have been specifically designed for blind analysis.

The first step shown in Fig.21 (by green circle) as the “isobar-mixed analysis" or “mixed-blind analysis" is truly the first step of blind analysis. This is also the most challenging steps from the point of view of the analysts. In this step the analysts are provided with data sample where each run comprise of events that are mixed samples from two species. In this step the analysts perform the full quality assurance (QA) and physics analysis of the data, document every details of steps of the procedure and freeze the codes. After the completion of this step no changes to the analysis code is permissible. Also, no changes in the analysis procedure is allowed. The only permissible change in the following step is to reject bad runs or pile-up events. However, in order to avoid unconscious bias in analysis such rejection cannot be done arbitrarily and an automated algorithm must be developed in this step and the related codes have to be frozen. The stability of the automated QA algorithm is tested with some of the existing data sets of Au+Au and U+U collisions.

The second step shown in Fig.21 (by blue circle) is referred to as the “isobar-blind analysis" or “unmixed-blind analysis". From this step on-wards the analysts are allowed to run their previously frozen codes. The main purpose of this step is to perform run-by-run QA of the data sample. For this the analysts are provided with files each of which contain data from a single species that is either Ru or Zr. However, there are two conditions: the files contain limited number of events that cannot lead to any statistically significant result and

the species information is not revealed. Although a pseudo-run-number is used for each file, the time ordering is preserved with a unique mapping that is unknown to the analysts. It is important to maintain the time ordering to identify time-dependent changes in detectors and run conditions as a part of the run-by-run quality assurance. With this limited data sample the analysts need run the frozen automated algorithm to identify bad runs. A similar automated algorithm is also used for identifying and rejecting bad runs. After this step no more changes are allowed in terms of QA.

The final step of isobar blind analysis is shown by red circle in Fig.21 is referred to as "isobar-unblind" analysis. In this step the species information will be revealed and the physics results will be produced by the analysts using the previously frozen codes. The finding from this step will be directly be submitted for publication without any kind of alteration. If a mistake is found in the analysis code, the erroneous results will also accompany the corrected results.

1.2.5 Observables for Isobar Blind Analyses

Isobar blind analysis will specifically focus on these five observables. The following five sections describe these procedures in brief with comments on the outlook for isobar blind analysis: 1) Differential measurements of $\Delta\gamma$ to identify and quantify backgrounds, 2) measurement of higher order harmonics of γ-correlator, 3) exploiting the relative charge separation across participant and spectator planes, 4) the use of R-observable to measure charge separation and 5) the use of signed balance function. The first three approaches are based on aforementioned three-particle correlator and the last two employ slightly different approaches to quantify charge separation.

Differential measurements of $\Delta\gamma$ to identify and quantify background *Invariant mass dependence of charge separation*: Differential measurements of $\Delta\gamma$ with invariant mass and relative pseudorapidity provide interesting prospects to identify and quantify the sources of flow and non-flow driven backgrounds. The idea to use invariant mass is simple and was first introduced in Ref [85]. Resonances are widely identified by observing structures in the invariant mass spectra of the decay daughters. Take a pair of opposite sign pions for example, a large fraction of them come from the neutral resonances that show up in the invariant mass spectrum of $m_{inv}(\pi^+ + \pi^-)$. If we restrict the analysis to pairs of pions, differential measurements of $\Delta\gamma$ with $m_{inv}(\pi^+ + \pi^-)$ should also show similar peak like structures if background from neutral resonances dominate the charge separation. Indeed similar peak structures are observed and a careful analysis is performed by STAR collaboration to extract the possible fraction of CME signals from measurements [86]. This analysis relies on the assumption that CME signals do not show peak like structures in $m_{inv}(\pi^+ + \pi^-)$ therefore calls for more theoretical inputs in this direction.

Relative pseudorapidity dependence: The relative pseudorapidity dependence of azimuthal correlations are widely studied to identify sources of long-range components that are dominated by early time dynamics as compared to late time correlations that are prevented by

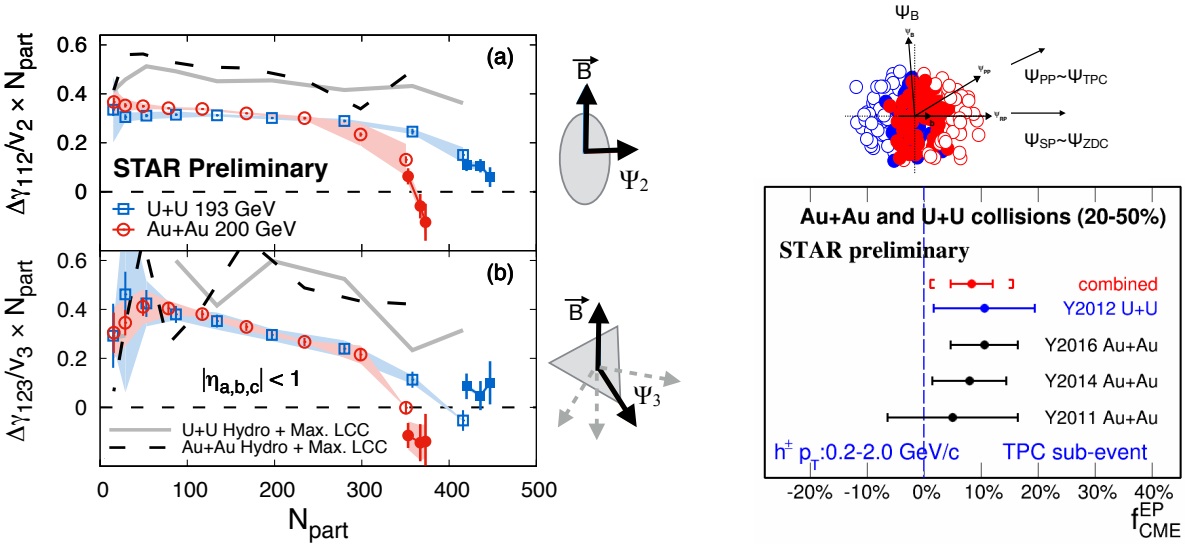

Figure 22: (Left) Measurement of charge separation along second and third order event planes in Au+Au and U+U collisions. (Right) Fraction of possible CME signal in the measurement of $\Delta\gamma$ with respect to spectator and participant planes [88].

causality to appear as short-range correlations. The same can be extended to charge dependent correlations that provides the impetus to explore the dependence of $\Delta\gamma$ on the pseudorapidity gap between the charge carrying particles $\Delta\eta_{ab} = |\eta_a - \eta_b|$ in $\langle\cos(\phi_a^\alpha + \phi_b^\beta - 2\Psi_{RP})\rangle$. Such measurements have been performed in STAR with Au+Au and U+U data. It turns out that the possible sources of short range correlations due to photon conversion of $e^+ - e^-$, HBT and Coulomb effects can be identified and described as Gaussian peaks at small $\Delta\eta_{ab}$, the width and magnitude of which strongly depend on centrality and system size. Going to more peripheral centrality bins it becomes harder and harder to identify such components as they overlap with sources of di-jets fragmentation that dominate both same-sign and opposite sign correlations. An effort to decompose different components of $\Delta\gamma$ via study of $\Delta\eta_{ab}$ can be challenging although a clear sign of different sources of correlations are visible in change of shape of individual same-sign and opposite sign measurements of γ-correlator [87].

In any case, these differential measurements of $\Delta\gamma$ in isobar collisions provide the prospect to extract the $m_{inv}(\pi^+ + \pi^-)$ and $\Delta\eta$ dependence of CME signals that will provide much deeper insights on the origin of the effect.

Mixed harmonics measurements with second and third order event planes In order to proceed in this section it is better to rewrite the conventional γ-correlator by a more general notation as $\gamma_{112} = \langle\cos(\phi_a^\alpha + \phi_b^\beta - 2\Psi_2)$. The idea is to measure charge separation across the third harmonic event plane by constructing a new correlator $\Delta\gamma_{123} = \gamma_{123}(OS) - \gamma_{123}(SS)$, where $\gamma_{123} = \langle\cos(\phi_a^\alpha + 2\phi_b^\beta - 3\Psi_3)\rangle$ that was introduced by CMS collaboration in Ref [89]. Since the Ψ_3 plane is random and not correlated to B-field direction (see Fig.22), γ_{123} is purely driven by non-CME background, the contribution of

which should go as v_3/N. This is very useful to contrast signal and background scenario by comparing the measurements in two isobaric collision systems. Since Ru+Ru has larger B-field than Zr+Zr but have comparable background, the case for CME would be as follows: $(\Delta\gamma_{112}/v_2)^{\rm Ru+Ru}/(\Delta\gamma_{112}/v_2)^{\rm Zr+Zr} > 1$ and $(\Delta\gamma_{112}/v_2)^{\rm Ru+Ru}/(\Delta\gamma_{112}/v_2)^{\rm Zr+Zr} > (\Delta\gamma_{123}/v_3)^{\rm Ru+Ru}/(\Delta\gamma_{123}/v_3)^{\rm Zr+Zr}$. Fig.22 (left) shows the measurement of these observables in U+U and Au+Au collisions. Within the uncertainties of the measurements no significant difference in the trend of $\Delta\gamma_{112}/v_2$ and $\Delta\gamma_{123}/v_3$ is observed for the two collision systems except for the very central events. Predictions from hydrodynamic model calculations with maximum possible strength of local charge conservation [36] is shown on the same plot. Overall observation indicates background dominate the measurements and a similar analysis of the isobar data is highly anticipated.

Charge separation along participant and spectator planes This analysis makes use of the fact that B-field driven signal is more correlated to spectator plane in contrast to flow driven background which is maximum along the participant planes. The idea was first introduced in Ref [90] and later on followed up in Ref [91]. It requires measurement of $\Delta\gamma$ with respect to the plane of produced particles, a proxy for participant plane as well as with respect to the plane of spectators. In STAR the two can be done by using Ψ_2 from TPC and Ψ_1 from ZDC respectively. The approach is based on three main assumptions: 1) measured $\Delta\gamma$ has contribution from signal and background that can be expressed as $\Delta\gamma = \Delta\gamma^{\rm bkg} + \Delta\gamma^{\rm sig}$, 2) the background contribution to $\Delta\gamma$ should follow the scaling $\Delta\gamma^{\rm bkg}({\rm TPC})/\Delta\gamma^{\rm bkg}({\rm ZDC}) = v_2({\rm TPC})/v_2({\rm ZDC})$ and, 3) the signal contribution to $\Delta\gamma$ should follow the scaling $\Delta\gamma^{\rm sig}({\rm TPC})/\Delta\gamma^{\rm sig}({\rm ZDC}) = v_2({\rm ZDC})/v_2({\rm TPC})$. The first two have been known to be working assumptions, widely used for a long time and can be used to test the case of CME [91] if $(\Delta\gamma/v_2)\,({\rm ZDC})/\,(\Delta\gamma/v_2)\,({\rm TPC}) > 1$. The validity of the last one was studied and demonstrated in Ref [90]. Using all three equations one can extract [88] the fraction of possible CME signal $f_{\rm CME} = \Delta\gamma^{\rm sig}/\Delta\gamma$ in a fully data-driven way as shown in Fig.22(right). This analysis will be done with the isobar data and the case for CME will be $f_{\rm CME}^{\rm Ru+Ru} > f_{\rm CME}^{\rm Zr+Zr} > 0$.

Alternate measure: The novel R-observable The R-observable is actually a distribution, introduced in Ref [94], and defined as the ratio of two distribution functions of the quantity ΔS parallel and perpendicular to B-field direction defined as $R_{\Psi_m}(\Delta S) = C_{\Psi_m}(\Delta S)/C^{\perp}_{\Psi_m}(\Delta S)$. Here ΔS measures the difference in the dipole moment of the positive and negative charge in an event (see Ref [94] for details). The shape of $R_{\Psi_2}(\Delta S)$ will be sensitive to CME as well as non-CME background whereas $R_{\Psi_3}(\Delta S)$ is purely driven by non-CME background and serves as a baseline. Model calculations have established several unique features of this observable: 1) presence of CME signal will lead to a concave shape of the $R_{\Psi_2}(\Delta S)$, 2) increasing strength of CME signal will increase the concavity of $R_{\Psi_2}(\Delta S)$, 3) in presence of CME, the concavity of $R_{\Psi_2}(\Delta S)$ will be larger than that of $R_{\Psi_3}(\Delta S)$. The measurement of R_{Ψ_m} is shown in Fig.23. The quantity $\Delta S''$ shown is a slight variant of (ΔS) that incorporates correction for particle number fluctuations and event plane resolution. The

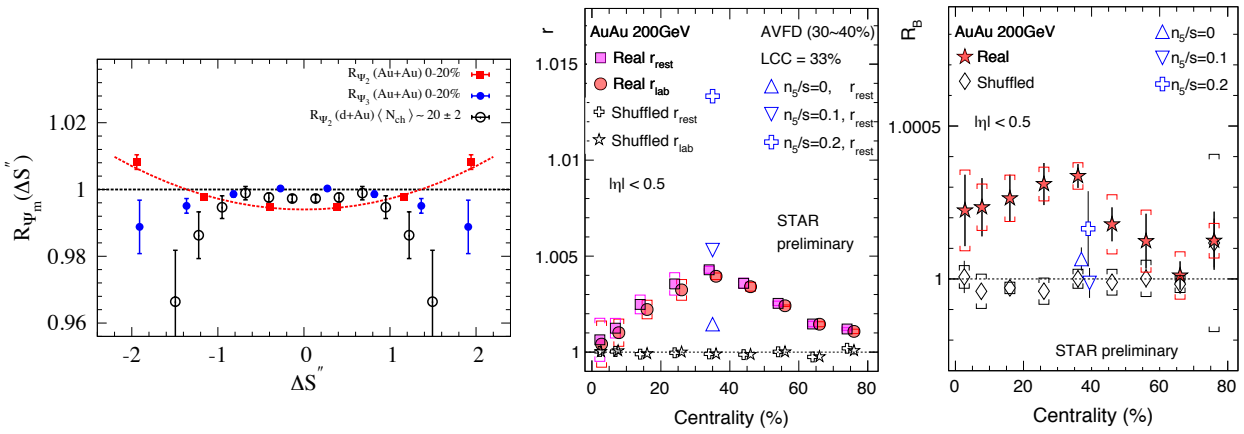

Figure 23: (Left) The R-observable shown for different collision systems, concave shape is consistent with CME expectation [92]. (Right) The two main quantities r and R_B derived from signed balance function, deviation from unity is consistent with CME expectation [93].

observation of Fig.23 indicates more concave shape for R_{Ψ_2} compared to R_{Ψ_3} in Au+Au whereas flat or convex shapes for $p/d+Au$ indicating that the measurements are consistent with expectations of CME [92]. For isobar collisions the case of CME will be confirmed if: 1) a concave shape is observed for the ratio of the observables $R_{\Psi_2}(\Delta S)^{\rm Ru+Ru}/R_{\Psi_2}(\Delta S)^{\rm Zr+Zr}$ and 2) the concavity should be weaker for $R_{\Psi_3}(\Delta S)^{\rm Ru+Ru}/R_{\Psi_3}(\Delta S)^{\rm Zr+Zr}$.

Alternate measure: The signed Balance function A very recently proposed observable to search for CME is the signed balance function (SBF) [95]. The idea is to account for the ordering of the momentum of charged pairs measured by the width of SBF that is expected to be different for out-of-plane as compared to in-plane measurement captured in the ratio $r_{\rm lab}$. In addition, one can also account for the boost due to collective expansion of the system that forces all pairs to move in the same direction and measure the ratio in pair rest frame $r_{\rm rest}$. In presence of CME the individual ratios as well as the double ratio $R_B = r_{\rm rest}/r_{\rm lab}$ is expected to be greater than unity. The preliminary measurements shown in Fig.23 (right) from STAR in Au+Au 200 GeV seems to be consistent with CME expectation. This observable will be studied with the isobar data in STAR but not as a part of the blind analysis and the CME expectation will be: 1) $r({\rm Ru+Ru}) > r({\rm Zr+Zr})$, and 2) $R_B({\rm Ru+Ru}) > R_B({\rm Zr+Zr})$.

Prospect of CME search beyond isobar-era It is important to discuss the strategy for CME search beyond the isobar-era. It is true that such strategy needs to be planned based on the outcome of the isobar program. We would like to get started by considering two possible scenarios at the top RHIC energy: 1) isobar program results in a significance of 3σ and below, 2) isobar program results in a significance of 3σ and above.

In the first scenario one can infer from the projection plot of fig.24(left) that the upper limit of the fraction of CME signal should be less than or equal to 8%. Question is under such

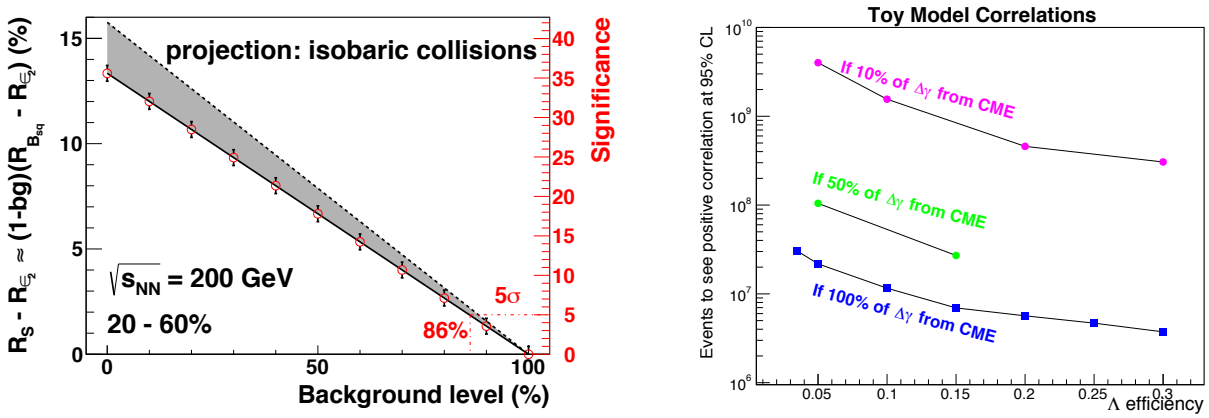

Figure 24: (Left) Projection plot taken from a previous beam user request document [83] indicating the anticipated significance in the measurement of charge separation as a function of the CME signal fraction. (Right) Estimation of the number of events required to see positive correlation between net Λ helicity with out-of-plane charge separation sensitive to local parity violation at 95% confidence level, plotted against the efficiency of $\Lambda(\bar{\Lambda})$ reconstruction (see [96] for details).

a scenario can STAR perform a follow up measurement to achieve a decisive 5σ significance and establish a conclusive evidence of CME? It turns out such a measurement is possible even with a single Au+Au 200 GeV data set during the year 2023 running of STAR concurrently with sPHENIX. Current analysis of aforementioned CME signal in Au+Au 200 GeV extraction using elliptic flow and charge separation with respect to spectator and participant planes yields 4% statistical uncertainty with 2.4 B events ($2-3\sigma$ significance). In order to get 5 σ significance with the same analysis one needs to have statistical uncertainty of order 1.6% which would require about $(4/1.6)^2 \times 2.4 = 15$ Billion events. Therefore, as per the previous estimates of anticipated 10 Billion events that can be collected by STAR during the 2023 year, one can achieve about 4σ significance on the upper limit of possible CME signal fraction in the measurement of charge separation. This estimate does not account for two important facts that can lead to higher significance and a decisive measurement of CME. The first one is that the magnitude of projected B-field on reaction plane is higher in Au+Au collisions as compared to isobar collisions. The second one is that iTPC upgrade enhances the charge particle multiplicity by 50% and therefore triplets($\sim dN/d\eta^3$) (pairs $\sim dN/d\eta^2$) statistics by a factor of 3.4 (2.3). So the final conclusion is that even if isobar program results in a 3 σ measurement running STAR in the year 2023 will result in a $> 4\sigma$ measurement. This conclusion assumes that the systematic uncertainty can be controlled to be smaller than the statistical uncertainty, i.e. below 2%.

For the second scenario ($> 3\sigma$ measurement from isobar program) we will also be able to establish an upper limit of the fraction of CME signal. For example, in fig.24(left) we see that 5σ significance will establish 13% CME signal and a discovery of the CME phenomenon in heavy ion collisions. The impact of such a discovery will set a milestone in physics. Running STAR in the year 2023 concurrently with sPHENIX would be essential to perform

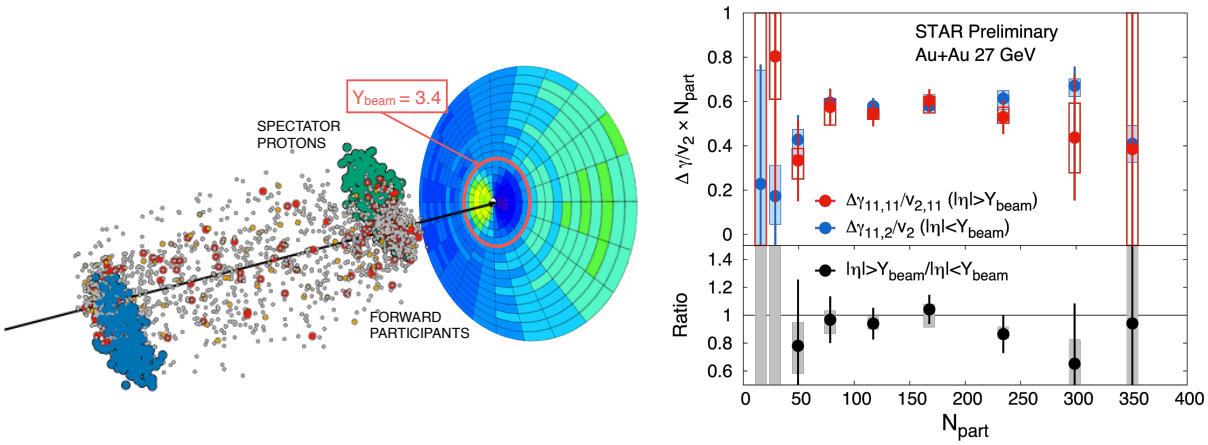

Figure 25: Prospect of precision CME search with the BES-II data. (Left) Single simulated UrQMD event and EPD detector acceptance that covers beam rapidity and detects both forward participants and spectators in 27 GeV Au+Au collisions that have large directed flow which changes sign at $\eta = Y_{\rm bean} = 3.4$. (Right) γ-correlators scaled by v_2 across different event-planes and double ratio of spectators/participant event planes which should be unity for no-CME scenario.

dedicated precision measurements to further investigate and characterize the phenomena. In this context STAR collaboration has stated a new analysis to understand the origin of parity violation in hot QCD by measuring the correlation of net-Λ helicity with charge separation across reaction plane [96]. The difference between the number of positive and negative helicity $\Lambda(\bar{\Lambda})$ $N_L^\Lambda - N_R(\Lambda)$ should be associated with net-chirality, i.e. the difference between right and left handed quarks, in a given event. Since net chirality in the event also drives out-of-plane charge separation (a_1) in the presence of B-field, one expects a correlation between a_1 and $N_L^\Lambda - N_R(\Lambda)$ as a results of local parity violation. Currently available data sets do not allow us to perform a significant measurement for this observable. Using a toy model simulation, shown in fig.24(right), we estimate the number of event required to see non-zero correlations between a_1 and $N_L^\Lambda - N_R(\Lambda)$ at the 95% confidence level as a function of the efficiency of $\Lambda(\bar{\Lambda})$ reconstruction. Different curves correspond to different magnitudes of CME fraction in the measurement of γ-correlator. With about 10 B Au+Au 200 GeV events in run 2023 it will be possible to perform a significant measurement to study this phenomenon.

Regardless of the outcome of the measurements with the isobar program, that will be performed at the top RHIC energy, one question will remain. What happens at lower collision energy? In this context a new idea has emerged. The newly installed event-plane detector (EPD) upgrade provides a new capability at STAR towards CME search at lower collision energy and for the Beam Energy Scan phase-II program [18]. The idea is simple, at lower energies EPD acceptance ($2.1 < |\eta| < 5.1$) falls in the region of beam rapidity ($Y_{\rm beam}$) and can measure the plane of strong directed flow (Ψ_1) of spectator protons, beam fragments and stopped protons, therefore strongly correlated to the B-field direction (See fig25). The next step is to measure $\Delta\gamma$ with respect to Ψ_1 and compare it with the measurement of

$\Delta\gamma$ along Ψ_2 planes from outer regions of EPD and TPC at mid-rapidity that are weakly correlated to the B-field directions. A test of CME scenario will be to see if large difference is observed in the measurements. First preliminary measurements from STAR as shown in Fig 25 is dominated by uncertainty but seems to show a lot of prospects for the CME search at lower energies. With higher statistics data from the BES-II program (7.7-19.6 GeV) and STAR fixed target run more precise measurement is possible.

1.3 Highlights from the Spin and Cold QCD Program

Introduction

The goal of the STAR Cold QCD program is to probe the spin and flavor structure of the proton and understand the role of spin in Quantum Chromodynamics, exploiting the unique capability of RHIC to provide longitudinally and transversely polarized p+p and p+A collisions at multiple energies. Measurements with longitudinal beam polarizations have given new insights into the helicity structure of the proton, while measurements with transverse polarizations have provided new ways to probe polarized parton distribution functions (PDFs) in the collinear and transverse momentum dependent frameworks. Additionally, the cross-section measurements in the unpolarized p+p collisions provide valuable information to constrain collinear and transverse momentum dependent unpolarized PDFs. This program is complemented by studies of polarized p+p elastic scattering and central exclusive production, in which a far-forward proton is detected intact.

Table 5: Summary of polarized p+p and p+A running periods at RHIC since 2009, including center-of-mass energy, STAR's integrated luminosity and the average beam polarization for blue (B) and yellow (Y) beams from the H-jet polarimeter.

Year	System	$\sqrt{s}$ (GeV)	Recorded Lumi. (pb^{-1})	Polarization	B/Y $\langle P \rangle$ (%)
2009	pp	200	25	Longitudinal	55/55
2009	pp	500	10	Longitudinal	39/39
2011	pp	500	12	Longitudinal	48/48
2011	pp	500	25	Transverse	48/48
2012	pp	200	22	Transverse	61/56
2012	pp	510	82	Longitudinal	50/53
2013	pp	510	300	Longitudinal	51/52
2015	pp	200	52	Transverse	53/57
2015	pp	200	52	Longitudinal	53/57
2015	pAu	200	0.45	Transverse	60/–
2015	pAl	200	1	Transverse	54/–
2017	pp	510	320	Transverse	55/55

Since 2009, RHIC STAR has completed several highly successful polarized p+p runs

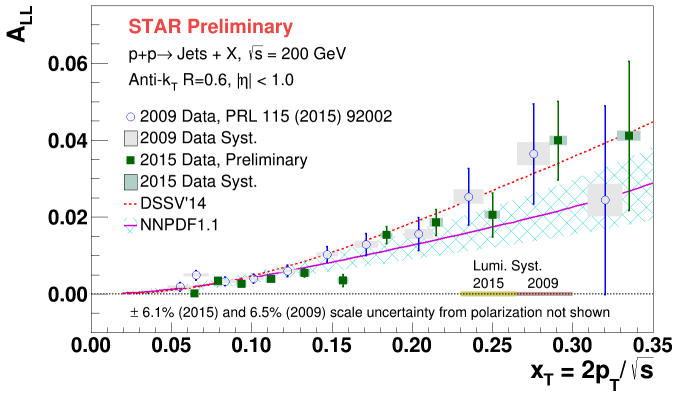

Figure 26: A_{LL} for inclusive jets with $|\eta| < 1.0$ versus x_T. The filled points show 2015 preliminary results [97], whereas the open points show the 2009 data of Ref. [99]. The bars show the size of the statistical uncertainties, whereas the boxes indicate the size of systematic uncertainties. The curves show the expected A_{LL} values for the DSSV14 [101] and NNPDFpol1.1 [102] parton distributions.

both at $\sqrt{s} = 200$ GeV and $\sqrt{s} = 500/510$ GeV. Moreover, p+Au and p+Al datasets with a transversely polarized proton beam have been recorded in 2015 at $\sqrt{s} = 200$ to address important physics problems, including the ridge phenomenon and the possible onset of gluon saturation effects. Table 5 summarizes the STAR sampled luminosity and the luminosity averaged beam polarization as measured by the hydrogen jet (H-jet) polarimeter.

Longitudinal program

Since last year's PAC meeting, the STAR spin and cold QCD physics working group has released preliminary results focused on double-spin asymmetries A_{LL} of inclusive jet [97] and dijet [98] production in longitudinally polarized p+p collisions at a center-of-mass energy $\sqrt{s} = 200\,\text{GeV}$ based on the 2015 data set. These analyses are aimed at providing additional constraints to the gluon helicity distribution $\Delta G(x, Q^2)$, especially for the medium gluon momentum fractions in the range from $x \simeq 0.05$ to $x \simeq 0.5$. Figures 26 and 27 show the preliminary results of inclusive jet A_{LL} together with the 2009 data results of Ref. [99] and dijet A_{LL} together with the 2009 results from [100] respectively. Expected A_{LL} values for the DSSV14 [101] and NNPDF-pol1.1 [102] parton distributions are also presented. The results are in good agreement with previous measurements at $\sqrt{s} = 200\,\text{GeV}$ and with the theoretical evaluations of prior world data. They have better precision and thus provide further evidence that $\Delta G(x, Q^2)$ is positive for $x > 0.05$.

The results for the inclusive jet and dijet A_{LL} based on the 2012 $\sqrt{s} = 510$ GeV longitudinally polarized p+p data, which enabled exploration of $\Delta G(x, Q^2)$ down to $x \simeq 0.015$, were discussed in the previous PAC report and have since been published in Physical Review D [103].

Transverse program

There have been several new STAR preliminary results on transverse spin physics released since the last PAC meeting. Highlights include the Collins asymmetry for charged pions inside a jet [104] and the dijet Sivers asymmetry [105] at $\sqrt{s} = 200$ GeV p+p collisions.

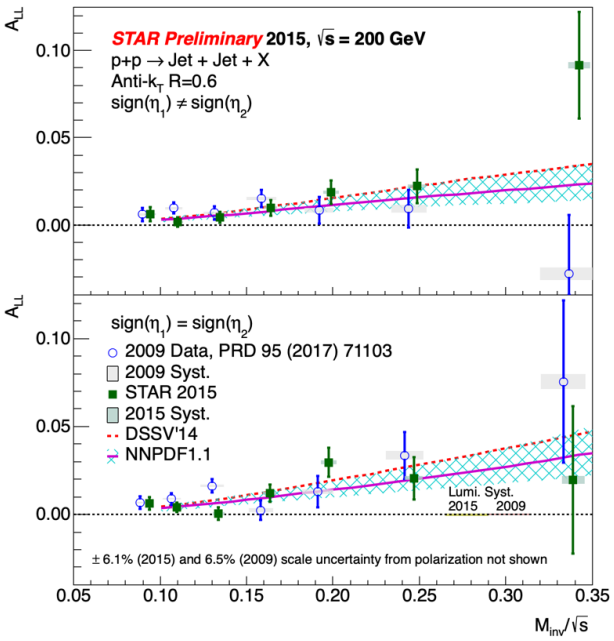

Figure 27: A_{LL} as a function of the parton-level invariant mass for dijets with the opposite-sign (top) and same-sign (bottom) event topologies. The filled points show 2015 preliminary results [98], whereas the open points show the 2009 data of Ref. [100]. The bars show the size of the statistical uncertainties, whereas the boxes indicate the size of systematic uncertainties. The curves show the expected A_{LL} values for the DSSV14 [101] and NNPDF-pol1.1 [102] parton distributions.

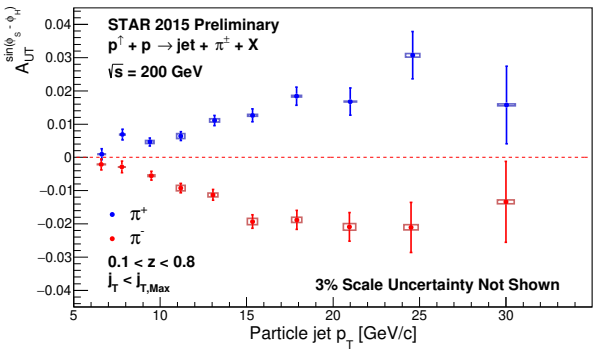

Figure 28: Preliminary results for the Collins asymmetry plotted for identified π^+ (blue) and π^- (red) particles as a function of jet p_T for jets that scatter forward to polarized beam ($x_F > 0$) [104]. The full range of both z and j_T are integrated over.

Moreover, the final publications of the transverse single spin asymmetries (TSSA) for neutral pions produced at forward rapidity in $\sqrt{s} = 200$ GeV for p+p, p+Au and p+Al [106], and 500 GeV p+p [107] collisions are in God Parent Committees.

The Collins asymmetry in p+p collisions combines the collinear quark transversity in the proton with the transverse momentum dependent Collins fragmentation function [108–110], thus provides a cleaner probe of the Collins fragmentation functions than that in semi-inclusive deep inelastic scattering (SIDIS), and enables tests of evolution, universality and factorization breaking in the TMD formalism. Figure 28 shows the preliminary Collins asymmetries for charged pions inside jets that scatter forward ($x_F > 0$) to the polarized beam from 2015. The measured asymmetries are consistent with previous measurements from 2012 [111], but have 30% smaller statistical uncertainty.

The Sivers effect describes the correlation of the parton transverse momentum with the transverse spin of the nucleon. Figure 29 shows the first observation of non-zero Sivers asymmetries in dijet production of transversely polarized proton collisions using the STAR

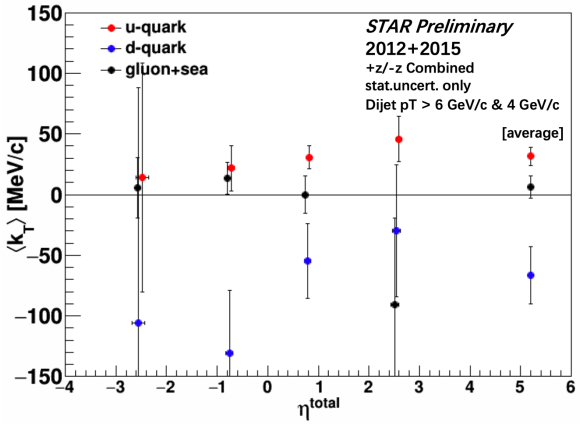

Figure 29: Preliminary results for the spin-dependent k_T values for u, d and $gluon + sea$ from the dijet Sivers measurement as a function of the sum of dijet pseudorapidities $\eta_1 + \eta_2 \sim \ln(\frac{x_1}{x_2})$ [105].

2012+2015 polarized p+p data. Compared to the previous 2006 result [112], fully reconstructed jets are analyzed with 33 times more statistics. Charge-tagging methods are employed in order to separate the u and d quark signals. With detailed simulation, the individual parton spin-dependent $\langle k_T \rangle$ are extracted for u, d and $gluon+sea$ quarks, and indicates that $\langle k_T^u \rangle \approx 32$ MeV/c, $\langle k_T^d \rangle \approx -67$ MeV/c and $\langle k_T^{g+sea} \rangle \approx 0$ MeV/c.

The transverse single spin asymmetry (TSSA) for forward neutral pions produced in polarized proton collisions with protons (p+p), with aluminium nuclei (p+Al) and with gold nuclei (p+Au) at $\sqrt{s} = 200$ GeV from FMS are also measured using the data taken in 2015. The preliminary results for (p+p) and (p+Au) have been released [106] and the final publication is soon to be submitted to Physical Review D. Measured asymmetries presented in Fig. 30 are found to rise with transverse momentum at $x_F < 0.5$, while they flatten or fall at larger x_F. The results are consistent with a weak nuclear A dependence. Moreover, a further observation is that TSSA is significantly larger for isolated π^0s than for non-isolated π^0s, which are accompanied by additional jet-like fragments.

The transverse single-spin asymmetry of neutral pions at $\sqrt{s} = 200$ GeV and 500 GeV from FMS data are compared in Fig. 31. The 200 GeV data are from 2015, while the 500 GeV data are from 2011. The theoretical calculations presented in the plot are based on the Transverse Momentum Dependent (TMD) and collinear twist-3 functions from a recent global analysis [113], which also includes previous forward π^0 and charged hadron TSSA data from RHIC in the fit. The theoretical calculation differs from our measurement and only provides a reasonable description of the non-isolated π^0 in the low-x_F region. A continuous increase of the TSSA with Feynman-x indicates the independence on the center-of-mass energy. Pions with no nearby particles, which may not arise from conventional jet fragmentation, tend to have a higher TSSA than non-isolated pions, which suggests that a different mechanism other than the Sivers or Collins effects is required to explain these results.

Unpolarized Results

The azimuthal correlation of forward di-pions produced in p+p and p+Au collisions provides an essential tool to access the underlying gluon dynamics in the nonlinear evolution

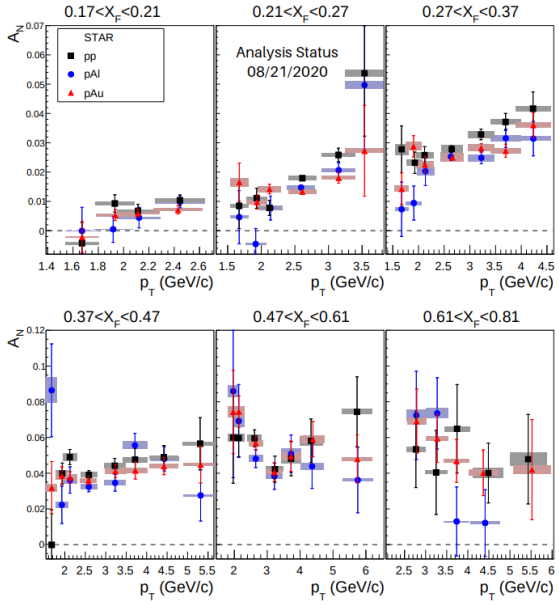

Figure 30: Transverse single spin asymmetry for forward π_0 production as a function of transverse momentum for six Feynman x_T regions. Results for three collisions systems are shown, black squares for p+p, blue circles for p+Al and red triangles for p+Au collisions. The statistical uncertainties are shown with vertical error bars and the filled boxes indicate the horizontal and vertical systematic uncertainties. Analysis status on 08/21/2020. Preliminary results available in Ref. [106].

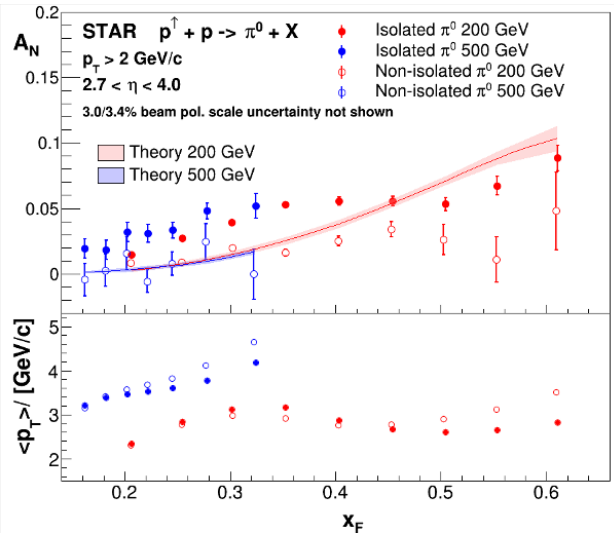

Figure 31: Preliminary results for the transverse single-spin asymmetry as function of Feynman-x for the isolated and non-isolated π^0 in transversely polarized proton-proton collisions at 200 and 500 GeV [107]. Theory curves based on a recent global fit [113] are also shown. The average transverse momentum of the π^0 for each x_F bin is shown in the lower panel.

region. π^0 measured in the FMS in the pseudorapidity region $2.5 < \eta < 4.0$ probe low momentum fraction partons down to $x \approx 0.001$ at $\sqrt{s} = 200$ GeV, which are dominated by gluons. 2015 p+Au collisions have a unique opportunity to study this phenomenon with much higher luminosities and smaller background than 2008 d+Au [114]. Figure 32 shows the status of di-pion correlation measurement from Run15 p+p and p+Au collisions. The away-side peak is suppressed in high activity p+Au collisions compared with p+p. This effect is more significant when the more central part of the nucleus is probed (with higher multiplicity as indicated by BBCE). Further analysis to characterize the p_T dependence and compare with theoretical expectations is ongoing.

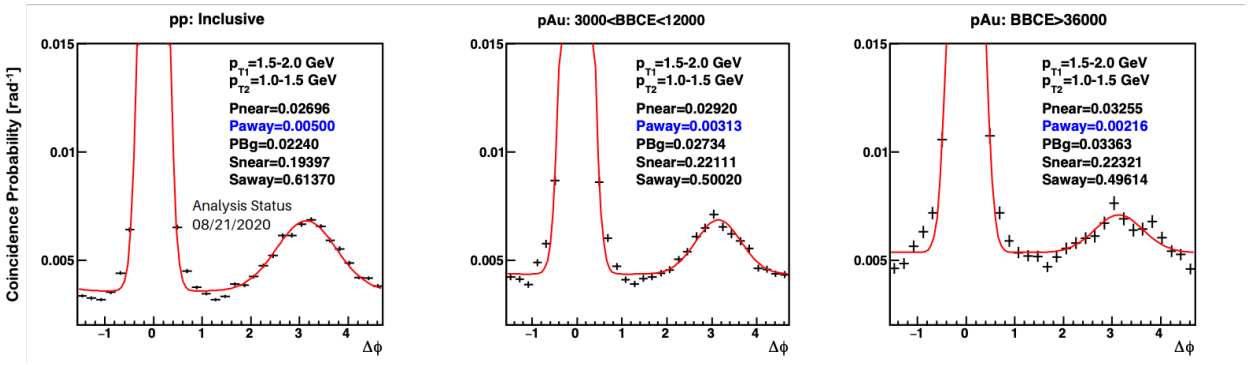

Figure 32: Coincidence probability as a function of azimuthal angle difference between two forward neutral pions in p+p, peripheral and central p+Au collisions. Analysis status on 08/21/2020.

The STAR measurement of the unpolarized cross-section ratio of the W^+ and W^- bosons from the STAR 2011 to 2013 data at $\sqrt{s} = 500/510$ GeV has released preliminary results [115] and is soon to be submitted to Physical Review D. Figure 33 shows the ratio plotted as a function of lepton pseudorapidity. This unique measurement is sensitive to the unpolarized $\bar{d}/\bar{u}$ quark distribution and will provide insights into unpolarized light quark distributions $\bar{d}(x)$ and $\bar{u}(x)$ at $x > 0.05$. The measurement at STAR is complementary to the Drell-Yan results from NuSea [116] and SeaQuest [117], covering the overlapping x region of about $0.1 - 0.3$ at higher $Q^2 = M_W^2$.

Differential cross sections of Z^0-boson production as function of transverse momentum are valuable input to global fits of TMD parton distribution functions, and STAR kinematics ($0.1 < x < 0.3$) are complementary to LHC and Tevatron data. Figure 34 shows preliminary results from 2011-2013 data with an integrated luminosity of 350 pb^{-1} [118]. Data on disk from 2017 comprise about the same luminosity, and preliminary results are expected soon along with transverse single-spin asymmetries. While the measurement of Z^0-bosons is an experimentally very clean observable, it requires a good understanding of the calorimeter performance. These will inform the background studies of the measurements of Sivers asymmetries for W-bosons, which are also expected very soon.

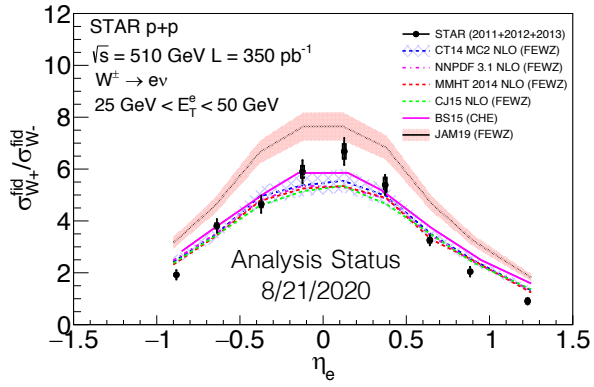

Figure 33: W^+ and W^- cross-section ratio as a function of lepton pseudorapidity for the combined 2011, 2012, and 2013 datasets. The central values correspond to the mean value of η_e distribution for that bin. The error bars represent the statistical uncertainty, whereas the rectangular boxes represent the systematic uncertainty for the respective data point. These measurements are compared to various theory frameworks, which use several different PDF inputs. Analysis status on 08/21/2020. Preliminary results available in Ref. [115].

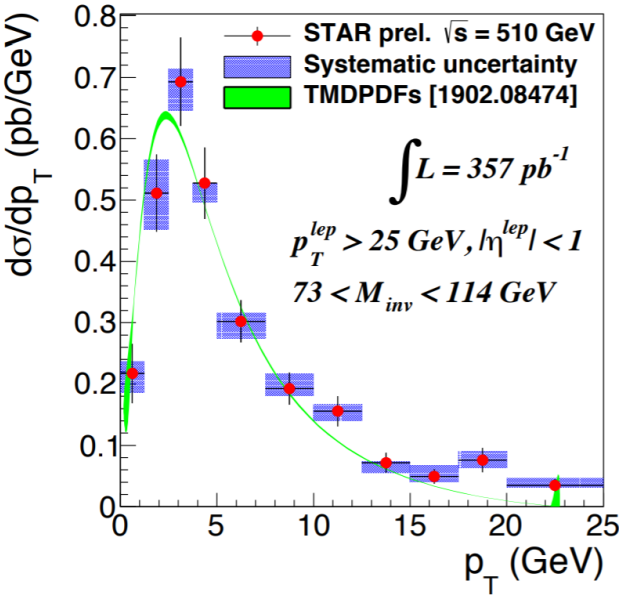

Figure 34: Preliminary results for the differential cross-section of Z^0-bosons as function of transverse momentum p_T [118] and comparison with theory predictions based on calculations developed in [119]. Results are based on data from 2011-2013.

1.4 Run-20 Performance

In this section, we will review the BES-II collider and fixed-target performance to date. Careful study of these performance metrics will be used to make projections about the required time to complete the 7.7 GeV collider system in run 21.

The BES-II collider program performance is over-viewed in table 6. The 27 GeV system, which was run in 2018, was not officially part of the BES-II physics program, however it is close enough in energy to help provide some performance evaluation. The most important lines in the table from the point of view of performance evaluation are the *good event rate*, which is a measure of the useful luminosity, and the *data hours per day*. In general, we had seen improvements over the luminosities recorded in 2010/2011 of a factor of three to four. For the 27 GeV system, which was run in 2018 we saw the good event rate rise to 620 Hz, which implies a luminosity increase of factor of 3.3 over the 2011 performance.

The 19.6 GeV system was completed in 2019. For this system, the good event rate rose from 100 Hz in 2011 to 400 Hz in 2019 for a factor of 4.0 increase. We should note that it took 5.1 calendar weeks to complete the energy, however during the running period for the 19.6 GeV system, the facility was dedicating two twelve hour shifts per week to LEReC development. Correcting the 5.1 calendar weeks by 6/7 means that 4.4 beam weeks were used to complete this energy which should be compared to the 4.5 weeks which was requested in the STAR BUR for 2019. Historically, it has been shown that the luminosities scale with γ^2 above injection energy (9.8 GeV) and with γ^3 below injection energy. Scaling the 27 GeV performance would have predicted a good event rate of 330 Hz at 19.6 GeV. One should also note that the number of events recorded exceeded the required number significantly. Overall, the performance for the 19.6 GeV system significantly exceeded expectations.

The 14.6 GeV system was completed in 2019. This energy had been run previously in 2014, however the STAR good event rate was unusually low at that time so comparing the 23 Hz rate from 2014 to the 170 Hz rate in 2019 is not a good metric for performance. It required 8.6 calendar weeks to complete the required number of events, however during the running of the 14.6 GeV system, 40% of the beam time was used for LEReC development. Scaling the 8.6 calendar weeks by 60% yields effectively 5.1 weeks of beam time which favorably compares with the 5.5 weeks estimated in the BUR for 2019. Using the performance at 19.6 GeV (good event rate of 400 Hz), and the γ^3 scaling, we would have expected a good event rate at 14.6 GeV of 165 Hz. This compares well the the 170 Hz rate which was achieved for this energy. Performance at this energy slightly exceeded expectations.

The 11.5 GeV system was completed in 2020. The good event rate rose from 30 Hz in 2010 to 80 Hz in 2020 for a factor of 2.67 increase. It took 8.9 calendar weeks achieve the required event statistics. In the BUR for 2020 a range from 7.5 (optimistic) to 10 (pessimistic) was proposed. The actual time required fell in the middle of the expected range. Scaling the good event rate from 14.6 GeV by γ^3 predicted that the good event rate for 11.5 GeV would be 83 Hz, which compares favorably with the 80 Hz actually achieved for the run. Overall, performance at this energy met expectations.

The 9.2 GeV system will be completed in 2020 and is far enough along that we can project to completion. This energy was not run during BES-I, so there is not a historical

comparison. Scaling the good event rate from 11.5 GeV by γ^3 predicts that we should have seen a good event rate of 38 Hz. Prior to the shutdown of the laboratory in March, we had achieved an average good event rate of 38 Hz and we had been averaging 16 hours of data taking per day, however the challenges of running in the summer have reduced the average number of hours of data taking to 13 and the average good event rate to 33. It is projected that this system will take 14.0 weeks to achieve the required event statistics, which is at the high end of the range that was included in the BUR for 2020.

Quality assurance studies of the BES-II and FXT data indicate that roughly 98% of the data recorded will ultimately be used in physics analyses. The quality assurance takes place on multiple levels. At the time of data acquisition, online performance plots are reviewed as each run starts by the shift crew member. There are two levels of online plots; the first use the raw detector specific data to overview the performance of all systems; the second level does event-by-events tracking and vertex reconstruction using the High Level Trigger (HLT) computer farm to generate event level performance plots and to tag the good Au+Au collision events. The next level of quality assurance uses a FastOffline production of a small percentage of all recorded events. The plots generated by this review take place on a daily basis a provide the opportunity for corrections to any issues that might arise. A third level of quality assurance takes place in a weekly QA meeting which reviews the overlap between the events flagged as good from the HLT system, a significant fraction of which are recorded and available to preliminary offline physics analysis, and the events identified as good using the FastOffline processed data, which utilizes a more sophisticated tracking algorithm. The overlap of good events has been at the 98% level for all BES-II collider and FXT systems. The QA meeting also reviews preliminary physics working group quality assurance analysis of the FastOffline data sets. The final level of quality assurance comes from preliminary physics analyses using the FastOffline and the ExpressStream data sets. This multi-level to quality assurance guarantees that the data will meet the needs of the physics analyses for the BES-II science program.

The relevant data sets recorded in 2018 have been fully calibrated and produced. These data sets are the 27 GeV collider system and the 3.0 and 7.2 GeV FXT datas sets. Preliminary results for all of the key physics analyses have been performed and highlights of these new results are reviewed in the previous section of this document. The 2019 data sets have required extensive calibrations of the new detector systems, the iTPC and the eTOF. The large volume of cosmic ray data that were recorded have been used to do the fine spatial alignment of the new iTPC modules. New methods needed to be developed to calibrate the precise start timing for each event, which is needed to get the correct reconstruction of the z-location of the hits in the TPC to account for the long bunches used to maximize the luminosity for BES-II and the FXT programs. The complete set of calibrations for the first collider energy from 2019, the 19.6 GeV system, have been completed and a test production using these calibrations has been generated and are undergoing.

As several of the physics opportunities discussed in the following sub-sections utilize fixed-target systems, it is best to review the performance in this mode of operation. An overivew of the preformance for all fixed-target energies is shown in table 7. The first fixed-target physics

Table 6: Achieved and projected experiment performance criteria for the BES-II collider program.

Collision Energy (GeV)	7.7	9.2	11.5	14.6	17.1	19.6	27
Performance in BES-I	2010	NA	2010	2014	NA	2011	2011
Good Events (M)	4.3	NA	11.7	12.6	NA	36	70
Days running	19	NA	10	21	NA	9	8
Data Hours per day	11	NA	12	10	NA	9	10
Fill Length (min)	10	NA	20	60	NA	30	60
Good Event Rate (Hz)	7	NA	30	23	NA	100	190
Max DAQ Rate (Hz)	80	NA	140	1000	NA	500	1200
Performance in BES-II (**achieved**)	2021	2020	2020	2019	2021	2019	2018
Required Number of Events	100	160	230	300	250	400	NA
Achieved Number of Events	2.9	160	**235**	**324**	TBD	**582**	**560**
fill length (min)	20-45	**45**	**25**	**45**	50	**60**	**120**
Good Event Rate (Hz)	16-24	**33**	**80**	**170**	265	**400**	**620**
Max DAQ rate (Hz)	400	**700**	**550**	**800**	1300	**1800**	**2200**
Data Hours per day	12-15	**13**	**13**	**9**	15	**10**	**9**
Projected number of weeks	11-20	8.5-14	7.6-10	5.5	2.5	4.5	NA
weeks to reach goals	TBD	**14.0**	**8.9**	**8.6**	TBD	**5.1**	**4.0**

run was in 2018 using a 3.85 GeV beam. A total of three and half days was spent on this system; first developing the conduct of operation and then recording a robust data sample. The lowest energy beam was selected for this first run in 2018 because at that time the iTPC and eTOF upgrades were not yet available; the lowest beam energy means the lowest center-of-mass boost, which meant that we could still complete the physics program even without the detector upgrades. Additionally in 2018, fixed-target data were recorded with a single beam energy of 26.5 GeV. Obviously, at such a high energy the detector upgrades would be essential for the mid-rapidity physics program. However, the 26.5 GeV beam was not requested by STAR; this beam was being using by the Coherent Electron Cooling program, and STAR was simply taking these data parasitically. This parasitic data taking gave us further opportunities to refine the fixed-target conduct of operations, which gave us confidence going forward that we could average 100 M good events per day in fixed-target mode. This is limited by the STAR data acquisition system and not by RHIC.

In 2019, eTOF detector upgrade system suffered damage at the start of the 14.6 GeV collider system. This meant that it would be unavailable for any fixed-target energies taken that year. It was felt that the physics program could still be achieved using the 4.59 GeV beam, but that for all higher energies the loss of the eTOF system would compromise the physics, so only modest samples at 5.75 and 31.2 GeV were taken.

The eTOF detector was repaired for 2020, and relatively early in the run it was decided to spend one week cycling through the seven remaining fixed-target energies. Roughly one

day was spent at each energy. The conclusion from this series of fixed target energies is that the collider and the experiment can quickly and efficiently set up and run fixed-target systems. STAR can efficiently trigger on good fixed-target events with roughly 80-90% of triggers passing the HLTgood test. The operators monitor the STAR event rate to keep the current on target at a level to keep the STAR DAQ system running at full capacity and minimizing the pile-up of multiple collisions in the target. Stores last for many hours (8-24 hours) and refill and realignment are fast and efficient.

Preliminary physics results from the 3.0 and 7.2 GeV data sets recorded in 2018 are available and highlights have been shown the the previous sections. Internal preliminary physics analyses of the ExpressStream and FastOffline data sets have been preformed and these confirm the quality of the data taken.

Table 7: Event statistics (in millions) needed in the fixed-target part of the BES-II program for various observables, and the total number of events acquired (those events taken in 2018 did not include the iTPC or eTOF detectors; those taken in 2019 did not include the eTOF).

$\sqrt{s_{NN}}$ (GeV)	3.0	3.2	3.5	3.9	4.5	5.2	6.2	7.2	7.7
Beam Energy	3.85	4.59	5.75	7.3	9.8	13.5	19.5	26.5	31.2
μ_B (MeV)	721	699	666	633	589	541	487	443	420
Rapidity y_{CM}	1.06	1.13	1.25	1.37	1.52	1.68	1.87	2.02	2.10
Observables									
Elliptic Flow	300	150	80	40	20	40	60	70	80
CME	70	60	50	50	50	70	80	90	100
Directed Flow	20	30	35	45	50	60	70	80	90
Femtoscopy	60	50	40	50	65	70	80	90	100
Kurtosis	36	50	75	125	200	400	950	NA	NA
Strange hadrons	300	100	60	40	25	30	50	75	100
Hypertritons	200	100	80	50	50	60	70	85	100
Event Totals									
Good events (2018)	258							158	
Good events (2019)	3.7	200	53						50
Good events (2020)			116	117	108	103	118	TBD	112

2 Proposed Program - Hot QCD in Run-21, 23, and 25

2.1 Beam Request for Run-21

2.1.1 Completion of the BES-II Program

The highest priority for Run-21 is the completion of the proposed BES-II program. At this time, the only system that remains to be taken is the 7.7 GeV collider data set. This energy is extremely important for several reasons. First, theoretical calculations suggest that the highest baryon density is achieved in collisions at this energy; second, several of the BES-I experimental signatures which have been put forth to be sensitive to the presence of deconfined matter either lose significance or are no longer present at this energy; third, the BES-I data showed enhanced fluctuations at this energy; finally, this energy provides the best acceptance overlap with the fixed-target program. Although the 7.7 GeV collider data set is extremely important from the point of view of the science, it is also technically the most challenging data set. The technical challenge of achieving a viable collision rate at this energy was the motivation to develop the Low Energy RHIC electron Cooling (LEReC) and is the reason that this energy has been left to the final year of the program.

The specific physics goals (are required statistics) include: measurement of the elliptic flow of the phi meson for which the the constituent quark scaling was suggested to break down in the lowest energy BES-I data (80 M events required); measurement of the correlators associated with the charge separation induced by the chiral magnetic effect which were seen to collapse at the lowest BES-I energies (50 M events required); differential measurements of the directed flow of protons which was seen to show evidence of a softening of the equation of state in the lowest BES-I data (20 M events required); Azimuthal femtoscopy measurements of protons to study the tilt angle of the source (35 M events required); measurement of the net-proton kurtosis which showed significant enhanced fluctuations at 7.7 GeV in the BES-I data (70 M events required); measurements of the di-lepton invariant mass distributions to determine in the excess in the low mass region is proportional to the total baryon density (100 M events required); and the global lambda polarization to determine the magnetic field significance (50 M events required). These analyses are being pursued at all of the BES-II collider energies; for several of the physics measurements, the 7.7 GeV energy is expected to be either the most significant or the most challenging.

The 7.7 GeV collider system provides the essential bridge between the collider and fixed-target energy scans. Although in later sections we detail a request to acquire fixed-target data at higher overlap energies, there is the largest region of common coverage at this energy. This will provide critical cross checks between the different modes.

Although the 7.7 GeV collider system is the most technically challenging system of the suite of BES-II and FXT energies, one can use the performances which have already been achieved during the BES-II program to help develop projections for the 7.7 GeV collider energy. These BES-II performance trends have been detailed in 6. In 2010, STAR achieved a good event rate of 7 Hz; a factor of three improvement would result in a 21 Hz rate. Scaling the performance at 9.2 GeV by γ^3 would predict a good event rate of 19.3 Hz. We project the

good event rate to fall between 16 and 24 Hz. We project the range of hours of data taking per day to fall between 12 and 15. These numbers suggest a range in the expected number of weeks to reach the goals from 11 to 20 weeks. We should note that CAD has provided projections which suggest that it will take 28 weeks to reach the goals. Our projections are more optimistic. Although we recognize that it is likely that running the 7.7 system will require all the available beam time in 2021, the optimistic range of our predictions suggests that we should prepare for success and we have therefore considered and prioritized other programs which could be run in 2021 if time were to be available.

2.1.2 Au+Au Collisions in FXT Mode at $\sqrt{s_{\rm NN}} = 3.0$ GeV - I: 300 million goal

QCD matter at high baryon chemical potential region contains a wealth of unexplored physics and is one the central focus of current and future heavy-ion collision programs in few GeV energy range around the world. RHIC has been able to deliver beams with the energy as low as 3.85 GeV per nucleon. Utilizing the gold fixed target (FXT) installed in the STAR experiment, we were able to record collision events at the center-of-mass-energy as low as $\sqrt{s_{\rm NN}}$ = 3.0 GeV, which corresponds to baryon chemical potential of μ_B ~720 MeV in central collisions. STAR detector configuration (including the iTPC and eTOF) has the full midrapidity coverage ($|y| < 0.5$) at this energy and enables us to carry a systematic investigation of the dynamics of the QCD matter created in these collisions at $\sqrt{s_{\rm NN}}$ from 3.0 up to 200 GeV.

At such a high μ_B region and moderate temperatures, baryon dynamics become important or even dominant in understanding the QCD matter properties. Strange quarks, due to their heavier masses, play an important role in study the high net-baryon density QCD matter. The combination of increased sensitivity of strange quarks with the existing high baryon density in low energy heavy-ion collisions offers a unique condition to create various light hypernuclei, which enables us to study *e.g.* the hyperon-nucleon (Y-N) interactions, which have potential implications for the inner structure of compact stars in nuclear astrophysics.

STAR has collected ~ 250 million FXT Au+Au events at $\sqrt{s_{\rm NN}}$ = 3.0 GeV in 2018, however without the iTPC and eTOF. We propose to collect a minimum of 300 million events with the extended phase-space coverage enabled by iTPC and eTOF for the following measurements:

- high moments of proton multiplicity distributions covering the same midrapidity acceptance $|y| <0.5$, $0.4<p_T<2.0$ GeV/c, comparable to that with the BES-I and BES-II measurements in collider mode.

- precision ϕ meson production at midrapidity to test the validity of Canonical Ensemble (CE) for strangeness production at high baryon density region.

- systematic measurements of lifetime, binding energy, production yield, collective flow of light hypernuclei ($^3_\Lambda$H, $^4_\Lambda$H, $^5_\Lambda$He etc.). as well as towards a discovery of double-Λ hypernuclei.

- measurement of low- and intermediate-mass dileptons to extract fireball lifetime, its average temperature and to access the microscopic properties of matter. This would be the first measurement of electromagnetic radiation at this energy which will guide the future high μ_B facilities at FAIR, NICA.

With additional beam time allowed, we would like to further collect up to 2 billion Au+Au FXT events at $\sqrt{s_{\rm NN}} = 3.0$ GeV which will be elaborated in the next section.

One feature we would like to point out is that the single beam energy for FXT collisions at $\sqrt{s_{\rm NN}} = 3.0$ GeV is 3.85 GeV per nucleon, the same beam energy to be used for colliding to collect the major 7.7 GeV collision dataset in year 2021. This leads to a negligible transition time for operation between $\sqrt{s_{\rm NN}}$= 7.7 GeV collider mode and $\sqrt{s_{\rm NN}}$= 3.0 GeV FXT mode.

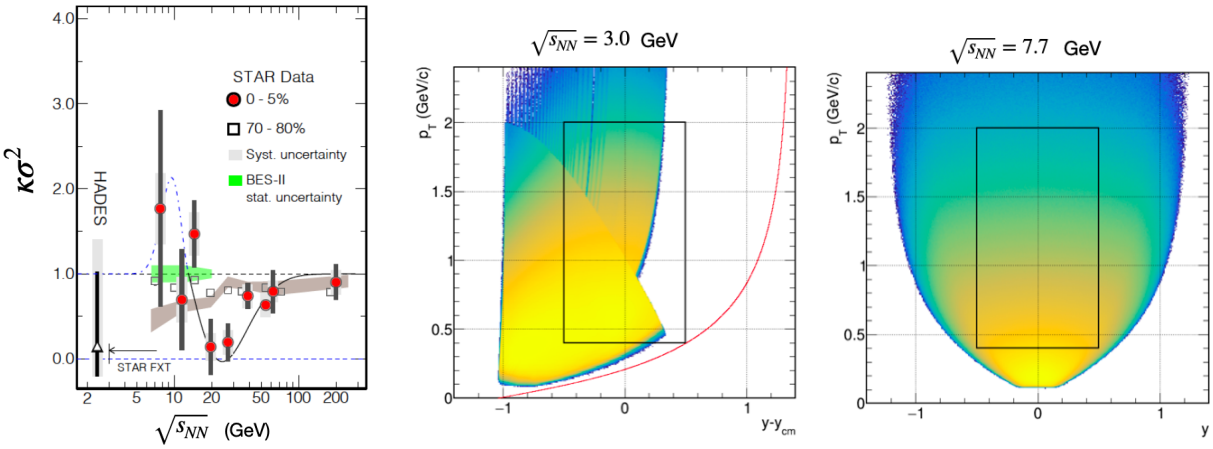

Figure 35: (Left) The net-proton $\kappa\sigma^2$ in most central (0-5%) and peripheral (70-80%) Au+Au collisions as a function of collision energy. (Middle/Right) Proton acceptance plot p_T vs. y in the center-of-mass frame at $\sqrt{s_{\rm NN}} = 3.0$ GeV (FXT data from 2018) and 7.7 GeV (collider data from 2010), respectively. The red curve in the middle panel indicates the acceptance boundary with iTPC and eTOF.

High moments of proton multiplicity distributions A non-monotonic behavior of net-proton high moments $\kappa\sigma^2$ as a function of collision energy has been suggested to be an evidence of the existence of QCD critical point [120, 121]. Figure 35 (left panel) shows the final STAR measurement from the BES-I data as a function of energy exhibiting a suggestive non-monotonic behavior [122, 123]. A complete picture of the non-monotonic behavior requires measurements at collision energies below the lowest collider mode energy (7.7 GeV) by utilizing the FXT mode collisions. STAR detector configuration has the best midrapidity coverage for fixed target collisions at the lowest collision energy $\sqrt{s_{\rm NN}} = 3.0$ GeV. Figure 35 middle and right panels show the proton acceptance with TPC and barrel TOF in 2018 FXT data at 3.0 GeV and 2010 collider data at 7.7 GeV, respectively. In the 2018 FXT data, to ensure $> 95\%$ purity of the proton sample, one needs to utilize the barrel TOF for high momentum particle identification. With this requirement, the proton acceptance in

2018 covers full negative rapidity region (-0.5< y <0, 0.4<p_T<2.0 GeV/c), while missing a considerable acceptance in the positive rapidity region. A new run, with eTOF and iTPC, would allow for phase space coverage comparable to the one in collider mode (indicated by the box in the middle panel). The estimated acceptance boundary for protons is indicated by the red line shown in Fig. 35 middle panel. We can therefore cover the full midrapidity $|y| < 0.5$ region from $0.4 < p_T < 2.0$ GeV/c which will be the same as these measurements conducted in collider mode data, shown in the right panel. This would allow to perform a systematic scan of the net-proton high moments analysis within the same mid-rapidity acceptance across the collision energy from 3.0 up to 200 GeV.

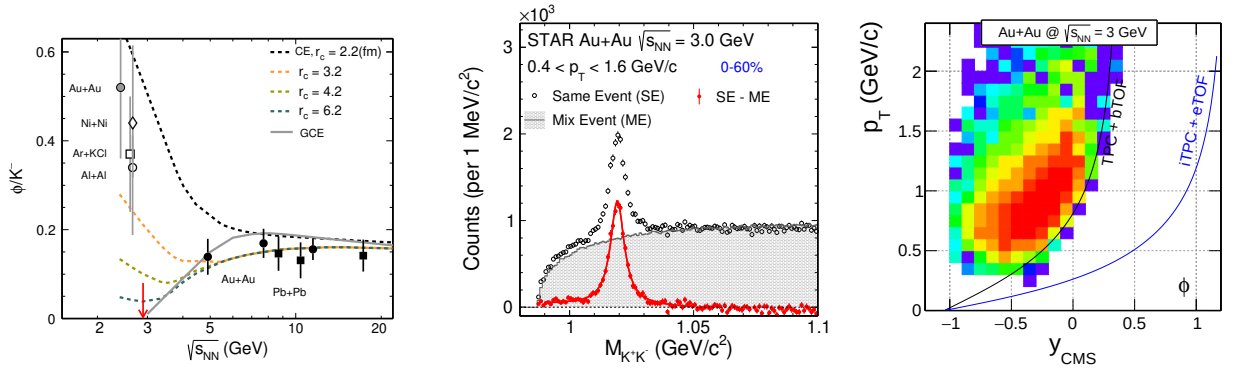

Figure 36: (Left) ϕ/K^- ratio as a function of collision energy from several heavy-ion experiments in comparison to thermal model calculations assuming strangeness following GCE and CE with different canonical radius. (Middle) Invariant mass distributions of K^+K^- pairs and the ϕ meson signal in 2018 FXT data at $\sqrt{s_{\rm NN}}$=3.0 GeV. (Right) Reconstructed ϕ meson candidate phase space distributions using 2018 FXT data taken at $\sqrt{s_{\rm NN}}$=3.0 GeV. The black line shows the boundary of combining the TPC and barrel TOF detector for kaon identification. The blue line indicates the anticipated boundary extended by iTPC and eTOF for kaon identification in the proposed 2021 FXT run at $\sqrt{s_{\rm NN}}$=3.0 GeV.

ϕ meson production Yields of strange hadron produced in relativistic heavy-ion collisions from RHIC BES-I energies up to the LHC energy ($\sqrt{s_{\rm NN}}$=7.7–5500 GeV) can be well described by thermal model with Grand Canonical Ensemble (GCE) in which strange quark number is conserved on average [124–127]. It has been argued that at low energy heavy-ion collisions when the fireball created in these collisions becomes small enough the GCE for strange quarks will break down. Strangeness needs to be conserved on the event-by-event basis, therefore only Canonical Ensemble (CE) is applicable to strange hadron production [125, 127]. Strange hadrons with finite strangeness number (e.g. K, Λ etc.) will suffer from a suppression due to the strangeness number conservation, often characterized by a canonical radius (r_c) for strange quark profile in comparison to the regular radius (r) for light quarks [128, 129]. The ϕ meson is the lightest bound state of s and $\bar{s}$ quarks with zero net-strangeness number. Its production yield, on the contrary, will not suffer from the canonical suppression. Therefore CE models predict the ϕ/K^- ratio will show an enhance-

ment in very low energy heavy-ion collisions while GCE models calculate the ϕ/K^- ratio will gradually drop to zero at the ϕ production threshold in pp collisions. ($\sqrt{s_{\rm NN}}$ = 2.89 GeV).

Experimentally, the measured ϕ/K^- values stay around 0.15 at $\sqrt{s_{\rm NN}}$ >5 GeV up to the LHC energy. At collision energies below the ϕ production threshold in pp collisions, measurements from HADES and FOPI suggest an enhancement compared to those at high energies, consistent with the CE description for strange quarks at such low energies within appreciable uncertainties [130, 131]. High precision measurement of the ϕ/K^- at such low energies will be of great interest to systematic investigate the ϕ meson and strangeness production mechanism in heavy-ion collisions.

We have performed such a measurement using the FXT data at $\sqrt{s_{\rm NN}}$ = 3 GeV taken in 2018. Fig. 36 middle panel shows the reconstructed K^+K^- invariant mass distributions in 0-60% centrality. The shaded histogram shows the K^+K^- pair distributions from the mixed-event technique while normalized at the mass region above the ϕ meson signal. The red data points show the mixed-event background subtracted distributions and the ϕ meson signal obtained in this data is about 60σ. The right panel shows the ϕ meson acceptance coverage in center-of-mass frame. Due to the small production yield of kaons, one needs to rely on clean particle identification using TOF detector to obtain a control background in the ϕ meson reconstruction. The black curve indicates the single track acceptance boundary from TPC and barrel TOF in 2018 year run. One can see the ϕ meson p_T acceptance at midrapidity is limited at ~0.6-0.8 GeV/c. This covers roughly only 40% of the ϕ meson yield in the full p_T region, leading to a considerable amount of systematic uncertainty due to the p_T extrapolation. The blue curve in the same panel indicates the anticipated single track boundary with iTPC and eTOF. The p_T lower limit can be extended down to ~0.2 GeV/c, yielding a p_T coverage of ~90% of total dN/dy at midrapidity. This will greatly reduce the systematic uncertainty in the total ϕ meson yield measurement.

We therefore request to take the FXT data at $\sqrt{s_{\rm NN}}$ = 3 GeV with iTPC and eTOF detectors in RHIC 2021 year run. A roughly similar amount of statistics (300 million) will allow us to perform the measurement of ϕ/K^- ratio with high precision both statistically and systematically.

Hypernuclei production and potential discovery for double-Λ hypernuclei Hypernuclei are those nuclei with one or more nucleons replaced with hyperons (typically Λs). The study of hypernuclei lifetime, binding energy and their production mechanism offer insights to the understanding of hyperon-nucleon (Y-N) interactions. The Y-N interactions could have significant implications to our understanding of the internal structure of compact stars in nuclear astrophysics.

Heavy-ion collisions have shown great potential in studying the light hypernuclei properties and their production mechanism. There have been unprecedented measurements from RHIC and LHC on both the lifetime and binding energy (anti-)hypertriton ($^3_\Lambda$H and $\overline{^3_\Lambda\rm H}$). At low energy heavy-ion collisions, due to the high baryon density and high strangeness population, statistical hadronization thermal model predicts a significant enhancement of various light hypernuclei production yield, shown in Fig. 37 left panel [132]. The STAR FXT energy

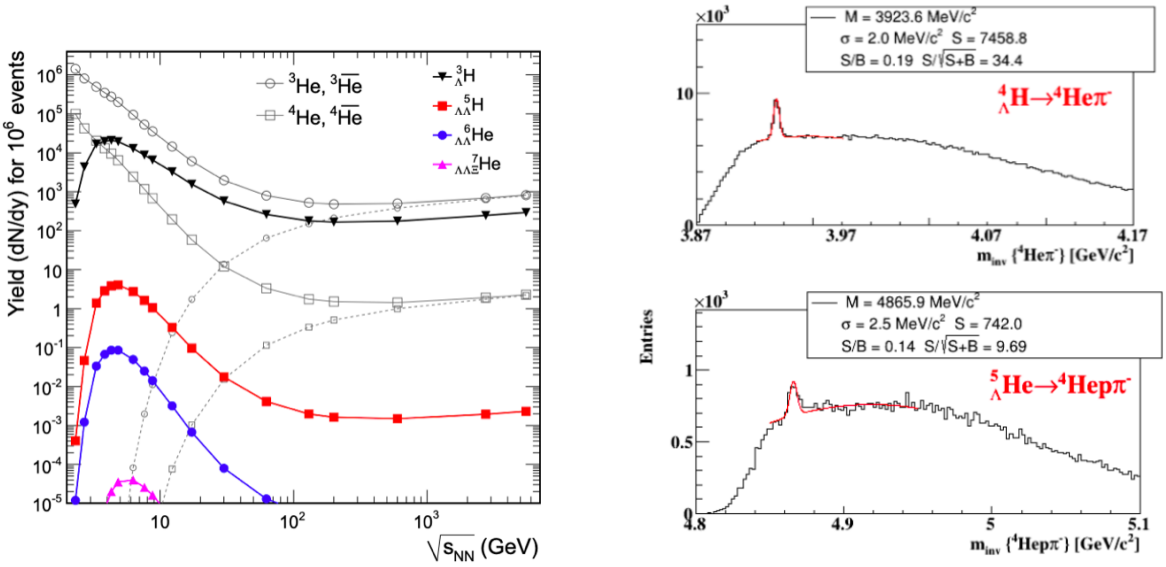

Figure 37: (Left) Thermal model predictions of various light nuclei and hypernuclei production yield at midrapidity in central heavy-ion collisions as a function of collision energy [132]. (Right) Invariant mass distribution of ${}^4He\pi^-$ (top) ${}^4Hep\pi^-$ (bottom) from 2018 FXT data at $\sqrt{s_{\rm NN}}$=3.0 GeV. The ${}^4_\Lambda$H and ${}^5_\Lambda$He hypernuclei signal is clearly visible on top of background.

region from $\sqrt{s_{\rm NN}}$ = 3.0 – 7.7 GeV sits nicely in the maximum mid-rapidity production yield of various hypernuclei while STAR detector layout has the best midrapidity acceptance coverage at 3.0 GeV. Figure 37 right panel shows the reconstructed ${}^4_\Lambda$H and ${}^5_\Lambda$He signal from the 2018 FXT dataset at $\sqrt{s_{\rm NN}}$ = 3.0 GeV. These are so far the most unprecedented statistics on these light nuclei that will allow us to systematically investigate their lifetimes, binding energies as well as their production yield and collective flow behavior in heavy-ion collisions.

2.1.3 Au+Au Collisions in FXT Mode at $\sqrt{s_{\rm NN}}$ = 9.2, 11.5, and 13.7 GeV

The BES-II program aims to study the nature of QCD matter by varying the temperature and baryon chemical potential. High baryon chemical potentials are achieved by 'stopping' the baryons which made up the two colliding nuclei. To better understand the development of the baryon chemical potential and its profile through the interaction region, it is necessary to study the rapidity density distribution of the protons across a broad range in rapidity. It is important that the rapidity range covered includes the peak of the participants which have been accelerated during the collision process. For all collider energies available at RHIC (7.7 GeV and above), the peak of the rapidity distribution of the stopped protons is outside or at the edge of the acceptance of the STAR TPC (which only extends 0.6 units beyond mid-rapidity with particle identification via dE/dx, this is extended to 1.0 units of rapidity using eTOF particle ID); for $\sqrt{s_{\rm NN}}$ = 9.2, 11.5, and 13.7 GeV, the shifted 0.9, 1.0, and 1.1 units away from mid-rapidity respectively. However, in fixed-target mode the STAR detector is excellent for studies of stopping as the acceptance extends 1.7 units from target rapidity

(see figure 38 toward mid-rapidity; for $\sqrt{s_{\rm NN}}$ = 9.2, 11.5, and 13.7 GeV, y_{CM} = 2.28, 2.50, and 2.68 respectively. Combining collider and fixed-target measurements at each energy will provide full coverage from target rapidity to center-of-mass rapidity. The stopping of the incident protons is the key to changing the baryon chemical potential in the interaction region and the changing baryon chemical potential is the key to mapping out the phase diagram of QCD matter.

Complete rapidity density distribution for identified particles will provide important constraints for models. It has been noted by Shen [**?**] that the high rapidity tails of the dN/dy distributions are very important and that high rapidity data are rare. In the energy range from $\sqrt{s_{\rm NN}}$ = 5.0 to 200 GeV, the only available proton rapidity density distribution measurements are from NA49 at 8.77 and 17.3 GeV [133] and from BRAHMS at 62.4 and 200 GeV [134]. Shen used these data to constrain his 3-D models of the collisions to better understand the elliptic flow measurements in heavy-ion collisions. In the BES-II energy range, around 10 GeV, these models can set strong constraints on the dependence of Quark-Gluon Plasma shear viscosity on temperature and net baryon chemical, however, in order to do so, it is necessary to have knowledge of the rapidity distributions of net-protons and produced particles.

It has been proposed that the trend of the rapidity shift of the stopped protons with collision energy will provide a signature of the softening of the equation of state at the phase transition [135]. Specifically, the model which has a two phase equation of state shows that the increase in the rapidity shift with collision energy stalls in the $\sqrt{s_{\rm NN}}$ = 8 to 12 GeV range.

We proposed to extend the studies to proton stopping through the BES-II energy regime. Specifically we propose to add three more energies to the high end of the FXT energy range. These energies are chosen to provide three more overlap energies with the collider program. Single beam energies of 44.5, 70, and 100 GeV will provide interactions at $\sqrt{s_{\rm NN}}$ = 9.2, 11.5, and 13.7 GeV (the top energy is not quite an overlap energy with the 14.6 GeV collider system). Combining the midrapidity coverage from the collider mode and the target rapidity coverage from the fixed-target mode will provide full rapidity coverage for inclusive observables. Since the focus for program will be inclusive observables, 50 M events will be sufficient at each energy. We propose that at each of these three energies, twelve hours be spent on beam development and twelve hours be spent taking data.

2.2 Further Opportunities in Run-21

2.2.1 Au+Au Collisions in FXT Mode at $\sqrt{s_{\rm NN}}$ = 3.0 GeV - II: 2 Billion Goal

In the previous section, we have discussed the great physics interests for low energy heavy-ion collisions utilizing the FXT setup at the STAR experiment. We have made our arguments of taking a minimum of 300 million Au+Au FXT events at $\sqrt{s_{\rm NN}}$ = 3.0 GeV. With further available beam time, we would like to request to collect up to 2 billion events with the same setup for the following physics measurements.

Proton correlations higher than 4-th order are useful to study the possible contributions

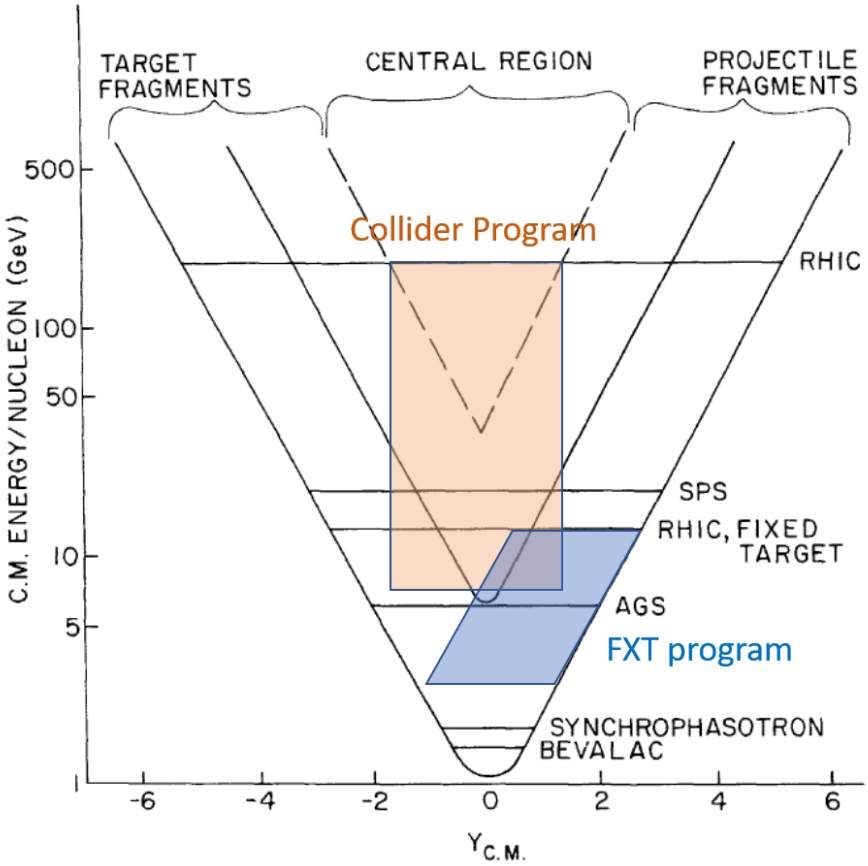

Figure 38: This figure has been modified from a figure in the introduction of the Conceptual Design Report for the RHIC facility. The black lines indicate different regions in the rapidity - center of mass energy space. The 'V' shaped region in the top center of the figure which is labeled at the central region have been predicted and demonstrate to be a low baryon chemical potential region characterized by a continuous phase transition between the QG and the hadron gas. The outer 'V' shaped region is dominated by the target fragments. Colored regions are overlaid to indicate the coverage of the STAR detector for collider (Orange) and FXT (Blue) modes. For the three higher energies currently being proposed, the FXT acceptance covers the region dominated by target fragments while the collider acceptance covers the equilibrated central region.

of protons from hadronic phase or QGP phase [136]. The requested 2 billion events statistics will enable us to perform the analyses of proton moments and cumulants up to 5-th and 6-th orders to search for the phase boundary in the high baryon density region. A much larger data sample (2 billion events) will enable us to further investigate the centrality/system size dependence of ϕ meson production as well as allow us to study the ϕ collective flow behavior in these collisions. The 2 billion events would potentially produce > 25 ${}^{5}_{\Lambda\Lambda}$H counts ($\sim 5\sigma$ discovery potential) within the STAR detector acceptance assuming the predicted yield from a thermal model [132].

While there have been tens of hypernuclei measured so far, there are only very few double-

Λ hypernuclei candidates reported from emulsion experiments [137–141]. Their properties are directly related to the ΛΛ interaction. Low energy heavy-ion collisions can be a unique environment to copiously produce these light double-Λ hypernuclei. For instance, according to the thermal model prediction, the ${}^{5}_{\Lambda\Lambda}$H production yield increases by more than 3 orders of magnitude at the low energies compared to that at top RHIC and LHC energies [132].

We performed a Monte Carlo simulation study for the decay chain ${}^{5}_{\Lambda\Lambda}\mathrm{H}\rightarrow{}^{5}_{\Lambda}\mathrm{He}+\pi^{-}$, and ${}^{5}_{\Lambda}\mathrm{He}\rightarrow{}^{4}\mathrm{He}+p+\pi^{-}$ within the STAR detector acceptance. Assuming the production yield based on the thermal model prediction, with 2 billion Au+Au FXT data at $\sqrt{s_{\mathrm{NN}}} = 3.0$ GeV and with the iTPC and eTOF detector, we will have a chance to observe ∼27 signal counts, corresponding to $\sim 5\sigma$ discovery potential assuming negligible background contribution based on the two-decay-vertices topology reconstruction.

2.2.2 Au+Au Collisions at $\sqrt{s_{\mathrm{NN}}} = 17.1$ GeV

Net-proton kurtosis and light nuclei yield ratio from RHIC BES-I One of the main goals of the RHIC Beam Energy Scan (BES) program is the search for the QCD critical point (CP), which is a distinct singular feature of the QCD phase diagram. The experimental confirmation of the existence of the CP would become a landmark in the exploration of the phase structure of hot dense nuclear matter. The characteristic feature of the CP is the divergence of the correlation length and density fluctuations. These critical phenomena can be probed by measuring event-by-event fluctuations of conserved quantities, such as baryon, electric charge, and strangeness numbers. The effect of the CP could show as a non-monotonic energy dependence of higher order moments of these conserved quantities in close proximity of the critical point during a beam energy scan [121].

In the years 2010-2017 RHIC finished the first phase of the Beam Energy Scan (BES) and took data in Au+Au collisions at $\sqrt{s_{\mathrm{NN}}} = 7.7, 11.5, 14.5, 19.6, 27, 39, 54.4, 62.4$, and 200 GeV. With these experimental data STAR measured the higher order fluctuations of net-proton, net-charge, and net-kaon multiplicity distributions [122, 143–147]. One striking observation is the behavior of the fourth-order cumulants, or kurtosis, of the net-proton fluctuation $\kappa\sigma^2$ in most central (0-5%) Au+Au collisions as a function of beam energy. As shown on the left of Fig. 39, the fourth order net-proton fluctuation is close to unity above 39 GeV but deviates significantly below unity at 19.6 and 27 GeV, then approaches or turns above unity at lower energies. This behavior may suggest that the created system skims close by the CP, and receive positive and/or negative contributions from critical fluctuations. The right of Fig. 39 shows the characteristic signature of the critical point for energy dependence of the fourth order fluctuations when the system passes through the critical region [121]. Along this argument, a peak structure above unity for net-proton kurtosis measurement at lower energies could be the signature of the CP. However, it is worth to point out that a first order phase transition could also cause a large increase of net-proton kurtosis [136]. When entering into the spinodal region (mixed phase), the double peak structure of σ field may cause the increase of the fourth order cumulants (C_4).

In addition, STAR has measured light nuclei (deuteron and triton) production in Au+Au collisions at RHIC BES energies. The ratio of these yields are predicted to be sensitive to the

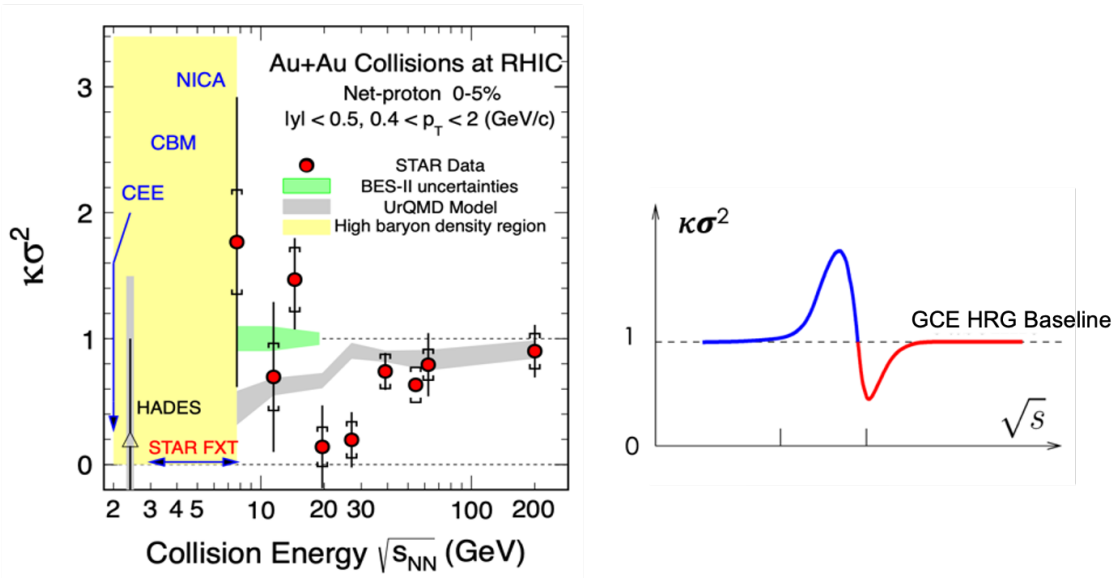

Figure 39: (Left) The fourth order net-proton fluctuations $\kappa\sigma^2$ in most central (0-5%) Au+Au collisions as a function of collision energy from STAR BES-I measurements [122]. (Right) The characteristic signature predicted by the theoretical model for energy dependence of the fourth order fluctuations when the system passes through the critical region [121].

neutron relative density fluctuations at kinetic freeze-out, which is expected to increase near the critical point and/or a first order phase transition [142]. The neutron density fluctuation is defined as $\Delta n = \langle(\delta n)^2\rangle/\langle n\rangle^2$, which can be approximated from:

$$\Delta n = \frac{1}{g}\frac{N_t \times N_p}{N_d^2} - 1,$$

where N_p, N_d and N_t are the proton, deuteron and triton yields, respectively and g is a constant factor of 0.29 [142]. In the left panel of Fig. 40, we show the yield ratio $N_t \times N_p/N_d^2$ in central Au+Au collisions as a function of collision energy. These light nuclei yield ratios are obtained by using the feed-down corrected proton yields [148], deuteron yield [149], and preliminary triton results [150]. The ratio as a function of energy exhibits a non-monotonic energy dependence with a peak around 19.6 GeV. The blue band showing a flat energy dependence represents the calculation of the light nuclei yield ratio in Au+Au collisions ($b < 3$ fm) from a transport JAM model [151]. Furthermore, the yield ratio shown in Fig. 40 seems to show a drop between 14.5 and 19.6 GeV. The experimental observation of non-monotonic energy dependence in yield ratio may suggest a double peak structure of the neutron density fluctuation, indicating that the system goes through the critical region and the first order spinodal region, as displayed in Fig. 40 right.

In RHIC 2021 run, we propose to take one more energy point in Au+Au collisions at 17.1 GeV based on the following two observations presented in Figs. 39 and 40, aiming at the QCD critical point search with net-proton kurtosis and light nuclei yield ratio:

1. Net-p kurtosis and light nuclei yield ratio, which are both sensitive to the critical

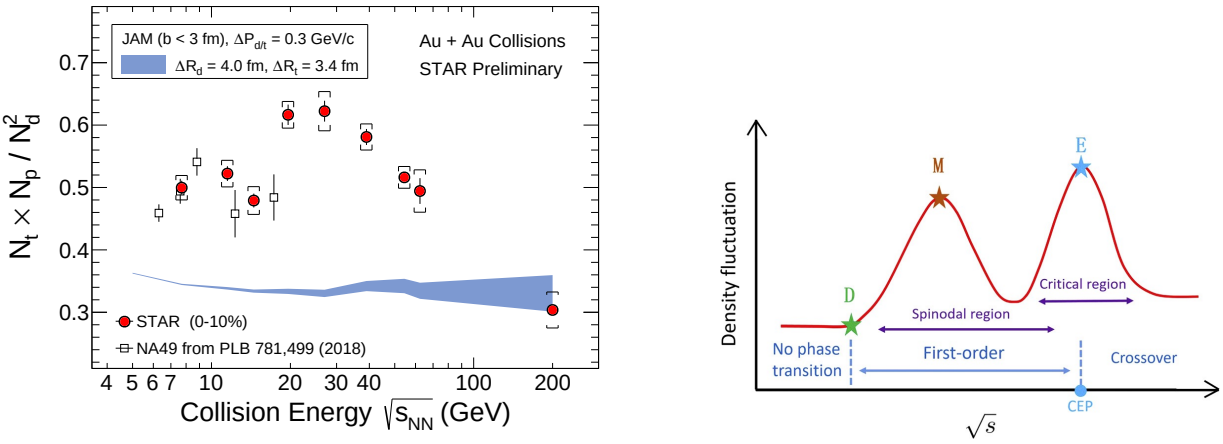

Figure 40: (Left) Collision energy dependence of the light nuclei yield ratio ($N_t \times N_p/N_d^2$) in central Au+Au collisions. The open square data based on NA49 results in central Pb+Pb collisions at $\sqrt{s_{\rm NN}}$=6.3 (0-7%), 7.6 (0-7%), 8.8 (0-7%), 12.3 (0-7%), and 17.3 (0-12%) energies. (Right) Illustration of the density fluctuation as a function of collision energy in the critical region and the spinodal region [142].

fluctuation, show dip and peak structures around 19.6 GeV. These may suggest that the system passed through the critical region around 19.6 GeV.

2. We observe sudden changes between 19.6 and 14.5 GeV in the energy dependence of net-p kurtosis and light nuclei ratio measurements in the BES-I data measured by the STAR experiment. The neutron density fluctuations at low energies below 14.5 GeV are consistent with the results from NA49 experiment [142].

These two observations indicate that the critical point may be close to 19.6 GeV. Since there are sudden changes in both observables between 19.6 (chemical freeze-out μ_B =205 MeV) and 14.5 GeV (μ_B =266 MeV), it is important to conduct a finer beam energy scan between these two energies. Therefore, we request a run with Au+Au collisions at $\sqrt{s_{\rm NN}}$=17.1 GeV (μ_B =235 MeV), which is just between 19.6 and 14.5 GeV with equal μ_B gap, about 30 MeV, on each side.

Answer to PAC questions from last year When this proposal was presented last year, we have received the following comments: "To make the case for a $\sqrt{s_{\rm NN}}$ = 17.1 GeV run, the key input will be results from measurements of fluctuation observables from Run-19 data taken at $\sqrt{s_{\rm NN}}$ = 19.6 and 14.6 GeV. If these measurements, with the smaller error bars that are anticipated, show evidence for a possible two-peaked structure in the plot of net proton kurtosis or other fluctuation observables as a function of $\sqrt{s_{\rm NN}}$, this could at that time become a strong argument for a run at $\sqrt{s_{\rm NN}}$ = 17.1 GeV."

To reply the comments from PAC last year, we have analyzed the net-proton fluctuation and light nuclei production from the Run-19 fast-offline data of Au+Au collisions at $\sqrt{s_{\rm NN}}$

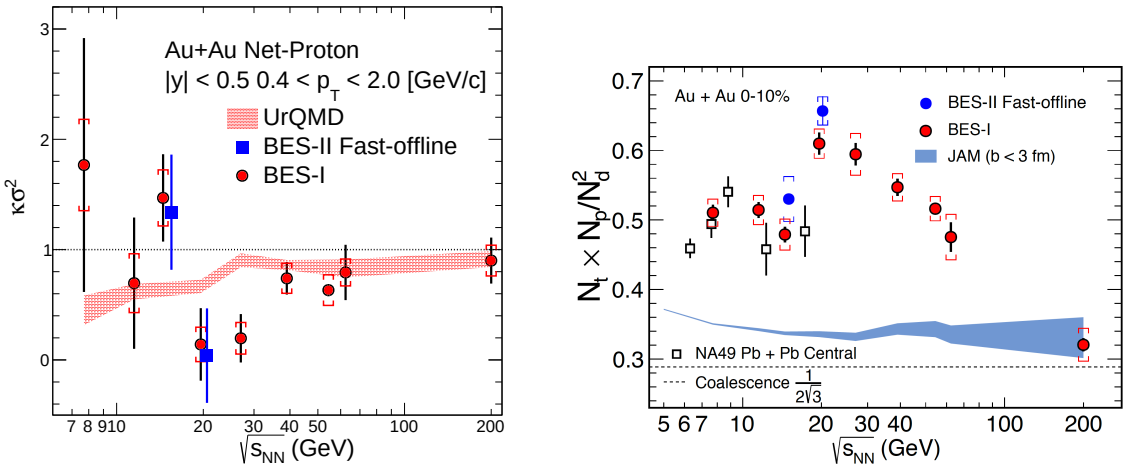

Figure 41: The red solid makers are the results from RHIC BES-I and the blue square represents the results of Run19 fast-offline data. (Left) The fourth order net-proton fluctuations $\kappa\sigma^2$ in most central (0-5%) Au+Au collisions as a function of collision energy. (Right) Collision energy dependence of the light nuclei yield ratio ($N_t \times N_p/N_d^2$) in central Au+Au collisions. The open square data based on NA49 results in central Pb+Pb collisions at $\sqrt{s_{\rm NN}}$=6.3 (0-7%), 7.6 (0-7%), 8.8 (0-7%), 12.3 (0-7%), and 17.3 (0-12%) energies.

= 14.6 and 19.6 GeV. The statistics of the Run-19 fast-offline data of 0-5% Au+Au collisions shown in Fig. 41 are about 580k and 750k events for 14.6 and 19.6 GeV, respectively, which are roughly about 5% of the full min.-bias statistics of these two data sets. It is found that both net-proton fluctuation and light nuclei yield ratios in 0-5% most central Au+Au collisions from BES-I are consistent with the results from Run 19 fast-offline data of 14.6 and 19.6 GeV. For clarity in Fig. 41, the X-axis positions of Run 19 fast-offline data are slightly shifted.

Table 8: Event statistics (in millions) needed in a Au+Au run at $\sqrt{s_{\rm NN}}$ = 17.1 GeV for fourth order net-proton fluctuations ($\kappa\sigma^2$) and light nuclei yield ratio ($N_t \times N_p/N_d^2$) measurements.

Triggers	Minimum Bias	net-p $\kappa\sigma^2$ (0-5%)	$N_t \times N_p/N_d^2$ (0-10%)
Number of events	250 M	6% error level	3.6% error level

Required number of minimum bias events and statistical uncertainty level According to the previous estimation of the required event statistics for BES-II energies presented in Table 6, we need about 250 million minimum-bias events for the net-proton kurtosis measurement at 17.1 GeV, which requirs 2.5 weeks data taking. It gives us about 12.5 million events (250/20) in 0-5% most central collisions. This will ensure that the relative statistical error of net-proton $\kappa\sigma^2$ in 0-5% most central Au+Au collisions will reach the 6% level (shown

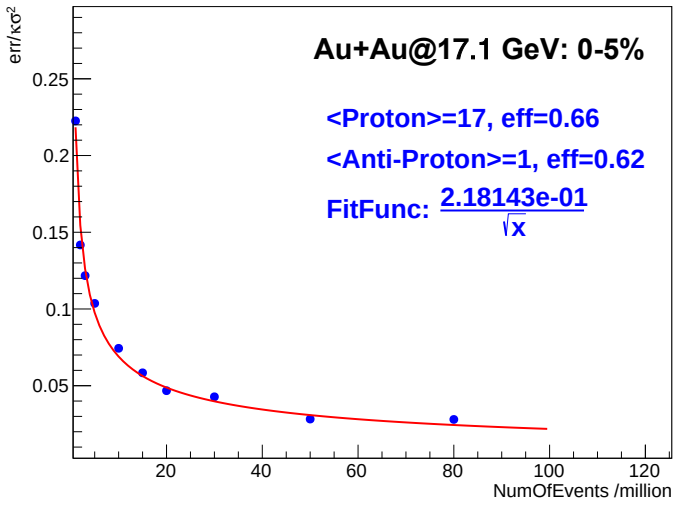

Figure 42: Monte Carlo simulation for the relative statistical errors of net-proton $\kappa\sigma^2$ in 0-5% most central Au+Au collisions at 17.1 GeV. A Skellam distribution for net-proton is assumed; the mean value for protons and anti-protons are 17 and 1, respectively. The average efficiencies for proton and anti-proton are 0.66 and 0.62, respectively.

in Fig. 42). This event statistics will also ensure that the relative statistical error of light nuclei ratio will reach about 3.6% level in 0-10% central Au+Au collisions. In additional to the improved statistics, utilizing the iTPC will enable the measurement of lower p_T light nuclei and will reduce the systematic uncertainties associated with the low p_T yield extrapolation.

If nature puts the critical point in the QCD phase diagram between 14.5 and 19.6 GeV (with μ_B around 200–270 MeV), RHIC has the best chance to discover it !

s

2.2.3 Small System Run: O+O at $\sqrt{s_{\rm NN}}$ =200 GeV

Introduction Collective long-range azimuthal correlations in A+A collisions have been successfully described as a hydrodynamic response by a fluid-like system to geometric shape fluctuations in the initial state. In recent years, observation of similar collective phenomena in small-system collisions, such as pp and p+A collisions, has attracted wide interests in the community. The interpretation of a fluid-like state formed there has been challenged, as the small size and short lifetime might prevent the system from quickly thermalizing and evolving hydrodynamically. Instead, collectivity arising either from initial momentum correlations motivated by gluon saturation models [152] or via a few scatterings among partons (without hydrodynamization) [153–155] has been proposed as alternative source of collectivity that may be dominant in small systems. Lots of experimental and theoretical efforts have been devoted to the study of collectivity in small-system collisions, with the goal of understanding the time-scale for the emergence of collectivity and the mechanism for

early-time hydrodynamization in large collision systems.

One key feature that distinguishes initial momentum correlation models (ISM) from final-state interaction models (FSM, including hydrodynamics or a few scatterings) is the connection to the initial-state geometry [156]. In FSM, the collectivity is a geometrical response to initial shape fluctuations, i.e., v_n is approximately proportional to the n^{th}-order initial-state eccentricity ε_n. In ISM, such a geometrical response is expected to be absent [157]. It was proposed that a geometry scan of various colliding systems with different spatial eccentricities can help distinguish between contributions of these two scenarios [158].

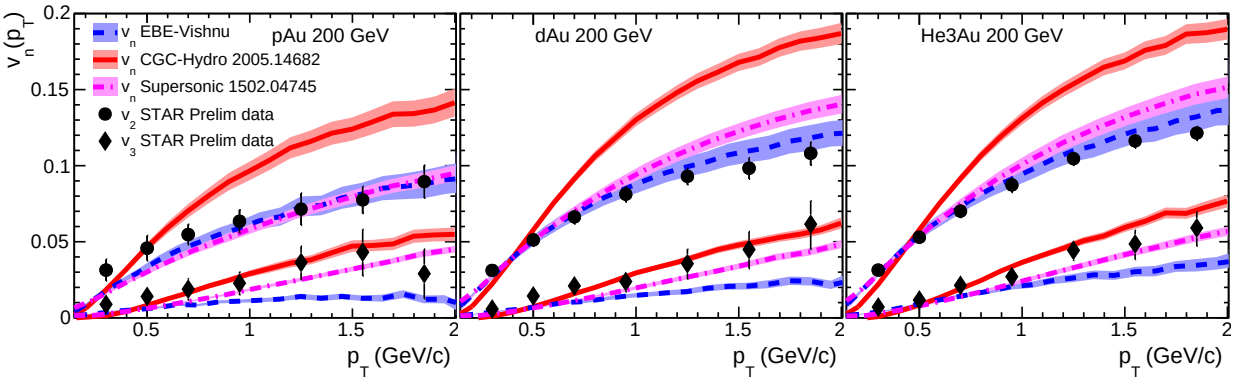

Figure 43: Comparison of v_2 and v_3 in p+Au, d+Au and ^{3}He+Au collisions at $\sqrt{s_{\text{NN}}} = 200$ between STAR data and various model calculations.

Such a small system scan program has been recently carried out at RHIC for a few asymmetric small systems including p+Au, d+Au and ^{3}He+Au, where studies of elliptic flow (v_2) and triangular flow (v_3) have been performed [43, 159, 160]. In a Glauber model that only considers the fluctuations of nucleon positions [158], ε_2 in d+Au and ^{3}He+Au is expected to be larger than in p+Au, while ε_3 in p+Au and d+Au are expected to be smaller than in ^{3}He+Au. However, once the fluctuations at subnucleonic scales are included [157], the ε_3 are expected to be similar among all three systems. Fig. 43 compares the STAR v_2 and v_3 results with three hydrodynamic models predictions with different assumptions about the initial state. Calculations [161, 162] that include initial momentum anisotropy and/or subnucleonic fluctuations indeed describe the STAR v_3 data in all three systems, but one of the model [161] overestimates the v_2 data. On the other hand, hydrodynamic model based on fluctuations only at nucleonic level [163] fails to describe the v_3 data. This implies that the initial state in these asymmetric small collision systems are not well constrained, in particular in p+Au and d+Au system (there is reasonable consensus that the flow results in ^{3}He+Au is dominated by FSM). The relative importance of FSM vs. ISM for the v_n data in small systems is an area of intense ongoing debate [164].

Physics case for a small A+A scan So far, both RHIC and the LHC carried out collisions for either relatively large (Pb+Pb, Au+Au, Xe+Xe, Cu+Cu, ...), which are well described by hydrodynamic models, or small asymmetric systems (p+Pb, p+Au, d+Au, and

^{3}He+Au), whose initial state are poorly constrained as discussed above. To quantitatively understand the initial momentum anisotropy and the role of subnucleonic fluctuations, collisions of small but symmetric systems, such as O+O, Al+Al and Ar+Ar will be necessary. They will also full the gap between pp and Cu+Cu systems is a crucial unexplored frontier[1], where a transition from ISM to FSM dominated collectivity may be observable. The list of key open questions related to collectivity in small systems includes:

- How much do initial-state correlations vs. geometry-driven final-state interactions contribute to the observed collectivity? Can we unambiguously establish experimental evidence of initial-state correlations?
- For final-state scenarios, to what extent does the collectivity arise from a hydrodynamic fluid-like QGP, as opposed to an off-equilibrium system with only a few scatterings per parton?
- What is the role of subnucleonic fluctuations in determining the initial-state geometry?
- Can we observe jet quenching in small systems?

A new comprehensive scan of colliding ion species at RHIC by systematically varying the system size and geometry between pp and Cu+Cu collisions, will provide a unique lever-arm to dial contributions from various mechanisms and impose strong constraints on both ISM and FSM. Since the last RHIC p/d/He+Au scan, the STAR experiment has completed several detector upgrades that extend p_{T} and particle identification to $|\eta| < 1.5$, and provide centrality and event plane determination in $2 < |\eta| < 5$ [17, 165, 166]. An ongoing forward upgrade to instrument the $2.5 < \eta < 4$ region with tracking detectors and calorimeters will be completed prior to 2021 run [167]. The extended detector capability will allow a full exploration of collectivity using all the observables and methods developed for large systems at RHIC/LHC. We will have better control of the non-flow systematics, leading to a better understanding of the multi-particle nature of the collectivity and the longitudinal correlations to constrain the full 3D initial conditions. As an illustration, model studies of v_2 and v_3 in a seris of small systems including symmetric (C+C, O+O, Al+Al, Ar+Ar) and asymmetric (p+Au, d+Au, ^{4}He+Au) collisions using the AMPT model are shown in Fig. 44. AMPT belongs to the category of final-state interaction models, where v_n is largely driven by the geometry of initial nucleon distributions. The v_2 values from asymmetric systems follow different trends: the v_2 in $d/^4$He+Au increases with N_{ch}, while it is relatively constant in p+Au. The v_3 values show a similar N_{ch} dependence as symmetric systems, except for d+Au which deviates from the common trend at large N_{ch}. This study demonstrates that, in a scenario driven by final-state interactions, a clear difference is expected between $d/^4$He+Au and A+A for v_2, while a relatively similar behavior should be observed for v_3. Contributions from other sources, especially ISM, are expected to follow a drastically different behavior; as the system size increases, the ISM contribution will gradually become subdominant.

[1] RHIC has no limitation on small A+A systems, based on private communication with Wolfram Fischer

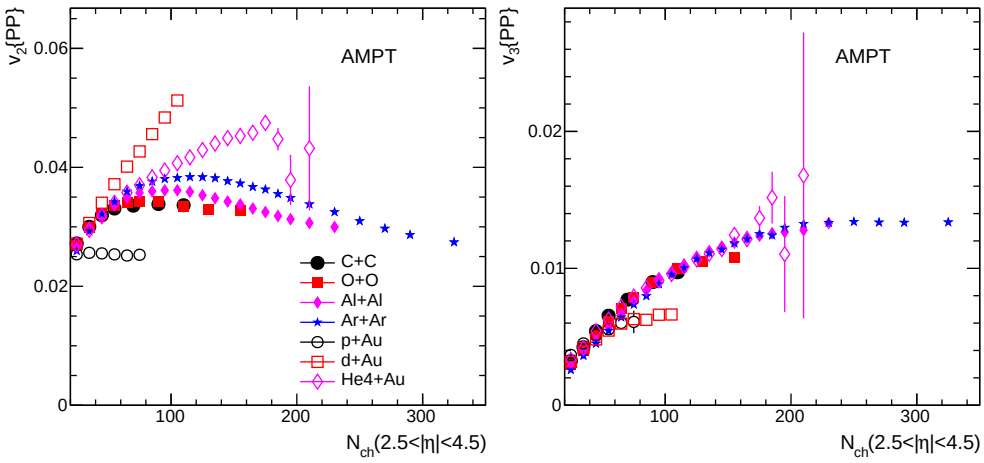

Figure 44: (Left) AMPT predictions for v_2 and (Right) v_3 as a function of $N_{\rm ch}$ in four symmetric and three asymmetric small collision systems.

Arguments for a short O+O run in 2021 In this BUR, we propose a O+O run at $\sqrt{s_{\rm NN}}$ =200 GeV towards the end of the BES-II in 2021, to be followed up with a comprehensive scan of symmetric and asymmetric small collision systems using the STAR forward upgrade after 2021, possibly in collaboration with sPHENIX. The choice of O+O collisions as the starting point is motivated by the following reasons: 1) O+O has an $N_{\rm part}$ coverage comparable to p+Au and d+Au but with a much flatter distribution (see Fig 45), which allows much better control of initial geometry and centrality bias, 2) the Oxygen is a reasonably sized system for which the both the nucleonic and subnucleonic DOF are important, which together with p/dAu data can be used disentangle these contributions, 3) a strong synergy with the proposed higher-energy O+O run at the LHC around around 2023–2024 to enable a direct comparison of the same small-system collision species at drastically different energies. More details, including hydrodynamic model predictions, are presented and discussed below.

The recent yellow report on the future LHC heavy-ion physics program discusses the possibility for smaller A+A collisions [168]. This includes a proposal of an O+O run at $\sqrt{s_{\rm NN}}$ = 2.76–7 TeV in 2022[2], and other light-ion species such as Ar+Ar beyond 2028. As mentioned earlier, one big advantage of the O+O system is that it allows a better control of $N_{\rm part}$ and ε_n, compared to peripheral Pb+Pb collisions [168]. An O+Orun at RHIC right after the BES-II would provide a timely comparison of the same small system at very different collision energies (0.2 TeV vs. 2.76–7 TeV). This "RHIC-LHC energy scan" provides a unique opportunity to study systems with nearly identical initial nucleon geometry but very different subnucleon fluctuations and different saturation scales. The large lever-arm in collision energy should provide new insights on the onset behavior of collectivity, jet quenching, or any other final-state effects in small systems: any model has to describe results at both energies, which naturally leads to a better understanding of results at each energy.

[2]According the latest schedule of the LHC run 3, O+O run will most likely be scheduled in 2023.

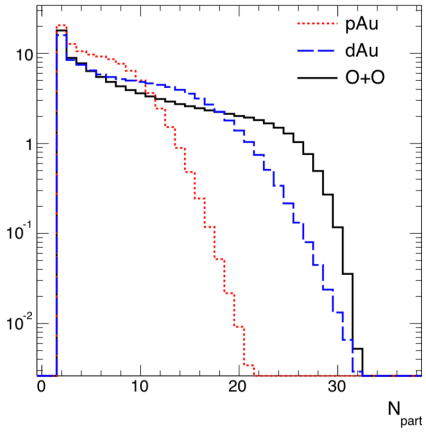

	pAu	dAu	^{16}O+^{16}O
$\langle N_{part} \rangle$	5.8	8.8	9.5

Figure 45: The $N_{\rm part}$ distribution in O+O collisions compared with p+Au and d+Au collisions at $\sqrt{s_{\rm NN}}$ =200 GeV estimated from Glauber model. The table to the right shows the average $N_{\rm part}$ values in the three systems.

Figure. 46 compares the $v_n(p_{\rm T})$ data and hydrodynamic calculations for $n = 2$ and 3 at two energies in a large A+A system (left) and in a p+A system (right). It is well-known that $v_n(p_{\rm T})$ for charged hadrons in large systems has very little $\sqrt{s_{\rm NN}}$ dependence from RHIC to LHC [169], as well as from 39 to 200 GeV at RHIC [170, 171]. This is confirmed by the left panel which compares Pb+Pb [172] with Au+Au [173] data at 30–40% centrality, as well as calculations from the CGC-Hydro model. However, a comparison of $v_n(p_{\rm T})$ between p+Pb [174] and p+Au [160] central data suggests a small difference in v_2, while the v_3 data are nearly identical. In the FSM picture, this suggests that the contributions of subnucleonic fluctuations to the initial eccentricities are very different between the two collision energies. In the ISM picture, it may be the result of an energy dependence of initial momentum anisotropy. It would be exciting to see whether the $\sqrt{s_{\rm NN}}$ dependence for v_2 and v_3 in p+A collisions also persists in small A+A systems such as O+O collisions between RHIC and LHC. The CGC-Hydro model calculations of v_2 and v_3 in O+O collisions at RHIC and the LHC energies are shown in Fig. 46 (middle), where a split in both v_2 and v_3 between two energies is predicted. These rather non-trivial $\sqrt{s}$ dependence across different collision systems reflects the rich physics mechanisms behind origin of collectivity.

We propose a one-week O+O program in 2021 right after BES-II. Assuming a total interaction rate of ∼10–15 kHz (based on recent isobar runs), the STAR DAQ rate of 2 kHz and the RHIC uptime of 50% (12 hour/day), tentative numbers of events we expect to record for different triggers are summarized in Table 9 for one week, default run plan, and two weeks as a more optimal running scenario. Note that we do not have an estimation of minimum-bias trigger efficiency at this point, and assumed it to be ∼100%.

The event statistics listed in Table 9 should allow precision measurements of many types of two-particle correlations, including the N_{ch} dependence of integral v_n, $p_{\rm T}$ dependence of v_n in 0-5% for identified particles (π, K, p and ϕ) to test the NCQ-scaling. The non-flow effects for these observables can be studied in detail thanks to the large acceptance of iTPC and EPD. Based on a Glauber model estimation, the $\langle N_{\rm part} \rangle$ value is 9.5 and 26 for minimum-bias

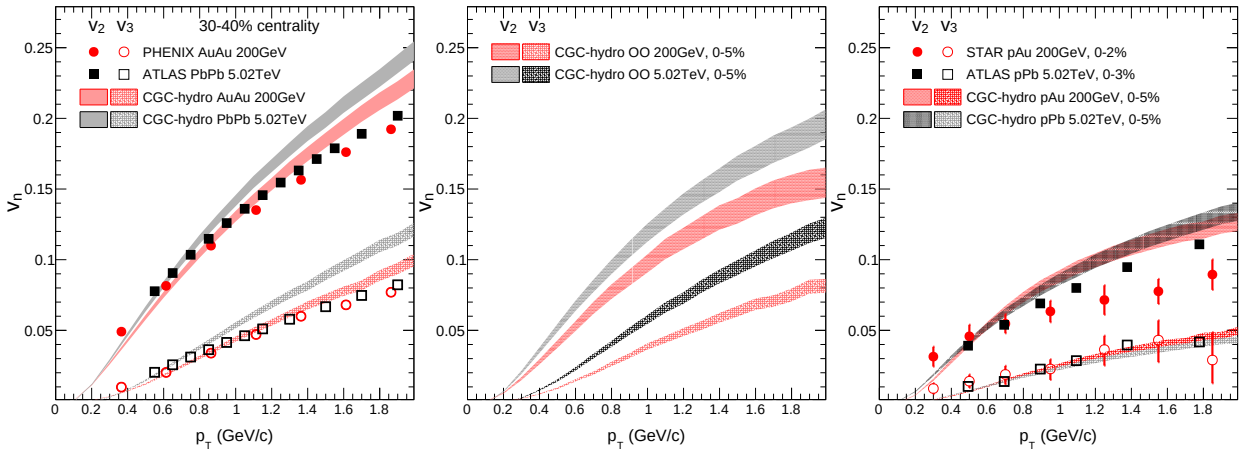

Figure 46: Comparison of measured v_2 and v_3 between Pb+Pb and Au+Au 30–40% centrality events (Left) and high-multiplicity p+Pb and p+Au data (Right) at RHIC and the LHC energies. The CGC-Hydro model calculations are also shown for Au+Au and Pb+Pb (Left), p+Au and p+Pb (Right), and O+O as a prediction (Middle) at both energies.

Table 9: Number of events (in millions) needed in an O+O run at $\sqrt{s_{\rm NN}}$ =200 GeV for various triggers for one week (default) and two weeks (optimistic) running scenarios.

Triggers	Minimum bias	0–5% centrality
Events (1 week)	400 M	200 M
Events (2 week)	800 M	400 M

and 0-5% central O+O collisions, respectively.

Figure 47 shows the projection of the statistical precision for the ϕ meson $v_2(p_{\rm T})$ in 0–5% centrality O+O collisions. Under the assumption that its v_2 in O+O is similar to that of a charged hadron in p+Au around $p_{\rm T}$ ~2–3 GeV/c, the estimation scales the ϕ $v_2(p_{\rm T})$ in peripheral Au+Au collisions [175] to approximately match the charged hadron v_2 in p+Au collisions in Fig. 46, accounting for differences in $\langle N_{\rm part}\rangle$, event plane resolution, and event statistics. A decent measurement of ϕ meson v_2 can be achieved with one week of running.

In fact, the statistics requirement in Table 9 is mainly driven by multi-particle correlations, for example four-particle cumulants for single harmonics $c_2\{4\} = \langle v_n^4\rangle - 2\langle v_2^2\rangle^2$, four-particle symmetric cumulants $SC(2,3) = \langle v_2^2 v_3^2\rangle - \langle v_2^2\rangle\langle v_3^2\rangle$ and three-particle asymmetric cumulants $AC(2,4) = \langle v_2^2 v_4 \cos 4(\Phi_2 - \Phi_4)\rangle$ (Φ_n is the event plane). These observables are sensitive to event-by-event fluctuations of collectivity, and measurements of them at LHC in pp, p+Pb and Pb+Pb collisions have led to high impact results which provide evidence for geometry response in small systems [176–179].

Figure 48 shows the projection of the statistical precision for the $c_2\{4\}$ measurement. The projected precision should allow a measurement of $c_2\{4\}$ signal, assuming a $v_2\{4\}$ value

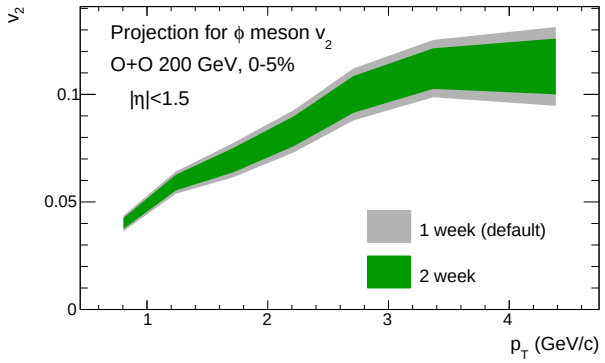

Figure 47: Projected statistical error on ϕ meson $v_2(p_{\mathrm{T}})$ in central O+O collisions within the TPC acceptance.

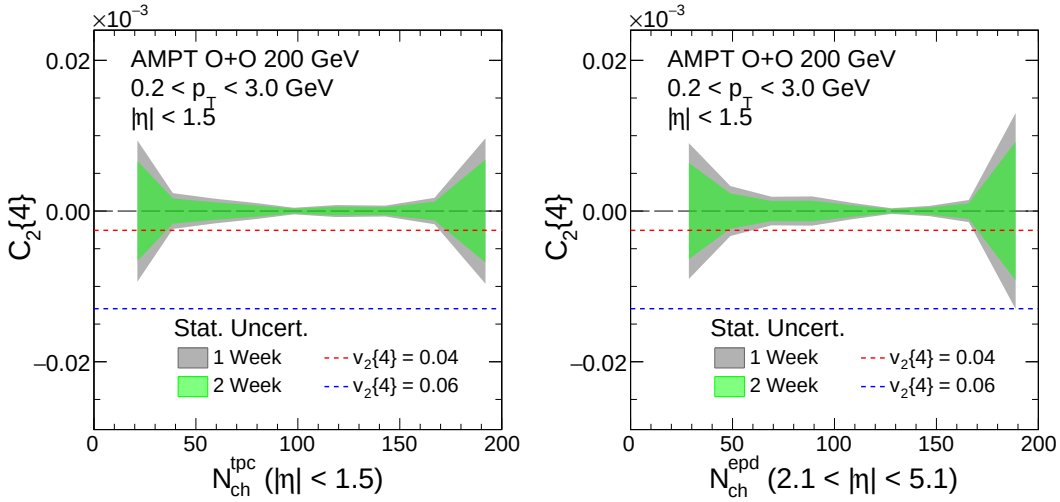

Figure 48: (Left) The projected statistical error bar on $c_2\{4\}$ in 0.2-3 GeV/c in the TPC acceptance as a function of number of charged particles in TPC acceptance and (Right) EPD acceptance.

to be between 4–6% [3].

Figure 49 shows the projection of the statistical precision for the charged hadron R_{AA} measurement for minimum bias O+O collisions (assume 400 Million). This calculation includes the state-of-art knowledge of nPDF effects and jet quenching modeling of Refs. [181, 182]. A significant suppression of $R_{AA} = 0.85 - 0.9$ is expected which should be measurable with decent statistical uncertainty out to 15 GeV.

Answer to PAC questions from last year When this proposal was presented last year, we have received the following comments: "With regards to an O+O run, the case for this could become persuasive if, between now and next year, theorists with expertise in hydrodynamics can provide some simulations that demonstrate what hydrodynamics predicts for v2 and v3 behavior in O+O collisions, and how this compares to results from p+A, Cu+Cu,

[3] The p_{T} integrated $v_2\{4\}$ in d+Au from PHENIX [180] at forward rapidity is about 4%

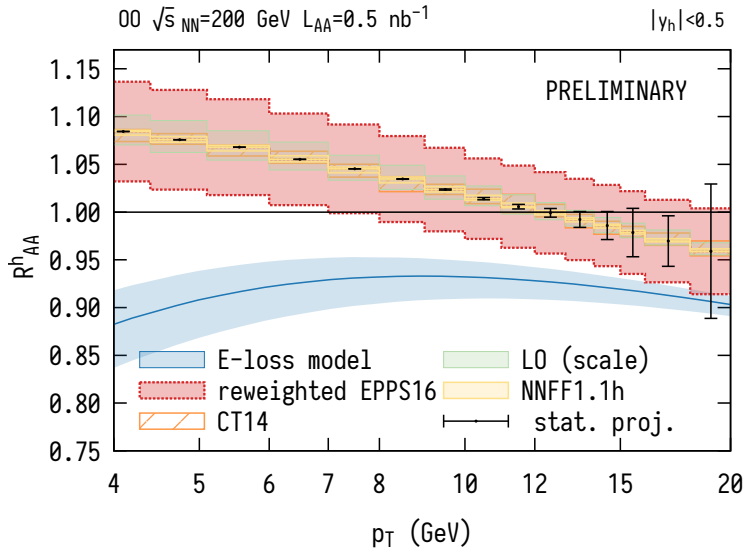

Figure 49: Prediction of minimum bias hadron nuclear modification factor for $\sqrt{s_{\rm NN}} = 200$ GeV O+O collisions following Refs. [181, 182]. A particular parton energy loss model predictions (blue line) is overlaid with the baseline in the absence of parton rescattering. The blue band represents model uncertainty only due to experimental uncertainties in $\sqrt{s_{\rm NN}} = 5.02$ TeV Pb+Pb collisions used to fit a free model parameter. The red band shows nPDF uncertainties reweighted with additional CMS pPb dijet data. Proton PDF (orange), leading order scale (green) and fragmentation function (yellow) uncertainties are fully correlated and cancel. Error bars illustrate statistical uncertainties for OO mock data at 100% efficiency.

and Au+Au collisions. We also suggest that these calculations should be undertaken for $\alpha + \alpha$, Be+Be, Al+Al and Ar+Ar collisions also, as well as for O+Au and other asymmetric small+large nuclear collision options, so as to be able to make the case that O+O is the optimal physics choice, most likely to yield new or substantially improved understanding of questions relating to how small droplets of QGP equilibrate and what is the smallest droplet of QGP that is possible to be formed in collisions at 200 GeV".

We have prepared the following answers to these comments:

- Why O+O? 1) O+O collisions cover similar $N_{\rm part}$ range as p+Au/d+Au (see Figure 45) where the collectivity debate is ongoing, 2) O+O has similar $N_{\rm part}$ but different nucleon/sub-nucleon fluctuations, 3) leverage similar measurement at LHC for new insight and precision.

- Are there theoretical calculations? Many model studies on O+O exist by now, which reflects the community interests: 1812.08096,1904.10415,1908.06212, 1910.09489, 2003.06747, 2005.14682. Figure 46 shows the new prediction on O+O taken from 2005.14682,

- Why not other collision systems? Analyzing power for 2k-particle cumulants $v_n\{2k\}$ scales as $N_{events} \times N_{\rm part}^{2k}$, system smaller than O+O, such as C+C require much longer running time and also difficult to setup the high-multiplicity triggers due to steeply

falling N_{ch} distributions. Also these systems will not have compatible $N_{\rm part}$ coverage as p/d+Au systems. One may suggest to repeat the p/d+Au. But this will require long running time, since previous p+Au (d+Au) data was taken over 5 (1.5) weeks period in run15 (run16).

- Why not larger small systems? Larger asymmetric system we already have Cu+Au and ^{3}He+Au. Results from both are consistent with final-state interpretation from both experiments and theory. Any system in between such as O+Au with $\langle N_{\rm part}\rangle$=60 is expected to be dominated by final state effects.

2.3 Future Possibilities

2.3.1 Exploring the Nuclear Equation-of-State (EoS) with Heavy Ion Collisions

In the interior of the fireball created in HI collisions, nuclear densities of up to 10 ρ_0 can be achieved depending on the energy of the colliding nuclei [183]. Similar densities are predicted to be present in the core of neutron stars (NS). However, the composition and maximal mass of NS is highly dependent on the nuclear equation-of-state (EoS) which is close related to the compressability of nuclear matter. Therefor HI collisions are considered as a ideal tool to study the EoS at high nuclear densities and establish a bridge between astrophysics and nuclear physics.

Already in the early 80s several observables probing the EoS (i.e. which are sensitive on the density and pressure of the system) like particle production [184, 185], transverse momentum analysis [186], directed and elliptic flow [187,188] were proposed. At low energies and densities up to about 2.5 ρ_0 elliptic flow analysis favour a soft EoS [189] while at AGS energies (between 2.5 and 4.5 ρ_0) no clear picture could be established yet. Transverse flow measurements hint to a soft (K $\leq$ 210) EoS while elliptic flow measurements indicate a stiff (K $\approx$ 300) EoS [188]. Another method to probe the equation-of-state of nuclear matter was proposed already 1985 by Aichelin and Ko [190] by measuring the sub-threshold production of strange particles which are created in the dense medium early in the reaction. Especially the multi-strange particle production at sub-threshold energies should be highly sensitive to the density of the medium since multiple-collision processes are required. So the information on the EoS is stored in the yield and slope of the excitation function of the sub-threshold produced particles which can be compared to various theoretical models. It is also clear that the abundance of produced particles is highest at heavy systems like $Au + Au$ since the reaction volume is big. Therefor comparison measurements with light system like $C + C$ can be used as a reference where the influence of the EoS is small. In addition, systematic errors both in experiment and theory cancel out to a large extent by taking the yield ratio of produced (multi-) strange particles at both systems.

Figure 50 shows the normalized yield ratio $((M_{K^+}/A)_{Au+Au}/(M_{K^+}/A)_{C+C})$ of sub-threshold produced K^+ as a function of 4 different beam energies [191]. A comparison to different models [192, 193] predict a soft EoS at low bombarding energies around $E_{beam} \approx 1.5\,GeV$. On the other hand the finding of neutron stars with masses above 2 solar masses can only be ex-

plained by a stiff EoS [194] which should be measurable in flow observable at higher incident energies.

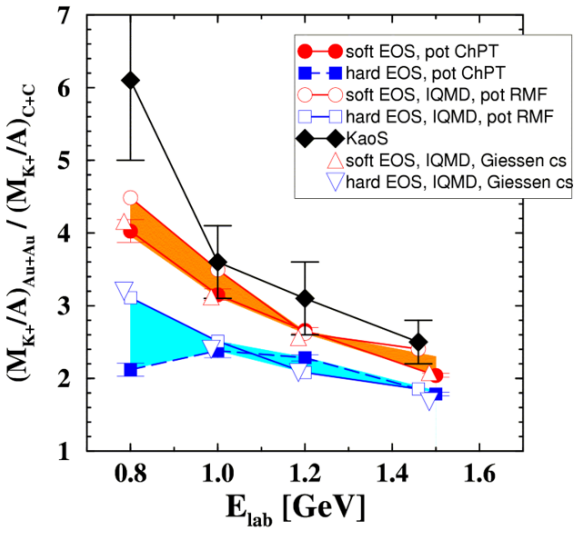

Figure 50: Excitation function of the ratio of K^+ multiplicity obtained in $Au + Au$ over $C + C$ reactions [191] together with model calculations [192, 193] indicating a soft EoS at this bombarding energies.

An independent observable at these higher energies are the production rates of multi-strange baryons, of which several have their NN production threshold in the reach of BES II: Ξ^- (production threshold $\sqrt{s_{\rm NN}}$=3.247 GeV), Ω^- (production threshold $\sqrt{s_{\rm NN}}$=4.092 GeV), Ξ^+ (over $\Xi^+\Xi^-$-channel, production threshold $\sqrt{s_{\rm NN}}$=4.520 GeV) and Ω^+ (over $\Omega^+\Omega^-$-channel, production threshold $\sqrt{s_{\rm NN}}$=5.222 GeV). A beam energy scan in small steps (with 3 to 4 points with distance of about 200 to 300 MeV) below the production threshold energy for the various particles species for $Au + Au$ collisions could give access to the properties of the EoS as function of colliding energy and density. In fact a big fraction of the measurements were already finished during the BESII campaign and only a few additional fixed target points have to be performed which depends on the number of investigated particles used as probes. The measurement of the pressure as function of energy in small steps could even allow for the discovery of a 1^{st} order phase transition in the covered energy range [195]. The measurements at the heavy system could be accompanied by a reference measurement of a light system (for example $C + C$) for at least one particle species and extrapolated to the others. However, since the production yield scales with the number of participants the time needed for the light system is significantly longer (few weeks) as for the heavy system which needs typically btw. 12 h and a day.

Nevertheless the proposed measurements have a high discovery potential and could be an opportunity for a future fixed target HI program at STAR.

2.4 Exploring the Microstructure of the QGP (Run-23 and Run-25 Au+Au)

The completion of the RHIC's scientific mission involves the two central goals [196] of (i) mapping out the phase diagram of the QCD, and (ii) probing the inner workings of the QGP by resolving its properties at short length scales. The complementarity of the RHIC and LHC facilities to study the latter is scientifically as essential as having more than one experiment independently study the microstructure of the QGP. With several years of operating the recently installed iTPC upgrade and the soon-to-be installation and operation of STAR's forward detectors, the STAR collaboration will be in an excellent position to take advantage of its vastly improved detection capabilities. Combine this with the prospect of a substantial increase in beam luminosities and RHIC will be uniquely positioned to fully engage in a detailed exploration of the QGP's microstructure. Through careful discussions in its physics working groups, the STAR collaboration has identified a number of topics that together make a compelling case to take data during Runs 23-25 alongside sPHENIX, and successfully complete RHIC's scientific mission. In this section, we present a selection of those topics that will take full advantage of both STAR and RHIC's unique capabilities and address the following important questions about the inner workings of the QGP.

- What is the precise temperature dependence of the shear η/s, and bulk ζ/s viscosity?
- What is the nature of the 3-dimensional initial state at RHIC energies? How does a twist of the event shape break longitudinal boost invariance and decorrelate the direction of an event plane?
- How is global vorticity transferred to the spin angular momentum of particles on such short time scales? And, how can the global polarization of hyperons be reconciled with the spin alignment of vector mesons?
- What is the precise nature of the transition near $\mu_B = 0$, and where does the sign-change of the susceptibility ratio χ_6^B/χ_2^B take place?
- What is the electrical conductivity, and what are the chiral properties of the medium?
- What can we learn about confinement and thermalization in a QGP from charmonium measurements?
- What are the underlying mechanisms of jet quenching at RHIC energies?

The event statistics projections that are used in this section will rely on the CAD's recently update 2023E and 2025E Au+Au luminosities [197] and are listed in Table 10. For each year we presume 24 weeks of RHIC operations, and based on past run operations an overall average of 85% × 60% (STAR×RHIC) uptime, respectively. The minimum-bias rates assume a conservative 1.5 kHz DAQ rates which will allow sufficient bandwidth for specialized triggers which are listed as integral luminosities.

year	minimum bias [$\times 10^9$ events]	int. luminosity [nb^{-1}] all vz	|vz|<70cm	|vz|<30cm
2014 2016	2	26.5	19.1	15.7
2023	10	43	38	32
2025	10	58	52	43

Table 10: STAR minimum bias event statistics and luminosity projections for the 2023 and 2025 Au+Au runs. For comparison the 2014/2016 event statistics and luminosities are listed as well.

At RHIC it is possible to build detectors that can span from mid-rapidity to beam rapidity – with the two recent upgrades STAR is able to achieve this unique capability. STAR's BES-II upgrade sub-systems comprised of the inner Time Projection Chamber (iTPC, $1.0 < |\eta| < 1.5$) , endcap Time Of Flight (eTOF, $1 < \eta < 1.5$) and Event Plane Detector (EPDs, $2.1 < |\eta| < 5.1$), that are all commissioned and fully operational since the beginning of 2019 [16–18]. As will be discussed in Sect. 4, the STAR collaboration is constructing a forward rapidity ($2.5 < \eta < 4$) upgrade that will include charged particle tracking and electromagnetic/hadronic calorimetry [198]. For charge particle tracking the aim is to construct a combination of silicon detectors and small strip thin gap chamber detectors. The combination of these two tracking detectors will be referred to as the forward tracking system (FTS). The FTS will be capable of discriminating the hadron charge sign. It should be able to measure transverse momentum of charged particles in the range of $0.2 < p_{\rm T} < 2$ GeV/c with $20-30\%$ momentum resolution. In what follows, we will refer to the combination of the existing TPC ($|\eta| < 1$) and the iTPC upgrade as iTPC ($|\eta| < 1.5$) for simplicity.

The impetus for running STAR during the year of 2023-2025 in terms of bulk correlation measurements in Au+Au 200 GeV collisions comes from the gain in : i) extended acceptance and ii) enhanced statistics. In the first subsections, we briefly describe how these two opportunities can be exploited to perform correlations measurements that are unique to the physics goals of the RHIC heavy ion program.

Next, thanks to a reduced material budget between the beam and the iTPC, STAR will be uniquely positioned to perform dielectron measurements which we propose to probe degrees of freedom of the medium and its transport properties. For that we will use high precision dilepton excess yield, i.e. l^+l^- invariant mass distribution after subtraction of dilepton sources produced after freeze-out, and contributions from the initial collisions such as Drell-Yan and correlated charm-anticharm pairs. Furthermore, we propose to study the virtuality, Wigner function and final-state magnetic field in QGP. For the latter the photon-photon collisions in ultra-peripheral, peripheral,and midcentral reactions and p+A (all centralities) in both channels e^+e^-, $\mu^+\mu^-$ will be measured with high accuracy.

In the last subsections, we address our proposed charmonium measurements and motivate the importance of STAR's proposed program of precise jet measurements to explore the micro-structure of the QGP.

2.4.1 Correlation Measurements Utilizing Extended Acceptance

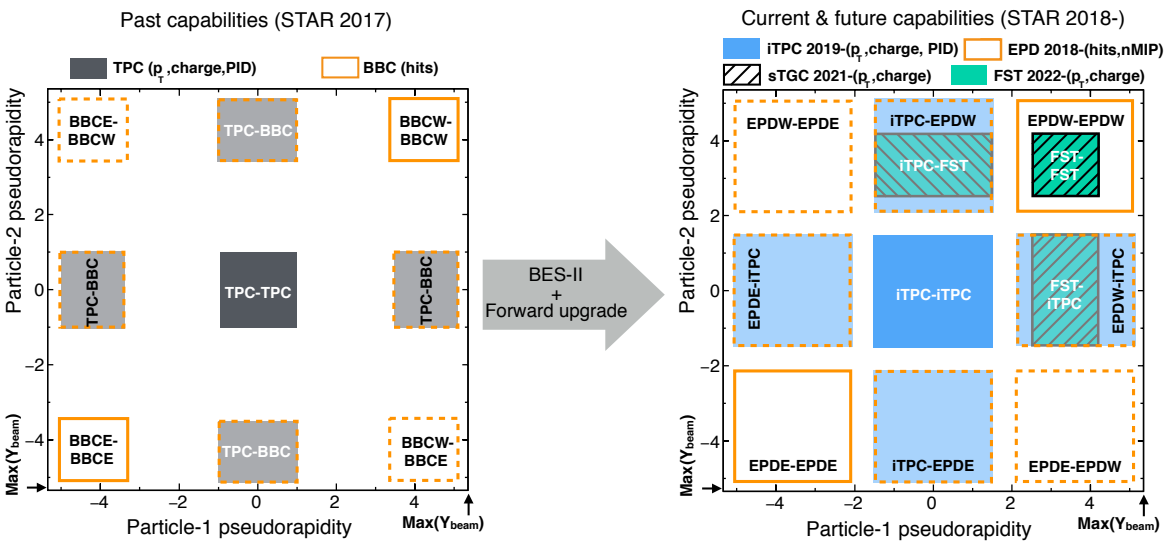

Figure 51: A visual representation of two-particle phase space in pseudorapidity covered by STAR detectors with respect to the region allowed by maximum beam rapidity (Y_{beam}=5.36 at 200 GeV Au+Au collisions) of RHIC. Left and right panels show the capabilities before and after BES-II and forward upgrade of the STAR detector, respectively.. Note that in addition to a larger pair acceptance, the EPD granularity is over an order of magnitude larger than that of the BBC, and individual EPD tiles are shown to be separable into 1, 2, 3 MIP responses.

Figure 51 demonstrates how STAR with the BES-II and forward upgrades will extend the two-particle phase-space (in terms of η_1 and η_2 with respect to beam rapidity) many times enabling us to perform correlation measurements over a wide window of relative pseudorapidity. Since many of the important correlation measures are based on two-particle correlations, this enhanced phase-space will provide STAR with many advantages: 1) increase the number of pairs to bring better precision, 2) reduction in different sources of the non-flow background by increasing pseudorapidity separation. Many multi-particle correlations will also get benefited due to increase in triplets, quadruplets and so on due to overall increase in acceptance. With this unique extended pseudorapidity reach offered by the BES-II and forward upgrade of the STAR detector, our goal is to perform correlation measurements aimed towards a deeper understanding of the largely unexplored three-dimensional structure of the initial state and temperature dependent transport properties of the subsequent fluid-like medium produced in heavy ion and small system collisions at RHIC.

Two key sets of measurements are of interests: 1) pseudorapidity dependence of azimuthal correlations, 2) pseudorapidity dependence of global hyperon polarization.

Pseudorapidity-dependent azimuthal correlation to tightly constrain temperature dependence of viscosity The idea of tightly constraining the temperature viscosity

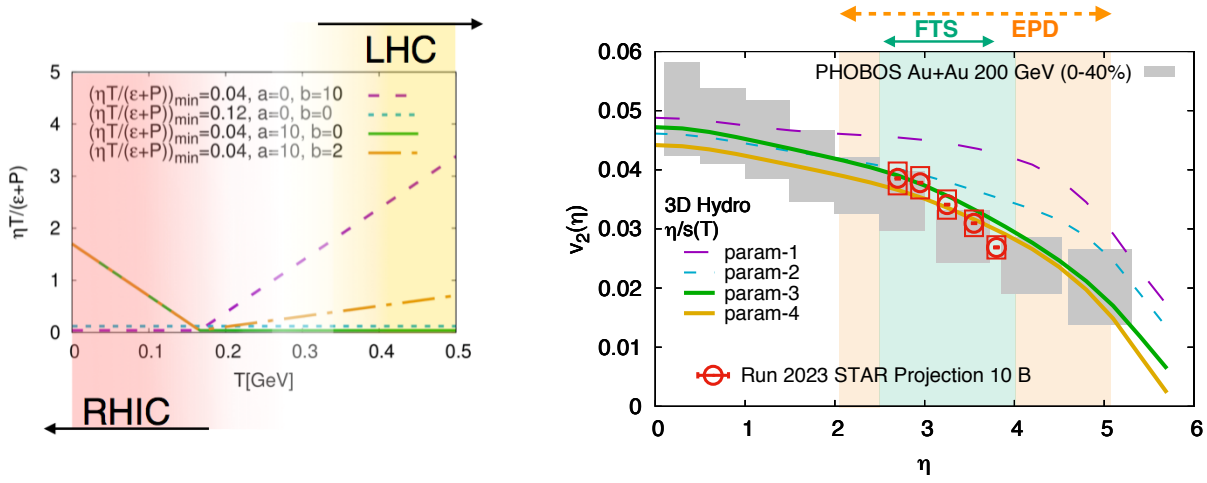

Figure 52: (Left) Different parameterizations of temperature dependence of shear viscosity to entropy η/s (T) (at zero chemical potential) used in the hydrodynamical simulation of Ref [199]. Interestingly, it has been demonstrated in Ref [200] that the region of lowest η/s is the one that can be probed at RHIC. (Right) Effects on the elliptic flow co-efficient v_2 due to the different parameterizations of the viscosity parameter indicating better constraints on η/s (T) can only be performed by measurements at forward rapidities at RHIC. The interpretation of the existing PHOBOS data is limited by the large uncertainties. The projection for STAR measurements are shown on the same plot.

of the QGP was envisioned in the 2015 Long Range Plan for Nuclear Science [196]. The QCD matter formed at RHIC shows nearly perfect fluidity characterized by the smallest viscosity to entropy ratio η/s known in nature. The temperature dependence of η/s and other transport parameters has not been fully constrained. One major aim is to perform precision measurements to contain the temperature dependence of shear η/s (T) and bulk ζ/s (T) viscosity. Hydrodynamic simulations have demonstrated that since the temperature of the produced fireball in HICs vary with the rapidity, the measurement of the rapidity dependence of flow harmonics has the potential to constrain η/s (T) and ζ/s (T) [199]. For this, RHIC measurements have advantage over LHC since smaller beam rapidity at RHIC provides stronger variations of the temperature with rapidity. The beam energy scan at RHIC provides an additional handle on temperature to map η/s (T), and ζ/s (T) over a wide range of temperature. Indeed, the hydrodynamic simulation of Ref [199] indicates that η/s (T) at lower temperatures, near its possible minimum ($T = T_c$), can be better constrained by RHIC measurements. Results from such simulations are shown in Fig. 52. In this simulation, a number of QCD-motivated parameterizations of the temperature dependence of the shear viscosity was assumed, as shown in Fig. 52 (left). Existing data from the PHOBOS collaboration suffer from large uncertainties, therefore only limited constrain on the temperature dependence of the transport parameters can be achieved. The BES-II and the forward upgrade of STAR will provide precise estimations of different azimuthal correlation observables: $v_n(\eta)$ and other higher-order ($n > 2$) flow coefficients $v_n(\eta)$, its fluctuations

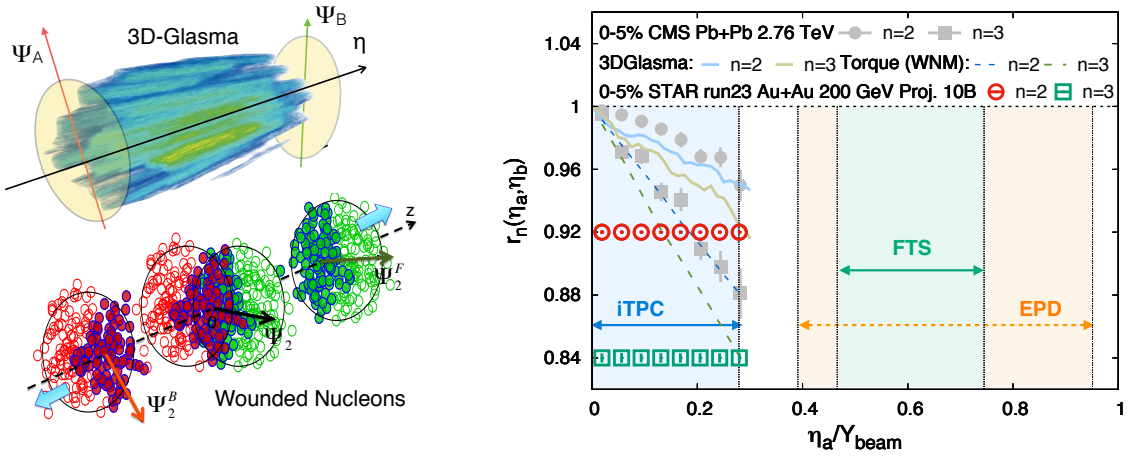

Figure 53: (Left) Cartoon to demonstrate the de-correlation of event planes in the longitudinal direction of collision from gluon saturation based 3D-Glasma model [201] and wounded nucleon model (WNM) [202, 203]. (Right) The longitudinal de-correlation of elliptic anisotropy plane as a function of the pseudorapidity in units of beam rapidity. CMS results are compared predictions from two models in the left with STAR projection for Run 2023 (using preliminary Run 19 results) for anticipated 10 B min-bias events. The colored regions show that the current and future capabilities at STAR (with iTPC+EPD+FTS) can extend such measurements with good precision by covering a large fraction of the beam rapidity at 200 GeV – this demonstrates the unique strength to STAR to study the physics of 3D initial state.

$\sigma(v_n)/v_n$ that have never been measured at forward rapidity and are essential in terms of constraining η/s (T) near its possible minimum. While transverse momentum integrated quantities can already constrain the shear viscosity, additional information of transverse momentum is essential to constrain the bulk viscosity ζ/s. With the forward tracking systems it will be possible to measure the $p_{\rm T}$ dependence of v_n – in particular the information of $\langle p_T \rangle$ is essential to constrain the bulk viscosity ζ/s(T). This can be done with a possible $A+A$ collisions with the forward upgrade and running of STAR during the year 2023.

Pseudorapidity-dependent azimuthal correlation to constrain the longitudinal structure of the initial state Initial-state longitudinal fluctuations and fluid dynamical response of the medium formed in heavy ion collisions can lead to de-correlations of the direction of the reaction planes Ψ_n (which determines the orientation of the harmonic anisotropies) with pseudorapidity (see Fig. 53). Such effects are often referred to as torque or twist of the event shape [203–205] that eventually leads to a breaking of longitudinal/boost/rapidity invariance. The magnitude of the de-correlation is determined by the details of the dynamics of initial state, the distribution of nucleons and partons inside the colliding nuclei. Several promising observables have been proposed to study this effect, Fig. 53 shows one which can be expressed as $r_n(\eta_a, \eta_b) = V_{n\Delta}(-\eta_a, \eta_b)/V_{n\Delta}(\eta_a, \eta_b)$, where $V_{n\Delta}(\eta_a, \eta_b)$ is the Fourier coefficient calculated with pairs of particles taken from three different pseudorapidity regions $-\eta_a$, η_a and η_b. The observable $r_n(\eta_a, \eta_b)$ was originally introduced

and measured by CMS collaboration in Ref [206] and also been measured by the ATLAS collaboration in [207]. An observable using three-particle correlations that is sensitive to this effect is [208] the relative pseudorapidity dependence of the three-particle correlator $C_{m,n,m+n}(\eta_a, \eta_b, \eta_c) = \langle \cos(m\phi_1(\eta_a) + n\phi_2(\eta_b) - (m+n)\phi_3(\eta_c)) \rangle$. Also, another one very similar to r_n in term of design but involves four-particle correlations is: $R_{n,n|n,n}(\eta_a, \eta_b)$ is also very useful to study this effect [209]. As shown in Fig. 53 CMS measurements of r_n show a strongest de-correlation ($\sim 16\%$ for n=3, $\sim 8\%$ for n=2) in central events within the range of their acceptance. Initial state, described by gluon saturation, as simulated by the 3D-Glasma model, the breaking of boost invariance is determined by the QCD equations which predict the evolution of gluons in saturation regime with Bjorken-x. At the LHC such models predict weaker de-correlation as compared to initial state described by wounded nucleon models and does a good job in explaining the r_2 data from CMS collaboration [201] but over-predicts r_3 results. One expect the nature of the initial state to change from LHC to RHIC, in particular the region of Bjorken-x probed is very different at RHIC. It is therefore extremely important to utilize the enhanced acceptance of the STAR detector with the Au+Au 200 GeV run to study this effect. In Fig.53 STAR projection using preliminary Run 19 results for 10 B events is shown for the measurement of r_n within the acceptance $|\eta| < 1.5$. The colored regions show that the current and future capabilities at STAR (with iTPC+EPD+FTS) can extend such measurements using observables $r_n, C_{m,n,m+n}, R_{n,n|n,n}$ with good precision by covering either equal (iTPC only) or larger (iTPC+FTS+EPDs) fraction of the beam rapidity at 200 GeV compared to the LHC measurements. This unique measurement capability will help pin down the nature of the 3-dimensional initial state of heavy ion collisions. It will also help constrain different models of QCD that predict the rapidity (or Bjorken-x) dependence of valance quark and gluon distribution inside colliding nuclei that has been demonstrated by theoretical calculations in Ref. [201, 210].

Pseudorapidity dependence of global hyperon polarization The global polarization of hyperons produced in Au+Au collisions has been observed by the STAR collaboration [20]. The origin of such a phenomenon has hitherto been not fully understood. Several outstanding questions remain. How exactly the global vorticity is dynamically transferred to the fluid like medium on the rapid time scales of collisions? Then, how does the local thermal vorticity of the fluid gets transferred to the spin angular momentum of the produced particles during the process of hadronization and decays? In order to address some of these questions one may consider measurement of the polarization of different particles that are produced in different spatial parts of the system, or at different times. A concrete proposal is to: 1) measure the $\Lambda(\bar{\Lambda})$ polarization with pseudorapidity and 2) measure it for different particles such as Ω and Ξ. Both are limited by the current acceptance and statistics available to the STAR collaboration. However, as shown in Fig.54 with the addition of iTPC, FTS and with high statistics data from run 2023 it will be possible to preform such measurements with a reasonable significance. iTPC (+TPC) has excellent PID capability to measure all these hyperons. Although FTS has no PID capability we can do combinatorial reconstruction of $\Lambda(\bar{\Lambda}$ candidates via displaced vertices. A similar analysis was performed and published by

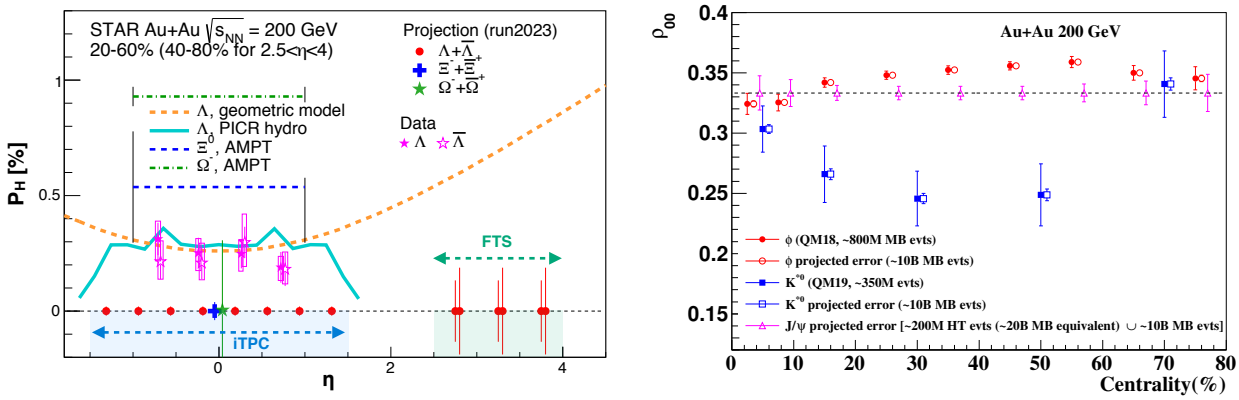

Figure 54: (Left) Projections (along with preliminary data) for differential measurement of $\Lambda(\bar{\Lambda}$ polarization over the extend range of pseudorapidity with the iTPC and FTS detectors of STAR that will help resolve tension between different theoretical model predictions (shown by curves) of polarization with η. In addition, projections for the measurements of spin-1/2 Ξ and spin-3/2 Ω particles is also shown. (Right) Spin alignment co-efficient ρ_{00} as a function of centrality, with projected errors based on $\sim$ 10 billion events. The enhanced statistics run 2023 combined with excellent dilepton capability of STAR will enable us to measure J/ψ alignment along with increasing the significance of ϕ and K^{*0} measurements.

the STAR collaboration using the FTPC detector of STAR in Ref [211]. In order to make a conservative projection we assume similar momentum resolution of $10-20\%$ for single charged tracks, similar overall tracking efficiency, charge state identification capability for FTS and FTPC (see forward upgrade section for exact numbers). We also assume the FTS with it's novel-tracking framework will be able to measure a minimum separation of 20 cm between the all pairs of one positive and one negative track (a possible decay vertex) from the main vertex of the event. This will give rise to about 5% efficiency of $\Lambda(\bar{\Lambda})$ reconstruction with about $15-20\%$ background contribution from $K^0_S \rightarrow \pi^+ + \pi^-$ [211] for which we can make projections for polarization measurement in Au+Au 200 GeV $40-80\%$ assuming 10 Billion minimum-bias events as shown in Fig. 54. Currently theoretical models predict contradictory trends for the pseudorapidity dependence Λ polarization. If the initial local orbital angular momentum driven by collision geometry [212] play dominant role it will lead to increases of polarization with pseudorapidity. On the other hand if the local thermal vorticity and hydrodynamic evolution [213] play a dominant role it will predict decreasing trend or weak dependence with pseudorapidity. Such tensions can be easily resolved with the future proposed measurement during the run 2023.

2.4.2 Correlation Measurements Utilizing the Enhanced Statistics

Over the past years the STAR collaboration has pursued dedicated measurements at Au+Au collisions at $\sqrt{s_{\rm NN}}$= 200 GeV that have major discovery potential but are intrinsically statistics hungry. In the past, attempts have been made to combine datasets from several years to increase the significance of such measurements. This results in additional uncorrectable sys-

tematic uncertainties in the measurements, mostly due to run-to-run variation of detector response and collision conditions. A single stable long run with similar detector conditions, as anticipated during Run-23 will not only reduce the statistical uncertainty but will also bring the systematics under control. In the following section and also in section 1.2.5 we propose correlation measurements that will utilize the enhanced statistics from Run-23 and that can lead to high-impact results. To start with we can assume STAR DAQ to collect data at the rate of 1.5 kHz and a combined RHIC×STAR uptime of 50% (12 hour/day) for 24 weeks of running during Run-23. This will lead to the accumulation of about $24 \times 7 \times 86400 \times 0.5 \times 1500 \approx 10$ billion events.

Global spin alignment of J/ψ: Surprisingly large signals of global spin alignment of vector mesons such as $\phi(1020)$ and $K^{*0}(892)$ have been measured via the angular distribution of one of their decay products. By far the experimental observation of vector meson spin alignment have not been interpreted satisfactorily by theory calculations. It has been realized that the mechanism driving the global polarization of hyperons can have its imprint on vector mesons spin alignment albeit the observed strength of signals for the two measurements cannot be reconciled. In fact the large quantitative difference between the measurements of $\phi(1020)$ and $K^{*0}(892)$ spin alignment as shown in Fig. 54 (right) cannot be simultaneously explained by conventional mechanisms of spin-orbit coupling, driven by angular momentum, without invoking the strong force fields. It is argued that the strong force field makes a dominant contribution to the spin-alignment coefficient ρ_{00} of ϕ, while for K^{*0}, the contribution is diminished due to the mixing of quark flavors (averaging-out of different meson fields) [214, 215]. Therefore, the current preliminary experimental data from STAR (Fig. 54, showing $\rho_{00}(\phi) > \rho_{00}(K^{*0})$) support the role of strong force field as a key mechanism that leads to global spin alignment. However, a stringent test of such a prediction can be performed by measuring the spin alignment of J/ψ. This is because the similar argument applies for both ϕ and J/ψ, i.e. like s and $\bar{s}$, the strong field component also couples to c and $\bar{c}$ quarks leading to larger ρ_{00} for J/ψ. In Fig. 54(right) we present the projected errors for ρ_{00} of J/ψ estimated for various centralities assuming 200 million events (24 weeks running) anticipated in Run-23 by implementing High Tower (HT) triggers with the Barrel Electromagnetic Calorimeter. It is worth to mention that apart from J/ψ spin alignment, such a large statistics data set will also allow addition differential study of global spin alignment of ϕ and K^{*0} and help to further elucidate the mechanism behind vector meson spin alignment.

Sixth order cumulant of net-proton distributions LQCD calculations [216, 217] predict a sign change of the susceptibility ratio χ_6^B/χ_2^B with temperature (T at $\mu_B = 0$) taking place in the range of 145-165 MeV. The observation of this ratio going from positive to negative values is considered to be a signature of crossover transition. As described in the previous section, the cumulants of net-proton distribution are sensitive to the chiral crossover transition at vanishing baryon chemical potential. Interestingly, as reported in the last BUR and in the recent Quark Matter 2019, the preliminary results from STAR [218] observed

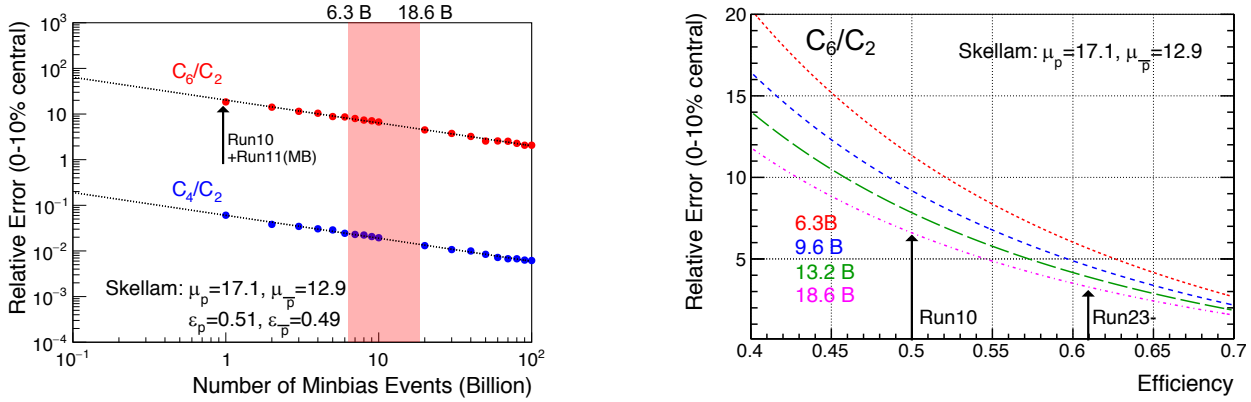

Figure 55: Projection for measurement of ratio of sixth order over second order cumulants of net-proton distribution.

$C_6/C_2 > 0$ in 54.4 GeV while $C_6/C_2 < 0$ in 200 GeV in central Au+Au collisions. The observation of positive C_6/C_2 at lower energies can be further confirmed by higher statistics data sets from the BES-II program over the energy range of 7.7-19.6 GeV, which also include the increased acceptance iTPC. The observation of negative C_6/C_2 is intriguing and by far only seen at 200 GeV and based on the current STAR data has less than 2.5σ significance in terms of statistical uncertainties. The currently systematic uncertainty is of similar order as statistical uncertainty mainly due to combining data sets from Runs 10 and 11. As shown in the projection plot of Fig. 55 it is possible to establish definitive observation of negative C_6/C_2 at 200 GeV with nearly 10 billion minimum-bias events collected during the Run-23 with 15% increase in the reconstruction efficiency and enhanced acceptance of the iTPC detector upgrade. A similar measurement can be performed at the LHC however only STAR measurements can pinpoint the region of T and μ_B where this phenomenon occurs. In other words it can establish if that the sign change occurs somewhere between 54.4 GeV and 200 GeV. Such measurement has the potential to establish the first experimental observation of QCD chiral crossover transition.

2.4.3 Electromagnetic Probes

Probing the degrees of freedom of the medium and its transport properties. As discussed in Sect. 1.1.3, at $\mu_B \sim 0$ Lattice QCD works and can be directly tested against experimental results. This will help to disentangle the ρ melting from other explanations such as collision broadening. In case the measured in-medium spectral function merges into QGP description this would indicate a transition from hadrons into a structure-less quark-antiquark continuum and thus providing the manifestation of chiral symmetry restoration. To study this, we will continue to search for a direct signature for chiral symmetry restoration via chiral ρ-a_1 mixing. The signal is predicted to be detectable in the dilepton intermediate mass range. Difficulties are related to the fact that correlated charm-anticharm and QGP saturate invariant mass region of 1.1 — 1.3 GeV/c^2. Therefore an accurate measurement

of the excess dilepton yield, i.e. dilepton yield after subtraction of the cocktail of contributions from final-state decays, Drell-Yan and those from correlated heavy-flavor decays, up to invariant mass of 2.5 GeV/c^2 is required. The challenging analysis on charmed-decayed dielectron is ongoing from the data sets taken with the Heavy Flavor Tracker at STAR [?]. Thus deeper understanding of origin of thermal radiation in Au+Au collisions at $\sqrt{s_{\rm NN}}$= 200 GeV from ∼zero mass up to 2.5 GeV/c^2 will become possible with rigorous theoretical efforts and improved dielectron measurements. Figure 56 shows the expected statistical and systematic uncertainties of dielectron excess mass spectrum with all the detector upgrades and for the anticipated total Run-23/Run-25 statistics of 20×10^9 events.

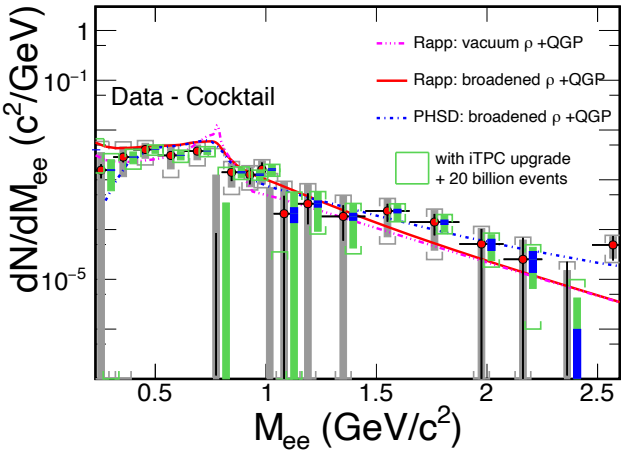

Figure 56: The expected statistical and systematic uncertainties of dielectron excess mass spectrum with the iTPC upgrade compared to the current TPC case. The data are from our measurements in $\sqrt{s_{\rm NN}}$= 200 GeV Au+Au collisions [58]. Model comparisons are also shown. The boxes represent systematic uncertainties from data and the brackets represent the total systematic uncertainties including those from cocktails. The grey ones are for the current case while the green ones are for the expected case. The blue bands represent statistical uncertainties from 20 billion minimum-bias events with the iTPC upgrade.

Another application of dileptons is to use them to measure transport coefficients. The electrical conductivity can be directly obtained as the low-energy limit of the EM spectral function. We aim to extract such information by studying excess dielectron yield at the low-energy regime of dilepton spectra and the conductivity peak at small invariant masses, i.e. at low invariant mass and low p$_T^{ee}$. Low field run could be profitable, however already now dileptons with pair p_T^{ee} down to 60 MeV/c could be measured. Measurement of Drell-Yan in p+A collisions at low p_T would provide an important reference to constrain dilepton cocktail.

To gain deeper understanding of the microscopic origin of the excess radiation, we will

- separate early from later time radiation by measuring dilepton elliptic flow (v_2) as a function of dilepton mass;
- identify the source of dilepton radiation by studying dilepton polarization versus invariant mass (helicity angle);

- measure precisely the lifetime of the interacting fireball. As an observable we will use integrated low-mass yield but also compare explicit model calculations with various $\tau_{fireball}$;

- extract an average radiating source temperature from the fit of Boltzmann distribution to the invariant mass slope in the range 1.1 - 2.5 GeV/c^2 spectrum. The higher the invariant mass, the stronger the QGP contribution to the spectrum, the higher the chance to measure temperature of QGP.

Last, but not least, concerning direct-photon emission, the existing difference, on the order of a factor of two, between the low momentum spectra from PHENIX and STAR in 200 GeV Au+Au collisions, has to be resolved. In order to clarify the direct photon puzzle we will measure direct virtual photon yield as well as its elliptic flow coefficient. We will particularly focus on low p_T η measurement which might be instrumental in clarifying this long standing question.

Studying virtuality, the Wigner function and final-state magnetic fields in the QGP. The unsuccessful description of STAR data by the STARLight model led to the attribution of the broadening to the possible residual magnetic field trapped in an electrically conducting QGP, which is the key information to study the chiral magnetic effect. Similarly, the ATLAS collaboration qualified the effect via the acoplanarity of lepton pairs in contrast to the measurements in UPC and explained the additional broadening by the multiple electromagnetic scatterings in the hot and dense medium, which is analogous to the medium $P_\perp$-broadening effects for jet quenching. These descriptions of the broadening effect in hadronic collisions are based on the assumption that there is no impact parameter dependence of the transverse momentum distribution for the electromagnetic production. Recent lowest-order QED calculation, in which the impact parameter dependence is recovered, could reasonably describe the broadening observed by STAR and ATLAS without any in-medium effect. To solve the puzzle, we propose to precisely study the initial $P_\perp$-broadening for the dilepton pair in ultra-peripheral collisions. Different neutron emission tag serve as the centrality definition, and will allow us to explore the broadening baseline variation with impact parameter. Furthermore, the differential spectrum as a function of pair $P_\perp$, rapidity, and mass enable us to study the virtuality and Wigner function of the initial electromagnetic field, which provide the information to extact the momentum and space correlation of EM field. As shown in Fig. 57, comparing with the latest QED calculation, there still exists additional broadening in peripheral collisions, although the significance is about 1σ, which still leave room for the medium effect. In Runs 23/25, as projected in the figure, we could judge the existence of additional broadening with much higher precision and further constrain the strength of final-state magnetic field in QGP.

2.4.4 Deconfinement and Thermalization With Charmonia Masurements

Measurements of charmonia in heavy-ion collisions provide important information about the thermodynamic properties of the created medium. Production of J/ψ mesons in Au+Au

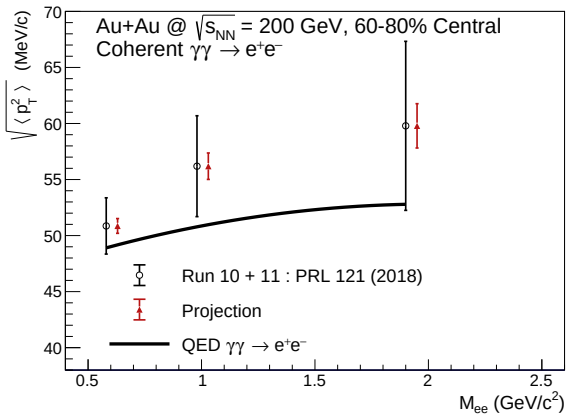

Figure 57: (Color online) The $\sqrt{\langle p_T^2 \rangle}$ of di-electron within the fiducial acceptance as a function of average pair mass, $\langle M_{ee} \rangle$,for 60-80% centrality class in Au+Au collisions at $\sqrt{s_{\rm NN}}$= 200 GeV.

collisions at RHIC was found to be suppressed compared to the production in proton+proton collisions. The suppression of charmonium states is due to a screening of the $c\bar{c}$ potential by the medium color charges. In addition, the J/ψ production can be affected by recombination of charm quarks in a later stage of the collision evolution. The regeneration mechanism is expected to contribute mostly at the low J/ψ transverse momentum range.

In particular, STAR proposes to utilize the Run-23/25 RHIC heavy-ion runs to measure: (i) low transverse momentum J/ψ elliptic flow (v_2) in order to study in more details the recombination mechanism (ii) J/ψ directed flow (v_1) that will allow us to study the initial tilt of the bulk medium (iii) suppression of the loosely bounded ψ(2S) state to explore the temperature profile of the medium.

An important observable for studying the properties of the deconfined medium is the second order flow harmonic of the Fourier expansion of the azimuthal distribution of the produced hadrons, the elliptic flow coefficient v_2. Similarly as in the case of light hadrons, a positive v_2 of D-mesons and electrons from heavy-flavor hadron decays was observed at RHIC energies of 54.4 and 200 GeV. Which suggests that the charm quarks may (partially) thermalize and participate in the bulk medium collective evolution. On the other hand, the v_2 of heavier J/ψ reported by STAR based on the 2010 Au+Au 200 GeV data sample was found to be consistent with zero, albeit within large statistical uncertainties and systematic uncertainties due to non-flow effects. The precision of the measurement was also not enough to distinguish between theoretical model calculations that assume only primordial J/ψ production and the ones that include additional J/ψ production via the recombination. This calls for a larger sample of heavy-ion data at 200 GeV, as will be provided by RHIC in 2023 and 2025, in order to observe a possible non-zero J/ψ v_2 at RHIC energies and put more constraints on the J/ψ production models especially regarding its regeneration. Particularly important for these studies will be the STAR potential to measure low transverse momentum J/ψ with a very good precision. This excellent low-$p_{\rm T}$ performance at STAR can be achieved thanks to its low material budget and great particle identification capabilities.

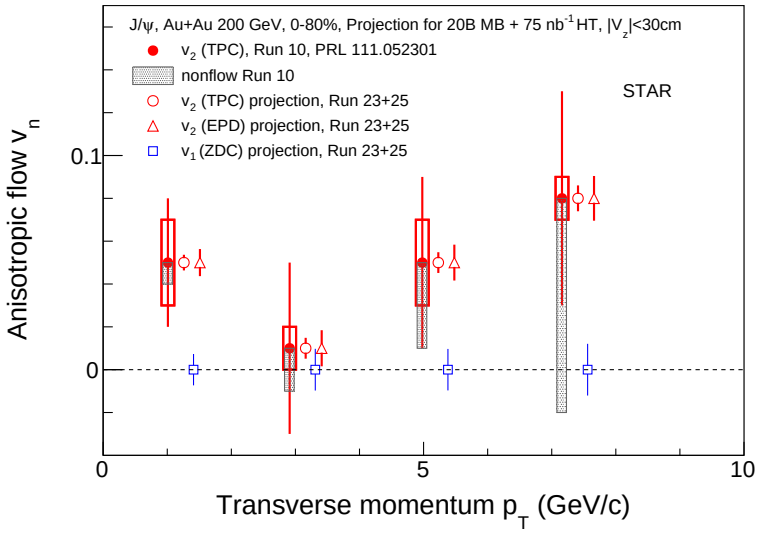

Figure 58: Projections for the J/ψ ($J/\psi \rightarrow e^+e^-$) directed ($v_1$) and elliptic ($v_2$) flow vs J/$\psi$ $p_{\rm T}$ in 0-80% Au+Au collisions at 200 GeV, assuming 20B MB events and HT triggered events corresponding to an integrated luminosity of 75 nb^{-1} with $|{\rm V_Z}| < 30$ cm.

Moreover, the second order Event Plane (EP) can be reconstructed using the new Event Plane Detectors (EPD) installed before the 2018 run. It is expected that using the EPD, that are forward detectors, will significantly decrease the contribution from the non-flow effects and consequently the measurement systematic uncertainties. Also, an inverse of the EP resolution enters directly the J/ψ v_2 uncertainty calculation. Thanks to EPD, the resolution of the EP reconstruction at forward rapidity for the J/ψ v_2 measurement at STAR will improve. Figure 58 presents statistical projections for the J/ψ v_2 measurement in 0-80% central Au+Au collisions assuming 20B MB events and HT triggered events corresponding to an integrated luminosity of 75 nb^{-1}. Both cases of the second order EP reconstruction, using forward EPD and mid-rapidity TPC detectors, are considered and shown. However, measurements for which the TPC is utilized for the EP reconstruction suffer from a substantial non-flow contribution which would be greatly reduced by reconstructing the second order Event Plane with the EPD. A clear significant improvement in the precision of the J/ψ v_2 can be seen across the whole experimentally accessible J/ψ $p_{\rm T}$ coverage of the previous measurement. In addition, the new larger dataset would allow to extend the measured $p_{\rm T}$range beyond 10 GeV/c.

Studies of the directed flow v_1 as a function of rapidity provide crucial information to understand the initial tilt of the medium produced in heavy-ion collision. The heavy quarks are produced in the early stage of a heavy-ion collision and thus are of a particular interest for the medium initial asymmetry studies. STAR recently reported the first measurement of D-meson v_1 in Au+Au collisions at 200 GeV where the magnitude of the heavy-flavor meson v_1 is about 25 times larger than the v_1 for charged kaons. With the 2023-2025 data, STAR would have a unique opportunity to also study the v_1 of a bound $c\bar{c}$ state, the J/ψ mesons,

for which even larger directed flow can be expected [219]. In addition to the STAR excellent capability to reconstruct low-p_{T} J/ψ, as discussed above, the iTPC detector completed in 2018 will improve the momentum resolution and extend the STAR pseudorapidity coverage around the mid-rapidity. This will provide a better precision for the slope extraction of the v_1 vs y measurement, that quantifies the strength of directed flow. The expected precision of a J/ψ v_1 measurement vs p_{T} at STAR in 2023-2025, assuming 20B MB events and HT triggered events corresponding to an integrated luminosity of 75 nb^{-1}, in 0-80% central Au+Au collisions at 200 GeV is shown in Fig. 58. Together with the J/ψ v_2 measurements, v_1 would provide a more complete picture of the J/ψ production mechanism as well as the medium properties in heavy-ion collisions at RHIC.

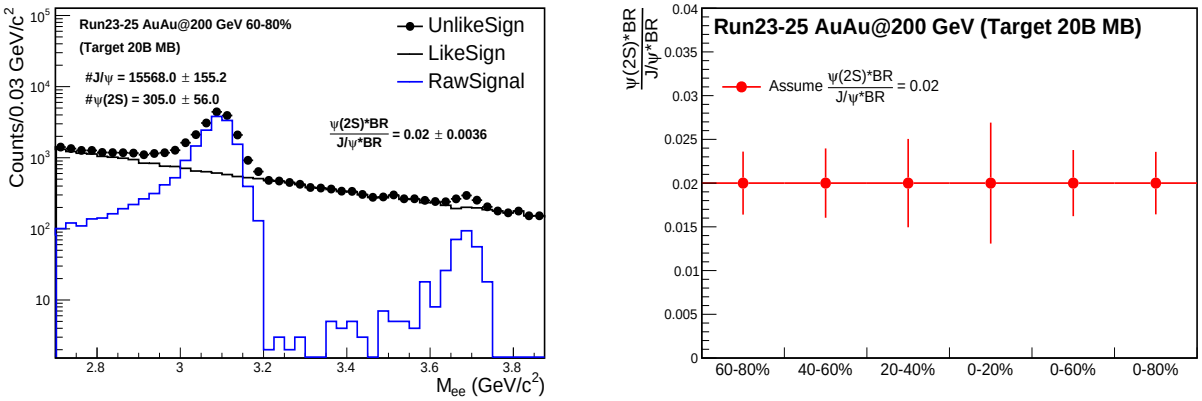

Figure 59: Projections for the J/ψ and ψ(2S) signals in 60-80% Au+Au collisions at 200 GeV and the yield ratio in various centrality bins. The improvement of momentum and dE/dx resolution thanks to the STAR iTPC upgrade have not been taken into account.

ψ(2S) is the most loosely bounded quarkonium state accessible in the heavy-ion collision experiments. Its dissociation temperature is predicted to be around or below the critical temperature and is much less than that of J/ψ and Υ states. It is more likely to be dissociated in the early stage and in the core of the fireball and the ψ(2S) survived may have significant contribution from the regeneration at later stage in the evolution of the fireball. The relative suppression of ψ(2S) and J/ψ is sensitive to the the temperature profile of the fireball produced in heavy-ion collisions and its space-time evolution. It is also argued that the charmonium formation process from a $c\bar{c}$ pair may be affected by the QGP or the initial strong external magnetic field, altering the relative yields among different charmonium states [220, 221]. The measurement of ψ(2S) is much more difficult than that of J/ψ due to a much smaller production cross-section and dilepton decay branching ratio, resulting in a very low signal-to-background ratio. The ALICE Collaboration successfully measured the relative suppression of ψ(2S) and J/ψ in Pb+Pb collisions at forward rapidity [222], and the ATLAS and CMS Collaboration published the relative suppression in Pb+Pb collisions at mid-rapidity and high p_T [223, 224]. The attempt of measuring ψ(2S) suppression in heavy-ion collisions at RHIC has no success as to date. The low material budget and excellent

particle identification capability of the STAR detector together with the large data sample in 2023 and 2025 will provide a unique opportunity to measure the suppression of ψ(2S) at low p_T and mid-rapidity in heavy-ion collisions. Figure 59 shows the projections of ψ(2S) signal and the yield ratio of ψ(2S) and J/ψ in Au+Au collisions assuming 20B MB events. The improvement of momentum and dE/dx resolution thanks to the STAR iTPC upgrade will further enhance the signal-to-background ratio and the significance of ψ(2S) signal.

2.4.5 Jet Probes

Precise jet quenching measurements with reconstructed jets over a broad kinematic range at RHIC are essential to meet the goal of the NSAC 2015 Long Range Plan, to "probe the inner workings of the QGP" [196]. For example, the dependence of jet energy loss on the jet p_{T} and the resolution or angular scale tagged by jet substructure observables are key tools to discriminate jet quenching mechanisms [225–228]. In addition, the measurement of jet acoplanarity as a probe of in-medium jet scattering is most sensitive at low jet p_{T} to a given momentum transfer and to medium-induced radiative effects [229], and is least affected by background due to vacuum Sudakov radiation [230].

The highest-statistics STAR Au+Au collision datasets currently available were recorded in 2014 and 2016, with the integrated luminosity sampled by STAR BEMC triggers shown in Table 10. Preliminary jet analyses using the 2014 dataset are discussed in section 1.1.1 and are moving towards publication. STAR will continue to exploit these rich datasets to carry out high-precision measurements with fully reconstructed jets over the full RHIC phase space.

The 2023 and 2025 runs will generate another significant increase in sampled integrated luminosity, enabling a third generation of STAR heavy-ion jet measurements that are yet more differential and precise. STAR's open geometry near the beam pipe allows it to utilize a wide range in the vertex position along the beam direction (z_{vertex}) for jet analyses, thereby utilizing the RHIC luminosity efficiently. Optimization of the z_{vertex} range used in an analysis entails a balance between statistical precision and complexity of corrections, with the latter influencing the systematic uncertainty of the measurement. Recent STAR jet measurements in Au+Au collisions have employ two different z-vertex cuts: the inclusive charged-particle jet analysis [7] utilizes $|z_{\mathrm{vertex}}| < 30$ cm, whereas the γ_{dir}+jet analysis [10] utilizes $|z_{\mathrm{vertex}}| < 70$ cm. With the success of the γ_{dir} +jet analysis in analyzing this broad z_{vertex} range with good systematic precision, we will re-examine this cut for future jet measurements, including the inclusive jet analysis. In section 2.4 we present the sampled integrated luminosity in 2023 and 2025 for both the 30 cm and 70 cm z_{vertex} cuts. The following physics performance projections are based on the 70 cm cut, using the cumulative sampled integrated luminosity for Runs 2014, 2016, 2023 and 2025 together. For $|z_{\mathrm{vertex}}| < 70$ cm, this total is 110 nb^{-1}, which is a factor 11 increase in trigger statistics relative to the current analyses based on Run 14 data.

To quantify the effect of this marked increase in integrated luminosity, we utilize two mature jet measurements currently in progress and discuss their expected improvement with enhanced integrated luminosity. These analyses are the semi-inclusive distribution

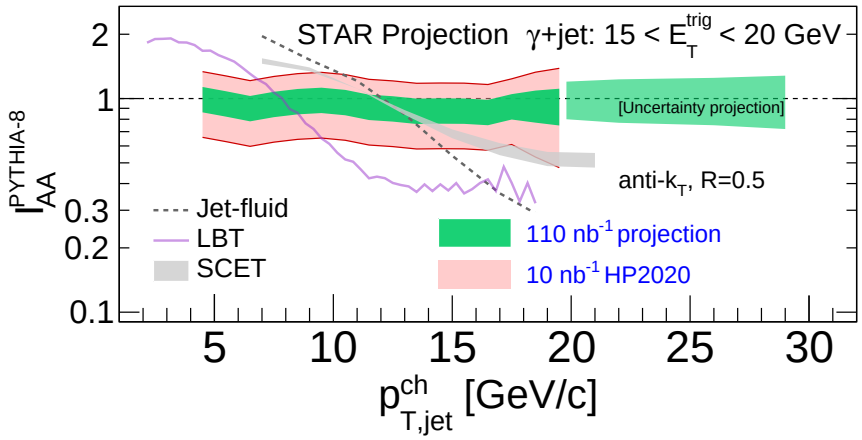

Figure 60: Ratio of semi-inclusive distributions of charged-particle jets (anti-k_{T}, $R = 0.5$) recoiling from a direct-photon trigger with $15 < E_{\mathrm{T}} < 20$ GeV for central Au+Au collisions at $\sqrt{s_{\mathrm{NN}}} = 200$ GeV measured by STAR (numerator) and p+p collisions simulated by PYTHIA (denominator). The pink band shows the cumulative uncertainty for the current analysis based on 10 nb^{-1} [10], while the green band shows the projected uncertainty for 110 nb^{-1}. Theory calculations are discussed in [10].

of charged-particle jets recoiling from a high-E_{T} direct-photon trigger ($\gamma_{\mathrm{dir}} + \mathrm{jet}$); and the differential measurement of energy loss for jet populations selected by varying a substructure metric. Since these analyses are mature, their analysis methodologies and correction schemes are optimized, so that their projections based on increased statistics are meaningful. We do not imply that these will be the only flagship measurements that STAR will make with the '23/'25 datasets; in addition we will focus for instance on fully reconstructed jets and utilize additional substructure observables, including those not yet developed. However, these analyses are most mature at present, and therefore provide the most accurate projections of gain in precision.

Semi-inclusive $\gamma_{\mathrm{dir}} + \mathrm{jet}$ measurement

Figure 60 shows I_{AA} for fully-corrected semi-inclusive distributions of charged-particle jets (anti-k_{T}, $R = 0.5$) recoiling from a direct-photon trigger with $15 < E_{\mathrm{T}} < 20$ GeV in central Au+Au collisions at $\sqrt{s_{\mathrm{NN}}} = 200$ GeV, for the current analysis based on 10 nb^{-1} [10] within $|z_{\mathrm{vertex}}| < 70$ cm, and projected for 110 nb^{-1}. Significant reduction in the uncertainty band is seen to result from the increase in integrated luminosity, together with significant increase in kinematic reach.

Note that the projection to 110 nb^{-1} only takes into account the increase in statistical precision, and assumes that the systematic uncertainty remains the same. The reduction in width of the uncertainty band is therefore less than the factor $1/\sqrt{11}$ expected from statistical considerations alone, indicating the magnitude of the systematic component. Experience shows that systematic uncertainty can also be improved by an increase in statistical precision, since additional and more differential systematic studies can be carried out. However, it is

not possible to project that improvement with confidence at present; thus Fig. 60 should therefore be regarded as a conservative estimate of the improvement in precision of this measurement channel with the projected integrated luminosity increase.

Broadening of the back-to-back di-jet angular distribution due to jet scattering from constituents of the QGP (medium-induced acoplanarity) was proposed over three decades ago as a diagnostic probe of the QGP [231, 232]. While the physical picture of this process is intuitive and compelling, such measurements are extremely challenging, because of both the large jet backgrounds in heavy ion collisions, and the large contribution of vacuum QCD processes (Sudakov radiation) to the di-jet angular distribution [230]. In addition, minimization of these two effects nominally drives the experimentalist in opposite directions: minimization of background effects prefers larger $p_{\mathrm{T,jet}}$, whereas minimization of Sudakov broadening and higher sensitivity to medium-induced momentum transfer prefers lower $p_{\mathrm{T,jet}}$ [230]. These contradictory requirements were resolved only with the development of absolutely normalized semi-inclusive jet measurements in heavy-ion collisions, with statistically-based background corrections that enable measurements at low $p_{\mathrm{T,jet}}$ and large R [1, 233].

The first generation searches for medium-induced acoplanarity using this approach did not exhibit a significant signal above background [1, 233], though with limited statistical precision. Higher-precision measurements of medium-induced acoplanarity over a broad $p_{\mathrm{T,jet}}$ range – including low $p_{\mathrm{T,jet}}$ – are clearly of great interest at both RHIC and the LHC. Such measurements may provide a direct probe of $\hat{q}$ [230], or evidence of large-angle jet scattering off of quasi-particles in the QGP [234]. Consideration of higher-order processes suggests that the contribution of radiative corrections to this distribution may be negative [229], thereby narrowing rather than broadening the recoil jet azimuthal distribution; a recent preliminary measurement by the ALICE Collaboration at the LHC may indeed have observed such an effect [235]. Complementary measurements of medium-induced acoplanarity over wide phase space by STAR at RHIC and ALICE at the LHC, using similar instrumentation and similar analysis techniques, promise to provide strong constraints on theoretical descriptions of this fundamental process, providing new insight into the inner workings of the QGP [196].

Figure 61 shows the semi-inclusive distribution of the azimuthal separation between a direct-photon trigger with $15 < E_{\mathrm{T}} < 20$ GeV and a charged-particle jet (anti-k_{T}, $R = 0.5$) with $10 < p_{\mathrm{T,jet}}^{\mathrm{ch}} < 15$ GeV/c, in central Au+Au collisions at $\sqrt{s_{\mathrm{NN}}} = 200$ GeV with only statistical error bars, based on the analysis described in [10]. Azimuthal smearing of this observable due to uncorrelated background is small, and such acoplanarity measurements are therefore strongly statistics-dominated [1, 233]. The grey points are from the current analysis based on 10 nb^{-1} [10], whereas the red points correspond to 110 nb^{-1}. A marked increase in measurement precision is projected, with corresponding qualitative increase in physics impact. Similar improvements in precision for this observable are expected at the LHC in Run 3, due to detector upgrades and enhanced machine luminosity [168].

Jet measurement with a varying substructure metric

An important facet of the third generation of STAR jet measurements is a systematic exploration of parton energy loss based on controlled variation of the jet shower topology.

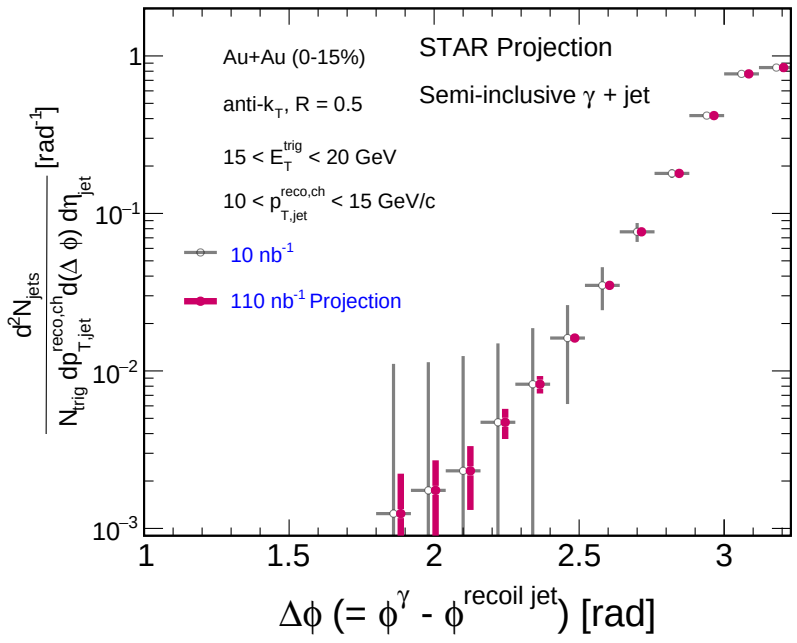

Figure 61: Semi-inclusive azimuthal distribution of charged jets (anti−k_{T}, R=0.5) with $10 < p_{\mathrm{T,jet}}^{\mathrm{ch}} < 15$ GeV/c recoiling from a direct photon trigger with $15 < E_{\mathrm{T}}^{\mathrm{trig}} < 20$ GeV, in central Au+Au collisions at $\sqrt{s_{\mathrm{NN}}} = 200$ GeV. Grey points: current analysis with 10 nb^{-1} [10]; red points: projection for 110 nb^{-1}. Error bars are statistical only.

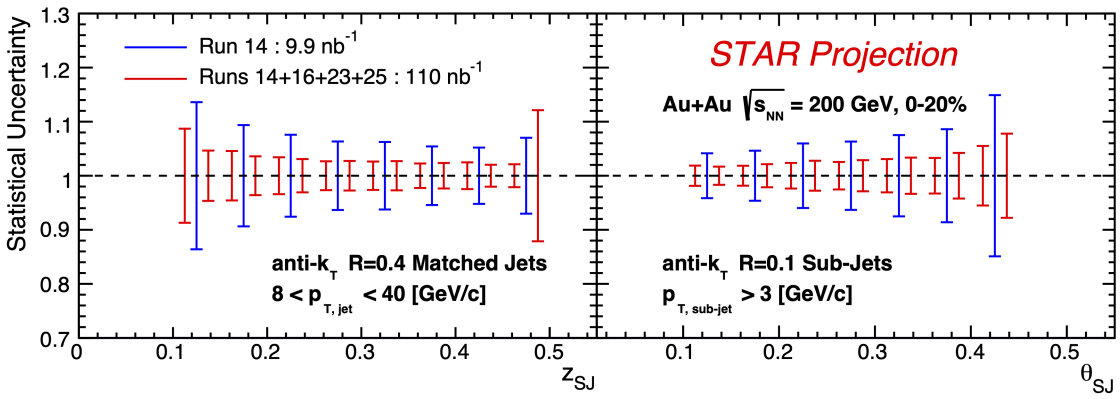

Figure 62: Two-panel figure showing statistical uncertainty for the two-subjet observables in 0-20% central Au+Au collisions for 10 nb^{-1} in blue and projection for 110 nb^{-1} in red.

Jet evolution produces a unique pattern of radiation in both angle and momentum, and jet substructure observables are a broad class of measurements of combinations of the jet constituents' angle and/or momentum via algorithms or correlations. As the jet undergoes interactions with the medium, jet substructure modification for a given jet energy (e.g. comparing the heavy-ion results to those in p+p collisions) has been used as a way to access the microscopic properties of the medium. By selecting on jets based on their substructure, we can study how a particular class of jets interacts with the medium to determine the effects of e.g. color coherence, dead cone, etc. on parton-medium interactions. In other words, the STAR jet program for Runs 23–25 will focus on jet substructure as a jet-tagger.

Recent theory calculations have shown significant differences between energy loss signatures for jets that are perceived by the medium as a single or multiple color charges [227]. Algorithms such as SoftDrop and sub-jets [236, 237] provide observables that correspond to the splitting within jets via momentum fractions and an inherent angular scale which then serve as a proxy for the resolution scale in the medium. This is often referred to as coherent vs. de-coherent energy loss where the coherent length of the medium is related to its temperature and $\hat{q}$ [**?**]. By isolating population of jets based on their substructure, one can directly probe energy loss for varying resolution scales. The integrated luminosity from Runs '23/'25 datasets will not only provide a substantial increase in statistics in the current measurements of jet substructure, they also make the phase space available for rare processes such as wide angle emissions from high-p_{T} jets. This enables STAR to extend our current measurements of differential energy loss [2] to fine binning in the opening angles and momentum fractions, as shown in Fig. 62. The current resolution of $\delta\theta_{\mathrm{SJ}} = 0.1$ [2] is predominantly due to statistical limitations in our older dataset sample. The significant increase in integrated luminosity for Runs 23-25, coupled with excellent tracking resolution of the STAR TPC will reduce the opening angles resolution to 0.025 and have significant population of jets where we can further identify and select jet topologies in both z and θ and study energy loss in a three-dimensional fashion. By extending to high energy splittings within jets, at varied

opening angles, we can probe earlier formation times whereby vacuum-like emissions and medium induced radiations are expected to occur.

STAR is uniquely situated to perform high impact differential measurements of parton energy loss starting from the unbiased, semi-inclusive jet population, to a topologically special population of jets, selected via jet substructure observables.

Given the unique nature of jet-medium interactions at RHIC, with the jet and sub-jet scales sufficiently closer to the medium scale, the aforementioned measurements bolster the importance of the STAR jet program with the goal of extracting the microscopic properties of the QGP as outlined in the 2015 LRP.

3 Cold QCD Physics with $p^{\uparrow}p^{\uparrow}$ and $p^{\uparrow} + A$ Collisions at 510 and 200 GeV

The exploration of the fundamental structure of strongly interacting matter has always thrived on the complementarity of lepton scattering and purely hadronic probes. As the community eagerly anticipates the future Electron Ion Collider, an outstanding scientific opportunity remains to complete "must-do" measurements in p+p and p+A physics during the final years of RHIC. These measurements will be essential if we are fully to realize the scientific promise of the EIC, by providing a comprehensive set of measurements in hadronic collisions that, when combined with future data from the EIC, will establish the validity and limits of factorization and universality. The Run-22 and Run-24 program outlined here will, on the one hand, lay the groundwork for the EIC, both scientifically and in terms of refining the experimental requirements of the physics program at the EIC, and thus are the natural next steps on the path to the EIC. On the other hand, while much of the physics in this program is unique to proton-proton and proton-nucleus collisions and offers discovery potential on its own, when combined with data from the EIC it will provide a broad foundation to a deeper understanding of fundamental QCD.

The separation between the intrinsic properties of hadrons and interaction-dependent dynamics, formalized by the concept of factorization, is a cornerstone of QCD and largely responsible for the predictive power of the theory in many contexts. While this concept and the associated notion of universality of the quantities that describe hadron structure have been successfully tested for unpolarized and, to a lesser extent, longitudinally polarized parton densities, its experimental validation remains an unfinished task for much of what the EIC is designed to study – the three-dimensional structure of the proton and the physics of dense partonic systems in heavy nuclei. To establish the validity and limits of factorization and universality, it is essential to have data from *both* lepton-ion and proton-ion collisions, with experimental accuracy that makes quantitative comparisons meaningful.

Beginning in Run-22, STAR will be in a unique position to provide this essential p+p and $p + A$ data. A full suite of forward detectors will be installed, providing excellent charged-particle tracking at high pseudorapidity ($2.5 < \eta < 4$) for the first time, coupled with both electromagnetic and hadronic calorimetry. This will enable STAR to explore the interesting regimes of high-x (largely valence quark) and low-x (primarily gluon) partonic physics with unparalleled precision. In addition, mid-rapidity detector upgrades motivated primarily by the BES-II program – the iTPC, eTOF, and EPD systems – will substantially extend STAR's already excellent kinematic reach and particle identification capabilities beyond those that existed during previous p+p and $p + A$ runs.

For the case of p+p spin physics, it's important to recognize the complementary roles that will be played by Run-22 at 510 GeV and Run-24 at 200 GeV. The combination of 510 GeV p+p collisions and the STAR Forward Upgrade will provide access to forward jet physics at perturbative scales, thereby enabling measurements at the highest and lowest x values. In parallel, mid-rapidity measurements at 510 and, especially, 200 GeV will interpolate between the high and low x values, with significant overlaps to probe evolution effects

and provide cross-checks. Together, the two runs will allow STAR to measure fundamental proton properties, such as the Sivers and transversity distributions, over nearly the entire range $0.005 < x < 0.5$.

Run-24 will also provide outstanding opportunities to probe fundamental questions regarding QCD in cold nuclear matter. The STAR Forward Upgrade will enable an extensive suite of measurements probing the quark-gluon structure of heavy nuclei and the regime of low-x non-linear gluon dynamics, as predicted by saturation models. STAR will also explore how a nucleus, serving as a color filter, modifies the propagation, attenuation, and hadronization of colored quarks and gluons.

For these reasons, STAR requests at least 16 weeks of polarized p+p data-taking at $\sqrt{s} =$ 510 GeV in Run-22. All data taking will involve proton beams polarized transversely relative to their momentum direction in order to focus on those observables where factorization, univerality, and/or evolution remain open questions, with spins aligned either vertically or radially at the STAR IR (still to be determined through more detailed simulation studies). Based on the latest guidance from CAD, and mindful of 'lessons learned' in previous $p + p$ runs at full energy, we will ask for luminosity-leveling of the collision rate to maximize the efficiency of our main tracking detectors. Assuming we will have running conditions similar to those achieved in Run-17, we expect to sample at least 400 pb^{-1} for our rare / non-prescaled triggers.

STAR also requests at least 11 weeks of polarized $p + p$ data-taking at $\sqrt{s} = 200$ GeV and 11 weeks of polarized p+Au data-taking at $\sqrt{s_{NN}} = 200$ GeV during Run-24. Similar to Run-22, all of the running will involve transversely polarized protons, with the choice between vertical or radial polarization to be determined during the coming year. Based on recent (08-21-20) C-AD guidance, we expect to sample at least 235 pb^{-1} of p+p collisions and 1.3 pb^{-1} of p+Au collisions. These totals represent 4.5 times the luminosity that STAR sampled during transversely polarized $p + p$ collisions in Run-15, and 3 times the luminosity that STAR sampled during transversely polarized p+Au collisions in Run-15.

3.1 Run-22 Request for $p^{\uparrow}p^{\uparrow}$ Collisions at 510 GeV

3.1.1 Inclusive transverse spin asymmetries at forward rapidities

The experimental study of spin phenomena in nuclear and particle physics has a long history of producing important, and often surprising, results. Attempts to understand such data have pushed the field forward, forcing the development of both new theoretical frameworks and new experimental techniques. Recent and ongoing detector upgrades at STAR, at mid- and forward-rapidity, coupled with the versatility of RHIC, will allow us to gain new insights into long-standing puzzles, and to probe more deeply the complexities of emergent behavior in QCD.

Results from PHENIX and STAR have shown that large transverse single-spin asymmetries (TSSA) for inclusive hadron production, first seen in p+p collisions at fixed-target energies and modest p_T, extend to the highest RHIC center-of-mass energies, $\sqrt{s} = 500$ GeV, and surprisingly large p_T. Figure 63 summarizes the world data for the inclusive pion asym-

metries A_N as a function of Feynman-x. The asymmetries are seen to be nearly independent of $\sqrt{s}$ over the very wide range of roughly 5 to 500 GeV.

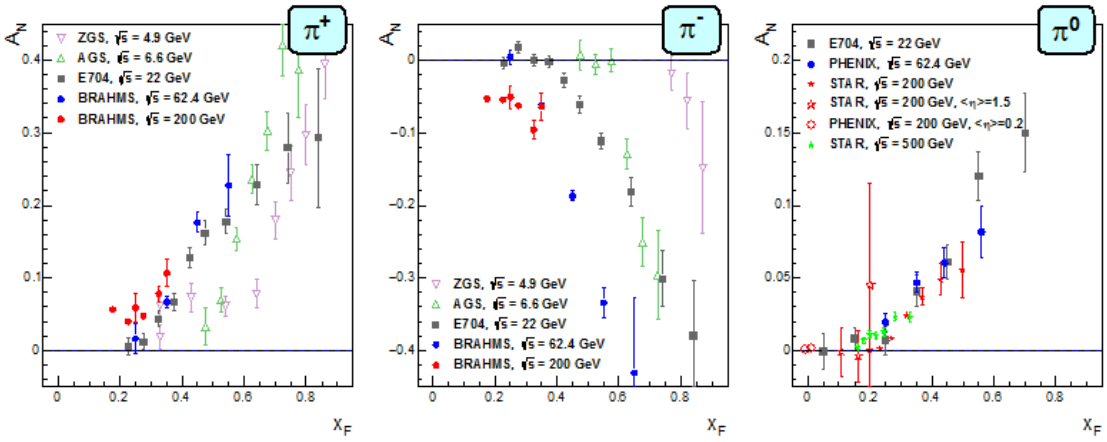

Figure 63: Transverse single-spin asymmetry A_N measurements for charged and neutral pions at different center-of-mass energies as a function of Feynman-x.

To understand the observed TSSAs, one needs to go beyond the conventional leading-twist (twist-2) collinear parton picture for the hard-scattering processes. Two theoretical formalisms have been developed to try to explain these sizable asymmetries in the QCD framework: transverse-momentum-dependent (TMD) parton distribution and fragmentation functions, such as the Sivers and Collins functions; and transverse-momentum-integrated (collinear) quark-gluon-quark correlations, which are twist-3 distributions in the initial state proton or in the fragmentation process. For many of the experimentally accessible spin asymmetries, several of these functions can contribute, and need to be disentangled in order to understand the experimental data in detail, in particular the observed p_T dependence. These functions manifest their spin dependence either in the initial state–for example, the Sivers distribution and its twist-3 analog, the Efremov-Teryaev-Qui-Sterman (ETQS) function [238]–or in the final state via the fragmentation of polarized quarks, such as in the Collins function and related twist three function $\hat{H}_{FU}(z, z_z)$.

Incorporating the fragmentation term within the collinear twist-3 approach demonstrated the ability of this formalism to describe the large values of A_N for π^0 production observed at RHIC [239]. In this work, the relevant (non-pole) 3-parton collinear fragmentation function $\hat{H}_{FU}(z, z_z)$ was fit to the RHIC data. The so-called soft-gluon pole term, involving the ETQS function $T_{q,F}(x_1, x_2)$, was also included by fixing $T_{q,F}$ through its well-known relation to the TMD Sivers function $f_{1T}^{\perp}$. The authors obtained a very good description of the data due to the inclusion of the non-pole fragmentation function and based on this work they were able to make predictions for π^+ and π^- production asymmetries A_N at the forward rapidities covered by the STAR upgrades, $2.5 < \eta < 4$. The results are shown in Fig. 64 for $\sqrt{s}$= 200 and 500 GeV for two rapidity ranges, $2 < \eta < 3$ and $3 < \eta < 4$.

In Run-22, with the full suite of forward tracking detectors and calorimetry installed, STAR will for the first time be able to map out inclusive charged-hadron asymmetries up to

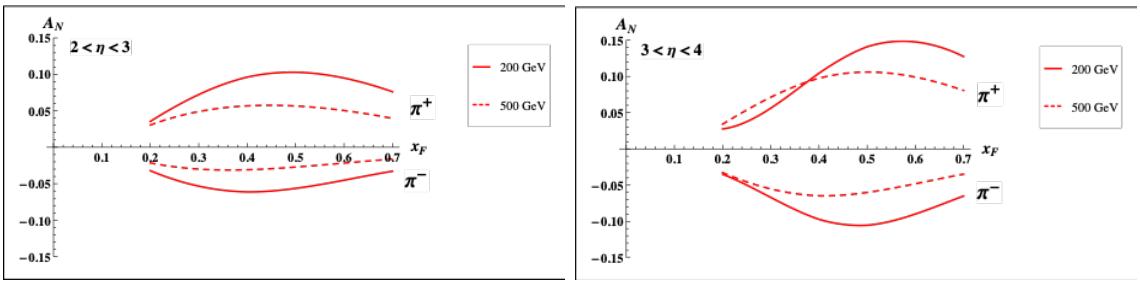

Figure 64: Predictions for A_N for π^+ and π^- production over the ranges $2 < \eta < 3$ (left) and $3 < \eta < 4$ (right) at $\sqrt{s} = 200$ GeV (solid lines) and 500 GeV (dashed lines). The $\sqrt{s} = 200$ GeV BRAHMS A_N data for charged pions cover up to x_F of 0.3.

the highest energies achievable at RHIC and at these forward rapidities. It would be very interesting to confirm that these asymmetries are indeed largely independent of center-of-mass energy. The measurements of A_N for charged hadrons, together with analogous data (from Run-22 as well as previous STAR runs) on A_N for direct photons and neutral pions, should provide the best data set in the world to constrain the evolution and flavor dependence of the twist-3 ETQS distributions and to determine if the 3-parton collinear fragmentation function H_{FU} is the main driver of the large forward inclusive asymmetries.

3.1.2 Sivers and Efremov-Teryaev-Qui-Sterman Function

There is great theoretical interest in testing the relation between the ETQS correlation functions and the Sivers function. As discussed above, both the Sivers and the ETQS functions encapsulate partonic spin correlations within the proton, but they are formally defined in different frameworks. While the Sivers function is a TMD quantity that depends explicitly on spin-dependent transverse partonic motion k_T, the ETQS function is a twist-3 collinear distribution, in which SSAs are generated through soft collinear gluon radiation

Measurements of forward jet production from the ANDY collaboration [240] indicated rather small asymmetries. This was argued to be consistent with the idea that the twist-3 parton correlation functions for up and down valence quarks should cancel, because their behavior reflects the Sivers functions extracted from fits to the SIDIS data that demonstrate opposite sign, but equal magnitude, up and down quark Sivers functions. Preliminary STAR results on charge-tagged dijets at mid-rapidity (see Fig. 29) support this interpretation, with the caveat that the measured observable (a spin-dependent $\langle k_T \rangle$) is defined in the TMD, and not the twist-3, framework.

To better test quantitatively the relation between the two regimes, one can measure spin asymmetries for jets which are *intentionally* biased towards up or down quark jets via detection of a high-z charged hadron within the jet. Higher-twist calculations of jet asymmetries based on the Sivers function predict sizeable effects for these flavor-enhanced jets. With the suite of new forward detectors installed at STAR, full jet reconstruction, along with identification of a high-z hadron of known charge sign, will be possible at high pseudorapidity. Using realistic jet smearing in a forward calorimeter and tracking system, and requiring a

charged hadron with $z > 0.5$, the asymmetries can be separated and compared to the predictions for the Sivers function based on current SIDIS data. The expected uncertainties, plotted at the predicted values, can be seen in Figure 65. Dilutions by underlying event and beam remnants were taken into account. The simulations have assumed only an integrated luminosity of 100 pb^{-1} at $\sqrt{s} = 200$ GeV, which is significantly lower than what is currently expected for a 200 GeV polarized p+p run in 2024. The same measurement is possible at 500 GeV.

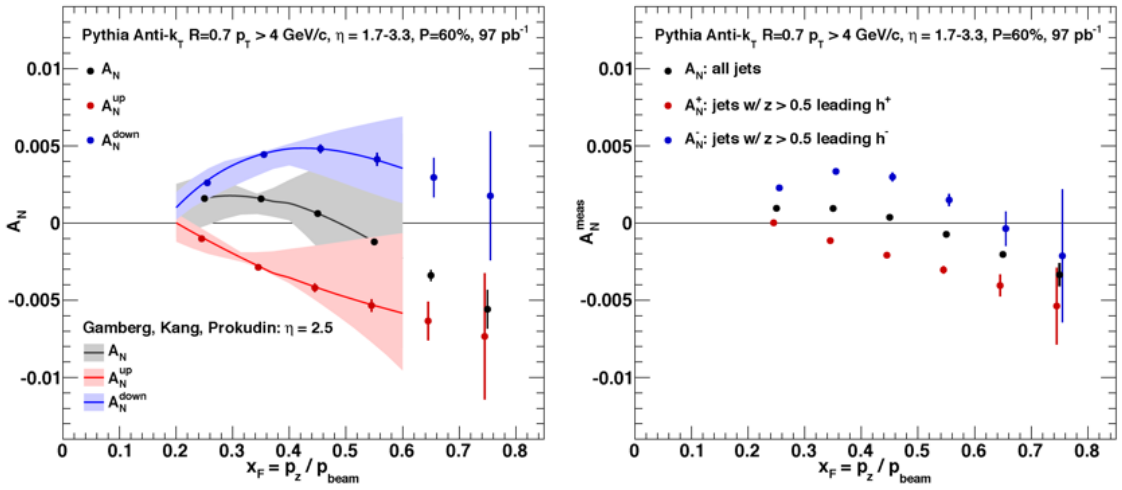

Figure 65: Left: up quark (red points), down quark (blue points) and all jet (black points) single spin asymmetries as a function of x_F as calculated by the ETQS based on the SIDIS Sivers functions. Right: Expected experimental sensitivities for jet asymmetries tagging in addition a positive hadron with z above 0.5 (red points), a negative hadron with z above 0.5 (blue points) or all jets (black) as a function of x_F. Note: these figures are for 200 GeV center-of-mass energy proton collisions – the 500 GeV results are expected to be qualitatively similar.

In a TMD framework, the Sivers effect manifests itself as a correlation (a triple product) between the transverse momentum of a parton ($\overrightarrow{k}_T$) with momentum fraction x, and the transverse spin ($\overrightarrow{S}$) of a polarized proton moving in the longitudinal ($\overrightarrow{p}$) direction. Thus, for transversely polarized protons, the Sivers effect probes whether the k_T of the constituent quarks is preferentially oriented in a direction perpendicular to both the proton momentum and its spin. Momentum conservation then implies that the two jets in the final state will not emerge back-to-back on average, but instead will 'tilt' in the direction of the summed k_T of the initial state partons. Moreover, the (average) tilt of interest will reverse direction under a 'flip' of the proton spin; a spin-dependent $\langle k_T \rangle$ can then be extracted by associating the azimuthal opening angle of the jet pair with this tilt.

STAR carried out an earlier measurement of this transverse single-spin asymmetry using a dijet dataset with ∼1 pb^{-1} of integrated luminosity [112], and found it to be consistent with zero within 2σ. An ongoing, and much improved analysis, has been described in the Highlights section of this document, Sect. 1.3. Perhaps most significantly, the jets were sorted according to their net charge Q, calculated by summing the signed momentum of all

particle tracks with $p > 0.8$ GeV, to minimize underlying event contributions, yielding jet samples with enhanced contributions from u quarks (positive Q) and d quarks (negative Q), with a large set near $Q = 0$ dominated by gluons. Simple kinematics allow for conversion from the spin-dependent 'tilt' of the dijet pair to a value of k_T on an event-by-event basis; these are then sorted by the Q of the jet and binned by the summed pseudorapidities of the outgoing jets, $\eta^{\text{total}} \equiv \eta_3 + \eta_4$. Because the contributions of different partons (u, d, all else) to $\langle k_T \rangle$ vary with both Q and also η^{total}, in a way that can be estimated robustly using simulation, the data can be inverted to yield values of $\langle k_T \rangle$ for the individual partons, though with coarser binning in η^{total}.

With the new forward detectors in place, along with the enhanced reach in η afforded by the iTPC, this technique can be expanded in Run-22 to cover pseudorapidities at STAR from roughly -1 to +4, though with a gap at $1.5 < \eta < 2.5$. Despite this gap, values of $\langle k_T \rangle$ can be extracted for u and d quarks for η^{total} ranging from ~ -1.5 to as high as 7 with reasonable statistics. This latter regime will probe $2 \rightarrow 2$ hard scattering events in which $x_1 \gg x_2$, *i.e.*, a sample enriched in valence quarks interacting with low-x gluons. Such measurements, exploiting the full kinematic reach of STAR, will not only allow precise determinations of the average transverse partonic motion, $\langle k_T \rangle$, exhibited by individual partonic species in the initial state, but will provide important information on the x dependence of the proton Sivers functions.

Collisions at $\sqrt{s} = 510$ GeV will also allow STAR to continue our successful program to study the evolution and sign change of the Sivers function. By focusing on interactions in which the final state involves only weakly interacting particles, and hence the transverse partonic motion (in a TMD framework) or the collinear gluon radiation (in twist-3) must be in the initial state, one can test for the predicted sign change in A_N relative to interactions in which these terms must appear in the final state, such as SIDIS measurements. The improved tracking capabilities provided by the iTPC upgrade will allow us to push our mid-rapidity $W^{\pm}$ and Z^0 measurements to larger rapidity $y_{W/Z}$, a regime where the asymmetries are expected to increase in magnitude and the anti-quark Sivers' functions remain largely unconstrained. Figure 66 demonstrates the expected precision of asymmetry measurements after data from the 2017 run has been fully analyzed. In addition to the noted extension of our kinematic reach, an additional 16 or more weeks of beam time at $\sqrt{s} = 510$ GeV in Run-22 would increase our data set by more than a factor of 2. This experimental accuracy would significantly enhance the quantitative reach of testing the limits of factorization and universality in lepton-proton and proton-proton collisions.

3.1.3 Transversity, Collins Function and Interference Fragmentation Function

A complete picture of nucleon spin structure at leading twist must include contributions from the unpolarized and helicity distributions, as well as those involving transverse polarization, such as the transversity distribution [243–245]. The transversity distribution can be interpreted as the net transverse polarization of quarks within a transversely polarized proton. The difference between the helicity and transversity distributions for quarks and antiquarks provides a direct, x-dependent connection to nonzero orbital angular momen-

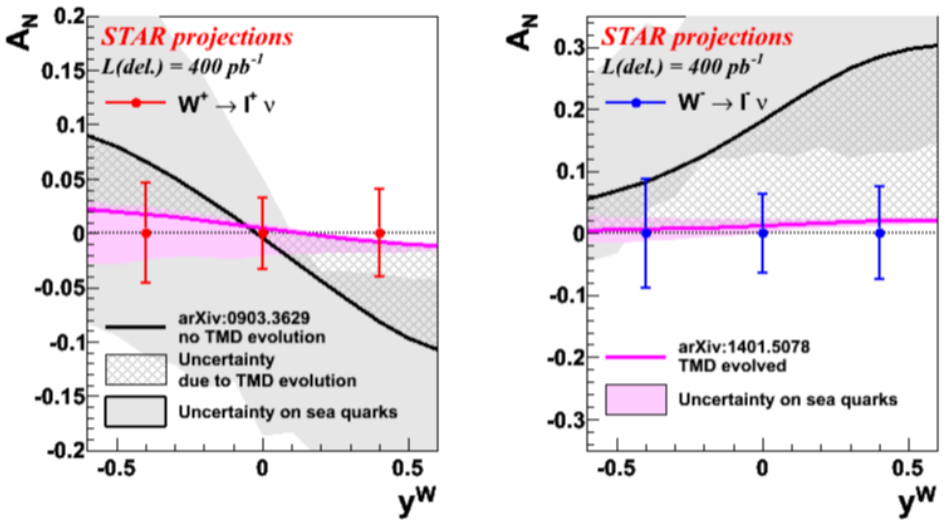

Figure 66: Projected uncertainties for transverse single-spin asymmetries of $W^{\pm}$ and Z^0 bosons as functions of rapidity for a delivered integrated luminosity of 400 pb^{-1} and an average beam polarization of 55%. The solid light gray and pink bands represent the uncertainties on the KQ [241] and EIKV [242] known sea-quark Sivers functions. The crosshatched dark grey region indicates the current uncertainty in the theoretical predictions due to TMD evolution.

tum components in the wave function of the proton [246]. Recently, the first lattice QCD calculation of the transversity distribution has been performed [247]. In addition, the measurement of transversity has received substantial interest as a means to access the so-called 'tensor charge' of the nucleon, defined as the integral over the valence quark transversity: $\delta q^a = \int_0^1 [\delta q^a(x) - \delta \overline{q}^a(x)]\, dx$ [244, 248]. Measuring the tensor charge is very important for several reasons. First, it is an essential and fundamental quantity to our understanding of the spin structure of the nucleon. Also, the tensor charge can be calculated on the lattice with comparatively high precision, due to the valence nature of transversity, and hence is one of the few quantities that allow us to compare experimental results on the spin structure of the nucleon directly to *ab initio* QCD calculations. Finally, the tensor charge describes the sensitivity of observables in low-energy hadronic reactions to beyond the standard model physics processes with tensor couplings to hadrons. Examples are experiments with ultracold neutrons and nuclei.

Transversity is difficult to access due to its chiral-odd nature, requiring the coupling of this distribution to another chiral-odd distribution. Semi-inclusive deep-inelastic scattering (SIDIS) experiments have successfully probed transversity through two channels: asymmetric distributions of single pions, convoluting the TMD transversity distribution with the TMD Collins fragmentation function, and azimuthally asymmetric distributions of dihadrons, coupling transversity to the so-called "interference fragmentation function" (IFF) in the framework of collinear factorization. Yet in spite of a wealth of lepton-scattering

data, the kinematic reach of existing SIDIS experiments limits the precision with which the proton's transversity can be extracted, as the range of Bjorken-x values that can be accessed does not extend above $x \sim 0.3$

In hadronic collisions, the k_T integrated quark transversity distribution may be accessed via two channels. The first is the single spin asymmetry of the azimuthal distribution of hadrons in high energy jets [108]. In the jet+hadron channel, the collinear transversity distribution couples to the TMD Collins function [108, 109]. This makes p+p collisions a more direct probe of the Collins fragmentation function than Collins asymmetries in SIDIS [108], where a convolution with the TMD transversity distribution enters. This also makes the Collins asymmetry in p+p collisions an ideal tool to explore the fundamental QCD questions of TMD factorization, universality, and evolution. The second channel is the single spin asymmetry of pion pairs, where transversity couples to the collinear interference fragmentation function [249]. STAR mid-rapidity IFF data [250] have been included in the first extraction of transversity from SIDIS and proton-proton IFF asymmetries [251].

The universality of TMD PDFs and fragmentation functions in p+p collisions has been an open question. General arguments [252, 253] have shown that factorization can be violated in hadron-hadron collisions for TMD PDFs like the Sivers function, though very recent calculations indicate the violations might be quite small [254, 255]. In contrast, while there is no general proof that the Collins effect in p+p collisions is universal to all orders, explicit calculations [108, 109, 256, 257] have shown that diagrams like those that violate factorization of the Sivers function make no contribution to the Collins effect at the one- or two-gluon exchange level, thereby preserving its universality at least to that level.

Comparisons of the transversity distributions extracted from the Collins and IFF channels will allow STAR to study the size and nature of any factorization breaking effects for TMD observables in hadronic collisions. Likewise, comparisons with the transversity, Collins and IFF distributions extracted from SIDIS collisions will shed light on universality and constrain evolution effects. The measurement of evolution effects in TMD distributions is particularly important because, unlike the collinear case, TMD evolution contains a non-perturbative component that cannot be calculated directly. Measurements at $\sqrt{s}$ of 200 and 510 GeV will provide additional experimental constraints on evolution effects and provide insights into the size and nature of TMD observables at the future Electron-Ion Collider.

Extending measurements of di-hadron and Collins asymmetries to the forward direction during Run-22 will allow access to transversity in the region $x > 0.3$. This valence quark region is not currently probed by any experiments and is essential for the determination of the tensor charge, which receives 70% of its contributions from $0.1 < x < 1.0$. In addition, probing transversity in p+p collisions also provides better access to the d-quark transversity than is available in SIDIS, due to the fact that there is no charge weighting in the hard scattering QCD $2 \to 2$ process in p+p collisions. This is a fundamental advantage of p+p collisions, as any SIDIS measurement of the d-quark transversity has to be on a bound system, *e.g.* He-3, which ultimately requires nuclear corrections to extract distributions. The high scale we can reach in 500 GeV collisions at RHIC has allowed STAR [258] to demonstrate, for the first time, that previous SIDIS measurements at low scales are in fact

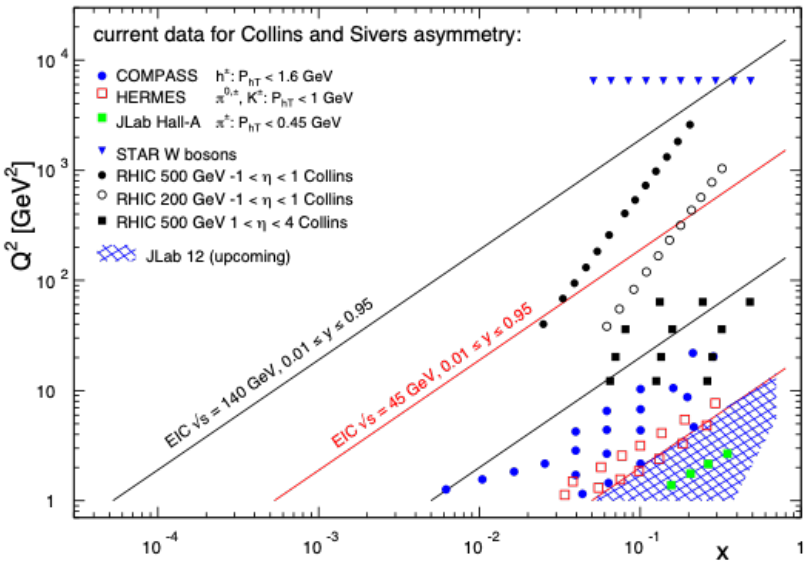

Figure 67: $x - Q^2$ coverage of RHIC measurements compared to existing Collins and Sivers effect measurements in SIDIS and the future coverage of the EIC.

accessing the nucleon at leading twist. Figure 67 shows the $x - Q^2$ coverage spanned by the RHIC measurements compared to the future EIC, JLab-12, and the current SIDIS world data.

Another fundamental advantage of p+p collisions is the ability to access gluons directly. While gluons cannot be transversly polarized in a transversely polarized spin 1/2 hadron, they can be linearly polarized. Similarly, there exists an equivalent of the Collins fragmentation function for the fragmentation of linearly polarized gluons into unpolarized hadrons [259]. The linear polarization of gluons is a largely unexplored phenomenon, but it has been a focus of recent theoretical work, in particular due to the relevance of linearly polarized gluons in unpolarized hadrons for the p_T spectrum of the Higgs boson measured at the LHC. Polarized proton collisions with $\sqrt{s} = 510$ GeV at RHIC, in particular for asymmetric parton scattering if jets are detected in the backward direction, are an ideal place to study the linearly polarized gluon distribution in polarized protons. (Note that the distributions of linearly polarized gluons inside an unpolarized and a polarized proton provide independent information). A first measurement of the "Collins-like" effect for linearly polarized gluons has been done by STAR with data from Run-11 [258], providing constraints on this function for the first time.

Figure 68 shows projected uncertainties for Collins asymmetries at 510 GeV with the Forward Upgrade during Run-22. As indicated on the figure, jets with $3 < \eta < 4$ and $3 < p_T < 9$ GeV/c will explore transversity in the important region $0.3 < x < 0.5$ that has not yet been probed in SIDIS. A realistic momentum smearing of final state hadrons as well as jets in this rapidity range was assumed and dilutions due to beam remnants (which become substantial at rapidities close to the beam) and underlying event contributions have been taken into account. As no dedicated particle identification at forward rapidities will be

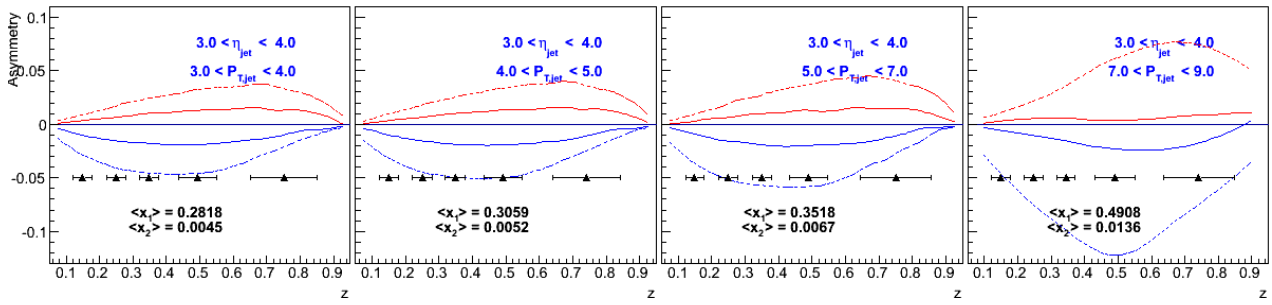

Figure 68: Expected h^- Collins asymmetry uncertainties at $3 < \eta < 4$ (black points) from a sampled luminosity of 268 pb^{-1} at $\sqrt{s} = 510$ GeV, compared to positive (red) and negative (blue) pion asymmetries based on the Torino extraction (full lines) and the Soffer bound (dashed lines) as a function of hadron z for bins in jet p_T. Most uncertainties are smaller than the height of the triangles.

available for these measurements, only charged hadrons were considered. This mostly reduces the expected asymmetries due to dilution by protons (10-14%) and a moderate amount of kaons (12-13%). As anti-protons are suppressed compared to protons in the beam remnants, especially the negative hadrons can be considered a good proxy for negative pions ($\sim$78% purity according to PYTHIA6). Given their sensitivity to the down quark transversity via favored fragmentation, they are particularly important since SIDIS measurements, due to their electromagnetic interaction, are naturally dominated by up-quarks. We have estimated our statistical uncertainties based on an accumulated luminosity of 268 pb^{-1}, which leaves nearly invisible uncertainties after smearing. These expected uncertainties are compared to the asymmetries obtained from the transversity extractions based on SIDIS and Belle data [260] as well as from using the Soffer positivity bound for the transversity PDF [261]. More recent global fits have slightly different central up and down quark transversity distributions. But due to the lack of any SIDIS data for $x > 0.3$, the upper uncertainties are compatible with the Soffer bounds. This high-x coverage will give important insights into the tensor charge, which is essential to understand the nucleon structure at leading twist.

Although the studies presented here are for the Collins asymmetries, the resulting statistical uncertainties will be similar for other measurements using azimuthal correlations of hadrons in jets. One important example is the measurement of "Collins-like" asymmetries to access the distribution of linearly polarized gluons. As described earlier, the best kinematic region to access this distribution is at backward angles with respect to the polarized proton and at small jet p_T. Figure 68 shows that a high precision measurement of the distribution of linearly polarized gluons down to $x \sim 0.005$ will be performed concurrently.

It is also important to recognize that these hadron-in-jet measurements with the STAR Forward Upgrade will provide very valuable experience detecting jets close to beam rapidity that will inform the planning for future jet measurements in similar kinematics at the EIC.

While the STAR Forward Upgrade will provide sensitivity to transversity to the highest x, concurrent mid-rapidity measurements (see Fig. 67) will provide the most precise information as a function of x, z, j_T, and Q^2 to probe questions of TMD factorization, universality,

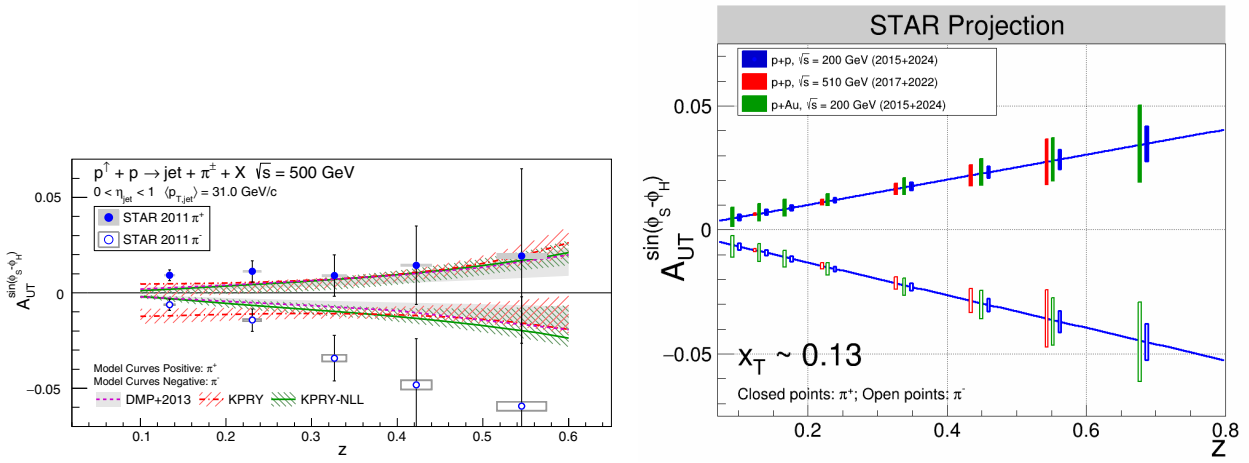

Figure 69: The left panel shows STAR measurements of the Collins asymmetry vs. pion z in 500 GeV p+p collisions from Run-11, compared to several model calculations. See [258] for details. The right panel shows projected statistical uncertainties for STAR Collins asymmetry measurements at $0 < \eta < 0.9$ in p+p at $\sqrt{s} = 200$ and 510 GeV and p+Au at $\sqrt{s_{\rm NN}} = 200$ GeV. The points have arbitrarily been drawn on the solid lines, which represent simple linear fits to the STAR preliminary 200 GeV p+p Collins asymmetry measurements from 2015. (Note that only one bin is shown spanning $0.1 < z < 0.2$ for 510 GeV p+p, whereas three bins are shown covering the same z range for the 200 GeV measurements.)

and evolution. The left panel of Fig. 69 shows published STAR measurements of the Collins asymmetry vs. pion z in 500 GeV p+p collisions from 2011 [258]. The results, which represented the first ever observation of the Collins effect in p+p collisions, are consistent at the 2-sigma level with model predictions, with and without TMD evolution, derived from fits to e^+e^- and SIDIS data [108, 262]. However, greater precision is clearly necessary for a detailed universality test, as well as to set the stage for the EIC.

In 2017, STAR sampled about 14 times the luminosity that we recorded in 2011. In Run-22, we propose to record another data set equivalent to 16 times the sampled luminosity from 2011. Furthermore, during Run-22 the iTPC will improve the dE/dx particle identification compared to the previous years. Studies using the dE/dx distributions seen in our 200 GeV p+p data from 2015 and the actual dE/dx resolution improvements that have been achieved during BES-II indicate the iTPC will yield a $20-25\%$ increase in the effective figure-of-merit for pions with $|\eta| < 0.9$. The right-hand panel of Fig. 69 shows the projected STAR statistical uncertainties for the Collins asymmetry at $0 < \eta < 0.9$ in 510 GeV p+p collisions once the Run-17 and Run-22 data sets are fully analyzed. It's also important to recognize that the iTPC will also enable STAR to measure the Collins asymmetry over the region $0.9 < \eta < 1.3$ during Run-22, in addition to the projections that are shown in Fig. 69.

Statistical improvements from 2011 data [250] to 2017+'22 data comparable to those shown for the Collins effect in Fig. 69 are also expected for mid-rapidity measurements of transversity in 510 GeV p+p collisions using IFF asymmetries.

3.1.4 Spatial Imaging of the Nucleon

Diffractive and Ultra Peripheral processes at RHIC are an essential tool that can elucidate the origin of single-spin asymmetries in polarized p+p collisions and access the orbital motion of partons inside the proton. Also at an EIC diffractive processes have been identified as the golden tool to study several key physics programs

- What is the spatial distribution of quarks and gluons inside the nucleon?
- What is the role of orbital motion of sea quarks and gluons in building the nucleon spin?
- saturation in nuclei.

Diffraction: The essential characteristics of diffraction in QCD are summarized by two facts:

- The event is still called diffractive if there is a rapidity gap. Due to the presence of a rapidity gap, the diffractive cross-section can be thought of as arising from an exchange of several partons with zero net color between the target and the projectile. In high-energy scattering, which is dominated by gluons, this color neutral exchange (at the lowest order) consists of at least two exchanged gluons. This color singlet exchange has historically been called the pomeron, which had a specific interpretation in Regge theory. A crucial question in diffraction is the nature of the color neutral exchange between the protons. This interaction probes, in a novel fashion, the nature of confining interactions within hadrons.
- The proton/nuclear target is not always an opaque "black disk" obstacle of geometric optics. A projectile, which interacts more weakly due to color-screening and asymptotic freedom, is likely to produce a different diffractive pattern from a larger, more strongly interacting, projectile.

HERA discovered that 15% of the total ep cross-section is given by diffractive events (for details see [263] and references therein), basically independent of kinematics. At RHIC center-of-mass energies diffractive scattering events constitute $\sim$ 25% of the total inelastic p+p cross-section [264]. As described above diffraction is defined as an interaction that is mediated by the exchange of the quantum numbers of the vacuum, as shown in Figure 70. Experimentally these events can be characterized by the detection of a very forward scattered proton and jet (singly diffractive) or two jets (doubly diffractive) separated by a large rapidity gap. Central diffraction, where two protons, separated by a rapidity gap, are reconstructed along with a jet at mid-rapidity, are also present, but suppressed compared to singly and doubly diffractive events. To date, there have been no data in p+p collisions studying spin effects in diffractive events at high $\sqrt{s}$ apart from measuring single spin asymmetries in elastic p+p scattering [265–268].

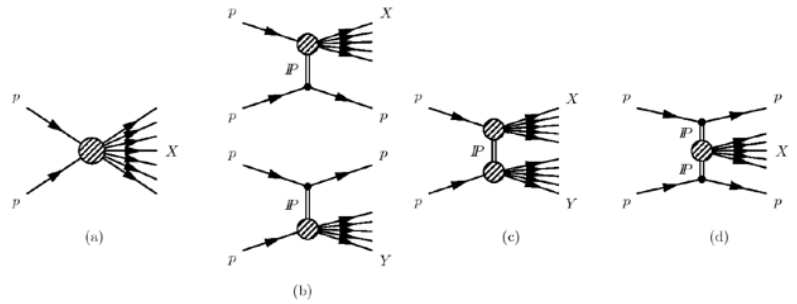

Figure 70: Schematic diagrams of (a) nondiffractive, $pp \to X$, (b) singly diffractive, $pp \to Xp$ or $pp \to pY$, (c) doubly diffractive, $pp \to XY$, and (d) centrally diffracted, $pp \to pXp$, events.

A discovery of large transverse single spin asymmetries in diffractive processes would open a new avenue to study the properties and understand the nature of the diffractive exchange in p+p collisions. One of the primary observables of STAR to access transverse spin phenomena has been forward neutral pion production in transversely polarized p+p collisions at both $\sqrt{s}$ = 200 and 500 GeV. Figure 31 shows the isolated and non-isolated transverse single spin asymmetries A_N for π^0 detected in the STAR FMS at $2.5 < \eta < 4.0$ as a function of x_F.

All these observations might indicate that the underlying subprocess causing a significant fraction of the large transverse single spin asymmetries in the forward direction are not of $2 \to 2$ parton scattering processes but of diffractive nature. Figure **??** shows the inclusive π^0 cross-section for p+p collisions at $\sqrt{s}$=200 GeV versus the leading π^0 energy for three fixed forward pseudorapidities [269]. PYTHIA-8 [14] was used to evaluate the fraction of hard diffractive events [270] contributing to the inclusive π^0 cross-section at forward rapidities. Figure 71 shows the hard diffractive cross-section for π^0 production at $\sqrt{s}$=200 GeV and 500 GeV for a rapidity range of $2.5 < \eta < 4.0$ with and without applying several experimental cuts, i.e. the proton in the STAR Roman Pot acceptance. The prediction from this PYTHIA-8 simulation is that 20% of the total inclusive cross-section at forward rapidities is of diffractive nature. This result is in agreement with measurements done over a wide range of $\sqrt{s}$ (see Figure 12 in Ref. [263]).

In 2015 STAR collected data in $\sqrt{s}$ = 200 GeV transversely polarized p+p collisions, where an isolated π^0 is detected in the forward pseudorapidity range along with the forward-going proton p, which scatters with a near-beam forward pseudorapidity into Roman Pot detectors. The sum of the π^0 and the scattered proton energies is consistent with the incident proton energy of 100 GeV, indicating that no further particles are produced in this direction. Correlations between the π^0 and scattered proton have been presented [271], along with single-spin asymmetries which depend on the azimuthal angles of both the pion and the proton. This is the first time that spin asymmetries have been explored for this process, and a model to explain their azimuthal dependence is needed.

The STAR Forward Upgrade will be a game changer for diffractive measurements at RHIC. It will allow the reconstruction of full jets both at $\sqrt{s}$=200 GeV and 500 GeV. As at HERA we will be able to reconstruct jets produced with the scattered proton tagged in Roman Pots and/or requiring rapidity gaps. Measuring spin asymmetries for diffractive events as function of $\sqrt{s}$ might reveal surprises, which will inspire new physics opportunities

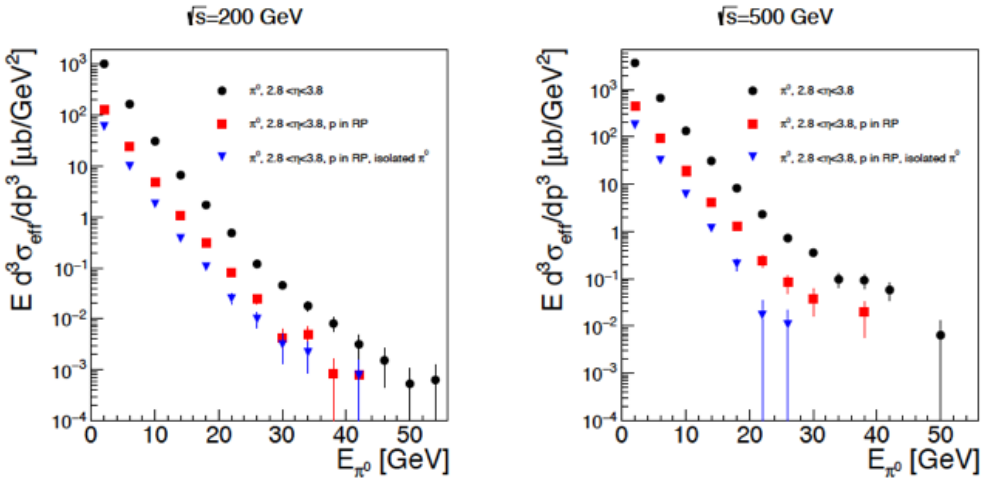

Figure 71: Estimate of the cross-section for hard diffractive processes at $\sqrt{s}$=200 GeV and 500 GeV using Pythia 8. The different points reflect different analysis cuts applied: π^0 in rapidity 2.8 $< \eta <$ 3.8 (black), one proton is required to be detected in the STAR Roman Pot acceptance (red) and an isolation cut of 35 mrad around the π^0 (blue).

for EIC, i.e SSA in polarized eA collisions.

3.2 Run-24 Request for Polarized p+p and p+A Collisions at 200 GeV

Run-24, with polarized p+p and p+Au collisions at $\sqrt{s_{\rm NN}}$ = 200 GeV, will likely be the last RHIC spin/cold QCD run. This run will provide STAR with the unique opportunity to investigate these 200 GeV collision systems with the Forward Upgrade providing full tracking and calorimetry coverage over the region $2.5 < \eta < 4$ and the iTPC providing enhanced particle identification and expanded pseudorapidity coverage at mid-rapidity. These powerful detection capabilities, when combined with substantially increased sampled luminosity compared to Run-15, will enable critical measurements to probe universality and factorization in transverse spin phenomena and nuclear PDFs and fragmentation functions, as well as low-x non-linear gluon dynamics characteristic of the onset of saturation. This will provide unique insights into fundamental QCD questions in the near term, and essential baseline information for precision universality tests when combined with measurements from the EIC in the future.

We therefore request at least 11 weeks of polarized p+p data-taking at $\sqrt{s}$ = 200 GeV and 11 weeks of polarized p+Au data-taking at $\sqrt{s_{NN}}$ = 200 GeV during Run-24. All of the running will involve transversely polarized protons, with the choice between vertical or radial polarization to be determined during the coming year. Based on recent (08-21-20) C-AD guidance, we expect to sample at least 235 pb^{-1} of p+p collisions and 1.3 pb^{-1} of p+Au collisions. These totals represent 4.5 times the luminosity that STAR sampled during transversely polarized p+p collisions in Run-15 and 3 times the luminosity that

STAR sampled during transversely polarized p+Au collisions in Run-15.

3.2.1 Spin Physics with Polarized p+p and p+Au Collisions at 200 GeV

Section 1.3 described several very mature STAR analyses that are based on the transversely polarized p+p and p+Au data sets that we recorded during 2015. Run-24 will enable STAR to probe these questions with a far more capable detector and much larger data sets than were available during Run-15, thereby allowing us to set the stage for related future measurements at the EIC. Here we give brief descriptions of several of the opportunities presented by Run-24.

Forward transverse spin asymmetries: Section 1.3 presents a small subset of the results that STAR will publish very soon in a pair of papers discussing forward transverse spin asymmetries in p+p, p+Al, and p+Au collisions measured with the Forward Meson Spectrometer (FMS). One paper focuses on the dynamics that underlie the large asymmetries that have been seen to date. Figure 31 shows that A_N for forward π^0 production in p+p collisions at 200 and 500 GeV is substantially larger when the π^0 is isolated than when it is accompanied by additional nearby photons. The same analysis also shows that A_N for inclusive electromagnetic jets (EM-jets) in 200 and 500 GeV collisions is substantially larger than that for EM-jets that contain three or more photons and that the Collins asymmetry for π^0 in EM-jets is very small. The other paper focuses on the nuclear dependence of A_N for π^0 in $\sqrt{s_{NN}} = 200$ GeV collisions. It presents a detailed mapping of A_N as functions of x_F and p_T for all three collision systems. Figure 30 shows the observed nuclear dependence is very weak. The same analysis shows that isolated *vs.* non-isolated π^0 behave similarly in p+Al and p+Au collisions as they do in p+p collisions.

These two papers will provide a wealth of new data to inform the ongoing discussion regarding the origin of the large inclusive hadron transverse spin asymmetries that have been seen in p+p collisions at forward rapidity over a very broad range of collision energies. Nonetheless, the STAR Forward Upgrade will be a game changer for such investigations. It will enable measurements of A_N for $h^{+/-}$, in addition to π^0. It will enable isolation criteria to be applied to the $h^{+/-}$ and π^0 that account for nearby charged, as well as neutral, fragments. It will enable full jet asymmetry and Collins effect measurements, again for $h^{+/-}$ in addition to π^0, rather than just EM-jet measurements. It will permit all of these measurements to be performed at both 510 GeV, as discussed in Sects. 3.1.1 and 3.1.2, and at 200 GeV. And all of these observables can be tagged by forward protons detected in the STAR Roman pots to identify the diffractive component of the observed transverse spin asymmetries. For p+p there will be considerable overlap between the kinematics at the two energies, but the 510 GeV measurements will access higher p_T, while the 200 GeV measurements will access higher x_F. Meanwhile, at 200 GeV we will also perform the full suite of measurements in p+Au to identify any nuclear effects. Figure 64 shows one set of predictions for the inclusive $\pi^{+/-}$ A_N in 200 and 500 GeV p+p collisions, while Fig. 65 shows the estimated sensitivity of one hadron-in-jet measurement that will help to isolate the Sivers effect contribution at 200 GeV.

Sivers effect: Sections 1.3 and 3.1.2 describe the first ever observation of the Sivers effect in dijet production. Such measurements are crucial to explore questions regarding factorization of the Sivers function in dijet hadroproduction [252–255]. Those results were derived from 200 GeV transverse spin data that STAR recorded in 2012 and 2015 (total sampled luminosity ~ 75 pb^{-1} for the two years combined). Nonetheless, the uncertainties remain large, as can be seen in Fig. 29. Run-24 data will reduce the uncertainties for $|\eta_3 + \eta_4| < 1$ by a factor of two. The increased acceptance from the iTPC will reduce the uncertainties at $|\eta_3 + \eta_4| \approx 2.5$ by a much larger factor, while the Forward Upgrade will enable the measurements to be extended to even larger values of $|\eta_3 + \eta_4|$. When combined with the 510 GeV data from 2017 and 2022 (see Sect. 3.1.2), the results will provide a detailed mapping *vs.* x for comparison to results to Sivers functions extracted from SIDIS, Drell-Yan, and vector boson production.

Transversity and related quantities: As described in Sect. 3.1.3, measurements of the Collins asymmetry and IFF in p+p collisions at RHIC probe fundamental questions regarding TMD factorization, universality, and evolution. Data from 200 GeV p+p collisions will play an essential role toward answering these questions. Figure 67 shows that 200 GeV p+p collisions interpolate between the coverage that we will achieve during Run-22 at high-x with the Forward Upgrade and at low-x with the STAR mid-rapidity detectors. They will also provide a significant overlapping region of x coverage, but at Q^2 values that differ by a factor of 6. This will provide valuable information about evolution effects, as well as cross-checks between the two measurements. Furthermore, for most of the overlapping x region, 200 GeV p+p collisions will also provide the greatest statistical precision (see for example Fig. 69), thereby establishing the most precise benchmark for future comparisons to *ep* data from the EIC.

The high statistical precision of the Run-24 data will enable detailed multi-dimensional binning for the Collins asymmetry results. This is particularly valuable because, as emphasized in [108, 109], hadron-in-jet measurements in p+p collisions provide a direct probe of the Collins fragmentation function because they combine it with the *collinear* transversity distribution. In general, the observed asymmetries are functions of jet (p_T, η), hadron (z, j_T), and Q^2. However, the physics interpretations associated with these variables separate, with p_T and η primarily coupling to the incident quark x and the polarization transfer in the hard scattering, while z and j_T characterize the fragmentation kinematics. Thus, A_{UT} *vs.* p_T, as shown in Fig. 28 for the preliminary 2015 analysis, provides information about the transversity distribution. In parallel, the (z, j_T) dependence, integrated over a wide range of jet p_T, as shown in Fig. 72 for the preliminary 2015 results, provides a detailed look at the Collins fragmentation function. Note that STAR finds the maximum value of A_{UT} shifts to higher j_T as z increases. The statistical uncertainties in Figs. 28 and 72 will be reduced by a factor of 2.5 when Run-15 and Run-24 data are combined together.

The 2015 Collins analysis has also, for the first time, measured the Collins effect for charged kaons in p+p collisions, as shown in Fig. 73. The asymmetries for K^+, which like π^+ have a contribution from favored fragmentation of u quarks, are about 1.5-sigma larger than those for π^+ in Fig. 28, while those for K^-, which can only come from unfavored

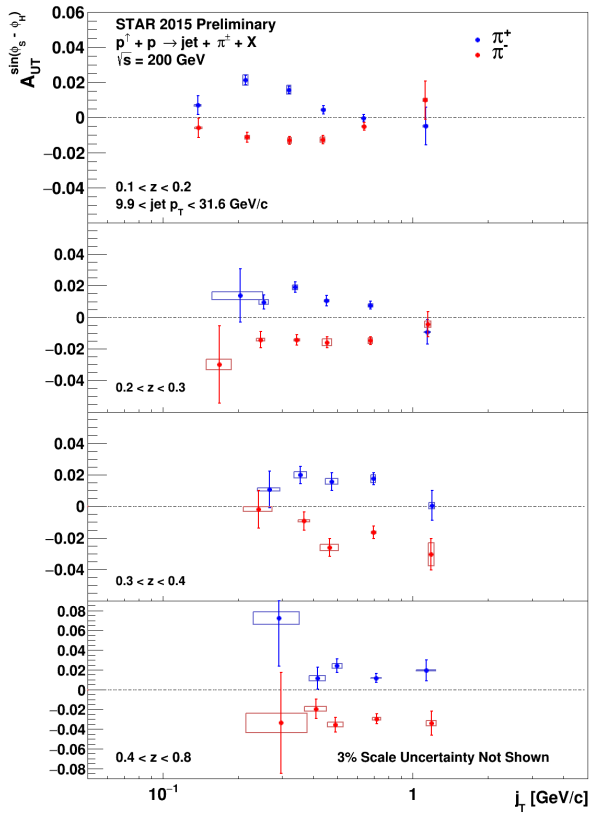

Figure 72: Preliminary 2015 results for the Collins asymmetry for charged pions in 200 GeV p+p collisions as a function of z and j_T, integrated over $9.9 < p_T < 31.6$ GeV/c and $0 < \eta < 0.9$.

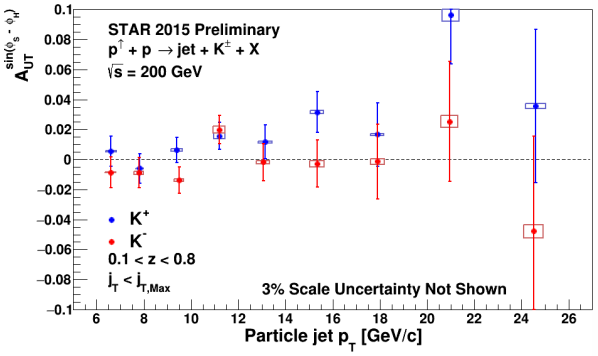

Figure 73: Preliminary 2015 results for the $K^{+/-}$ Collins asymmetries *vs.* jet p_T for $0 < \eta < 0.9$ in 200 GeV p+p collisions.

fragmentation, are consistent with zero at the 1-sigma level. These trends are similar to those found in SIDIS by HERMES [272] and COMPASS [273], and provide additional insight into the Collins fragmentation function. This same analysis with Run-24 data will yield statistical uncertainties a factor of 3 smaller than those in Fig. 73. This is a much greater improvement than would be expected from the increase in sampled luminosity thanks to the improved dE/dx resolution provided by the iTPC. In addition, the iTPC will enable the measurements in Figs. 28, 72, and 73 to be extended to an additional higher η bin ($0.9 < \eta < 1.3$).

RHIC has the unique opportunity to extend the Collins effect measurements to nuclei. This will provide an alternative look at the universality of the Collins effect in hadroproduction by dramatically increasing the color flow options of the sort that have been predicted to break factorization for TMD PDFs like the Sivers effect [252, 253]. This will also explore the spin dependence of the hadronization process in cold nuclear matter. STAR collected a proof-of-principle data set during the 2015 p+Au run that is currently under analysis. Those data will provide a first estimate of medium-induced effects. However, the small nuclear effects seen by STAR for forward inclusive π^0 A_N (see Fig. 30) indicate that greater precision will likely be needed. Figure 69 shows the projected 2015+'24 statistical uncertainties for the p+Au Collins asymmetry measurement at $\sqrt{s_{\rm NN}} = 200$ GeV, compared to those for the p+p at the same energy.

Ultra-peripheral collisions: The formalism of generalized parton distributions (GPDs) provides a theoretical framework which addresses some of the above questions [274–277]. Constraints on GPDs have mainly been provided by exclusive reactions in DIS, e.g. deeply virtual Compton scattering. RHIC, with its unique capability to collide transversely polarized protons at high energies, has the opportunity to measure A_N for exclusive J/Ψ production in ultra-peripheral collisions (UPCs) [278]. In such a UPC process, a photon emitted by the opposing beam particle (p or A) collides with the polarized proton. The measurement is at a fixed $Q^2 \sim M^2_{J/\psi} \approx 10$ GeV^2 and $10^{-4} < x < 10^{-1}$. A nonzero asymmetry would be the first signature of a nonzero GPD E_g for gluons, which is sensitive to spin-orbit correlations and is intimately connected with the orbital angular momentum carried by partons in the nucleon and thus with the proton spin puzzle.

The 2015 p$^\uparrow$+Au data allowed a proof-of-principle of such a measurement. A trigger requiring back-to-back energy deposits in the Barrel Electromagnetic Calorimeter selected J/Ψ candidates. The e^+e^- mass distribution after selection cuts is shown in the left of Fig. 74, and the pair p_T distribution of the J/ψ mass peak is shown on the right of the figure. The data are well described by the STARlight model [279] (colored histograms in the figure), including the dominant γ+p$\uparrow\to J/\psi$ signal process and the γ+Au$\to J/\psi$ and $\gamma+\gamma\to e^+e^-$ background processes. The left of Fig. 75 shows the transverse asymmetry A_N^γ for the signal J/ψ, which have a mean photon-proton center-of-mass energy $W_{\gamma p} \approx 24$ GeV. The result is consistent with zero. Also shown is a prediction based on a parameterization of E_g [280]; the present data provide no discrimination of this prediction.

This measurement can be greatly improved with a high statistics transversely polarized p$\uparrow$+Au run in 2024. The integrated luminosity for the 2015 measurement was 140 nb^{-1}; the

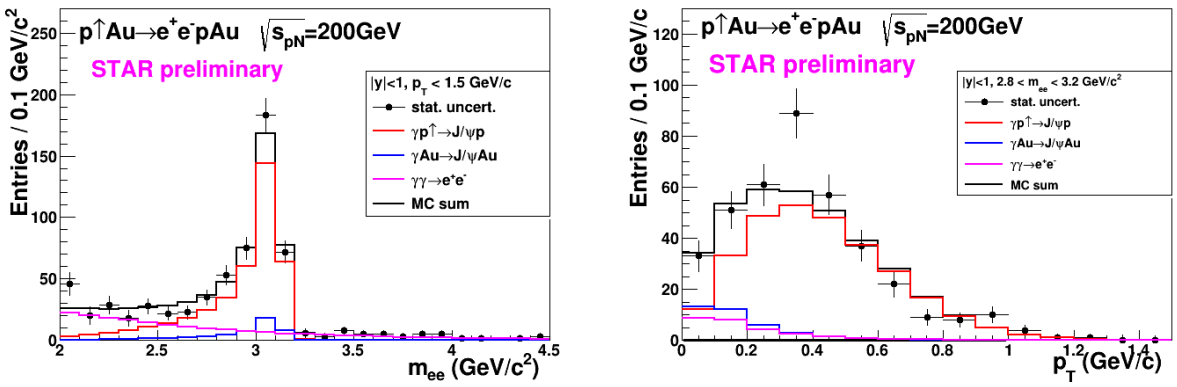

Figure 74: Mass distribution of selected e^+e^- pairs (left), and p_T distribution of the J/ψ mass peak (right). The colored histograms are the indicated processes modelled by STARlight and the sum fit to the data.

2024 run will provide 1.3 pb^{-1}, allowing a sizeable reduction of statistical uncertainty in the same $W_{\gamma p}$ range. However, the Forward Upgrade and iTPC will also provide a significant extension of the $W_{\gamma p}$ range of the measurement. The right of Fig. 75 shows the accepted cross section for γ+p$^\uparrow \rightarrow J/\psi$ for various detector pseudorapidity ranges. With the full detector, the sensitive cross section is a factor of five times the central barrel alone and the expected asymmetry is substantially larger. The statistical uncertainty on A_N^γ as shown in the left of Fig. 75 will be ≈ 0.02, offering a powerful test of a non-vanishing E_g. Also, the accepted region has a lower mean $W_{\gamma p} \approx 14$ GeV. Predictions based on E_g parameterizations such as shown in the figure have a larger asymmetry at lower $W_{\gamma p}$, with increased possibility of a nonzero result. Alternatively, the increased statistics will allow a measurement of A_N^γ in bins of $W_{\gamma p}$.

Similar measurements are also possible with future p$^\uparrow$+p$^\uparrow$ runs at $\sqrt{s} = 200$ and 510 GeV. However, the UPC cross section scales with Z^2 of the the nucleus emitting the photon; for protons this is $1/79^2$ relative to Au nuclei, which makes analogous measurements in p+p collisions extremely luminosity hungry.

3.2.2 Physics Opportunities with Unpolarized proton-Nucleus Collisions

Our quest to understand QCD processes in Cold Nuclear Matter (CNM) centers on the following fundamental questions:

- Can we experimentally find evidence of a novel universal regime of non-linear QCD dynamics in nuclei?
- What is the role of saturated strong gluon fields, and what are the degrees of freedom in this high gluon density regime?
- What is the fundamental quark-gluon structure of light and heavy nuclei?

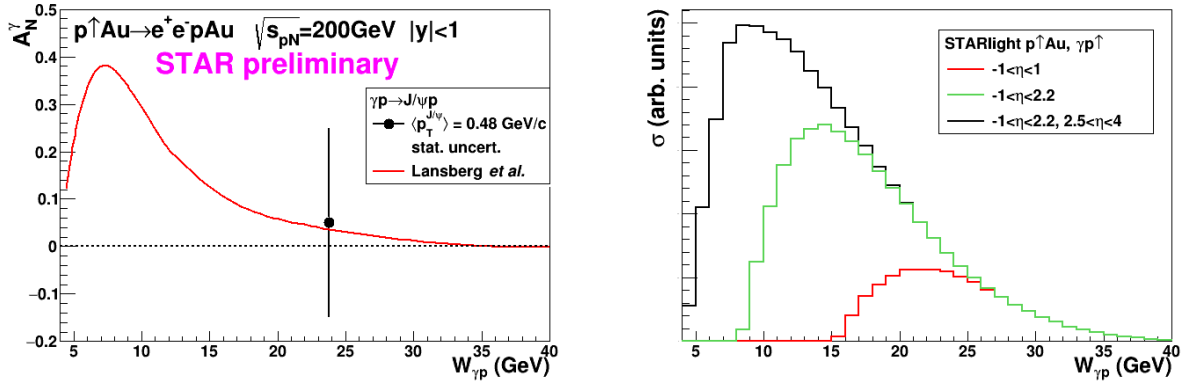

Figure 75: Left: The measured J/ψ transverse asymmetry A_N^γ and a prediction based on a parameterization of E_g. Right: The accepted cross section for γ+p↑→ J/ψ for various detector pseudorapidity η ranges; the black curve shows the result for the full STAR detector with the Forward Upgrade and the iTPC.

- Can a nucleus, serving as a color filter, provide novel insight into the propagation, attenuation and hadronization of colored quarks and gluons?

Various aspects of these questions have been addressed by numerous experiments and facilities around the world, most of them at significantly lower center-of-mass energies and kinematic reach than RHIC. Deep inelastic scattering on nuclei addresses some of these questions with results from, for instance, HERMES at DESY [281–283], CLAS at JLab [284], and in the future at the JLab 12 GeV. This program is complemented by hadron-nucleus reactions in fixed target p+A at Fermilab (E772, E886, and E906) [285] and at the CERN-SPS.

In the following we propose a measurement program unique to RHIC to constrain the initial state effects in strong interactions in the nuclear environment. We also highlight the complementarity to the LHC p+Pb program and stress why RHIC data are essential and unique in the quest to further our understanding of nuclei. The uniqueness of the RHIC program is based on the flexibility of the RHIC accelerator to run collisions of different particle species at very different center-of-mass energies. This in combination with the enhanced STAR detector capabilities in Run-24 allows to disentangle nuclear effects in the initial and final state as well as leading twist shadowing from saturation effects in a kinematic regime where all these effects are predicted to be large. Most of the discussed measurements critically rely on the Forward Upgrade.

The initial state of nuclear collisions:

Nuclear parton distribution functions: A main emphasis of the 2015 and later p+A runs is to determine the initial conditions of the heavy ion nucleus before the collision to support the theoretical understanding of the A+A program both at RHIC and the LHC.

In the following, the current status of nPDFs will be discussed, including where the unique contribution of RHIC lie, in comparison to the LHC and the future EIC.

Our current understanding of nuclear parton distribution functions (nPDFs) is still very limited, in particular, when compared with the rather precise knowledge of PDFs for free protons collected over the past 30 years. Figure 76 shows an extraction of nPDFs from available data, along with estimates of uncertainties. All results are shown in terms of the nuclear modification ratios, i.e., scaled by the respective PDF of the free proton. The yellow bands indicate regions in x where the fits are not constrained by data [286] and merely reflect the freedom in the functional form *assumed* in the different fits. Clearly, high precision data at small x and for various different values of Q^2 are urgently needed better to constrain the magnitude of suppression in the x region where non-linear effects in the scale evolution are expected. In addition, such data are needed for several different nuclei, as the A-dependence of nPDFs cannot be predicted from first principles in pQCD and, again, currently relies on assumptions. Note that the difference between DSSZ [287] and EPS09 for the gluon modification arise from the different treatment of the PHENIX midrapidity $\pi^0 R_{dAu}$ data [288], which in the EPS09 [289] fit are included with an extra weight of 20. The $\pi^0 R_{dAu}$ data are the only data, which can probe the gluon in the nucleus directly, but these data also suffer from unknown nuclear effects in the final state (see [290]). Therefore, it is absolutely critical to have high precision data only sensitive to nuclear modification in the initial state over a wide range in x and intermediate values of Q^2 (away from the saturation regime) to establish the nuclear modification of gluons in this kinematic range.

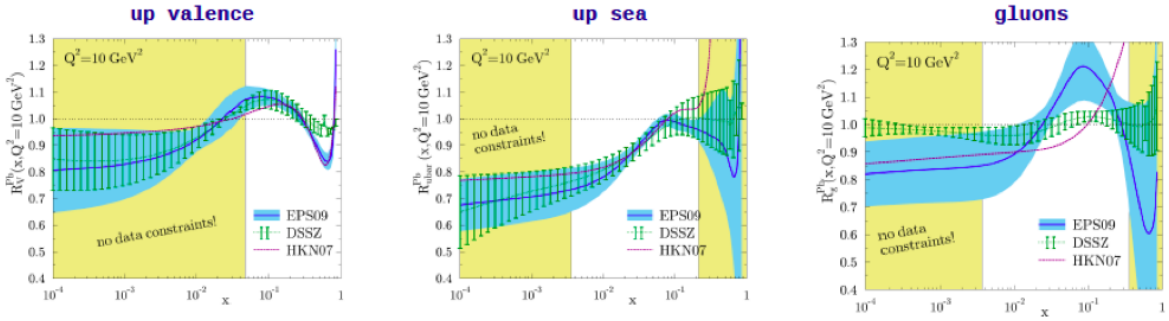

Figure 76: Summary of the most recent sets of nPDFs. The central values and their uncertainty estimates are given for the up valence quark, up sea quark, and the gluon. The yellow bands indicate regions in x where the fits are not constrained by any data (taken from Ref. [286]).

It is important to realize that the measurements from RHIC are compelling and essential even when compared to what can be achieved in p+Pb collisions at the LHC. Due to the higher center-of-mass system energy most of the LHC data have very high Q^2, where the nuclear effects are already reduced significantly by evolution and are therefore very difficult to constrain. Two recent articles [291,292] assessed the impact of the available LHC Run-I p+Pb data on determinations of nPDFs. The rather moderate impact of these data is illustrated in Figure 77. Note that the extra weight factor of 20 for the PHENIX midrapidity $\pi^0 R_{dAu}$ data [288] in the original EPS09 [289] fit was removed in all of the new fits, leading to a

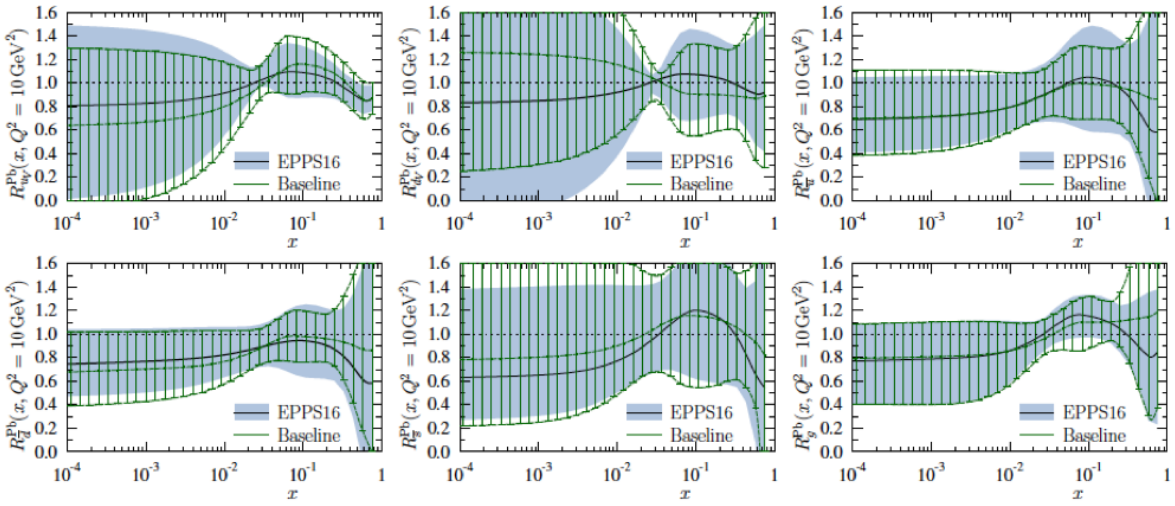

Figure 77: The nuclear modifications at Q^2=10GeV^2 from the EPPS-16 fit (black central line and light-blue bands) compared with the Baseline fit (green curves with hatching) which uses only the data included in the EPS09 fit.

much smaller nuclear modification factor for gluons, especially at medium to high x.

RHIC has the *unique* capability to provide data in a kinematic regime (moderate Q^2 and medium-to-low x) where the nuclear modification of the sea quark and the gluon is expected to be sizable and currently completely unconstrained. In addition, and unlike the LHC, RHIC has the potential to vary the nucleus in p+A collisions and as such also constrain the A-dependence of nPDFs.

Extraction of this information is less ambiguous if one uses processes in which strong (QCD) final-state interactions can be neglected or reduced. Such golden channels would include: a measurement of R_{pA} for Drell-Yan production at forward pseudo-rapidities with respect to the proton direction ($2.5 < \eta < 4.$) to constrain the nuclear modifications of sea-quarks; and of R_{pA} for direct photon production in the same kinematic regime to constrain the nuclear gluon distribution. The first measurement of R_{pA} for direct photon production has been done already during the p+Au and p+Al runs in 2015, with recorded luminosities by STAR of $L_{pAu} = 0.45$ pb^{-1} and $L_{pAl} = 1$ pb^{-1}, respectively. The anticipated statistical precision for pA runs in 2015 and projections for the run in 2024 are shown in Fig. 78. The Forward Upgrade with its tracking at forward rapidities will also provide the possibility to measure R_{pA} for positive and negatively charged hadrons.

Figure 79(left) shows the significant impact of the Run-2015 and 2024 R_{pA} for direct photon production on the corresponding theoretical expectations and their uncertainties obtained with the EPPS-16 set of nPDFs. The uncertainty bands are obtained through a reweighting procedure [293] by using the projected data shown in Fig. 78 and randomizing them according to their expected statistical uncertainties around the central values obtained with the current set of EPPS-16 nPDFs. Figure 79(right) shows how these measurements will help significantly in further constraining the nuclear gluon distribution in a broad range

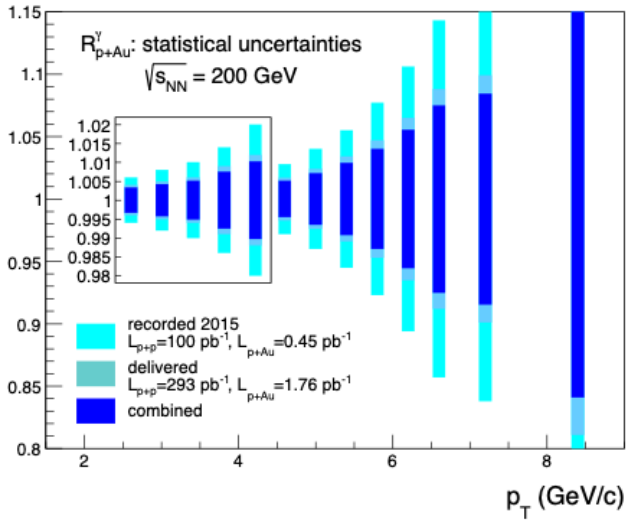

Figure 78: Projected statistical uncertainties for R_{pA} for direct photons in Run-2015 (light blue) and a run in 2024 (blue) and the sum of both (dark blue). The recorded luminosity for Run-2015 was $L_{pAu} = 450$ nb^{-1} and $L_{pp} = 100$ pb^{-1}. The delivered luminosity for Run-2024 is assumed to be $L_{pAu} = 1.8$ pb^{-1} and $L_{pp} = 300$ pb^{-1}.

of x that is roughly correlated with accessible transverse momenta of the photon, i.e., few times $10^{-3} < x <$ few times 10^{-2}. The relevant scale Q^2 is set be $\sim p_T^2$ and ranges from 6 GeV^2 to about 40 GeV^2. Like all other inclusive probes in p+p and pA collisions, e.g., jets, no access to the exact parton kinematics can be provided event-by-event but global QCD analyses easily account for that. After the p+Au run in 2024, the statistical precision of the prompt photon data will be sufficient to contribute to a stringent test of the universality of nuclear PDFs when combined with the expected data from the EIC (see Figure 2.22 and 2.23 in Ref [294]).

Figure 80 shows the kinematic coverage in x–Q^2 of past, present, and future experiments capable of constraining nuclear parton distribution functions. The experiments shown provide measurements that access the initial state parton kinematics on an event-by event basis (in a leading order approximation) while remaining insensitive to any nuclear effects in the final state. Some of the LHC experiments cover the same x-range as DY at forward pseudorapidities at RHIC but at a much higher scale Q^2, where nuclear modifications are already significantly reduced [292, 295, 296]. At intermediate Q^2, DY at RHIC will extend the low-x reach by nearly one decade compared to EIC.

The biggest challenge of a DY measurement is to suppress the overwhelming hadronic background: the total DY cross-section is about 10^{-5} to 10^{-6} smaller than the corresponding hadron production cross-sections. Therefore, the probability of misidentifying a hadron track as a lepton has to be suppressed to the order of 0.1% while maintaining reasonable electron detection efficiencies. To that end, we have studied the combined electron/hadron discriminating power of the Forward Upgrade. It was found that by applying multivariate analysis techniques to the features of EM/hadronic shower development and momentum measurements we can achieve hadron rejection powers of 200 to 2000 for hadrons of 15 GeV to 50 GeV with 80% electron detection efficiency.

The same procedure as for the direct photon R_{pA} was used to study the potential impact of the DY R_{pA} data for the EPPS-19 sets of nPDFs. We expect again a significant impact

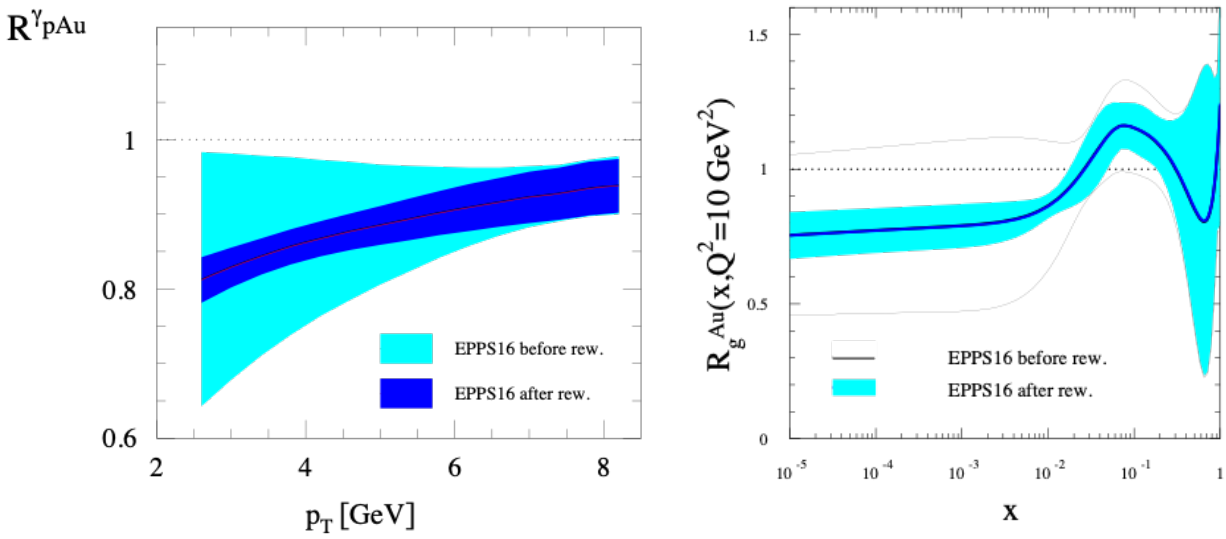

Figure 79: (left) The impact of the direct photon R_{pA} data measured in Run-2015 (blue band) and for the anticipated statistics for the future p+Au run in 2024 (dark blue band) compared with the current uncertainties (cyan band) from EPPS-16. (right) The impact of the direct photon R_{pA} data measured in Run-2015 and for the anticipated statistics for the future p+Au run in 2024 on EPPS-16. The impact is shown on the nuclear suppression factor R_g of nPDF to the proton PDF, the grey bands represent the uncertainties before including the RHIC pseudo data.

on the uncertainties of R_{pA} DY upon including the projected and properly randomized data. Clearly, the DY data from RHIC will be instrumental in reducing present uncertainties in nuclear modifications of sea quarks. Again, these data will prove to be essential in testing the fundamental universality property of nPDFs in the future when EIC data become available.

STAR's unique detector capabilities will provide the first data on J/Ψ-production in ultra-peripheral collisions. This measurement provides access to the spatial gluon distribution by measuring the t-dependence of $d\sigma/dt$. As follows from the optical analogy, the Fourier-transform of the square root of this distribution yields the source distribution of the object probed. To study the gluon distribution in the gold nucleus, events need to be tagged where the photon is emitted from the proton. For both observables a measurement with different nuclei is required to pin down the A-dependence of nPDFs. The J/Ψ-production in ultra-peripheral collisions requires significantly more statistics than accumulated to date.

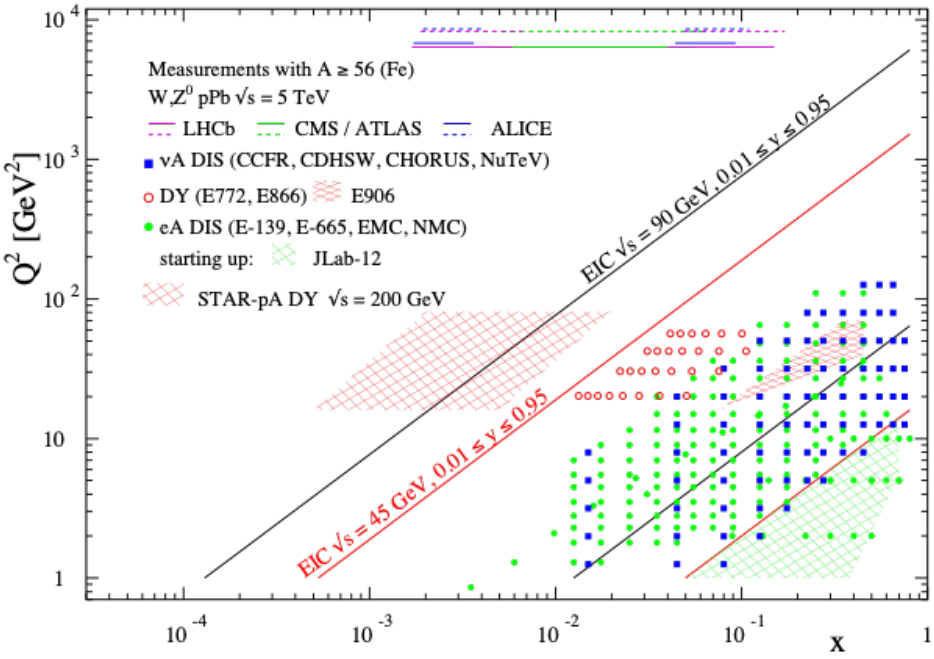

Figure 80: The kinematic coverage in $x^{\sim}Q^2$ of past, present and future experiments constraining nPDFs with access to the exact parton kinematics event-by-event and no fragmentation in the final state.

Gluon saturation: Our understanding of the proton structure and of the nuclear interactions at high energy would be advanced significantly with the definitive discovery of the saturation regime [297–303]. Saturation physics would provide an infrared cutoff for perturbative calculations, the saturation scale Q_s, which grows with the atomic number of the nucleus A and with decreasing value of x. If Q_s is large it makes the strong coupling constant small, $\alpha_s(Q_s^2) << 1$ allowing for perturbative QCD calculations to be under theoretical control.

It is well known that PDFs grow at small-x. If one imagines how such a high number of small-x partons would fit in the (almost) unchanged proton radius, one arrives at the picture presented in Figure 81: the gluons and quarks are packed very tightly in the transverse plane. The typical distance between the partons decreases as the number of partons increases, and can get small at low-x (or for a large nucleus instead of the proton). One can define the saturation scale as the inverse of this typical transverse inter-parton distance. Hence Q_s indeed grows with A and decreasing x.

The actual calculations in saturation physics start with the classical gluon fields (as gluons dominate quarks at small-x) [304–310], which are then evolved using the nonlinear small-x BK/JIMWLK evolution equations [311, 312, 312–320]. The saturation region can be well-approximated by the following formula: $Q_s^2 \sim (A/x)^{1/3}$. Note again that at small enough x the saturation scale provides an IR cutoff, justifying the use of perturbative calculations. This is important beyond saturation physics, and may help us better understand small-x evolution of the TMDs.

While the evidence in favor of saturation physics has been gleaned from the data collected at HERA, RHIC and the LHC, the case for saturation is not sealed and alternative explanations of these data exist. The EIC is slated to provide more definitive evidence for

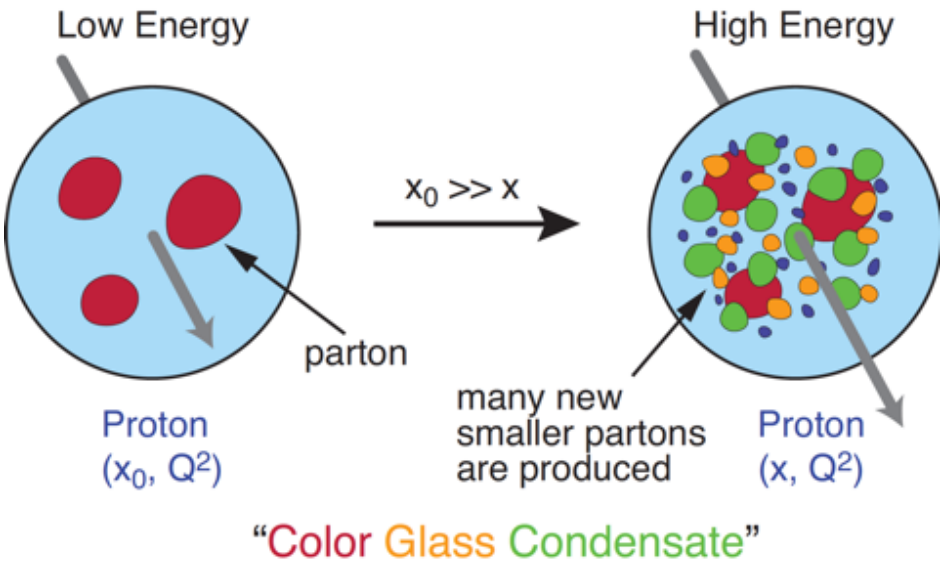

Figure 81: Proton wave function evolution towards small-x

saturation physics [321]. To help the EIC complete the case for saturation, it is mandatory to generate higher-precision measurements in p+A collisions at RHIC. These higher-precision measurements would significantly enhance the discovery potential of the EIC as they would enable a stringent test of universality of the CGC. We stress again that a lot of theoretical predictions and results in the earlier Sections of this document would greatly benefit from saturation physics: the small-x evolution of TMDs in a longitudinally or transversely polarized proton, or in an unpolarized proton, can all be derived in the saturation framework [322] in a theoretically better-controlled way due to the presence of Q_s. Hence saturation physics may help us understand both the quark and gluon helicity PDFs as well as the Sivers and Boer-Mulders functions.

The saturation momentum is predicted to grow approximately like a power of energy, $Q_s^2 \sim E^{\lambda/2}$ with $\lambda \sim 0.2$-0.3, as phase space for small-x (quantum) evolution opens up. The saturation scale is also expected to grow in proportion to the valence charge density at the onset of small-x quantum evolution. Hence, the saturation scale of a large nucleus should exceed that of a nucleon by a factor of $A^{1/3} \sim 5$ (on average over impact parameters). RHIC is capable of running p+A collisions for different nuclei to check this dependence on the mass number. This avoids potential issues with dividing say p+Pb collisions in N_{part} classes [323]. Figure 82 shows the kinematic coverage in the x-Q^2 plane for p+A collisions at RHIC, along with previous e+A measurements and the kinematic reach of an EIC. The saturation scale for a Au nucleus and the proton is also shown. To access at RHIC a kinematic regime sensitive to saturation with $Q^2 > 1$ GeV^2 requires measurements at forward rapidities. For these kinematics the saturation scale is moderate, on the order of a few GeV^2, so measurements sensitive to the saturation scale are by necessity limited to semi-hard processes.

Until today the golden channel at RHIC to observe strong hints of saturation has been the angular dependence of two-particle correlations, because it is an essential tool for testing

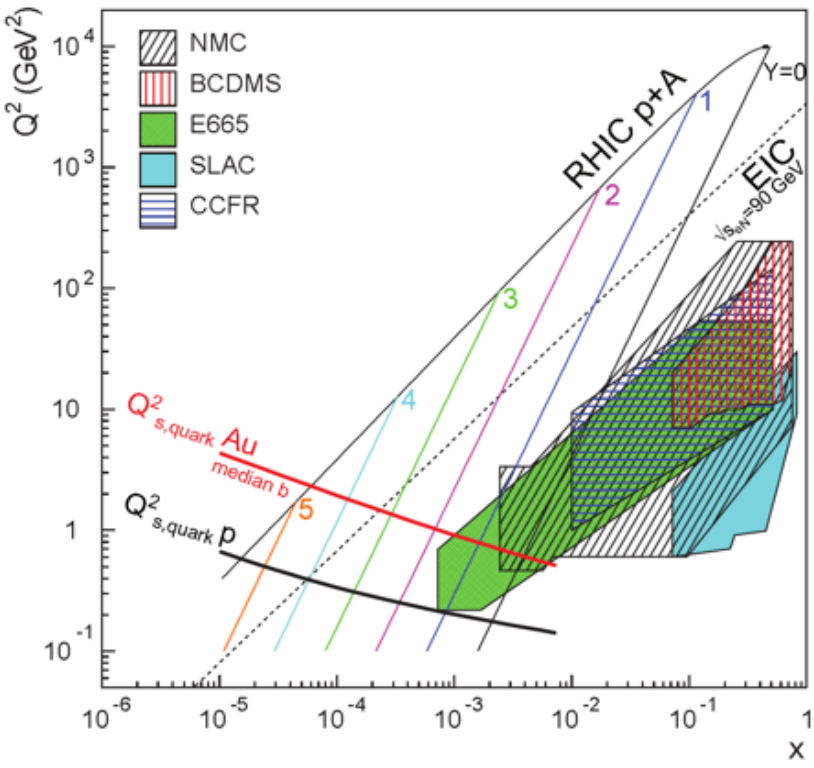

Figure 82: Kinematic coverage in the $x - Q^2$ plane for p+A collisions at RHIC, along with previous e+A measurements, the kinematic reach of an electron-ion collider, and estimates for the saturation scale Q_s in Au nuclei and protons. Lines are illustrative of the range in x and Q^2 covered with hadrons at various rapidities.

the underlying QCD dynamics [323]. In forward-forward correlations facing the $p(d)$ beam direction one selects a large-x parton in the p(d) interacting with a low-x parton in the nucleus. For $x < 0.01$ the low-x parton will be back-scattered in the direction of the large-x parton. Due to the abundance of gluons at small x, the backwards-scattered partons are dominantly gluons, while the large-x partons from the p(d) are dominantly quarks. The measurements of di-hadron correlations by STAR and PHENIX [324, 325], have been compared with theoretical expectations using the CGC framework based on a fixed saturation scale Q_s and considering valence quarks in the deuteron scattering off low-x gluons in the nucleus with impact parameter $b = 0$ [326,327]. Alternative calculations [328] based on both initial and final state multiple scattering, which determine the strength of this transverse momentum imbalance, in which the suppression of the cross-section in d+Au collisions arises from cold nuclear matter energy loss and coherent power corrections have also been very successful to describe the data.

The 2015 p+Au run at RHIC has provided unique opportunities to study this channel in more detail at STAR. The high delivered integrated luminosities allow one to vary the trigger and associated particle p_T from low to high values and thus crossing the saturation boundary as shown in Figure 82 and reinstate the correlations for central p+A collisions for forward-forward π^0's. Studying di-hadron correlations in p+A collisions instead of d+A collisions has a further advantage. In reference [329], the authors point out that the contributions from double-parton interactions to the cross-sections for $dA \to \pi^0\pi^0 X$ are not negligible. They find that such contributions become important at large forward rapidities, and especially in

the case of d+A scattering. Figure 83 shows the results for the di-hadron correlations for π^0 from the 2015 p+p and p+A run. Shown is the ratio of the area, the width and the level of pedestal of the backward peak for p+Au and p+p as function of the p_T of the trigger and the associated π^0 and the activity in the collision as measured by the BBC. The results show

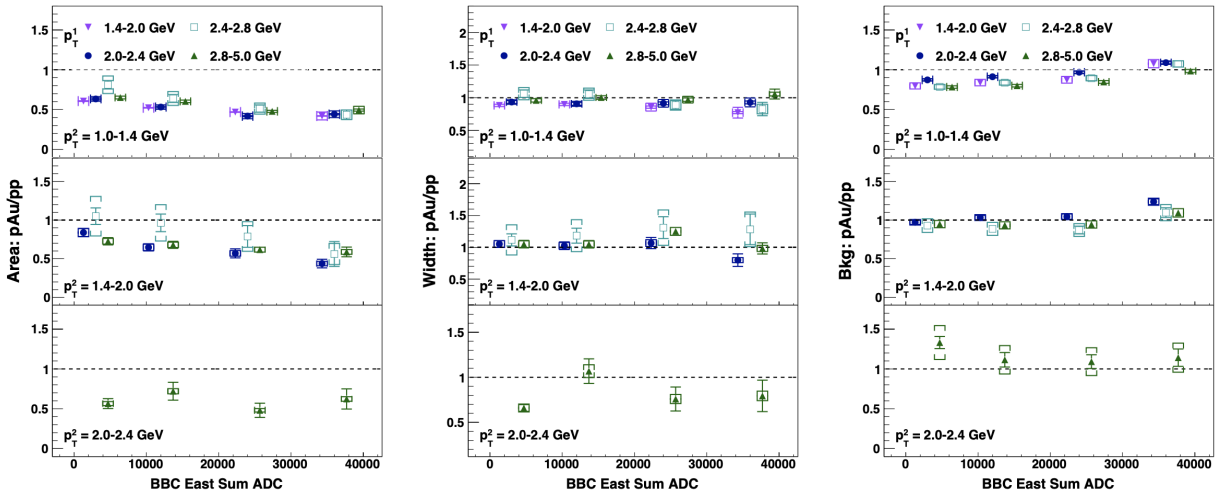

Figure 83: The results for the di-hadron correlations for π^0 from the 2015 p+p and p+A run.

basically no change in the width of the backward peak and the background/pedestal the peak is sitting on shows only up to a 20% increase in pA+u to p+p. But the area of the of the backward peak shows a large suppression with increasing activity in the collision. For fixed activity the biggest suppression is observed for the smallest trigger p_T in combination with the smallest p_T for the associated π^0. This behaviour is consistent with different calculations based on the CGC formalism. This result is the first clean observable, which cannot yet be explained in a different framework than CGC and as such a clear hint for non-linear effects. With the Forward Upgrade several other channels, i.e charged di-hadron and di-jets correlations, will also be available, which will allow a rigorous test of the calculation in the CGC formalism. It is noted that these results are crucial for the equivalent measurements at an EIC, which are planned at close to identical kinematics, because only if non-linear effects are seen with different complementary probes, i.e., ep and pA, one can claim a discovery of saturation effects and their universality.

It is important to note that for the measurements to date in p(d)+A collisions both initial and final states interact strongly, leading to severe complications in the theoretical treatment (see [331, 332], and references therein). As described in detail in the Section above in p+A collisions, these complications can be ameliorated by removing the strong interaction from the final state, by using photons and Drell-Yan electrons. The Run-2015 p+A run will for the first time provide data on R_{pA} for direct photons and therefore allow one to test CGC based predictions on this observable as depicted in Figure 84 (taken from Ref. [330]). The higher delivered integrated luminosity for the upcoming p+Au run in 2024 together with the Forward Upgrade will enable one to study more luminosity hungry

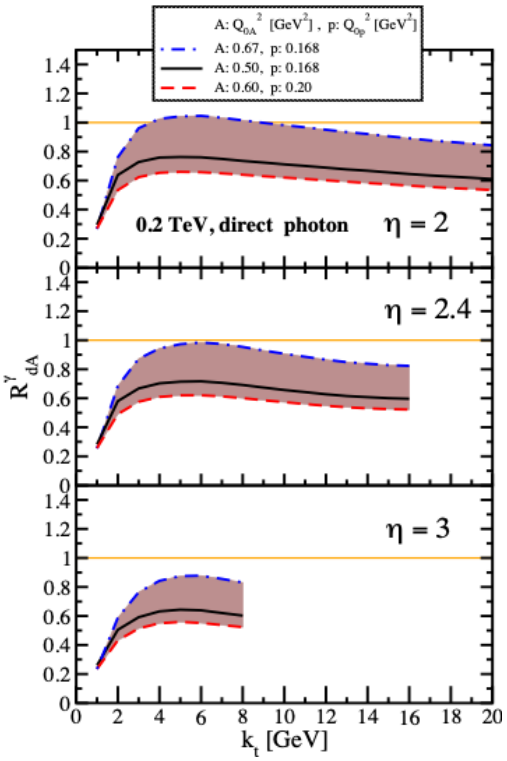

Figure 84: Nuclear modification factor for direct photon production in p(d)A collisions at various rapidities at RHIC $\sqrt{s} = 0.2$ TeV. The curves are the results obtained from Eq. (12) in Ref. [330] and the solution to rcBK equation using different initial saturation scales for a proton Q_{op} and a nucleus Q_{oA}. The band shows our theoretical uncertainties arising from allowing a variation of the initial saturation scale of the nucleus in a range consistent with previous studies of DIS structure functions as well as particle production in minimum-bias p+p, p+A and A+A collisions in the CGC formalism, see Ref. [330] for details.

processes and/or complementary probes to the di-π^0 correlations, i.e. di-hadron correlations for charged hadrons, photon-jet, photon-hadron and di-jet correlations.

We use direct photon plus jet (direct γ +jet) events as an example channel to indicate what can be done in 2024. These events are dominantly produced through the gluon Compton scattering process, g+q $\rightarrow \gamma$+q, and are sensitive to the gluon densities of the nucleon and nuclei in p+p and p+A collisions. Through measurements of the azimuthal correlations in p+A collisions for direct γ +jet production, one can study gluon saturation phenomena at small-x. Unlike di-jet production that is governed by both the Weizsäcker-Williams and dipole gluon densities, direct γ +jet production only accesses the dipole gluon density, which is better understood theoretically [330, 333],. On the other hand, direct γ +jet production is experimentally more challenging due to its small cross-section and large background contribution from di-jet events in which photons from fragmentation or hadron decay could be misidentified as direct photons. The feasibility to perform direct γ +jet measurements with the Forward Upgrade in unpolarized p+p and p+Au collisions at $\sqrt{s_{NN}} = 200$ GeV has been studied. PYTHIA-8.189 [334] was used to produce direct γ +jet and di-jet events. In order to suppress the di-jet background, the leading photon and jet are required to be balanced in transverse momentum, $|\phi^{\gamma} - \phi^{jet}| > 2\pi/3$ and $0.5 < \frac{p_T^{\gamma}}{p_T^{jet}} < 2$. Both the photon and jet have to be in the forward acceptance $1.3 < \eta < 4.0$ with $p_T > 3.2$ GeV/c in 200 GeV p+p collisions. The photon needs to be isolated from other particle activities by requiring the fraction of electromagnetic energy deposition in the cone of ΔR=0.1 around the photon is more than 95% of that in the cone of ΔR=0.5. Jets are reconstructed by an anti-k_T algo-

rithm with ΔR=0.5. After applying these selection cuts, the signal-to-background ratio is around 3:1 [335]. The expected number of selected direct γ +jet events is around 1.0M/0.9M at $\sqrt{s_{NN}}$ = 200 GeV in p+Au collisions for the proposed run in 2024. We conclude that a measurement of direct photon-hadron correlation from p+A collisions is feasible, which is sensitive to the gluon density in $0.001<x<0.005$ in the Au nucleus where parton saturation is expected.

The final state:

Nuclear fragmentation functions: In spite of the remarkable phenomenological successes of QCD, a quantitative understanding of the hadronization process is still one of the great challenges for the theory. Hadronization describes the transition of a quark or gluon into a final state hadron. It is a poorly understood process even in elementary collisions. RHIC's unique versatility will make it possible to study hadronization in vacuum and in the nuclear medium, and additionally with polarized beams (see Sect. 3.2.1 for the latter).

It has long been recognized that the hadron distributions within jets produced in p+p collisions are closely related to the fragmentation functions that have typically been measured in e^+e^- collisions and SIDIS. The key feature of this type of observable is the possibility to determine the relevant momentum fraction z experimentally as the ratio of the hadron to the jet transverse momentum. Recently [336] a quantitative relationship has been derived in a form that enables measurements of identified hadrons in jets in p+p collisions to be included in fragmentation function fits on an equal footing with e^+e^- and SIDIS data. Furthermore, hadrons in p+p jets provide unique access to the gluon fragmentation function, which is poorly determined in current fits [337], in part due to some tension found in the inclusive high p_T pion yields measured by the PHENIX and ALICE collaborations. Here, the proposed measurements can provide valuable new insight into the nature of this discrepancy.

This development motivated STAR to initiate a program of identified particle fragmentation function measurements using p+p jet data at 200 and 500 GeV from 2011, 2012, and 2015. Figure 85 shows the precision that is anticipated for identified π^+ and π^- in 200 GeV p+p collisions for three representative jet p_T bins after the existing data from 2012 and 2015 are combined with future 200 GeV p+p data from 2024. Identified kaon and (anti)proton yields will also be obtained, with somewhat less precision, over a more limited range of hadron z. Once the 2017 data are fully analyzed, the uncertainties for 510 GeV p+p collisions will be comparable to that shown in Fig. 85 at high jet p_T, and a factor of ~ 2 larger than shown in Fig. 85 at low jet p_T. Identified hadron yields will also be measured multi-dimensionally vs. j_T, z, and jet p_T, which will provide important input for unpolarized TMD fits.

Data from the HERMES experiment [281, 283, 338] have shown that production rates of identified hadrons in semi-inclusive deep inelastic e+A scattering differ from those in e+p scattering. These differences cannot be explained by nuclear PDFs, as nuclear effects of strong interactions in the initial state should cancel in this observable. Only the inclusion of nuclear effects in the hadronization process allows theory to reproduce all of the dependencies (z, x, and Q^2) of R_{eA} seen in SIDIS, as shown in Fig. 86.

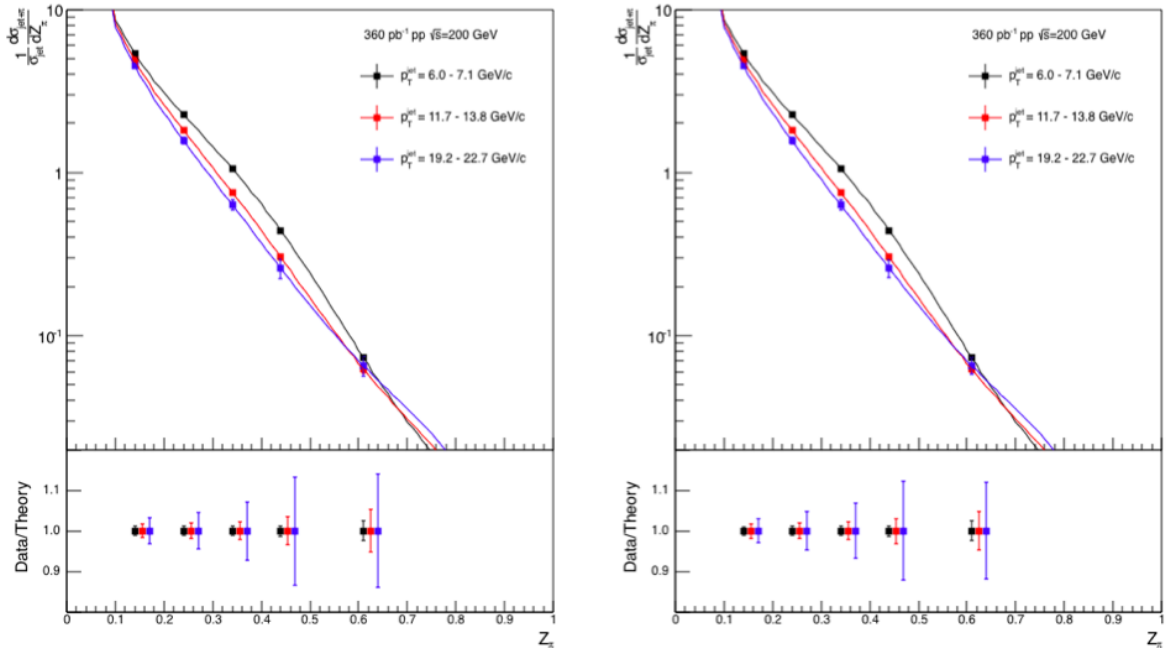

Figure 85: Anticipated precision for identified π^+(left) and π^-(right) within jets at $|\eta| < 0.4$ in 200 GeV p+p collisions for three representative jet p_T bins. The data points are plotted on theoretical predictions based on the DSS14 pion fragmentation functions [336, 337]. Kaons and (anti)protons will also be measured, over the range from $z < 0.5$ at low jet p_T to $z < 0.2$ at high jet p_T, with uncertainties a factor of ∼3 larger than those for pions.

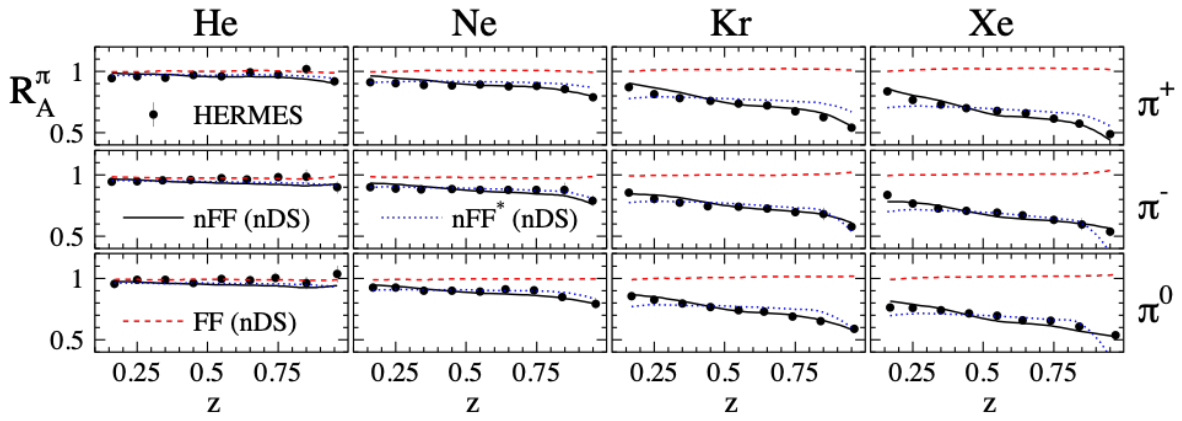

Figure 86: R_{eA} in SIDIS for different nuclei in bins of z as measured by HERMES [281, 283, 338]. The solid lines correspond to the results using effective nuclear FF [290] and the nDS medium modified parton densities [339]. The red dashed lines are estimates assuming the nDS medium modified PDFs but standard DSS vacuum FFs [340, 341] and indicate that nPDFs are insufficient to explain the data

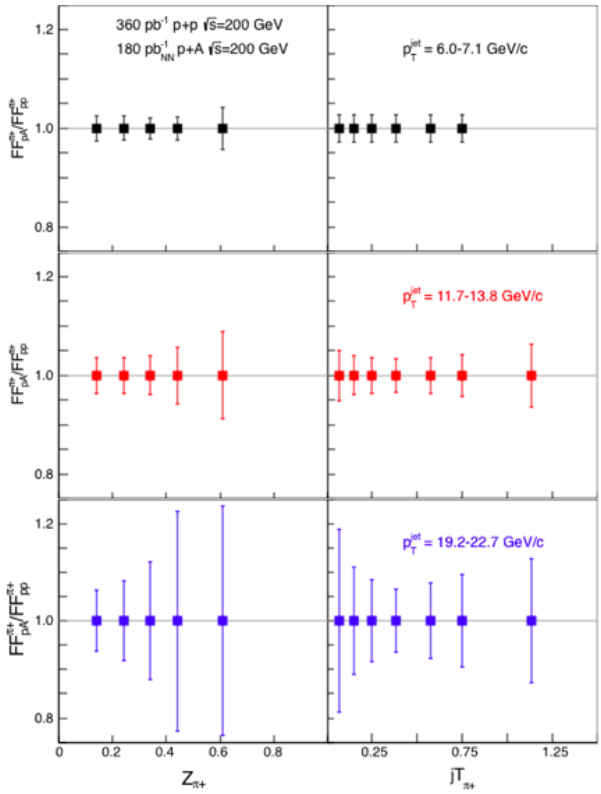

Figure 87: Anticipated precision for measurements of π^+ fragmentation functions in p+A/p+p at $|\eta| < 0.4$ vs. z and j_T in 2024 for three representative jet p_T bins. Uncertainties for π^- will be similar to those shown here for π^+, while those for kaons and (anti)protons will be a factor of $\sim$3 larger. Note that, to be species independent, the nucleon-nucleon equivalent luminosity is specified for p+A.

It is critical to see if these hadronization effects in cold nuclear matter persist at the higher $\sqrt{s}$ and Q^2 accessed at RHIC and EIC – both to probe the underlying mechanism, which is not understood currently, and to explore its possible universality. The combination of p+p jet data from RHIC and future SIDIS data from EIC will also provide a much clearer picture of modified gluon hadronization than will be possible with EIC data alone. Using the 200 GeV p+Au data collected in 2015, STAR will be able to make a first opportunistic measurement of these hadron-jet fragmentation functions in nuclei, but the precision will be limited. Additional data will be needed in 2024 in order to provide a sensitive test for universality, as shown in Figure 87.

4 Detector Updates, Operations, and Opportunities

In this section we discuss the performance of the endcap Time of Flight (eTOF) in Run-20 and progress of the construction of the Forward upgrades. The iTPC and EPD were fully integrated for Run-19.

4.1 Status and Performance of the eTOF

The full eTOF hardware installation was completed in Nov. 2018 followed by the first data taking started in Feb. 2019 by recording about 580 M Au+Au events at $\sqrt{s_{\rm NN}}$ = 19.6 GeV with an eTOF participation of 85%. However, due to several beam loss events causing instantaneous high currents on the readout strips all eTOF preamplifier boards got damaged and no further useful operation was possible during that year. It was decided to replace all preamplifier boards with an improved version using ESD protections diodes on the input. Beside minor issues eTOF showed an excellence performance during Run-20. A reliable start-up procedure and control interface was implemented that allows the full system to be controlled via only 2 commands issued by the shift crew. For Run-20 an improved clock distribution method was installed offering a system synchronization in the order of 35 ps over the full wheel. Figure 88 shows the width of the time distribution (red corresponds to the Gaussian sigma and blue to the RMS) obtained by measuring the arrival time of injected pulser signals on every TDC board. The stability of the system is demonstrated on the right plot of Fig. 88. Here the mean of time distribution width from all pulser channels is plotted vs. the run number. The range of 130 runs reflects a time period of several days.

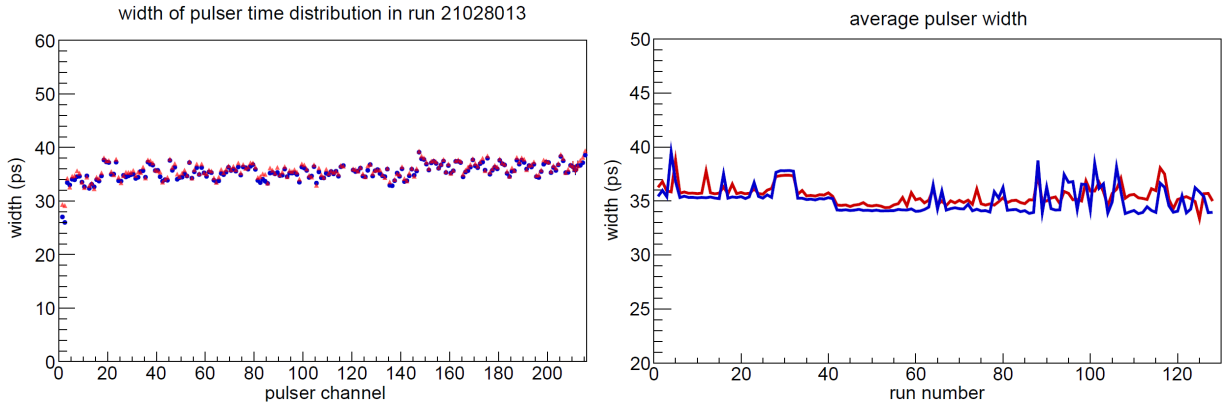

Figure 88: Left: Width of the time distribution obtained by measuring the arrival time of injected pulser signals on every GET4 board. Right: Mean of the time distribution width vs. the run number.

All fixed target runs in 2020 were successfully completed and about 100 M events with eTOF data were collected for each energy. For the $\sqrt{s_{\rm NN}}$ = 11.5 GeV collider run 235 M events with eTOF data were recorded.

In order to demonstrate the eTOF performance fixed target data at $\sqrt{s_{\rm NN}}$ = 7.7 GeV were calibrated and the matching efficiency with the TPC has been deduced as function of the

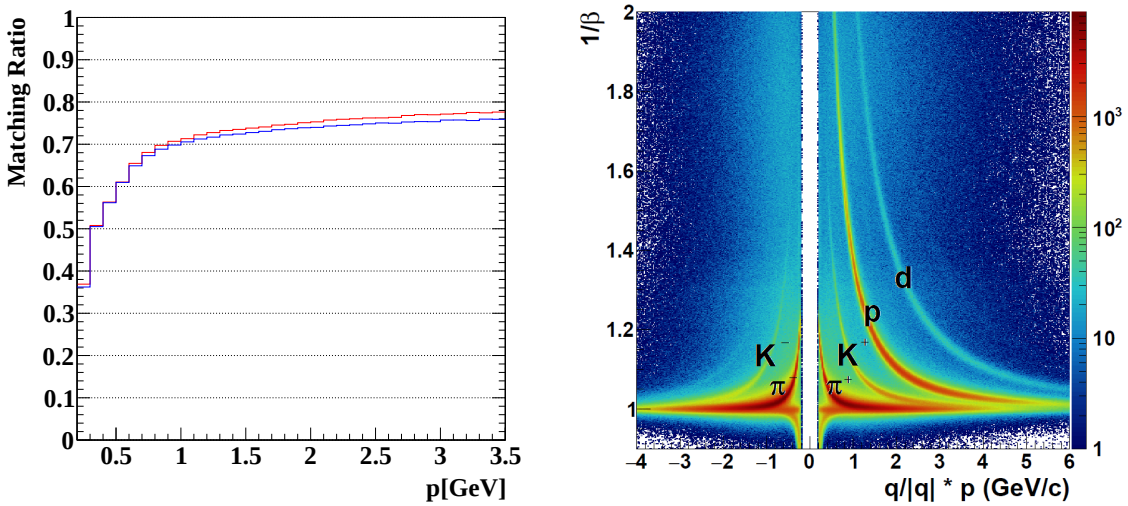

Figure 89: Left: Matching efficiency of MRPC hits in respect to the extrapolated TPC tracks as function of the particle momentum. Right: $1/\beta$ as function of particle momentum. The separation of kaons from pions up to a momenta of 2.5 GeV/c demonstrates the PID capability of eTOF.

particle momentum (see left Fig.89). At a momentum of 1 GeV/c a matching efficiency of 70% is obtained for both MRPC types (red and blue are different MRPC types with different electrode materials). Beyond 1 GeV/c the curve levels off at 75%. The time resolution (not shown here) was determined to be in the order of 80 ps. The good time resolution is reflected in the $1/\beta$ versus the particle momenta plot shown in the right Fig. 89. The narrow particle bands allow for a kaon to pion separation of up to a momentum of 2.5 GeV/c which demonstrates the excellent PID capability of eTOF.

For the upcoming period no major hardware changes for eTOF are foreseen. During Run-20 one MRPC counter developed a high dark current and noise and will be replaced at the next shutdown. Due to COVID-19 travel restrictions it is planed to ship a fully assembled module (3 MRPC counters) to BNL as a replacement for the module housing the broken counter. On a different module it is planned to replace one GBTx readout card, which is currently not working. A substantial eTOF upgrade will be performed on the firmware side of the readout FPGAs. This implies also small adaptations in the control software. With this upgrade an improved startup reliability and a more stable operation is intended.

4.2 Forward Upgrade

STAR is constructing a forward detector system, realized by combining tracking with electromagnetic and hadronic calorimeters for the years beyond 2021. It will have superior detection capability for neutral pions, photons, electrons, jets and leading hadrons covering a region of $2.5 < \eta < 4$. The design of the Forward Calorimeter System (FCS) is driven by consideration of detector performance, integration into STAR and cost optimization. For the electromagnetic calorimeter the refurbished PHENIX sampling EMCal is used, and the

hadronic calorimeter will be newly constructed as a sandwich iron scintillator plate sampling type, based on the extensive STAR Forward Upgrade and EIC Calorimeter Consortium R&D. The existing EPD will be used as a trigger detector especially for a 2 electron trigger. Both calorimeters share the same cost-effective readout electronics, with SiPMs as photo-sensors. This FCS system will have very good ($\sim 10\%/\sqrt{E}$) electromagnetic and ($\sim 50\%/\sqrt{E}+10\%$) hadronic energy resolutions. In addition, a Forward Tracking System (FTS) is being constructed. The FTS will be capable of discriminating hadron charge sign for transverse asymmetry and Drell-Yan measurements in p+A. In heavy ion collisions, measurements of charged particle transverse momenta of $0.2 < p_{\mathrm{T}} < 2$ GeV/c with 20-30% momentum resolution are required. To keep multiple scattering and photon conversion background under control, the material budget of the FTS must be small. Hence, the FTS design is based on three Silicon mini-strip detectors that consist of disks with a wedge-shaped design to cover the full azimuth and $2.5 < \eta < 4.0$; they are read out radially from the outside to minimize the material. The Si-disks are combined with four small-strip Thin Gap Chamber (sTGC) wheels following the ATLAS design [342, 343]. The Si mini-strip disks will be placed in the region $z = 146.6 - 173.7$ cm. The 4 sTGC wheels would be placed 30 cm apart starting from $z = 273$ cm. The Si-Disks readout is based on APV chips, which will reuse the readout chain of the IST, which was part of the STAR HFT. For the sTGC the readout will be based on the ATLAS VMM3 chip [344].

4.2.1 Status

Following the successful directors review in November 2018, the project submitted a proposal for a NSF MRI for construction of EMCAL and HCAL and the associated electronics. The NSF MRI was approved in Summer 2019 and work has been ongoing on all aspects of the upgrade.

4.2.2 Forward Calorimetry System

The platform that supports the HCAL and EMCAL was installed in 2019, followed by the installation of the refurbished PHENIX EMCAl blocks. The installed EMCAL blocks are depicted in Fig. 90. The HCAL absorber blocks are under production at Chapman Lake Instrumentation and Getto Industrial Plating. The first sets of blocks have arrived at BNL. The scintillating tiles have been produced and all 18200 are in hand. About 10,000 of these have been polished at ACU and Valpo and are ready for installation. Other parts are being fabricated at Rutgers, Temple and Ohio State. Front-end electronics cards with the SiPM and readout for both EMCAL and HCAL are in production and testing is underway. The front end cards will be readout by 78 DEP/ADC boards and 3 trigger processor boards housed in 5 crates. About half have been delivered and are undergoing testing at BNL. All DAQ PCs and receiver cards have been installed. The installation will commence once the Run-20b is completed by mid September, and key personnel has come to BNL. The commissioning of the FCS will be continue during Run-21, and will be ready for Run-22.

4.2.3 Forward Silicon Tracking

The procedures for the Si-detector module fabrication has been developed and documented. Several prototype mechanical structures with hybrids mounted have been produced and two wedges were assembled with Si-sensors. Performance of two fully assembled prototype wedges have been evaluated with cosmic ray data and show that all channels can be read out, the signal-to-noise meets requirements, and the efficiency is higher than 90%. The design of the support structures and the interface to the detector modules is nearly complete. If time allows in the upcoming shutdown a test installation of the support frame into STAR is planned. The cooling system, which was used previously for the HFT IST sub-system, has been revived and verification of its performance is on-going. An internal production readiness review with external reviewers was held on August 3, and the initial steps of the mass production have started. The review recommendations, which were useful, will be implemented. Currently there is only limited schedule float for the installation in August 2021.

4.2.4 sTGC Tracking

A full prototype module of the sTGC was designed and produced at Shandong University and tested. This module is now at BNL to undergo testing with the n-pentane gas system that is being built at BNL. Due to space constraints around the beam pipe the final detector will have pentagon shaped modules. The design is complete and production has started of the final pre-production module; mass production is expected to start in October. The read-out electronics are based on the ATLAS VMM3 chip [344] developed for the same kind of detector. The strips of each sTGC layer can be handled by 24 Front-End Boards (FEB). In total 96 FEBs are needed for 4 sTGC layers. The FEBs are vertically inserted in the sTGC chamber. The signals are send to Readout Boards (ROD) placed in standard VME crates and interfaced to the STAR DAQ. The electronics design and fabrication is done at USTC, Hefei. The FEB prototype boards have been tested, the prototype RDO is under construction, and the VMM3 chips are being procured. The design of the installation and mounting frames need to be finished. The n-pentane gas system and Interlocks have been designed and have been approved.

4.2.5 Software

The trigger algorithms for the FCS have been well defined and simulated, the FPGA codes are currently under development.

The forward tracking utilizing hits from the 4 sTGC planes and3 Si-layers has been developed and good performance has been demonstrated. As forward tracking is very different than mid-rapidity tracking new tools had to be developed. The tracking algorithm is based on modern techniques and depends on GENFIT, a general purpose tracking toolkit and in addition the iLCSoft KiTrack a Cellular Automata library are used to seed track finding.

Figure 90: A view of the installed forward ECal detector halves, left and right from the beam pipe.

References

[1] STAR, L. Adamczyk *et al.*, Phys. Rev. C **96**, 024905 (2017), 1702.01108.

[2] STAR, R. Kunnawalkam Elayavalli, PoS **HardProbes2018**, 090 (2018), 1903.12115.

[3] STAR, J. Adam *et al.*, Phys. Rev. D **101**, 052004 (2020), 1912.08187.

[4] STAR, J. Adam *et al.*, Phys. Rev. C **102**, 014905 (2020), 1911.12168.

[5] STAR, J. Adam *et al.*, (2019), 1906.09363.

[6] STAR, J. Adam *et al.*, (2020), 2003.02114.

[7] STAR, J. Adam *et al.*, (2020), 2006.00582.

[8] STAR, J. Adam *et al.*, Phys. Rev. D **100**, 052005 (2019), 1906.02740.

[9] STAR, R. Licenik, Measurement of inclusive jet production in Au+Au collisions at $\sqrt{s_{\mathrm{NN}}} = 200$ GeV by the STAR experiment, 2020, 2008.10006.

[10] STAR, N. R. Sahoo, Measurement of γ+jet and π^0+jet in central Au+Au collisions at $\sqrt{s_{\mathrm{NN}}} = 200$ GeV with the STAR experiment, 2020, 2008.08789.

[11] ATLAS, M. Aaboud *et al.*, Phys. Rev. Lett. **123**, 042001 (2019), 1902.10007.

[12] CMS, S. Chatrchyan *et al.*, Phys. Rev. C **90**, 024908 (2014), 1406.0932.

[13] STAR, S. Oh, Measurement of semi-inclusive jet fragmentation functions in Au+Au collisions at sqrt(s_NN) = 200 GeV in STAR, 2020, 2008.08631.

[14] T. Sjöstrand *et al.*, Comput. Phys. Commun. **191**, 159 (2015), 1410.3012.

[15] STAR, L. Adamczyk *et al.*, Phys. Rev. Lett. **119**, 062301 (2017), 1609.03878.

[16] SN0619 : A Proposal for STAR Inner TPC Sector Upgrade (iTPC) https://drupal.star.bnl.gov/STAR/starnotes/public/sn0619.

[17] STAR, CBM eTOF Group, The CBM Collaboration eTOF Group, (2016), 1609.05102.

[18] J. Adams *et al.*, Nucl. Instrum. Meth. A **968**, 163970 (2020), 1912.05243.

[19] STAR, J. Adam *et al.*, Phys. Rev. C **98**, 014910 (2018), 1805.04400.

[20] STAR, L. Adamczyk *et al.*, Nature **548**, 62 (2017), 1701.06657.

[21] W.-T. Deng and X.-G. Huang, Phys. Rev. C **93**, 064907 (2016), 1603.06117.

[22] STAR, J. Adams, Differential measurements of Λ polarization in Au+Au collisions and a search for the magnetic field by STAR, in *the XXVII-Ith International Conference on Ultra-relativistic Nucleus-Nucleus Collisions*, 2019, https://indico.cern.ch/event/792436/contributions/3535689/.

[23] I. Karpenko and F. Becattini, Eur. Phys. J. C **77**, 213 (2017), 1610.04717.

[24] Y. Jiang, Z.-W. Lin, and J. Liao, Phys. Rev. C **94**, 044910 (2016), 1602.06580, [Erratum: Phys.Rev.C 95, 049904 (2017)].

[25] K. Schilling, P. Seyboth, and G. E. Wolf, Nucl. Phys. B **15**, 397 (1970), [Erratum: Nucl.Phys.B 18, 332 (1970)].

[26] STAR, S. Singha, Measurement of global spin alignment of $k*0$, $k*\pm$ and ϕ vector mesons using the STAR detector at RHIC, in *the XXVII-Ith International Conference on Ultra-relativistic Nucleus-Nucleus Collisions*, 2019, https://indico.cern.ch/event/792436/contributions/3535685/.

[27] R. Bryan and B. Scott, Phys. Rev. **177**, 1435 (1969).

[28] M. Nagels, T. Rijken, and J. de Swart, Phys. Rev. D **17**, 768 (1978).

[29] STAR, L. Adamczyk *et al.*, Phys. Rev. Lett. **115**, 222301 (2015), 1505.07812.

[30] STAR, S. Huang, Explore the nuclei deformation with a expanding QGP fireball, in *The 36th Winter Workshop on Nuclear Dynamics*, 2020, https://indico.cern.ch/event/841247/contributions/3740391/.

[31] G. Giacalone, Phys. Rev. Lett. **124**, 202301 (2020), 1910.04673.

[32] U. Heinz and R. Snellings, Ann. Rev. Nucl. Part. Sci. **63**, 123 (2013), 1301.2826.

[33] STAR, J. Adam *et al.*, (2020), 2006.13537.

[34] ALICE, S. Acharya *et al.*, Phys. Lett. **B773**, 68 (2017), 1705.04377.

[35] P. Alba *et al.*, (2017), 1711.05207.

[36] B. Schenke, C. Shen, and P. Tribedy, Phys. Rev. **C99**, 044908 (2019), 1901.04378.

[37] H. Song, S. A. Bass, U. Heinz, T. Hirano, and C. Shen, Phys. Rev. Lett. **106**, 192301 (2011), 1011.2783, [Erratum: Phys.Rev.Lett. 109, 139904 (2012)].

[38] D. Teaney and L. Yan, Phys. Rev. **C83**, 064904 (2011), 1010.1876.

[39] Z. Qiu and U. W. Heinz, Phys.Rev. **C84**, 024911 (2011), 1104.0650.

[40] G. Denicol, H. Niemi, E. Molnar, and D. Rischke, Phys. Rev. D **85**, 114047 (2012), 1202.4551, [Erratum: Phys.Rev.D 91, 039902 (2015)].

[41] W. Florkowski, R. Ryblewski, and M. Spaliński, Phys. Rev. D **94**, 114025 (2016), 1608.07558.

[42] K. Dusling and R. Venugopalan, Phys. Rev. Lett. **108**, 262001 (2012), 1201.2658.

[43] PHENIX, C. Aidala *et al.*, Nature Phys. **15**, 214 (2019), 1805.02973.

[44] CMS, S. Chatrchyan *et al.*, Phys. Lett. B **724**, 213 (2013), 1305.0609.

[45] STAR, R. A. Lacey, Long-range collectivity in small collision-systems with two- and four-particle correlations @ STAR, in *28th International Conference on Ultrarelativistic Nucleus-Nucleus Collisions*, 2020, 2002.11889.

[46] L. D. McLerran and T. Toimela, Phys. Rev. D **31**, 545 (1985).

[47] H. Weldon, Phys. Rev. D **42**, 2384 (1990).

[48] R. Rapp and J. Wambach, Eur. Phys. J. A **6**, 415 (1999), hep-ph/9907502.

[49] P. M. Hohler and R. Rapp, Phys. Lett. B **731**, 103 (2014), 1311.2921.

[50] C. Jung and L. von Smekal, Phys. Rev. D **100**, 116009 (2019), 1909.13712.

[51] H.-T. Ding *et al.*, Phys. Rev. D **83**, 034504 (2011), 1012.4963.

[52] J. Atchison and R. Rapp, J. Phys. Conf. Ser. **832**, 012057 (2017).

[53] R. Rapp and H. van Hees, Phys. Lett. B **753**, 586 (2016), 1411.4612.

[54] R. Chatterjee, D. K. Srivastava, U. W. Heinz, and C. Gale, Phys. Rev. C **75**, 054909 (2007), nucl-th/0702039.

[55] J. Deng, Q. Wang, N. Xu, and P. Zhuang, Phys. Lett. B **701**, 581 (2011), 1009.3091.

[56] P. Mohanty *et al.*, Phys. Rev. C **85**, 031903 (2012), 1111.2159.

[57] E. Speranza, A. Jaiswal, and B. Friman, Phys. Lett. B **782**, 395 (2018), 1802.02479.

[58] STAR, L. Adamczyk *et al.*, Phys. Rev. Lett. **113**, 022301 (2014), 1312.7397, [Addendum: Phys.Rev.Lett. 113, 049903 (2014)].

[59] STAR, L. Adamczyk *et al.*, Phys. Rev. C **92**, 024912 (2015), 1504.01317.

[60] STAR, L. Adamczyk *et al.*, Phys. Lett. B **750**, 64 (2015), 1501.05341.

[61] STAR, J. Adam *et al.*, (2018), 1810.10159.

[62] B. B. Brandt, A. Francis, H. B. Meyer, and H. Wittig, JHEP **03**, 100 (2013), 1212.4200.

[63] STAR, J. Adam *et al.*, (2019), 1910.12400.

[64] C. Li, J. Zhou, and Y.-J. Zhou, Phys. Rev. D **101**, 034015 (2020), 1911.00237.

[65] S. Klein, A. Mueller, B.-W. Xiao, and F. Yuan, (2020), 2003.02947.

[66] STAR Collaboration, J. Adam *et al.*, Phys. Rev. Lett. **124**, 172301 (2020).

[67] J. Adam *et al.*, Physics Letters B **797**, 134917 (2019).

[68] STAR Collaboration, J. Adam *et al.*, Phys. Rev. Lett. **123**, 162301 (2019).

[69] STAR Collaboration, J. Adam *et al.*, Phys. Rev. C **99**, 034908 (2019).

[70] M. Djordjevic, Phys. Rev. Lett. **112**, 042302 (2014).

[71] H. van Hees, M. Mannarelli, V. Greco, and R. Rapp, Phys. Rev. Lett. **100**, 192301 (2008).

[72] S. Cao, G.-Y. Qin, and S. A. Bass, Phys. Rev. C **92**, 024907 (2015).

[73] P. B. Gossiaux and J. Aichelin, Phys. Rev. C **78**, 014904 (2008).

[74] M. Djordjevic and M. Djordjevic, Phys. Rev. C **90**, 034910 (2014).

[75] STAR Collaboration, L. Adamczyk *et al.*, Phys. Rev. Lett. **118**, 212301 (2017).

[76] STAR Collaboration, L. Adamczyk *et al.*, Phys. Rev. C **95**, 034907 (2017).

[77] D. Kharzeev and R. D. Pisarski, Phys.Rev. **D61**, 111901 (2000), hep-ph/9906401.

[78] D. Kharzeev, Phys.Lett. **B633**, 260 (2006), hep-ph/0406125.

[79] S. A. Voloshin, Phys. Rev. Lett. **105**, 172301 (2010), 1006.1020.

[80] W.-T. Deng, X.-G. Huang, G.-L. Ma, and G. Wang, Phys. Rev. C **97**, 044901 (2018), 1802.02292.

[81] H.-J. Xu *et al.*, Phys. Rev. Lett. **121**, 022301 (2018), 1710.03086.

[82] J. Hammelmann, A. Soto-Ontoso, M. Alvioli, H. Elfner, and M. Strikman, (2019), 1908.10231.

[83] STAR 2017 BUR https://drupal.star.bnl.gov/STAR/system/files/STAR_BUR_Run1718_v22_0.pdf.

[84] STAR, J. Adam *et al.*, (2019), 1911.00596.

[85] J. Zhao, H. Li, and F. Wang, Eur. Phys. J. C **79**, 168 (2019), 1705.05410.

[86] STAR, J. Adam *et al.*, (2020), arXiv:2006.05035.

[87] STAR, P. Tribedy, Nucl. Phys. A **967**, 740 (2017), 1704.03845.

[88] STAR, J. Zhao, (2020), 2002.09410.

[89] CMS, A. M. Sirunyan *et al.*, Phys. Rev. **C97**, 044912 (2018), 1708.01602.

[90] H.-j. Xu *et al.*, Chin. Phys. **C42**, 084103 (2018), 1710.07265.

[91] S. A. Voloshin, Phys. Rev. **C98**, 054911 (2018), 1805.05300.

[92] STAR, J. Adam *et al.*, (2020), arXiv:2006.04251.

[93] STAR, Y. Lin, (2020), 2002.11446.

[94] N. Magdy, S. Shi, J. Liao, N. Ajitanand, and R. A. Lacey, Phys. Rev. C **97**, 061901 (2018), 1710.01717.

[95] A. Tang, Chin. Phys. C **44**, 054101 (2020), 1903.04622.

[96] L. Finch and S. Murray, Phys. Rev. C **96**, 044911 (2017), 1801.06476.

[97] STAR, M. Zurek, Longitudinal double-spin asymmetries for inclusive jets produced in $\sqrt{s} = 200$ GeV proton-proton collisions at STAR, in *Nuclear Physics Seminar, Brookhaven National Laboratory*, 2020, https://indico.bnl.gov/event/8632/.

[98] STAR, N. Lukow, Longitudinal double-spin asymmetries for dijets produced in $\sqrt{s} = 200$ GeV proton-proton collisions at STAR, 2020, https://drupal.star.bnl.gov/STAR/blog/nlukow/dijet-all-2015-preliminary.

[99] STAR, L. Adamczyk *et al.*, Phys. Rev. Lett. **115**, 092002 (2015), 1405.5134.

[100] STAR, L. Adamczyk *et al.*, Phys. Rev. **D95**, 071103 (2017), 1610.06616.

[101] D. de Florian, R. Sassot, M. Stratmann, and W. Vogelsang, Phys. Rev. Lett. **113**, 012001 (2014), 1404.4293.

[102] NNPDF, E. R. Nocera, R. D. Ball, S. Forte, G. Ridolfi, and J. Rojo, Nucl. Phys. **B887**, 276 (2014), 1406.5539.

[103] J. Adam *et al.*, Physical Review D **100** (2019).

[104] STAR, T. Lin, Azimuthal Transverse Single-Spin Asymmetries of Charged Pions Within Jets from Polarized pp Collisions at $\sqrt{s} = 200$ GeV, in *Nuclear Physics Seminar, Brookhaven National Laboratory*, 2020, https://indico.bnl.gov/event/8633/.

[105] STAR, H. Liu, Measurement of transverse single-spin asymmetries for dijet production in polarized p+p collisions at $\sqrt{s} = 200$ GeV at STAR, in *Nuclear Physics Seminar, Brookhaven National Laboratory*, 2020, https://indico.bnl.gov/event/8633/.

[106] STAR, S. Heppelmann, Preview from RHIC Run 15 pp and pAu Forward Neutral Pion Production from Transversely Polarized Protons, in *7th International Workshop on Multiple Partonic Interactions at the LHC*, pp. 228–231, 2016.

[107] STAR, Z. Zhu, Measurement of transverse single spin asymmetries at forward rapidities by the STAR experiment at $\sqrt{s} = 200$ and 500 GeV at STAR, in *Nuclear Physics Seminar, Brookhaven National Laboratory*, 2020, https://indico.bnl.gov/event/8632/.

[108] Z.-B. Kang, X. Liu, F. Ringer, and H. Xing, JHEP **11**, 068 (2017), 1705.08443.

[109] Z.-B. Kang, A. Prokudin, F. Ringer, and F. Yuan, Phys. Lett. B **774**, 635 (2017), 1707.00913.

[110] U. D'Alesio, F. Murgia, and C. Pisano, Phys. Rev. D **83**, 034021 (2011), 1011.2692.

[111] J. K. Adkins, *Studying Transverse Momentum Dependent Distributions in Polarized Proton Collisions via Azimuthal Single Spin Asymmetries of Charged Pions in Jets*, PhD thesis, University of Kentucky, 2015, 1907.11233.

[112] STAR, B. Abelev *et al.*, Phys. Rev. Lett. **99**, 142003 (2007), 0705.4629.

[113] J. Cammarota *et al.*, (2020), 2002.08384.

[114] STAR, E. Braidot, Suppression of Forward Pion Correlations in d+Au Interactions at STAR, in *45th Rencontres de Moriond on QCD and High Energy Interactions*, pp. 355–338, 2010, 1005.2378.

[115] STAR, M. Posik, PoS **DIS2019**, 028 (2019), 1908.08490.

[116] NuSea, R. S. Towell *et al.*, Phys. Rev. **D64**, 052002 (2001), hep-ex/0103030.

[117] SeaQuest, K. Nagai, PoS **DIS2018**, 033 (2018).

[118] STAR, S. Fazio, Measuremens of weak boson production with the STAR detector, in *QCD Spin Physics: A Symposium to Honor Jacques Soffer, Brookhaven National Laboratory*, 2019, https://indico.bnl.gov/event/6274/.

[119] V. Bertone, I. Scimemi, and A. Vladimirov, JHEP **06**, 028 (2019), 1902.08474.

[120] M. A. Stephanov, K. Rajagopal, and E. V. Shuryak, Phys. Rev. D **60**, 114028 (1999), hep-ph/9903292.

[121] M. Stephanov, Phys. Rev. Lett. **107**, 052301 (2011), 1104.1627.

[122] STAR, J. Adam *et al.*, (2020), 2001.02852.

[123] HADES, J. Adamczewski-Musch *et al.*, (2020), 2002.08701.

[124] STAR, L. Adamczyk *et al.*, Phys. Rev. **C96**, 044904 (2017), 1701.07065.

[125] F. Becattini, J. Manninen, and M. Gazdzicki, Phys. Rev. C **73**, 044905 (2006), hep-ph/0511092.

[126] A. Andronic, P. Braun-Munzinger, and J. Stachel, Phys. Lett. B **673**, 142 (2009), 0812.1186, [Erratum: Phys.Lett.B 678, 516 (2009)].

[127] J. Cleymans, D. Elliott, A. Keranen, and E. Suhonen, Phys. Rev. C **57**, 3319 (1998), nucl-th/9711066.

[128] J. Cleymans, A. Forster, H. Oeschler, K. Redlich, and F. Uhlig, Phys. Lett. B **603**, 146 (2004), hep-ph/0406108.

[129] I. Kraus, J. Cleymans, H. Oeschler, K. Redlich, and S. Wheaton, Phys. Rev. C **76**, 064903 (2007), 0707.3879.

[130] HADES, J. Adamczewski-Musch *et al.*, Phys. Lett. B **778**, 403 (2018), 1703.08418.

[131] FOPI, K. Piasecki *et al.*, Phys. Rev. C **94**, 014901 (2016), 1602.04378.

[132] A. Andronic, P. Braun-Munzinger, J. Stachel, and H. Stocker, Phys. Lett. B **697**, 203 (2011), 1010.2995.

[133] NA49, T. Anticic *et al.*, Phys. Rev. **C83**, 014901 (2011), 1009.1747.

[134] BRAHMS, I. Arsene *et al.*, Phys. Rev. Lett. **93**, 242303 (2004), nucl-ex/0403005.

[135] Yu. B. Ivanov, Phys. Rev. **C87**, 064905 (2013), 1304.1638.

[136] A. Bzdak, V. Koch, D. Oliinychenko, and J. Steinheimer, Phys. Rev. **C98**, 054901 (2018), 1804.04463.

[137] M. Danysz *et al.*, Phys. Rev. Lett. **11**, 29 (1963).

[138] D. Prowse, Phys. Rev. Lett. **17**, 782 (1966).

[139] S. Aoki *et al.*, Prog. Theor. Phys. **85**, 1287 (1991).

[140] H. Takahashi *et al.*, Nucl. Phys. A **721**, 951 (2003).

[141] T. A. Rijken, M. Nagels, and Y. Yamamoto, Prog. Theor. Phys. Suppl. **185**, 14 (2010).

[142] K. J. Sun, L.-W. Chen, C. M. Ko, J. Pu, and Z. Xu, Phys. Lett. **B781**, 499 (2018), 1801.09382.

[143] STAR, L. Adamczyk *et al.*, Phys. Rev. Lett. **112**, 032302 (2014), 1309.5681.

[144] STAR, L. Adamczyk *et al.*, Phys. Rev. Lett. **113**, 092301 (2014), 1402.1558.

[145] STAR, L. Adamczyk *et al.*, Phys. Lett. **B785**, 551 (2018), 1709.00773.

[146] STAR, X. Luo, PoS **CPOD2014**, 019 (2015), 1503.02558.

[147] X. Luo, Nucl. Phys. **A956**, 75 (2016), 1512.09215.

[148] STAR, L. Adamczyk *et al.*, Phys. Rev. Lett. **121**, 032301 (2018), 1707.01988.

[149] STAR, J. Adam *et al.*, accepted by PRC **arXiv:1903.11778** (2019), 1903.11778.

[150] STAR, D. Zhang, Light Nuclei (d, t) Production in Au + Au Collisions at $\sqrt{s_{NN}}$ = 7.7 - 200 GeV, in *28th International Conference on Ultrarelativistic Nucleus-Nucleus Collisions*, 2020, 2002.10677.

[151] H. Liu *et al.*, Phys. Lett. B **805**, 135452 (2020), 1909.09304.

[152] K. Dusling, W. Li, and B. Schenke, Int. J. Mod. Phys. **E25**, 1630002 (2016), 1509.07939.

[153] L. He *et al.*, Phys. Lett. **B753**, 506 (2016), 1502.05572.

[154] A. Kurkela, U. A. Wiedemann, and B. Wu, Kinetic transport is needed to reliably extract shear viscosity from pA and AA data, in Vol. arXiv:1805.04081, 2018, 1805.04081.

[155] P. Romatschke, Eur. Phys. J. **C78**, 636 (2018), 1802.06804.

[156] J. L. Nagle and W. A. Zajc, Ann. Rev. Nucl. Part. Sci. **68**, 211 (2018), 1801.03477.

[157] B. Schenke, S. Schlichting, and R. Venugopalan, Phys. Lett. **B747**, 76 (2015), 1502.01331.

[158] J. L. Nagle *et al.*, Phys. Rev. Lett. **113**, 112301 (2014), 1312.4565.

[159] PHENIX, A. Adare *et al.*, Phys. Rev. Lett. **111**, 212301 (2013), 1303.1794.

[160] STAR, S. Huang, Nucl. Phys. A **982**, 475 (2019).

[161] B. Schenke, C. Shen, and P. Tribedy, (2020), 2005.14682.

[162] P. Romatschke, Eur. Phys. J. C **75**, 305 (2015), 1502.04745.

[163] C. Shen, J.-F. Paquet, G. S. Denicol, S. Jeon, and C. Gale, Phys. Rev. C **95**, 014906 (2017), 1609.02590.

[164] Workshop on collectivity of small systems in high-energy collisions, 14-16 march 2019, https://indico.cern.ch/event/771998/, Accessed May 2019.

[165] STAR, STAR Public Note SN0644 - Technical Design Report for the iTPC Upgrade, https://drupal.star.bnl.gov/STAR/starnotes/public/sn0644.

[166] STAR, STAR Public Note SN0666 - An Event Plane Detector for STAR, https://drupal.star.bnl.gov/STAR/starnotes/public/sn0666.

[167] STAR, STAR Public Note SN0648 - The STAR Forward Calorimeter System and Forward Tracking System beyond BES-II, https://drupal.star.bnl.gov/STAR/starnotes/public/sn0648.

[168] Z. Citron *et al.Report from Working Group 5: Future physics opportunities for high-density QCD at the LHC with heavy-ion and proton beams* Vol. 7 (, 2019), pp. 1159–1410, 1812.06772.

[169] ALICE, K. Aamodt *et al.*, Phys. Rev. Lett. **105**, 252302 (2010), 1011.3914.

[170] PHENIX, S. S. Adler *et al.*, Phys. Rev. Lett. **94**, 232302 (2005), nucl-ex/0411040.

[171] STAR, J. Adam *et al.*, Phys. Lett. **B784**, 26 (2018), 1804.08647.

[172] ATLAS, M. Aaboud *et al.*, Eur. Phys. J. **C78**, 997 (2018), 1808.03951.

[173] PHENIX, A. Adare *et al.*, Phys. Rev. Lett. **107**, 252301 (2011), 1105.3928.

[174] ATLAS, G. Aad *et al.*, Phys. Rev. C **90**, 044906 (2014), 1409.1792.

[175] STAR, B. I. Abelev *et al.*, Phys. Rev. Lett. **99**, 112301 (2007), nucl-ex/0703033.

[176] CMS Collaboration, Phys. Lett. B **765**, 193 (2017), 1606.06198.

[177] CMS Collaboration, Phys. Rev. Lett. **115**, 012301 (2015), 1502.05382.

[178] ATLAS, M. Aaboud *et al.*, Phys. Lett. **B789**, 444 (2019), 1807.02012.

[179] ALICE, S. Acharya *et al.*, Investigations of anisotropic flow using multi-particle azimuthal correlations in pp, p-Pb, Xe-Xe, and Pb-Pb collisions at the LHC, arXiv:1903.01790, 2019, 1903.01790.

[180] PHENIX, C. Aidala *et al.*, Phys. Rev. Lett. **120**, 062302 (2018), 1707.06108.

[181] A. Huss *et al.*, (2020), 2007.13758.

[182] A. Huss *et al.*, (2020), 2007.13754.

[183] I. Arsene *et al.*, Phys. Rev. C **75**, 034902 (2007), nucl-th/0609042.

[184] J. Harris *et al.*, Phys. Lett. B **153**, 377 (1985).

[185] R. Stock, Phys. Rept. **135**, 259 (1986).

[186] J. Molitoris and H. Stoecker, Phys. Rev. C **32**, 346 (1985).

[187] H. Kruse, B. Jacak, and H. Stoecker, Phys. Rev. Lett. **54**, 289 (1985).

[188] P. Danielewicz, R. Lacey, and W. G. Lynch, Science **298**, 1592 (2002), nucl-th/0208016.

[189] W. Reisdorf, Heavy ion collisions in the 1A GeV regime: how well do we join up to astrophysics?, in *International Workshop on Nuclear Symmetry Energy and Reaction Mechanisms*, 2013, 1307.4210.

[190] J. Aichelin and C. M. Ko, Phys. Rev. Lett. **55**, 2661 (1985).

[191] KAOS, C. T. Sturm *et al.*, Phys. Rev. Lett. **86**, 39 (2001), nucl-ex/0011001.

[192] C. Hartnack and J. Aichelin, J. Phys. G **28**, 1649 (2002).

[193] C. Fuchs *et al.*, J. Phys. G **28**, 1615 (2002), nucl-th/0103036.

[194] T. Klahn *et al.*, Phys. Rev. C **74**, 035802 (2006), nucl-th/0602038.

[195] T. Fischer *et al.*, Nature Astron. **2**, 980 (2018), 1712.08788.

[196] A. Aprahamian *et al.*, Reaching for the horizon: The 2015 long range plan for nuclear science, 2015, The 2015 Long Range Plan for Nuclear Science "Reaching for the Horizon" http://science.energy.gov/~/media/np/nsac/pdf/2015LRP/2015_LRPNS_091815.pdf.

[197] RHIC luminosity projection https://www.rhichome.bnl.gov//RHIC/Runs/RhicProjections.pdf.

[198] The STAR Forward Calorimeter System and Forward Tracking System beyond BES-II https://drupal.star.bnl.gov/STAR/files/Proposal.ForwardUpgrade.Nov_.2018.Review.pdf.

[199] G. Denicol, A. Monnai, and B. Schenke, Phys. Rev. Lett. **116**, 212301 (2016), 1512.01538.

[200] H. Niemi, G. S. Denicol, P. Huovinen, E. Molnar, and D. H. Rischke, Phys. Rev. **C86**, 014909 (2012), 1203.2452.

[201] B. Schenke and S. Schlichting, Phys. Rev. **C94**, 044907 (2016), 1605.07158.

[202] W. Li, Nucl. Phys. A **967**, 59 (2017), 1704.03576.

[203] P. Bozek, W. Broniowski, and J. Moreira, Phys. Rev. **C83**, 034911 (2011), 1011.3354.

[204] J. Jia and P. Huo, Phys. Rev. **C90**, 034915 (2014), 1403.6077.

[205] L.-G. Pang, H. Petersen, G.-Y. Qin, V. Roy, and X.-N. Wang, Eur. Phys. J. **A52**, 97 (2016), 1511.04131.

[206] CMS, V. Khachatryan *et al.*, Phys. Rev. C **92**, 034911 (2015), 1503.01692.

[207] ATLAS, M. Aaboud *et al.*, Eur. Phys. J. C **78**, 142 (2018), 1709.02301.

[208] STAR Collaboration, L. Adamczyk *et al.*, Manuscript under preparation (2016).

[209] A. Behera, M. Nie, and J. Jia, Phys. Rev. Res. **2**, 023362 (2020), 2003.04340.

[210] C. Shen and B. Schenke, Phys. Rev. **C97**, 024907 (2018), 1710.00881.

[211] STAR, B. Abelev *et al.*, Phys. Rev. C **76**, 064904 (2007), 0706.0472.

[212] Z.-T. Liang, J. Song, I. Upsal, Q. Wang, and Z.-B. Xu, (2019), 1912.10223.

[213] Y. Xie, D. Wang, and L. P. Csernai, Eur. Phys. J. C **80**, 39 (2020), 1907.00773.

[214] X.-L. Sheng, L. Oliva, and Q. Wang, Phys. Rev. D **101**, 096005 (2020), 1910.13684.

[215] X.-L. Sheng, Q. Wang, and X.-N. Wang, (2020), 2007.05106.

[216] A. Bazavov *et al.*, Phys. Rev. D **95**, 054504 (2017), 1701.04325.

[217] S. Borsanyi *et al.*, JHEP **10**, 205 (2018), 1805.04445.

[218] STAR, A. Pandav, (2020), 2003.12503.

[219] B. Chen, M. Hu, H. Zhang, and J. Zhao, Phys. Lett. B **802**, 135271 (2020), 1910.08275.

[220] X. Guo, S. Shi, N. Xu, Z. Xu, and P. Zhuang, Phys. Lett. B **751**, 215 (2015), 1502.04407.

[221] B. Chen, X. Du, and R. Rapp, Nucl. Part. Phys. Proc. **289-290**, 475 (2017), 1612.02089.

[222] ALICE, J. Adam *et al.*, JHEP **05**, 179 (2016), 1506.08804.

[223] ATLAS, M. Aaboud *et al.*, Eur. Phys. J. C **78**, 762 (2018), 1805.04077.

[224] CMS, A. M. Sirunyan *et al.*, Phys. Rev. Lett. **118**, 162301 (2017), 1611.01438.

[225] JETSCAPE, S. Cao *et al.*, Phys. Rev. C **96**, 024909 (2017), 1705.00050.

[226] JETSCAPE, A. Kumar *et al.*, Jet quenching in a multi-stage Monte Carlo approach, in *28th International Conference on Ultrarelativistic Nucleus-Nucleus Collisions*, 2020, 2002.07124.

[227] Y. Mehtar-Tani and K. Tywoniuk, Phys. Rev. D **98**, 051501 (2018), 1707.07361.

[228] Y. Mehtar-Tani and K. Tywoniuk, Nucl. Phys. A **979**, 165 (2018), 1706.06047.

[229] B. Zakharov, (2020), 2003.10182.

[230] L. Chen, G.-Y. Qin, S.-Y. Wei, B.-W. Xiao, and H.-Z. Zhang, Phys. Lett. B **773**, 672 (2017), 1607.01932.

[231] D. A. Appel, Phys. Rev. D **33**, 717 (1986).

[232] J. Blaizot and L. D. McLerran, Phys. Rev. D **34**, 2739 (1986).

[233] ALICE, J. Adam *et al.*, JHEP **09**, 170 (2015), 1506.03984.

[234] F. D'Eramo, K. Rajagopal, and Y. Yin, JHEP **01**, 172 (2019), 1808.03250.

[235] ALICE, J. Norman.

[236] A. J. Larkoski, S. Marzani, G. Soyez, and J. Thaler, JHEP **05**, 146 (2014), 1402.2657.

[237] Y.-T. Chien and R. Kunnawalkam Elayavalli, (2018), 1803.03589.

[238] J.-w. Qiu and G. F. Sterman, Phys. Rev. D **59**, 014004 (1999), hep-ph/9806356.

[239] K. Kanazawa, Y. Koike, A. Metz, and D. Pitonyak, Phys. Rev. D **89**, 111501 (2014).

[240] L. Bland *et al.*, Physics Letters B **750**, 660 (2015).

[241] STAR, L. Adamczyk *et al.*, Phys. Rev. Lett. **116**, 132301 (2016), 1511.06003.

[242] P. Sun, J. Isaacson, C. P. Yuan, and F. Yuan, Universal non-perturbative functions for sidis and drell-yan processes, 2014, 1406.3073.

[243] J. P. Ralston and D. E. Soper, Nuclear Physics B **152**, 109 (1979).

[244] R. Jaffe and X.-D. Ji, Nucl. Phys. B **375**, 527 (1992).

[245] P. Mulders and R. Tangerman, Nucl. Phys. B **461**, 197 (1996), hep-ph/9510301, [Erratum: Nucl.Phys.B 484, 538–540 (1997)].

[246] D. Sivers, Nuovo Cim. C **035N2**, 171 (2012), 1109.2521.

[247] C. Alexandrou *et al.*, Phys. Rev. D **98**, 091503 (2018).

[248] R. Jaffe and X.-D. Ji, Phys. Rev. Lett. **67**, 552 (1991).

[249] J. C. Collins, S. F. Heppelmann, and G. A. Ladinsky, Nucl. Phys. B **420**, 565 (1994), hep-ph/9305309.

[250] L. Adamczyk *et al.*, Phys. Lett. B **780**, 332–339 (2018).

[251] M. Radici and A. Bacchetta, Phys. Rev. Lett. **120**, 192001 (2018), 1802.05212.

[252] J. Collins and J.-W. Qiu, Phys. Rev. D **75**, 114014 (2007).

[253] T. C. Rogers and P. J. Mulders, Phys. Rev. D **81**, 094006 (2010).

[254] X. Liu, F. Ringer, W. Vogelsang, and F. Yuan, Factorization and its breaking in dijet single transverse spin asymmetries in pp collisions, 2020, 2008.03666.

[255] Z.-B. Kang, K. Lee, D. Y. Shao, and J. Terry, The sivers asymmetry in hadronic dijet production, 2020, 2008.05470.

[256] F. Yuan, Phys. Rev. Lett. **100**, 032003 (2008).

[257] F. Yuan, Phys. Rev. D **77**, 074019 (2008).

[258] STAR, L. Adamczyk *et al.*, Phys. Rev. D **97**, 032004 (2018), 1708.07080.

[259] M. Anselmino *et al.*, Phys. Rev. D **73**, 014020 (2006), hep-ph/0509035.

[260] M. Anselmino *et al.*, Phys. Rev. D **75**, 054032 (2007).

[261] J. Soffer, Phys. Rev. Lett. **74**, 1292 (1995).

[262] U. D'Alesio, F. Murgia, and C. Pisano, Phys, Lett. B **773**, 300–306 (2017).

[263] H1, ZEUS, F. Aaron *et al.*, Eur. Phys. J. C **72**, 2175 (2012), 1207.4864.

[264] CMS, V. Khachatryan *et al.*, Phys. Rev. D **92**, 012003 (2015), 1503.08689.

[265] S. L. Bueltmann *et al.*, Phys. Lett. B **579**, 245 (2004), nucl-ex/0305012.

[266] S. Bultmann *et al.*, Phys. Lett. B **632**, 167 (2006), nucl-ex/0507030.

[267] pp2pp, S. Bultmann *et al.*, Phys. Lett. B **647**, 98 (2007), nucl-ex/0610022.

[268] STAR, L. Adamczyk *et al.*, Phys. Lett. B **719**, 62 (2013), 1206.1928.

[269] SN0605: A polarized p+p and p+A program for the next years https://drupal.star.bnl.gov/STAR/starnotes/public/sn0605.

[270] I. Helenius, in *Talk at 7th International Workshop on Multiple Partonic Interactions at the LHC*, http://indico.ictp.it/event/a14280/session/266/contribution/1042/material/slides/0.pdf.

[271] STAR, C. Dilks, PoS **DIS2016**, 212 (2016), 1805.08875.

[272] A. Airapetian *et al.*, Phys. Lett. B **693**, 11–16 (2010).

[273] C. Adolph *et al.*, Phys. Lett. B **744**, 250–259 (2015).

[274] D. Müller, D. Robaschik, B. Geyer, F.-M. Dittes, and J. Hoˇ rejši, Fortsch. Phys. **42**, 101 (1994), hep-ph/9812448.

[275] X.-D. Ji, Phys. Rev. Lett. **78**, 610 (1997), hep-ph/9603249.

[276] A. Radyushkin, Phys. Lett. B **380**, 417 (1996), hep-ph/9604317.

[277] M. Burkardt, Phys. Rev. D **62**, 071503 (2000), hep-ph/0005108, [Erratum: Phys.Rev.D 66, 119903 (2002)].

[278] S. Klein and J. Nystrand, Photoproduction of J / psi and Upsilon in pp and anti-p p collisions, in *5th Workshop on Small x and Diffractive Physics*, 2003, hep-ph/0310223.

[279] S. R. Klein, J. Nystrand, J. Seger, Y. Gorbunov, and J. Butterworth, Comput. Phys. Commun. **212**, 258 (2017), 1607.03838.

[280] J. Lansberg, L. Massacrier, L. Szymanowski, and J. Wagner, Phys. Lett. B **793**, 33 (2019), 1812.04553.

[281] HERMES, A. Airapetian *et al.*, Phys. Lett. B **577**, 37 (2003), hep-ex/0307023.

[282] HERMES, A. Airapetian *et al.*, Nucl. Phys. B **780**, 1 (2007), 0704.3270.

[283] HERMES, A. Airapetian *et al.*, Phys. Lett. B **684**, 114 (2010), 0906.2478.

[284] W. Brooks and H. Hakobyan, Nucl. Phys. A **830**, 361C (2009), 0907.4606.

[285] NuSea, M. Vasilev *et al.*, Phys. Rev. Lett. **83**, 2304 (1999), hep-ex/9906010.

[286] DIS–2014 https://indico.cern.ch/event/258017/contributions/1588381/attachments/453934/629277/pA_DIS2014_Paukkunen.pdf.

[287] D. de Florian, R. Sassot, P. Zurita, and M. Stratmann, Phys. Rev. D **85**, 074028 (2012), 1112.6324.

[288] PHENIX, S. Adler *et al.*, Phys. Rev. Lett. **98**, 172302 (2007), nucl-ex/0610036.

[289] K. Eskola, H. Paukkunen, and C. Salgado, Nucl. Phys. A **855**, 150 (2011), 1011.6534.

[290] R. Sassot, M. Stratmann, and P. Zurita, Phys. Rev. D **81**, 054001 (2010), 0912.1311.

[291] K. J. Eskola, P. Paakkinen, H. Paukkunen, and C. A. Salgado, Eur. Phys. J. C **77**, 163 (2017), 1612.05741.

[292] N. Armesto, H. Paukkunen, J. M. Penín, C. A. Salgado, and P. Zurita, Eur. Phys. J. C **76**, 218 (2016), 1512.01528.

[293] H. Paukkunen and P. Zurita, JHEP **12**, 100 (2014), 1402.6623.

[294] E. Aschenauer *et al.*, (2014), 1409.1633.

[295] H. Paukkunen, K. J. Eskola, and C. Salgado, Nucl. Phys. A **931**, 331 (2014), 1408.4563.

[296] K. J. Eskola, H. Paukkunen, and C. A. Salgado, JHEP **10**, 213 (2013), 1308.6733.

[297] L. Gribov, E. Levin, and M. Ryskin, Phys. Rept. **100**, 1 (1983).

[298] E. Iancu and R. Venugopalan, The Color glass condensate and high-energy scattering in QCD, in *In *Hwa, R.C. (ed.) et al.: Quark gluon plasma* 249-3363*, 2003, hep-ph/0303204.

[299] H. Weigert, Prog. Part. Nucl. Phys. **55**, 461 (2005), hep-ph/0501087.

[300] J. Jalilian-Marian and Y. V. Kovchegov, Prog. Part. Nucl. Phys. **56**, 104 (2006), hep-ph/0505052.

[301] F. Gelis, E. Iancu, J. Jalilian-Marian, and R. Venugopalan, Ann. Rev. Nucl. Part. Sci. **60**, 463 (2010), 1002.0333.

[302] G. Giuliani, H. Zheng, and A. Bonasera, Prog. Part. Nucl. Phys. **76**, 116 (2014), 1311.1811.

[303] Y. V. Kovchegov and E. Levin *Quantum chromodynamics at high energy* Vol. 33 (Cambridge University Press, 2012).

[304] A. H. Mueller and J.-w. Qiu, Nucl. Phys. B **268**, 427 (1986).

[305] L. McLerran and R. Venugopalan, Phys. Rev. D **49**, 2233 (1994).

[306] L. McLerran and R. Venugopalan, Phys. Rev. D **49**, 3352 (1994).

[307] L. McLerran and R. Venugopalan, Phys. Rev. D **50**, 2225 (1994).

[308] Y. V. Kovchegov, Phys. Rev. D **54**, 5463 (1996).

[309] Y. V. Kovchegov, Phys. Rev. D **55**, 5445 (1997).

[310] J. Jalilian-Marian, A. Kovner, L. McLerran, and H. Weigert, Phys. Rev. D **55**, 5414 (1997).

[311] A. H. Mueller, Nucl. Phys. **B415**, 373 (1994).

[312] A. H. Mueller and B. Patel, Nucl. Phys. B **425**, 471 (1994), hep-ph/9403256.

[313] I. Balitsky, Nucl. Phys. **B463**, 99 (1996), hep-ph/9509348.

[314] I. Balitsky, Phys. Rev. D **60**, 014020 (1999), hep-ph/9812311.

[315] Y. V. Kovchegov, Phys. Rev. **D60**, 034008 (1999), hep-ph/9901281.

[316] Y. V. Kovchegov, Phys. Rev. D **61**, 074018 (2000), hep-ph/9905214.

[317] J. Jalilian-Marian, A. Kovner, and H. Weigert, Phys. Rev. D **59**, 014015 (1998), hep-ph/9709432.

[318] J. Jalilian-Marian, A. Kovner, A. Leonidov, and H. Weigert, Phys. Rev. D **59**, 014014 (1998), hep-ph/9706377.

[319] E. Iancu, A. Leonidov, and L. D. McLerran, Phys. Lett. B **510**, 133 (2001), hep-ph/0102009.

[320] E. Iancu, A. Leonidov, and L. D. McLerran, Nucl. Phys. **A692**, 583 (2001), hep-ph/0011241.

[321] A. Accardi *et al.*, Eur. Phys. J. A **52**, 268 (2016), 1212.1701.

[322] Y. V. Kovchegov and M. D. Sievert, Nucl. Phys. B **903**, 164 (2016), 1505.01176.

[323] CMS, S. Chatrchyan *et al.*, Eur. Phys. J. C **74**, 2951 (2014), 1401.4433.

[324] STAR, E. Braidot, Nucl. Phys. A **854**, 168 (2011), 1008.3989.

[325] PHENIX, A. Adare *et al.*, Phys. Rev. Lett. **107**, 172301 (2011), 1105.5112.

[326] C. Marquet, Nucl. Phys. A **796**, 41 (2007), 0708.0231.

[327] J. L. Albacete and C. Marquet, Phys. Rev. Lett. **105**, 162301 (2010), 1005.4065.

[328] Z.-B. Kang, I. Vitev, and H. Xing, Phys. Rev. D **85**, 054024 (2012), 1112.6021.

[329] M. Strikman and W. Vogelsang, Phys. Rev. D **83**, 034029 (2011), 1009.6123.

[330] J. Jalilian-Marian and A. H. Rezaeian, Phys. Rev. D **86**, 034016 (2012), 1204.1319.

[331] J. L. Albacete and C. Marquet, Nucl. Phys. A **854**, 154 (2011), 1009.3215.

[332] K. J. Eskola, H. Paukkunen, and C. A. Salgado, JHEP **07**, 102 (2008), 0802.0139.

[333] A. H. Rezaeian, Phys. Rev. D **86**, 094016 (2012), 1209.0478.

[334] T. Sjostrand, S. Mrenna, and P. Z. Skands, Comput. Phys. Commun. **178**, 852 (2008), 0710.3820.

[335] Di-jet production from pythia8.189 is scaled down due to its overestimation of inclusive π_0 yields compared to those reported by BRAHMS in phys. rev. lett. 98 (2007) 252001 and STAR in phys. rev. lett. 97 (2006) 152302.

[336] T. Kaufmann, A. Mukherjee, and W. Vogelsang, Phys. Rev. D **92**, 054015 (2015), 1506.01415, [Erratum: Phys.Rev.D 101, 079901 (2020)].

[337] D. de Florian, R. Sassot, M. Epele, R. J. Hernández-Pinto, and M. Stratmann, Phys. Rev. D **91**, 014035 (2015), 1410.6027.

[338] A. Khouaja *et al.*, Nucl. Phys. A **780**, 1 (2006).

[339] D. de Florian and R. Sassot, Phys. Rev. D **69**, 074028 (2004), hep-ph/0311227.

[340] D. de Florian, R. Sassot, and M. Stratmann, Phys. Rev. D **75**, 114010 (2007), hep-ph/0703242.

[341] D. de Florian, R. Sassot, and M. Stratmann, Phys. Rev. D **76**, 074033 (2007), 0707.1506.

[342] V. Smakhtin *et al.*, Nucl. Instrum. Meth. **A598**, 196 (2009).

[343] A. Abusleme *et al.*, Nucl. Instrum. Meth. **A817**, 85 (2016), 1509.06329.

[344] Iakovidis, George, EPJ Web Conf. **174**, 07001 (2018).